

Copyright

by

Suyog Suresh Benegalrao

2012

The Thesis committee for Suyog Suresh Benegalrao
Certifies that this is the approved version of the following thesis:

Performance Characterization of the Attitude Control
System for the GRACE Mission

APPROVED BY

SUPERVISING COMMITTEE:

Supervisor: _____
Srinivas Bettadpur

E. Glenn Lightsey

**Performance Characterization of the Attitude Control
System for the GRACE Mission**

by

Suyog Suresh Benegalrao, B.S.

Thesis

Presented to the Faculty of the Graduate School
of The University of Texas at Austin
in Partial Fulfillment
of the Requirements
for the Degree of

MASTER OF SCIENCE IN ENGINEERING

The University of Texas at Austin

August 2012

Dedicated to the two best classroom teachers of my educational career: Mrs. Deborah Sanders and Mr. Paul Kazmierczak. Thank you for infusing your teaching style with a demonstrable passion for both the subject at hand and the learning process itself. You have my undying gratitude for believing in my ability to succeed, and for encouraging me in all my academic pursuits.

Acknowledgments

I would like to first thank my advisor, Dr. Srinivas Bettadpur, for allowing me the opportunity to work on the GRACE mission in a graduate capacity, and for providing invaluable guidance and patience throughout my graduate tenure at the University of Texas. I want also like to thank Dr. E. Glenn Lightsey for acting as second reader for my thesis, and for assisting me during my graduate application process. Thanks to the entire GRACE team, especially my fellow graduate students: Sandeep Krishnan, Christopher McCullough, Alex Pini, and Carly Sakumura. Thanks also to my undergraduate advisor, Dr. James Craig, and to my career mentor, Neerav Shah, for giving me my first jobs in research and attitude control that have paved the way for all subsequent opportunities. A special thanks to my parents Yogini and Suresh Benegalrao for acting as shining examples that I have tried to emulate in my career as well as in life. A special thanks also to my grandparents Radha and Vasudev Naimpally for their dedication to my development as a student as well as a person. Finally, all gratitude goes to God for watching over me and guiding me in every action that I perform.

Performance Characterization of the Attitude Control System for the GRACE Mission

by

Suyog Suresh Benegalrao, M.S.E.

The University of Texas at Austin, 2012

SUPERVISOR: Srinivas Bettadpur

The Gravity Recovery and Climate Experiment (GRACE) mission is a breakthrough Earth science mission launched in the spring of 2002 that uses satellite-to-satellite tracking (SST) to map the Earth gravity field. In this framework, the non-uniform gravity distribution is inferred using the range change experienced between two satellites. The range change is measured using a microwave K-band ranging system, and non-gravitational forces are accounted for using accelerometer (ACC) data. The vector-offset between the satellite center of mass (CM) and the K-band phase center represents the correction between measured and modeled ranging data. In addition, the offset between the satellite CM and the ACC proof-mass multiplies the attitude angles, rates, and jitter which in turn add spurious signals to the ACC output. For both of these reasons, proper knowledge and control of attitude behavior is vital to successful mission performance. An examination of the GRACE attitude control system (ACS) is presented in this study.

The GRACE ACS system is composed of a PD control law, star camera sensing as the knowledge source, cold-gas thrusters as primary actuators, and magnetic torque rods as supplementary actuators. The dependencies inherent in the ACS are inferred using a sensitivity analysis performed on a simulation model of the GRACE science mode ACS. The results from this sensitivity study are applicable to the general controller class of which the GRACE ACS system is an exemplar.

In this study, the modeled attitude data quality is most sensitive to star camera measurement noise. It is hypothesized that this is because star cameras are used as the sole knowledge source in the ACS scheme. In contrast, the experimental results associated with magnetometer, thruster, and magnetic torque rod perturbations did not significantly affect attitude quality. However, these perturbations do cause thruster activity to significantly magnify. This results in higher attitude acceleration PSD for the frequency band in which time-variable gravity components are captured. A number of future experiments can be performed to improve both attitude quality performance and frequency-based magnifications. Examples include sensor fusion studies, reaction wheel versus thruster assessment, and gravity field estimation sensitivity in response to attitude quality degradation.

Table of Contents

Acknowledgments	v
Abstract	vi
List of Tables	xii
List of Figures	xiv
Chapter 1. Motivation and Background	1
1.1 Introduction	1
1.2 GRACE Mission Overview	2
1.3 GRACE Science Mode Reference Frames	6
1.4 ACS Overview	9
1.5 Attitude Motion and Requirements	14
1.6 Motivation and Case Study Description	18
Chapter 2. Dynamical Representation	20
2.1 Introduction	20
2.2 Angular Momentum	20
2.3 Moments of Inertia	23
2.4 Euler’s Equations of Motion	25
2.5 Linearized Representation	27
Chapter 3. Linear Control Theory	29
3.1 Introduction	29
3.2 Transfer Function	29
3.3 Spacecraft Plant Dynamics	30
3.4 Feedback Control	34
3.5 Proportional Control	36

3.6	Proportional Derivative (PD) Control	40
3.7	Proportional Integral Derivative (PID) Control	43
3.8	Stability Analysis through Frequency Response	48
3.9	GRACE PD Control	52
Chapter 4.	Simulation Construction and Validation	55
4.1	Introduction	55
4.2	Satellite Attitude Block Diagrams	55
4.3	GRACE ACS Validation Model	58
4.3.1	Angle Validation	61
4.3.2	Rate Validation	64
4.3.3	Magnetic Torque Validation	67
4.3.4	Thruster Pulse Width Validation	69
4.3.5	Attitude Acceleration Validation	71
4.4	GRACE ACS Experimental Model	74
4.4.1	Ideal Angle Results	78
4.4.2	Ideal Rate Results	84
4.4.3	Ideal Control Responses	87
4.4.4	Acceleration Response	90
4.5	Summary	92
Chapter 5.	Experimental Setup	93
5.1	Introduction	93
5.2	Experimental Selection and Procedure	94
5.3	Star Camera Experiments	96
5.3.1	SC1 - Star Camera White Noise	96
5.3.2	SC2 - Star Camera Colored Noise	99
5.3.3	SC3 - Star Camera Misalignment	104
5.3.4	Star Camera Experiments Simulation Implementation	105
5.4	Magnetometer Experiments	106
5.4.1	Mag1 - Magnetometer White Noise	107
5.4.2	Mag2 - Magnetometer Bias	107
5.4.3	Magnetometer Noise and Bias Simulation Implementation	108

5.4.4	Mag3 - Misalignment	109
5.4.5	Magnetometer Misalignment Simulation Implementation	110
5.5	Thruster Experiments	111
5.5.1	Th1 - Misalignment	113
5.5.2	Th2 - Misfire	114
5.5.3	Thruster Experiments Simulation Implementation . . .	115
5.6	Torquer Experiments	116
5.6.1	Tor1 - Residual Dipole	117
5.6.2	Magnetic Torquer Residual Dipole Simulation Implementation	117
5.6.3	Tor2 - Misalignment	118
5.6.4	Magnetic Torquer Misalignment Simulation Implementation	119
5.7	Analysis Procedure	120
5.8	General Guidelines	121
Chapter 6.	Results	123
6.1	Introduction	123
6.2	Star Camera Tests	124
6.2.1	SC1	125
6.2.2	SC2	131
6.2.3	SC3	137
6.2.4	Star Camera Implications	143
6.2.5	Star Camera Measurement Noise - Refinement Tests . .	148
6.2.6	Potential Future Experiments	167
6.3	Magnetometer Tests	170
6.3.1	Mag1	170
6.3.2	Mag2	176
6.3.3	Mag3	182
6.3.4	Magnetometer Implications	188
6.4	Thruster Tests	191
6.4.1	Th1	191
6.4.2	Th2	197

6.4.3	Thruster Implications	203
6.5	Magnetic Torquer Tests	206
6.5.1	Tor1	206
6.5.2	Tor2	212
6.5.3	Magnetic Torquer Implications	218
Chapter 7.	Conclusions	220
7.1	Scientific Implications	220
7.2	Summary of Results	222
Appendix		226
Bibliography		229
Vita		232

List of Tables

1.1	GRACE Orbit Configuration	5
1.2	GRACE Satellite Parameters	5
1.3	GRACE System Parameters - Instrument Suite	6
1.4	GRACE System Parameters - Science Mode ACS Suite	11
1.5	GRACE Attitude Angle Requirements for Science Mode	15
1.6	GRACE Attitude Acceleration Requirements for Science Mode	15
3.1	Effect of Increasing PID Gain	48
4.1	GRACE Validation Model Required Inputs	60
4.2	GRACE Validation Model Available Outputs	60
4.3	Attitude Angle Simulation/Telemetry Residual Mean and RMS	64
4.4	Attitude Rate Simulation/Telemetry Residual Mean and RMS	67
4.5	Magnetic Torque Simulation/Telemetry Residual Mean and RMS	69
4.6	Pulse Width Simulation/Telemetry Residual Mean and RMS	71
4.7	Attitude Acceleration Simulation/Telemetry Residual Mean and RMS	74
4.8	GRACE Experimental Model Required Inputs	77
5.1	Sensitivity Experiments Summary for ACS Science Mode	95
5.2	Star Camera White Noise	99
5.3	Star Camera Colored Noise: White Noise Component	102
5.4	Star Camera Colored Noise: Red Noise Component	103
5.5	Butterworth Filter Gains	104
5.6	Star Camera Misalignment Specifications	104
5.7	Magnetometer Noise Magnitudes	107
5.8	Magnetometer Biases	108
5.9	Magnetometer Misalignment Specifications	110
5.10	Attitude Thruster Locations	112

5.11 Thruster Forces	112
5.12 Thruster Torques	113
5.13 Thruster Misfire and Misalignment	115
5.14 Magnetic Torquer Residual Dipole and Misalignment	120

List of Figures

1.1	Non-Uniform Representation of the Earth Mass	3
1.2	GRACE Satellite Mission Architecture	4
1.3	Reference Frames for GRACE Science Mode	7
1.4	GRACE Satellite Top View	11
1.5	GRACE Satellite Bottom View	12
1.6	GRACE Satellite Internal View	12
1.7	Deadband Limited Control Example	13
1.8	Representative GRACE Attitude Angle PSD	16
1.9	Representative GRACE Attitude Acceleration PSD	17
2.1	Rigid Body Diagram	21
3.1	Transfer Function Block Diagram	31
3.2	Spacecraft Plant Root Location	32
3.3	Spacecraft Plant Step Response	34
3.4	Feedback Control Loop	35
3.5	Closed Loop Transfer Function	36
3.6	Proportional Control Root Location	37
3.7	Proportional Control Step Response	39
3.8	PD Control Root Location	41
3.9	PD Control Step Response	42
3.10	PID Control Root Location Configuration 1	44
3.11	PID Control Step Response Configuration 1	45
3.12	PID Control Root Location Configuration 2	46
3.13	PID Control Step Response Configuration 2	47
3.14	Frequency Response Schematic	49
3.15	Bode Plot Example	51
3.16	Step Resonse of PD Configuration used in GRACE Science Mode	53

4.1	GRACE ACS Science Mode Block Diagram	56
4.2	Validation Simulation Model	59
4.3	Validation/Telemetry Comparison: Attitude Angle Time-Domain	62
4.4	Validation/Telemetry Comparison: Attitude Angle Frequency-Domain	63
4.5	Validation/Telemetry Comparison: Attitude Rate Time-Domain	65
4.6	Validation/Telemetry Comparison: Attitude Rate Frequency-Domain	66
4.7	Validation/Telemetry Comparison: Magnetic Torque Time-Domain	68
4.8	Validation/Telemetry Comparison: Pulse Width Time-Domain	70
4.9	Validation/Telemetry Comparison: Attitude Acceleration Time-Domain	72
4.10	Validation/Telemetry Comparison: Attitude Acceleration Frequency-Domain	73
4.11	Experimental Simulation Model	76
4.12	Experimental Simulation - Ideal Attitude Angle Response . . .	79
4.13	Experimental/Telemetry Comparison - Attitude Angle Time-Domain	80
4.14	Experimental/Telemetry Comparison - Attitude Angle Frequency-Domain	81
4.15	Pulse Width Comparison - Attitude Angle Time-Domain . . .	83
4.16	Pulse Width Comparison - Attitude Angle Frequency-Domain	84
4.17	Experimental Simulation - Ideal Attitude Rate Response . . .	85
4.18	Experimental/Telemetry Comparison - Attitude Rate Time-Domain	86
4.19	Experimental/Telemetry Comparison - Attitude Rate Frequency-Domain	87
4.20	Experimental Simulation - Ideal Thruster Torque Response . .	88
4.21	Experimental Simulation - Ideal Magnetic Torque Response .	89
4.22	Experimental Simulation - Ideal Attitude Acceleration Response	91
5.1	Random Noise Process - Time Domain	97
5.2	Random Noise Process - Frequency Domain	98
5.3	Colored Noise Process - Time Domain	100
5.4	Colored Noise Process - Frequency Domain	101
5.5	Star Camera Experiments - Simulation Modification	106

5.6	Magnetometer Hardware Experiments - Simulation Modification	109
5.7	Magnetometer Misalignment Experiments - Simulation Modification	111
5.8	Thruster Experiments - Simulation Modification	116
5.9	Torquer Residual Dipole Experiment - Simulation Modification	118
5.10	Torquer Misalignment Experiment - Simulation Modification .	119
6.1	SC1 - Yaw Attitude Angle Time Response	125
6.2	SC1 - Yaw Attitude Angle PSD	126
6.3	SC1 - Yaw Attitude Acceleration Time Response	127
6.4	SC1 - Yaw Attitude Acceleration PSD	128
6.5	SC1 - Roll and Pitch Attitude Angle Behavior	129
6.6	SC1 - Roll and Pitch Attitude Acceleration Behavior	130
6.7	SC2 - Yaw Attitude Angle Time Response	131
6.8	SC2 - Yaw Attitude Angle PSD	132
6.9	SC2 - Yaw Attitude Acceleration Time Response	133
6.10	SC2 - Yaw Attitude Acceleration PSD	134
6.11	SC2 - Roll and Pitch Attitude Angle Behavior	135
6.12	SC2 - Roll and Pitch Attitude Acceleration Behavior	136
6.13	SC3 - Yaw Attitude Angle Time Response	137
6.14	SC3 - Yaw Attitude Angle PSD	138
6.15	SC3 - Yaw Attitude Acceleration Time Response	139
6.16	SC3 - Yaw Attitude Acceleration PSD	140
6.17	SC3 - Roll and Pitch Attitude Angle Behavior	141
6.18	SC3 - Roll and Pitch Attitude Acceleration Behavior	142
6.19	SC2 - Integrated Attitude Acceleration	144
6.20	Mag1 - Integrated Attitude Acceleration	145
6.21	Deadband Experiment - Attitude Angle Time Response	149
6.22	Deadband Experiment - Attitude Angle PSD	150
6.23	Deadband Experiment - Attitude Acceleration Time Response	151
6.24	Deadband Experiment - Attitude Acceleration PSD	152
6.25	Deadband Experiment - Integrated Attitude Acceleration . . .	153
6.26	PD Configuration Comparisons	155

6.27	PD Controller Experiment - Attitude Angle Time Response .	156
6.28	PD Controller Experiment - Attitude Angle PSD	157
6.29	PD Controller Experiment - Attitude Acceleration Time Response	158
6.30	PD Controller Experiment - Attitude Acceleration PSD	159
6.31	PD Controller Experiment - Integrated Attitude Acceleration .	160
6.32	LQE Estimation Experiment - Attitude Angle Time Response	162
6.33	LQE Estimation Experiment - Attitude Angle PSD	163
6.34	LQE Estimation Experiment - Attitude Acceleration Time Response	164
6.35	LQE Estimation Experiment - Attitude Acceleration PSD . .	165
6.36	LQE Estimation Experiment - Integrated Attitude Acceleration	166
6.37	Mag1 - Yaw Attitude Angle Time Response	170
6.38	Mag1 - Yaw Attitude Angle PSD	171
6.39	Mag1 - Yaw Attitude Acceleration Time Response	172
6.40	Mag1 - Yaw Attitude Acceleration PSD	173
6.41	Mag1 - Roll and Pitch Attitude Angle Time Response	174
6.42	Mag1 - Roll and Pitch Attitude Angle Time Response	175
6.43	Mag2 - Yaw Attitude Angle Time Response	176
6.44	Mag2 - Yaw Attitude Angle PSD	177
6.45	Mag2 - Yaw Attitude Acceleration Time Response	178
6.46	Mag2 - Yaw Attitude Acceleration PSD	179
6.47	Mag2 - Roll and Pitch Attitude Angle Behavior	180
6.48	Mag2 - Roll and Pitch Attitude Acceleration Behavior	181
6.49	Mag3 - Yaw Attitude Angle Time Response	182
6.50	Mag3 - Yaw Attitude Angle PSD	183
6.51	Mag3 - Yaw Attitude Acceleration Time Response	184
6.52	Mag3 - Yaw Attitude Acceleration PSD	185
6.53	Mag3 - Roll and Pitch Attitude Angle Behavior	186
6.54	Mag3 - Roll and Pitch Attitude Acceleration Behavior	187
6.55	Th1 - Yaw Attitude Angle Time Response	191
6.56	Th1 - Yaw Attitude Angle PSD	192
6.57	Th1 - Yaw Attitude Acceleration Time Response	193

6.58	Th1 - Yaw Attitude Acceleration PSD	194
6.59	Th1 - Roll and Pitch Attitude Angle Behavior	195
6.60	Th1 - Roll and Pitch Attitude Acceleration Behavior	196
6.61	Th2 - Yaw Attitude Angle Time Response	197
6.62	Th2 - Yaw Attitude Angle PSD	198
6.63	Th2 - Yaw Attitude Acceleration Time Response	199
6.64	Th2 - Yaw Attitude Acceleration PSD	200
6.65	Th2 - Roll and Pitch Attitude Angle Behavior	201
6.66	Th2 - Roll and Pitch Attitude Acceleration Response	202
6.67	Tor1 - Yaw Attitude Angle Time Response	206
6.68	Tor1 - Yaw Attitude Angle PSD	207
6.69	Tor1 - Yaw Attitude Acceleration Time Response	208
6.70	Tor1 - Yaw Attitude Acceleration PSD	209
6.71	Tor1 - Roll and Pitch Attitude Angle Behavior	210
6.72	Tor1 - Roll and Pitch Attitude Acceleration Behavior	211
6.73	Tor2 - Yaw Attitude Angle Time Response	212
6.74	Tor2 - Yaw Attitude Angle PSD	213
6.75	Tor2 - Yaw Attitude Acceleration Time Response	214
6.76	Tor2 - Yaw Attitude Acceleration PSD	215
6.77	Tor2 - Roll and Pitch Attitude Angle Behavior	216
6.78	Tor2 - Roll and Pitch Attitude Acceleration Behavior	217
1	Periodogram of an attitude signal	227
2	Thomson multitaper PSD of an attitude signal	228

Chapter 1

Motivation and Background

1.1 Introduction

The Gravity Recovery and Climate Experiment (GRACE) satellite mission was launched in the spring of 2002 with the purpose of mapping the gravity field of the Earth [1]. The gravity models produced have proven invaluable to scientists in numerous geoscience fields including hydrology, oceanography, and solid-Earth sciences. The success of GRACE has provided the impetus for future geodetic missions. Scientific accuracy depends on the ability to model flight data. The Attitude Control System (ACS) behavior is among the most important factors influential to the quality of flight data, and thus to mission success. Through an analysis of the ACS behavior for a heritage mission such as GRACE, contributing factors that influence successful performance can be identified and assessed. These provide valuable insight into how future ACS systems should be designed, which in turn can result in improved accuracy for subsequent geodetic missions.

1.2 GRACE Mission Overview

The Earth is a complex entity comprising non-uniform mass distributions, as seen in Figure 1.1 [2]. The total mass distribution is conceptualized as the integral of numerous differential components; each of which contributes to a local gravitational effect. The global gravity field includes mean and time-variable components. The mean field is used in conjunction with altimetry data to produce precise models of ocean surface currents and heat transport. The time-variable components depict the mass exchange between the Earth's atmosphere, oceans, and land mass [3]. In combination, they can be used to characterize long-term climate trends.

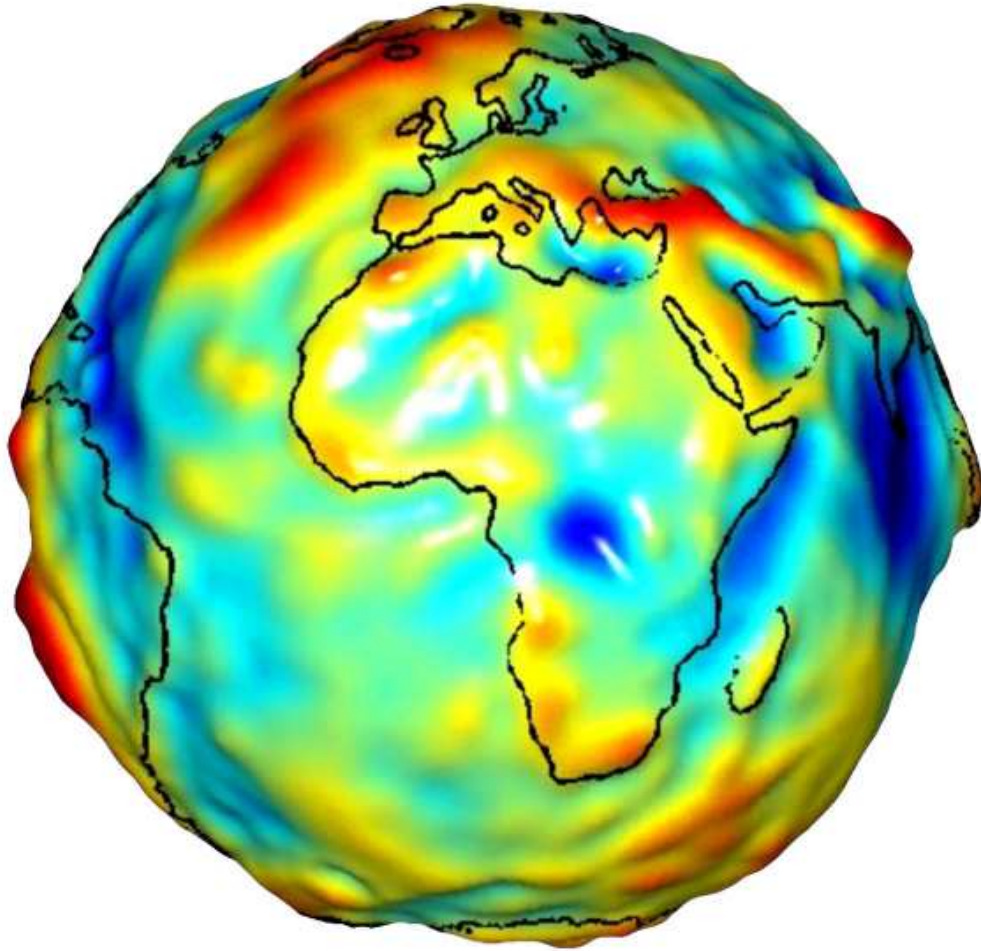


Figure 1.1: Non-Uniform Representation of the Earth Mass

The gravity field can be determined using a variety of techniques including satellite laser ranging (SLR), gradiometry, and satellite-to-satellite tracking (SST). The GRACE mission uses SST to produce high-resolution global grav-

ity models. The satellite mission architecture is given in Figure 1.2 [4]:

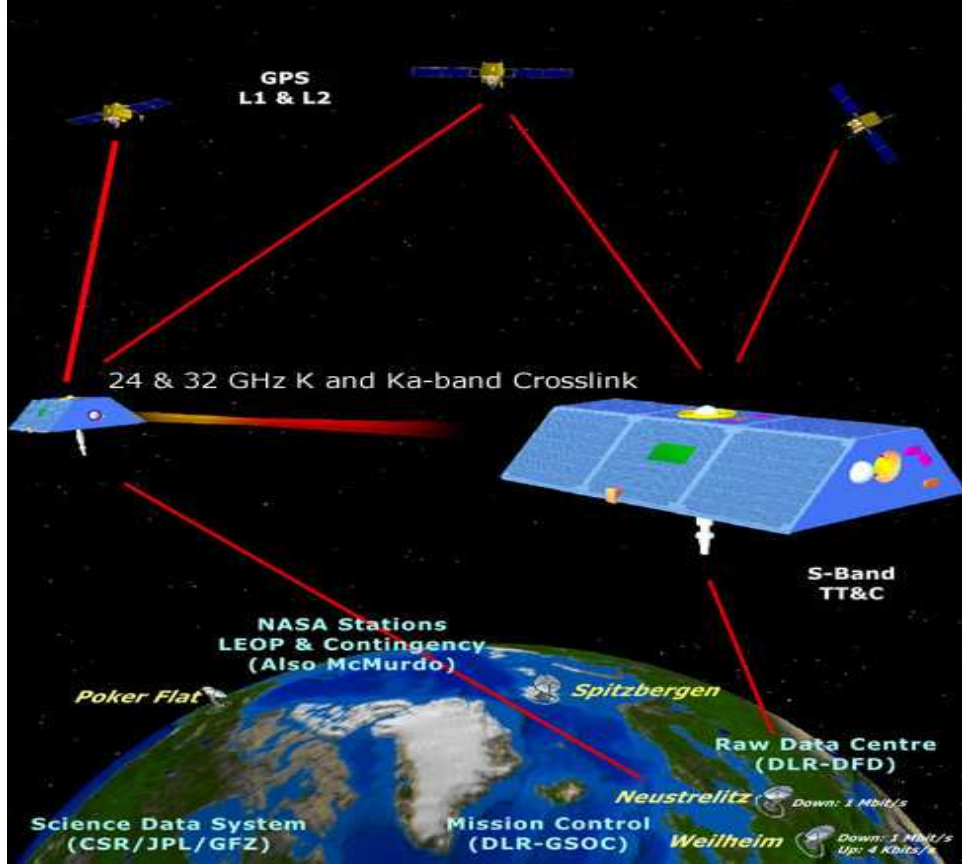


Figure 1.2: GRACE Satellite Mission Architecture

The orbital and spacecraft characteristics of this architecture are summarized in Tables 1.1 and 1.2 [5]:

Table 1.1: GRACE Orbit Configuration

Two Satellites
Altitude: 400-500 km
Separation Distance: 220 ± 50 km
Inclination: 89 degrees
Period: 94.114 min at launch
Repeat Cycle: None, ground track evolves naturally

Table 1.2: GRACE Satellite Parameters

Dimensions: $3.1 \times 0.8 \times (1.9-0.7)$ m
Mass: 460 (wet) kg
Power: 160 W
Fuel: 34 kg GN2 propellant
Average Data Rate: 1Mbps

Over the mission lifetime, the two trapezoid shaped GRACE satellites travel in a 400-500 km, near-circular, polar orbit with a nominal separation distance of 220 km. The spatial and temporal variations in the Earth gravity field affect the orbits of the two satellites slightly differently. This manifests itself as a time-varying range change in the separation distance. This change is detected using a K-band microwave ranging system [6]. Each satellite is equipped with an Ultra Stable Oscillator (USO) which produces the reference frequencies. The phase change between the two microwave carrier signals is calculated using the High Accuracy Inter-satellite Ranging System (HAIRS). Using precise relative timing between the two satellites from simultaneous Global Positioning System (GPS) tracking data, the dual one-way range is

reconstructed. Range change is also affected by non-gravitational forces. To account for this effect, a SuperSTAR Accelerometer is placed close to the spacecraft center of mass (CM) [7]. The accelerometer information is used to remove the non-gravitational influence from the range data. Finally, a dual Star-Camera Assembly (SCA) is used to obtain the precise orientation of the spacecraft. A summary of the GRACE instrument suite is given in Table 1.3 [5].

Table 1.3: GRACE System Parameters - Instrument Suite
High Accuracy Inter-satellite Ranging System (HAIRS)
Ultra Stable Oscillator (USO)
SuperSTAR Accelerometer (SSA)
Star Camera Assembly (SCA)
Global Positioning System (GPS) Receiver

1.3 GRACE Science Mode Reference Frames

A schematic of the representative reference frames for the GRACE science mode is given in Figure 1.3.

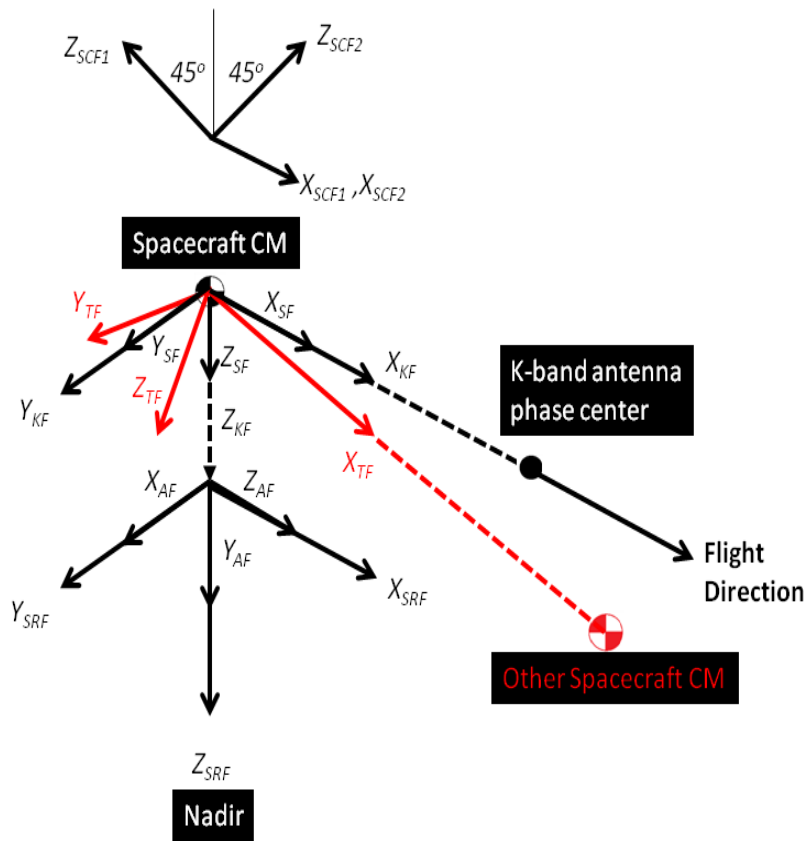


Figure 1.3: Reference Frames for GRACE Science Mode

The science products produced are referenced with respect to the Science Reference Frame (SRF). This frame has axes coincident with the Accelerometer

Frame (AF):

$$\begin{aligned}
X_{SRF} &\parallel Z_{AF} \\
Y_{SRF} &\parallel X_{AF} \\
Z_{SRF} &\parallel Y_{AF}
\end{aligned} \tag{1.1}$$

The satellite frame (SF) is fixed at a target location for the spacecraft CM, and points to a target location on the K-band antenna boresight. It is defined with X_{SF} as the line joining the satellite CM to the K-band antenna phase center, Z_{SF} normal to X_{SF} and to the plane of the main equipment platform and positive towards the satellite radiator, and Y_{SF} forming the triad. Each GRACE satellite carries two star camera assemblies. The origin of each Star Camera Frame (SCF) is located at the intersection of the star camera boresight with the mounting plane for the star camera head. The X_{SCF} for each star camera is aligned parallel with X_{SF} . The optical axis Z_{SCF} is positioned +45 and -45 degrees in the $Y_{SF}/-Z_{SF}$ orientation, for star camera 1 and 2 respectively [8].

The SF is approximately the same as the K-frame (KF), which is defined by:

$$\begin{aligned}
X_{KF} &= \text{Spacecraft CM} \rightarrow \text{K-band antenna phase center} \\
Z_{KF} &\parallel X_{KF} \times Y_{SRF} \\
Y_{KF} &\parallel Z_{KF} \times X_{KF}
\end{aligned} \tag{1.2}$$

Finally, a target vector X_{TF} is defined which points along the line that connects the CM of each spacecraft. In science mode, the goal of the ACS system aboard each satellite is to keep the attitude deviations of X_{KF} from the target line X_{TF}

at a minimum. This arrangement keeps the K-band antenna boresights in a line-of-sight configuration, maximizing the K-band data quality. The attitude deviations are characterized by small angles roll(ϕ), pitch(θ), and yaw(ψ) in X , Y , and Z respectively. Stringent attitude accuracy requirements are needed to produce high resolution gravity field data. As such, the GRACE science mode is a fine-pointing mode, with attitude accuracy requirements needed on the order of milliradians (or arcminutes) [9].

1.4 ACS Overview

From the accuracy requirements and scientific measurement type, the ACS system category is identified. ACS systems are divided into two classes: spin-stabilized and three-axis stabilized. In spin-stabilized control, the spacecraft is spun about its major principal axis of inertia. In the presence of disturbances, the gyroscopic effect resulting from the spin causes the satellite to move towards its equilibrium orientation. In three-axis stabilization, an active approach is used that moves the spacecraft to any desired orientation using various actuators. Three-axis stabilization generally produces higher accuracy results, and is required for specific fine-pointing modes such as the GRACE science mode [10].

Actuator selection for three-axis stabilized configurations is reliant upon scientific constraints and orbital environment makeup. The gravitational force is the weakest fundamental force, and is therefore the most difficult to accurately sense. For GRACE, the range-change becomes most pronounced at

low orbits, and much harder to detect at higher orbits. The GRACE orbit, therefore, is set at low-altitude, between 400-500 km, during the mission lifetime. At these low orbits, the Earth magnetic field strength is strong enough to allow the use of magnetic sensors and actuators, such as magnetometers and magnetic torque rods [10]. Both of these are used in GRACE science mode. Conversely, the disturbance torques in these environments are considerably higher in magnitude. In the GRACE orbit, disturbance torques are dominated by atmospheric drag and gravity gradient influences [9].

Many three-axis stabilized missions use reaction wheels as primary actuators [11]. Reaction wheels act by altering internal spacecraft momentum to compensate for external disturbance torques. Thrusters are then used as secondary actuators for wheel desaturation. However, reaction wheels are not ideal sensors for missions in which accelerometers are used as scientific instruments. Reaction wheels induce high vibration levels, significantly affecting the internal momentum within the spacecraft [12]. This influence on accelerations can become quite large and can affect data quality. Therefore, external cold-gas thrusters are used as the primary actuator [9].

Science mode control is specified by spacecraft angular behavior; therefore, attitude knowledge takes precedent over rate knowledge. For highest accuracy results, star camera sensors are used as the attitude knowledge source [12]. For GRACE, star cameras are used as the only knowledge source; additional sensors are not included in this mode due to systems-level power restrictions. Both sensors in the SCA are used for science purposes; for each

satellite, the star camera head facing away from the sun is used for ACS purposes. A summary of the sensors and actuators used for the GRACE science mode is given in Table 1.4 [9]:

Table 1.4: GRACE System Parameters - Science Mode ACS Suite

Science Mode ACS Suite
Star Camera Assembly (SCA)
Fluxgate Magnetometer
10 mN GM2 Thrusters (ATH)
30 A-m ² Magnetic Torquers (MTQ)

Top, bottom, and cutaway views depicting the sensors, actuators, and instruments integrated with the spacecraft bus are depicted in Figures 1.4, 1.5, and 1.6 [13]:

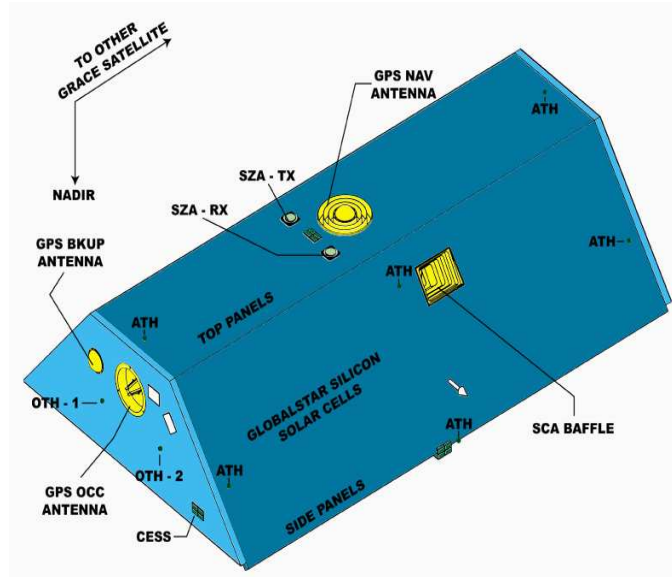


Figure 1.4: GRACE Satellite Top View

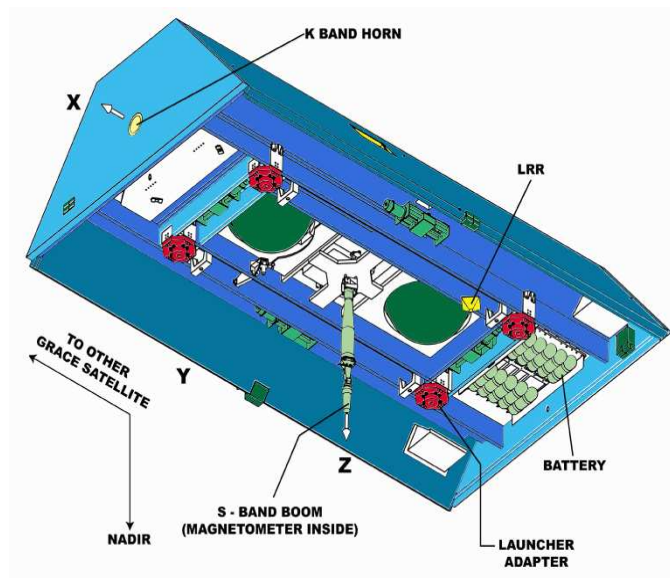


Figure 1.5: GRACE Satellite Bottom View

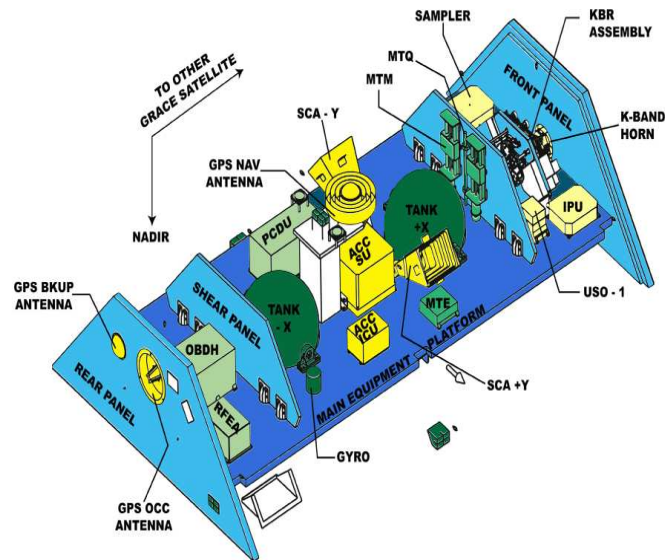


Figure 1.6: GRACE Satellite Internal View

GRACE, like most spacecraft missions in a 3-axis stabilized configuration, uses a standard proportional-derivative (PD) linear controller as its control law [12]. Advantages of PD control include extensive flight heritage, low design complexity, and standard techniques for stability, robustness, and performance assessment [14]. Attitude controllers for fine-pointing modes, like the GRACE science mode, are typically employed using deadband-limited control. A schematic of this implementation is given in Figure 1.7:

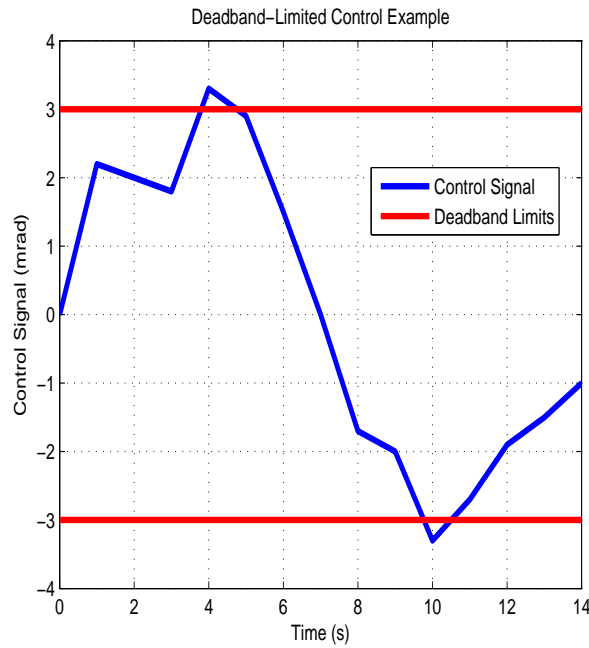


Figure 1.7: Deadband Limited Control Example

In reality, it is difficult and impractical to drive the attitude error perfectly to zero. The high disturbance environment, combined with hardware

imperfections, will cause constant actuator effort. This leads to high power usage and rapid loss of fuel. The deadband-limited construct is an efficient method that meets attitude performance within real-time constraints. In this scheme, the control system performs actuations only when the control signal magnitude exceeds a certain limit, referred to as the deadband. In Figure 1.7, this is denoted by the red lines. If the attitude error stays within this regime, then no control actuations are performed. The deadbands are determined based on the level of accuracy required by the scientific solution [12].

Each GRACE satellite contains identical versions of the specified attitude control suite, control logic, and deadband-limited implementation [9]. As previously mentioned, the control is performed to keep each spacecraft's KF axis close to its target TF axis. The target axis is uploaded as a referenced value for each spacecraft, and is calculated using orbital parameters. Using the uploaded target, attitude control is performed independently for each spacecraft with respect to the target.

1.5 Attitude Motion and Requirements

In the SST configuration, each satellite acts as a scientific instrument. This brings with it unique challenges in the attitude control regime. Attitude angular deviations must be minimized and limited to produce high accuracy gravity solutions. In addition, the geodetic quality of the measurements necessitates the use of an accelerometer. Angular acceleration requirements are not typically considered in the ACS design process; however, they are very

important for missions such as GRACE when accelerometer data is used as a science instrument. Due to imperfections in the spacecraft integration process, the accelerometer is not positioned perfectly at the spacecraft CM. The end-result of this CM offset is increased influence of angular acceleration data [15]. This offset is estimated using a combination of attitude knowledge and angular acceleration components [5]. Attitude angles and accelerations must satisfy sufficient performance requirements for accurate CM offset estimation and scientific data quality. A summary of these requirements is given in Tables 1.5 and 1.6 [16]:

Table 1.5: GRACE Attitude Angle Requirements for Science Mode

Deadband
3-5 mrad limit

Table 1.6: GRACE Attitude Acceleration Requirements for Science Mode

Frequency Range (mHz)	Peak Value of PSD ($\mu\text{rad/s}^2/\sqrt{\text{Hz}}$)
>5	1.0
0.2 - 5	0.005/f

The frequency content of attitude angles and accelerations is an important tool through which attitude character is assessed. The power spectral densities (PSD) of the GRACE attitudes are given in Figures 1.8 and 1.9. A PSD explanation is given in the Appendix. These graphs were produced using the periodogram representation of the PSD equations:

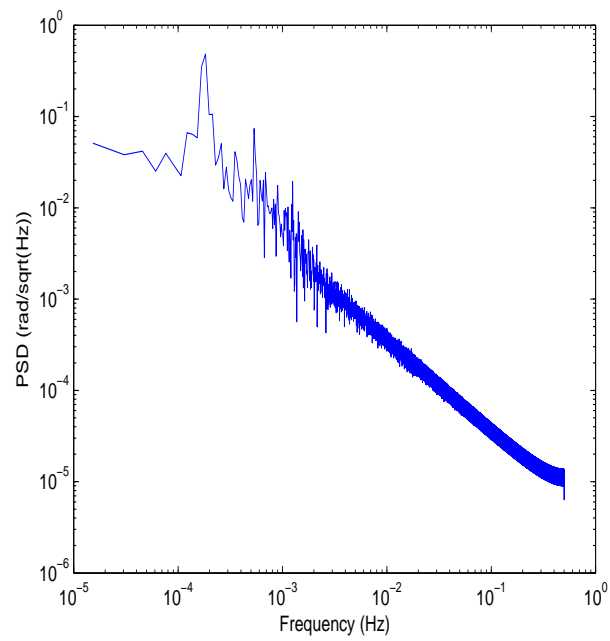


Figure 1.8: Representative GRACE Attitude Angle PSD

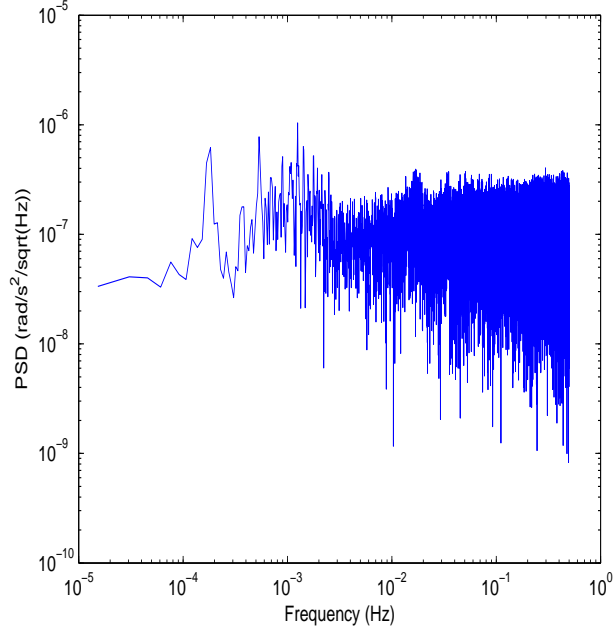


Figure 1.9: Representative GRACE Attitude Acceleration PSD

The GRACE in-flight processes generally operate at a 1 Hz sampling frequency [9]. The frequency content of the attitude spans from 10 μ Hz to the Nyquist frequency 0.5 Hz. The complete GRACE gravity field solution involves analyzing K-band residuals over a fairly wide range of frequencies. The low order gravity field terms lie at frequencies as low as 100 μ Hz, while higher order terms become visible in spectra up to around 30 mHz [1]. The size of this bandwidth is fairly typical for Earth science missions [12]. However, the range becomes important in the ACS context because it encompasses both attitude angular and acceleration information. As seen from Figure 1.8, the angular PSD decreases as the frequency increases. Conversely, as seen in Figure 1.9,

angular acceleration PSD behavior is relatively flat across the representative frequencies.

1.6 Motivation and Case Study Description

The GRACE science mode ACS has the interesting challenge of managing both attitude angle and attitude acceleration information over a fairly wide frequency bandwidth. This is a byproduct of the SST architecture and geodetic nature of the GRACE science measurements. The quality of the attitude response is a function of the physical components and control algorithms encompassed in the ACS structure. It is worthwhile to examine which of these components has the greatest effect on attitude performance; this, in turn, provides guidelines for how future ACS systems aboard SST/geodetic missions should be modified or refined. The goal of this case study is to examine how attitude behavior is affected for an ACS system that uses purely attitude knowledge, thrusters as primary actuators, magnetic torque rods as supplementary actuators, and a PD control law. In particular, an assessment of how extrinsic non-idealities affect attitude performance are examined.

This study is performed using a simulation environment that is validated against the GRACE ACS configuration as the exemplar. In this simulation, data from each physical component (i.e. star camera, magnetometer, cold-gas thrusters, and magnetic torque rods) is perturbed from a nominal working configuration. The effect of this perturbation on angles and accelerations is then assessed both in time and frequency domains. From these

component level interactions, conclusions are made regarding future design and improvement. In particular, the observed sensitivities in the sensor and actuator behavior determine future areas of study, involved with trade studies of sensor and/or actuator modifications. Any non-idealities that induce significant attitude sensitivities are also noted as areas of improvement for future ACS design.

The following chapters detail the derivation and analysis results comprised in this case study. First, a theoretical foundation for attitude dynamics is derived in Chapter 2. Next, a review of linearized attitude control logic is given in Chapter 3. In Chapter 4, a simulation model for the GRACE ACS science mode is constructed and validated using flight results. The various sensitivity tests performed for this work are explained in Chapter 5. The results from the tests are given in Chapter 6. Finally, conclusions from the results are summarized in Chapter 7.

Chapter 2

Dynamical Representation

2.1 Introduction

Proper representation of spacecraft attitude dynamics is an important prerequisite to systems-level control design. Attitude dynamics relates the rotational response of a dynamical system to external environmental influences. A standard technique for deriving these dynamics is through Newtonian mechanics. In this framework, rotational equations of motion are acquired by differentiating the spacecraft angular momentum vector with respect to an inertial reference frame. This process produces non-linear relationships between rotational behavior and external disturbances. These equations are then linearized to reduce modeling and control design complexity. In all mathematical equations used, *italics* are used to denote scalars, **bold** is used to denote vectors, and **bold underline** represents matrices. The exceptions are the origin points **O** and **O'**.

2.2 Angular Momentum

Using Newtonian methods, the first step in the attitude derivation process is definition of the angular momentum vector. Consider a rigid body,

shown in Figure 2.1. This body comprises individual differential masses. An inertial axis with basis vectors $\{\mathbf{n}_1, \mathbf{n}_2, \mathbf{n}_3\}^T$ is attached to an arbitrary non-accelerating, origin \mathbf{O}' which cannot rotate. A body-fixed axis with basis vectors $\{\mathbf{b}_1, \mathbf{b}_2, \mathbf{b}_3\}^T$ is placed on the rigid body. Three position vectors are defined: \mathbf{r}_i from \mathbf{O} to differential mass m_i , \mathbf{R} from \mathbf{O} to \mathbf{O}' , and $\boldsymbol{\rho}_i$ from \mathbf{O}' to m_i . The angular velocity of the rigid body is denoted by $\boldsymbol{\omega}$.

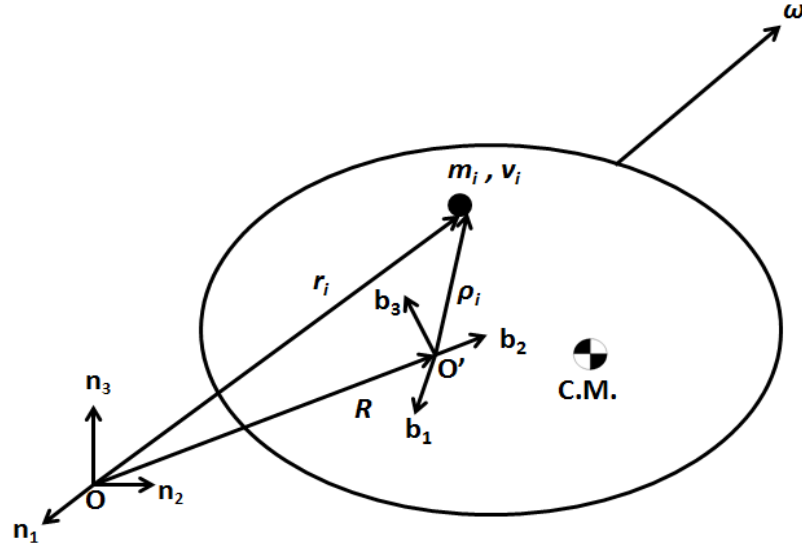


Figure 2.1: Rigid Body Diagram

The total angular momentum vector, \mathbf{L}_{total} is the integral over the rigid body of the cross products between the differential mass locations and the differential linear momentums [11]. This can be approximated as a summation over n

differential masses, where n is infinitesimally small:

$$\mathbf{L}_{total} \equiv \sum_{i=1}^n \mathbf{r}_i \times m_i \mathbf{v}_i \quad (2.1)$$

\mathbf{r}_i is written as the sum of \mathbf{R} and $\boldsymbol{\rho}_i$:

$$\mathbf{r}_i = \mathbf{R} + \boldsymbol{\rho}_i \quad (2.2)$$

Differentiating this expression with respect to time produces the velocity vectors:

$$\mathbf{v}_i = \mathbf{V} + \frac{d\boldsymbol{\rho}_i}{dt} \quad (2.3)$$

Substituting Equation 2.3 into Equation 2.1, and expanding the summation gives:

$$\mathbf{L}_{total} = M\mathbf{R} \times \mathbf{V} + \mathbf{R} \times \frac{d}{dt} \left[\sum_{i=1}^n m_i \boldsymbol{\rho}_i \right] + \left[\sum_{i=1}^n m_i \boldsymbol{\rho}_i \right] \times \mathbf{V} + \sum_{i=1}^n \left[m_i \boldsymbol{\rho}_i \times \frac{d\boldsymbol{\rho}_i}{dt} \right] \quad (2.4)$$

The total mass of the rigid body is the sum of all the differential masses:

$$M \equiv \sum_{i=1}^n m_i \quad (2.5)$$

If \mathbf{O}' is defined coincident with the Rigid Body CM, the following term drops out of Equation 2.4:

$$\sum_{i=1}^n m_i \boldsymbol{\rho}_i = 0 \quad (2.6)$$

In addition, the rigid body constraint allows the derivative of Equation 2.6 to drop out of Equation 2.4:

$$\frac{d}{dt} \left[\sum_{i=1}^n m_i \boldsymbol{\rho}_i \right] = 0 \quad (2.7)$$

The total angular momentum then reduces to:

$$\mathbf{L}_{total} = M\mathbf{R} \times \mathbf{V} + \sum_{i=1}^n \left[m_i \boldsymbol{\rho}_i \times \frac{d\boldsymbol{\rho}_i}{dt} \right] \quad (2.8)$$

The total angular momentum can now be separated into two components. In Equation 2.8, the left-hand term represents CM motion, while the right-hand term encompasses rigid body angular momentum relative to the CM. For analysis and modeling purposes, it is convenient to deal solely with the second term [11]. If the angular momentum is resolved in a non-fixed reference frame that moves with the CM, the first term vanishes. The standard rigid body angular momentum vector is thus defined as:

$$\mathbf{L} \equiv \sum_{i=1}^n \left[m_i \boldsymbol{\rho}_i \times \frac{d\boldsymbol{\rho}_i}{dt} \right] \quad (2.9)$$

The vector $d\boldsymbol{\rho}_i/dt$ is resolved in this frame as:

$$\frac{d\boldsymbol{\rho}_i}{dt} = \boldsymbol{\omega} \times \boldsymbol{\rho}_i \quad (2.10)$$

Substituting Equation 2.10 into Equation 2.9, and utilizing the vector triple product identity yields:

$$\mathbf{L} = \sum_{i=1}^n m_i \boldsymbol{\rho}_i \times (\boldsymbol{\omega} \times \boldsymbol{\rho}_i) = \sum_{i=1}^n m_i [\boldsymbol{\rho}_i^2 \boldsymbol{\omega} - (\boldsymbol{\rho}_i \cdot \boldsymbol{\omega}) \boldsymbol{\rho}_i] \quad (2.11)$$

2.3 Moments of Inertia

In its current form, the angular momentum vector is complicated by the existence of differential masses. The mass properties are more conveniently

represented through the use of an inertia tensor. This is a 3×3 matrix comprising the moments and products of inertia. These represent the along-axis and cross-axis mass property relationship respectively. The along-axis moments of inertia and are defined by [11]:

$$\begin{aligned} I_{11} &\equiv \sum_{i=1}^n m_i (\rho_{i2}^2 + \rho_{i3}^2) \\ I_{22} &\equiv \sum_{i=1}^n m_i (\rho_{i3}^2 + \rho_{i1}^2) \\ I_{33} &\equiv \sum_{i=1}^n m_i (\rho_{i1}^2 + \rho_{i2}^2) \end{aligned} \quad (2.12)$$

The cross-axis products of inertia and are defined by:

$$\begin{aligned} I_{12} = I_{21} &\equiv - \sum_{i=1}^n m_i \rho_{i1} \rho_{i2} \\ I_{23} = I_{32} &\equiv - \sum_{i=1}^n m_i \rho_{i2} \rho_{i3} \\ I_{13} = I_{31} &\equiv - \sum_{i=1}^n m_i \rho_{i1} \rho_{i3} \end{aligned} \quad (2.13)$$

Together, these components make up the inertia tensor:

$$\underline{\mathbf{I}} \equiv \begin{bmatrix} I_{11} & I_{12} & I_{13} \\ I_{21} & I_{22} & I_{23} \\ I_{31} & I_{32} & I_{33} \end{bmatrix} \quad (2.14)$$

Equation 2.11 can now be written as:

$$\mathbf{L} = \underline{\mathbf{I}} \boldsymbol{\omega} \quad (2.15)$$

2.4 Euler's Equations of Motion

The standard form of the attitude equations of motion are referred to as “Euler's Equation of Motion”. These are extracted from the time derivative of the angular momentum vector. In a body-fixed frame, the time derivative of the total angular momentum is:

$$\begin{aligned}\frac{d}{dt}\mathbf{L} &= \sum_{i=1}^n \frac{d}{dt}\mathbf{L}_i \\ &= \sum_{i=1}^n \frac{d}{dt}(\mathbf{r}_i \times m_i \mathbf{v}_i)\end{aligned}\tag{2.16}$$

The term on the right is expanded, with \mathbf{a}_i defined as the differential mass acceleration:

$$\frac{d\mathbf{L}}{dt} = \sum_{i=1}^n (\mathbf{v}_i \times m_i \mathbf{v}_i) + (\mathbf{r}_i \times m_i \mathbf{a}_i)\tag{2.17}$$

The first term in Equation 2.17 vanishes due to the cross product relationship between two identical vectors. The second term is re-written in terms of external forces \mathbf{F}_i using Newton's second law:

$$\frac{d\mathbf{L}}{dt} = \sum_{i=1}^n \mathbf{r}_i \times \mathbf{F}_i\tag{2.18}$$

The external torques are defined as:

$$\mathbf{T}_i = \mathbf{r}_i \times \mathbf{F}_i\tag{2.19}$$

The resultant external torque is the sum of all individual external torques:

$$\mathbf{T} = \sum_{i=1}^n \mathbf{T}_i\tag{2.20}$$

Finally, the angular momentum is written as:

$$\frac{d\mathbf{L}}{dt} = \mathbf{T} \quad (2.21)$$

Equation 2.21 is referred to as the law of conservation of angular momentum [11]. This law states that the angular momentum time derivative vector for a rigid body is equal to the sum of all external forces acting on that body. This derivative is taken with respect to an inertial frame, as per the Newton formulation. Recall the frames defined in Figure 2.1. The inertial frame basis is defined by n , and the body-fixed basis is defined by b . The time derivative relationship between the two frames are related through the following relationship, where P is any intrinsic parameter:

$$\left[\frac{d(P)}{dt} \right]^n \equiv \left[\frac{d(P)}{dt} \right]^b + \boldsymbol{\omega} \times (P) \quad (2.22)$$

Substituting \mathbf{L} for (P) yields [10]:

$$\left[\frac{d\mathbf{L}}{dt} \right]^n \equiv \left[\frac{d\mathbf{L}}{dt} \right]^b + \boldsymbol{\omega} \times \mathbf{L} \quad (2.23)$$

Within the body-fixed frame, the derivative of \mathbf{L} is equal to:

$$\left[\frac{d\mathbf{L}}{dt} \right]^b = \frac{d\mathbf{L}}{dt} = \mathbf{I} \frac{d\boldsymbol{\omega}}{dt} = \mathbf{I} \dot{\boldsymbol{\omega}} \quad (2.24)$$

Re-writing Equations 2.23 and 2.24 in terms of external torques results in:

$$\mathbf{I} \dot{\boldsymbol{\omega}} + \boldsymbol{\omega} \times \mathbf{I} \boldsymbol{\omega} = \mathbf{T} : \quad (2.25)$$

Expanding Equation 2.25 along all three axes produces:

$$\begin{bmatrix} I_{11} & I_{12} & I_{13} \\ I_{21} & I_{22} & I_{23} \\ I_{31} & I_{32} & I_{33} \end{bmatrix} \begin{bmatrix} \dot{\omega}_1 \\ \dot{\omega}_2 \\ \dot{\omega}_3 \end{bmatrix} + \begin{bmatrix} \omega_1 \\ \omega_2 \\ \omega_3 \end{bmatrix} \times \begin{bmatrix} I_{11} & I_{12} & I_{13} \\ I_{21} & I_{22} & I_{23} \\ I_{31} & I_{32} & I_{33} \end{bmatrix} \begin{bmatrix} \omega_1 \\ \omega_2 \\ \omega_3 \end{bmatrix} = \begin{bmatrix} T_1 \\ T_2 \\ T_3 \end{bmatrix} \quad (2.26)$$

An origin \mathbf{O}' can be selected such that the products of inertias disappear, referred to as a principal axis. This simplifies Equation 2.26 significantly:

$$\begin{aligned} I_{11}\dot{\omega}_1 - (I_{22} - I_{33})\omega_2\omega_3 &= T_1 \\ I_{22}\dot{\omega}_2 - (I_{33} - I_{11})\omega_3\omega_1 &= T_2 \\ I_{33}\dot{\omega}_3 - (I_{11} - I_{22})\omega_1\omega_2 &= T_3 \end{aligned} \quad (2.27)$$

Equation 2.27 is the standard form of Euler's equation of motion [10]. It relates the angular acceleration time history to the external torques acting on the rigid body.

2.5 Linearized Representation

The standard form of Euler's equations is non-linear in nature. Linearized assumptions are adequate for the purposes of this case study because science mode operates in a small angle regime. Small angle assumptions hold simplifying properties that allow for linearization. For a small angle θ and its derivative ω , the following relationships hold:

$$\begin{aligned} \cos(\theta) &\cong 1 \\ \sin(\theta) &\cong \theta \\ \theta^2 &\cong 0 \\ \omega^2 &\cong 0 \end{aligned} \quad (2.28)$$

Euler's equations now reduce to the linear form [10]:

$$\begin{aligned}I_{11}\dot{\omega}_1 &= T_1 \\I_{22}\dot{\omega}_2 &= T_2 \\I_{33}\dot{\omega}_3 &= T_3\end{aligned}\tag{2.29}$$

The GRACE satellite dynamics are modeled as rigid bodies. The most significant non-rigid contribution comes from slosh dynamics caused by on-board liquid propellant. These dynamics are excited during times of thruster fire. The attitude thrusters are designed to fire with 10 mN of force. In science mode, these thrusters are activated roughly every 70 minutes, with an impulse duration of approximately 200 msec. The resulting fuel slosh load is minimal, and can be neglected. Now that the linearized attitude dynamics for a rigid body have been derived, an explanation of linear control theory can be presented.

Chapter 3

Linear Control Theory

3.1 Introduction

The majority of spacecraft ACS systems use a linear control scheme called proportional-integral-derivative (PID) control. PID control is the preferred choice for spacecraft attitude control due to its robust methods for determining stability and flight performance, as well as an extensive flight heritage. The implementation of PID is developed using linearized representations of rigid-body dynamics. It is independently designed in a three-axis configuration using a single-input-single-output (SISO) framework.

3.2 Transfer Function

A controller is an algorithmic framework that generates an input to a dynamical system that commands the system output to a desired final state. Before control development can proceed, an input-output relationship for the dynamics must be established. In linear control theory for SISO systems, this is typically done using a transfer function in the Laplace domain. Consider the following relationship:

$$G(s) = \frac{Y(s)}{U(s)} \tag{3.1}$$

This is a standard Laplace notation of a transfer function. The term $Y(s)$ represents the output variable, and $U(s)$ represents the input variable [14].

3.3 Spacecraft Plant Dynamics

In control theory, the system dynamical realization is also referred to as the system plant. The transfer function for the system plant is derived before the controller can be designed. As previously mentioned, PID controllers are designed independently for each axis in a SISO framework. Consider the spacecraft attitude dynamics for a single axis:

$$I\ddot{\theta}(t) = T(t) \quad (3.2)$$

The objective of attitude control is to command the attitude angle θ to some desired value. In this framework, θ is the output and T is the input. The Laplace term can be utilized after zero initial conditions are assumed. Taking the Laplace transform on both sides of Equation 3.2 results in:

$$Is^2\theta(s) = T(s) \quad (3.3)$$

Re-arranging in transfer-function notation produces:

$$\begin{aligned} G_p(s) &= \frac{Y(s)}{U(s)} \\ &= \frac{\theta(s)}{T(s)} \\ &= \frac{1}{Is^2} \end{aligned} \quad (3.4)$$

Equation 3.4 is called the 'Open-Loop Transfer Function'. The open-loop transfer function does not rely on any feedback information. A schematic of an open-loop model is shown in Figure 3.1.

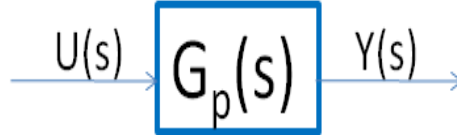


Figure 3.1: Transfer Function Block Diagram

System stability is determined by examining system poles and zeros. The system poles are the values of s where the component $U(s)$ equals zero, and the system zeros are the values of s where the component of $Y(s)$ equals zero. The system poles and zeros can be visualized using a root-location diagram. This diagram plots real components on the x-axis and imaginary components on the y-axis.

In root-location plots, poles tend to move towards zeros as the magnitude of the input signal is increased [14]. System stability is achieved when the real-value components of all system poles are negative. Using a nominal value of $I = 400 \text{ kg m}^2$, the root-location diagram for the example spacecraft axis is given in Figure 3.2. All control plots were generated using the Control Systems Toolbox in MATLAB.

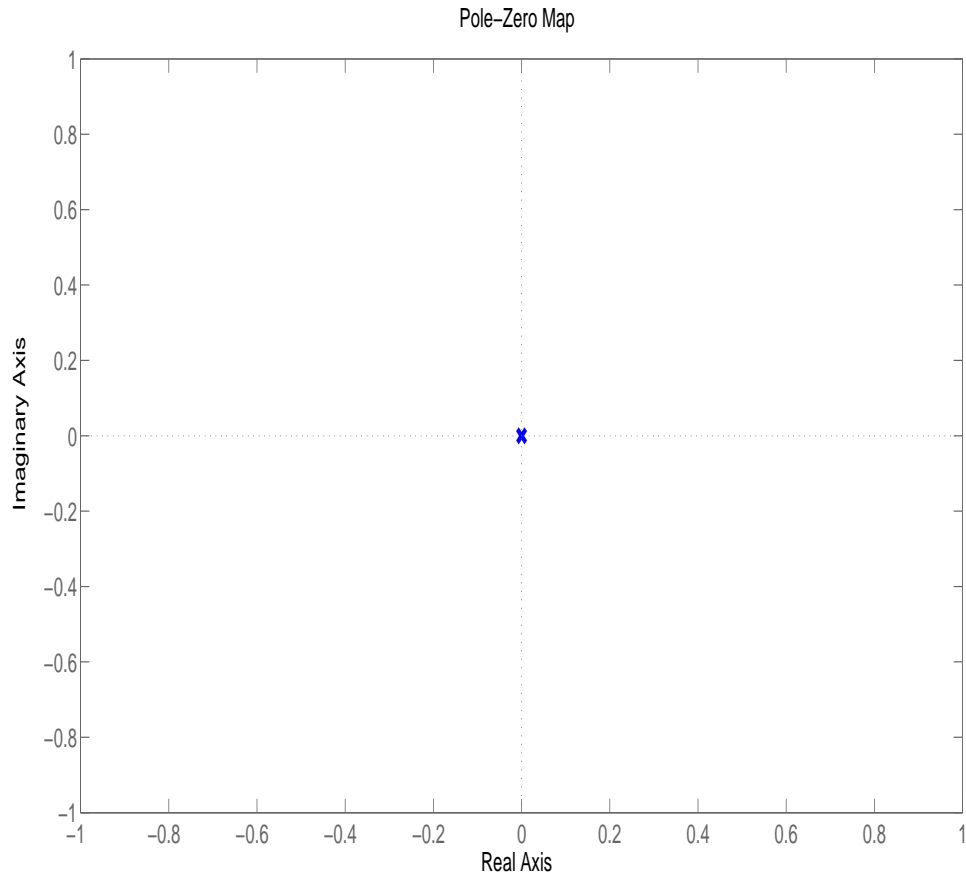


Figure 3.2: Spacecraft Plant Root Location

Poles with imaginary components oscillate at a characteristic frequency. The transient responses of systems with poles with negative real components decay at exponential rates. Conversely, the responses exponentially rise in the presence of positive real poles. From Figure 3.2, the spacecraft attitude behavior is characterized by two poles lying at the origin; these are also referred

to as integrators. The origin in the root-location diagram is an inflection point between the positive and negative real axis.

For open loop behavior, any small disturbance from this inflection point causes the behavior to diverge. Transient behaviors are analyzed by examining the plant system response to a unit step input. For the spacecraft open-loop system, this is given in Figure 3.3. As seen from this plot, the system behavior grows exponentially in response to a step input. This provides the main impetus for satellite attitude control.

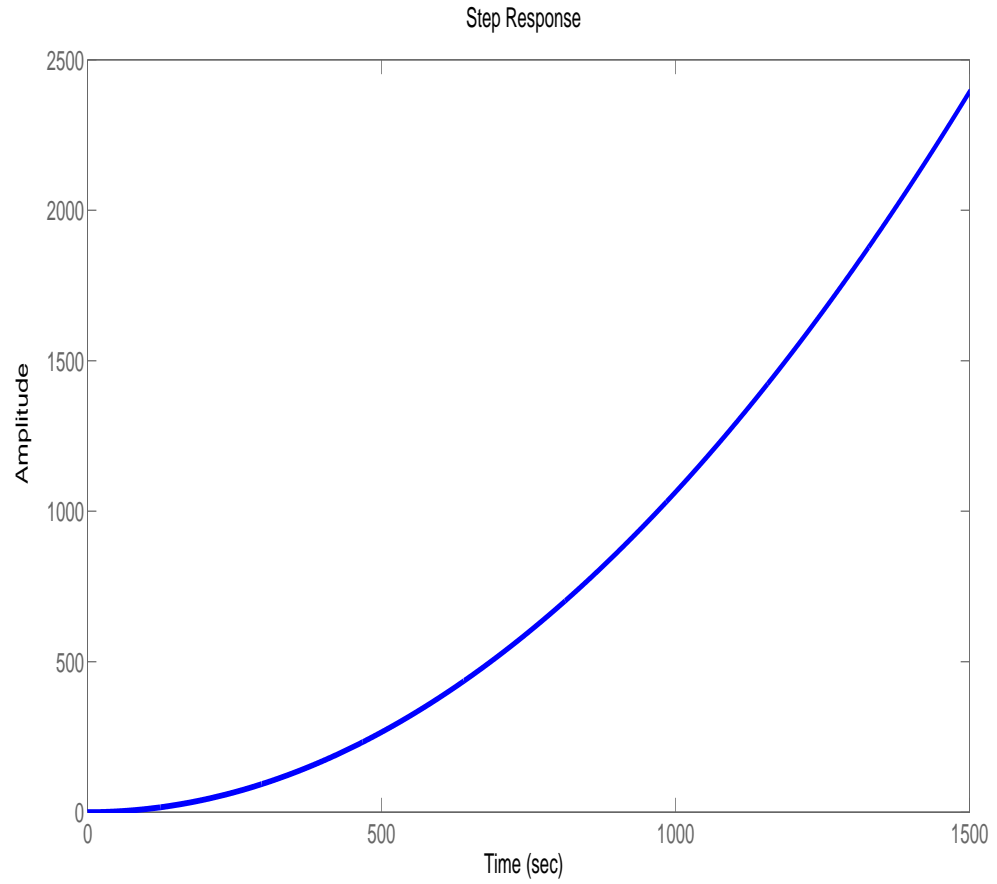


Figure 3.3: Spacecraft Plant Step Response

3.4 Feedback Control

Controllers are typically implemented using feedback loops. In this framework, the present value of the desired state, in this case the attitude angle θ_a , is compared with the commanded value θ_c to form an error vector.

The error vector $e = \theta_c - \theta_a$ is sent to the controller algorithm G_c . This controller is cascaded with the plant dynamics, from which the desired output is produced. A schematic of this process is given Figure 3.4. The goal of the control law is to drive the error to zero and ensure system stability.

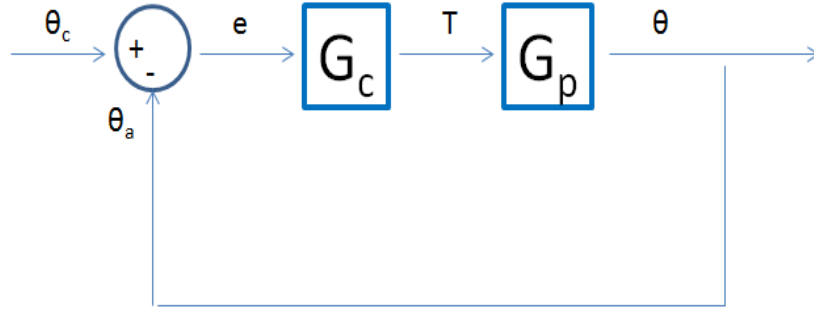


Figure 3.4: Feedback Control Loop

The negative feedback system can be decomposed to a closed-loop transfer function relationship. First, define the open-loop transfer function:

$$OL = G_c G_p \quad (3.5)$$

For a negative feedback system with no feedback gains, the closed-loop transfer function is defined as:

$$CL \equiv \frac{OL}{1 + OL} \quad (3.6)$$

This is equivalent to:

$$CL = \frac{G_c G_p}{1 + G_c G_p} \quad (3.7)$$

In SISO terms, the transfer function for the closed-loop process is given in Figure 3.5.

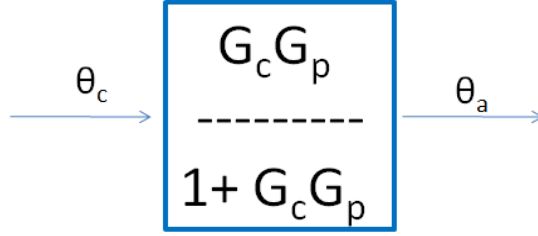


Figure 3.5: Closed Loop Transfer Function

3.5 Proportional Control

The most basic control law is a proportional weighting of the error, also called proportional control. First, define the attitude angle error as $e = \Delta\theta$. Proportional weighting is denoted by a constant gain K_p . The control law becomes:

$$U(t) = K_p \Delta\theta(t) \quad (3.8)$$

In Equation 3.8, the term $U(t)$ is the control input delivered to the dynamics. For spacecraft attitude, this input manifests as actuator torques. Using the Laplace transform, the transfer function of the controller is:

$$G_c = \frac{U(s)}{\Delta\theta(s)} = K_p \quad (3.9)$$

For spacecraft attitude, the minimum realization of the closed-loop transfer

function is:

$$CL = \frac{K_p}{Is^2 + K_p} \quad (3.10)$$

Using a gain configuration of $K_p = 1$, the root-location plot for the closed-loop system is given in Figure 3.6:

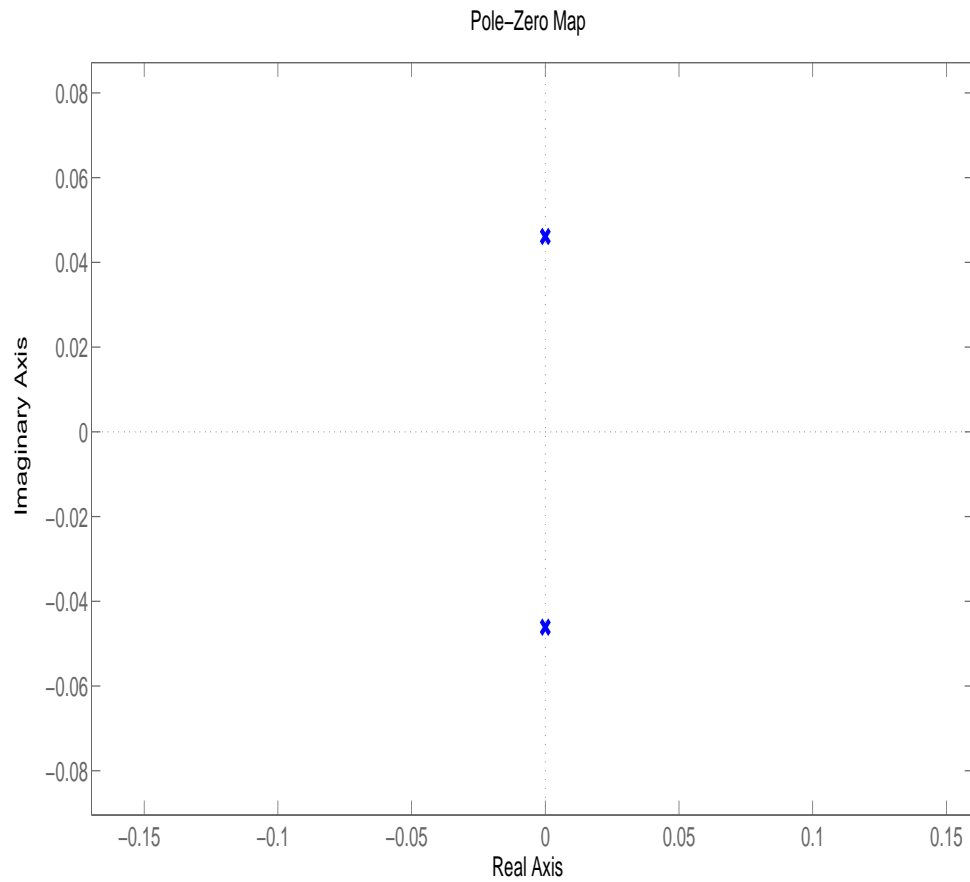


Figure 3.6: Proportional Control Root Location

For spacecraft attitude, adding a proportional gain moves the system poles along the imaginary axis. Changing the value of K_p alters the closed-loop pole positions on the imaginary axis. As the poles now have imaginary components, proportional control adds a characteristic frequency to the closed-loop behavior, creating a harmonic oscillator. However, the absence of negative real components results in zero system damping. Therefore, the closed-loop behavior tends to oscillate indefinitely around the commanded response. This behavior is observed from the closed-loop unit step response, given in Figure

3.7

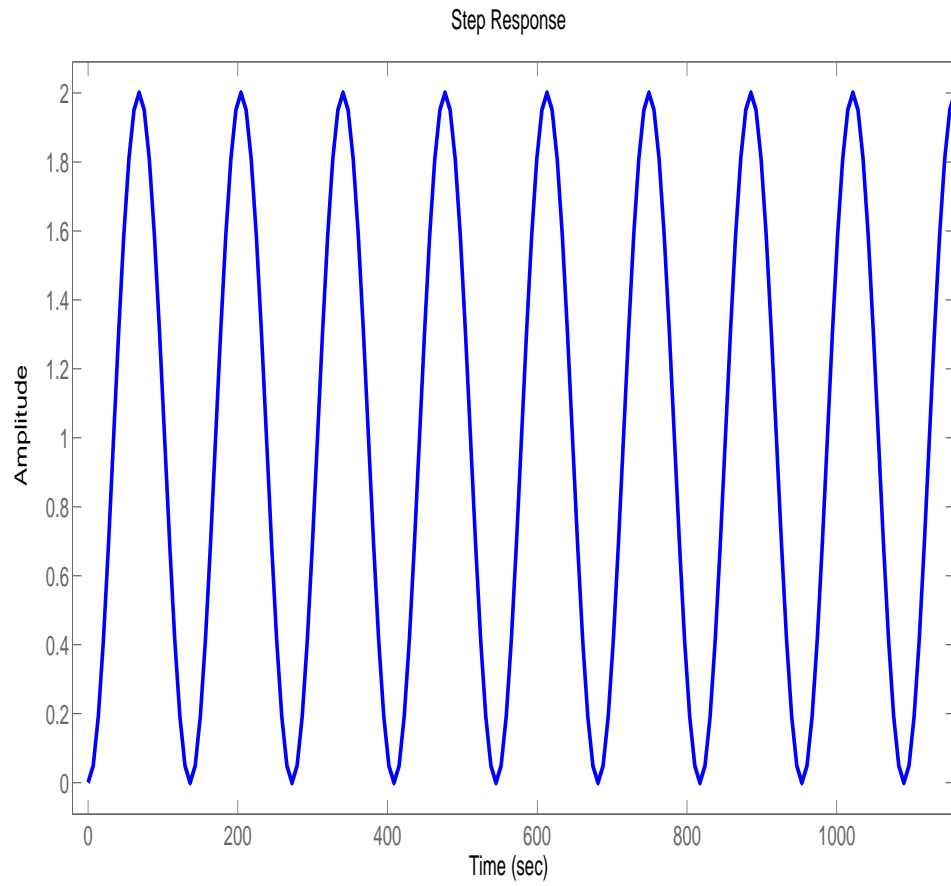


Figure 3.7: Proportional Control Step Response

From these results, it has been shown that proportional only control is insufficient for spacecraft attitude purposes. Augmenting this control law is necessary to achieve desired attitude behavior.

3.6 Proportional Derivative (PD) Control

Proportional control only accounts for the attitude error. If the error slope is also considered, it is proposed that actual behavior will approach the commanded behavior. First, define the proportional-derivative (PD) control law:

$$U(t) = K_p \Delta\theta(t) + K_d \Delta\dot{\theta}(t) \quad (3.11)$$

The control law now contains two gains, K_p which weights the error and K_d which weights the error rate. The transfer function for a PD control law is:

$$G_c = \frac{U(s)}{\Delta\theta(s)} = K_p + K_d s = K_d \left(\frac{K_p}{K_d} + s \right) \quad (3.12)$$

In an open-loop sense, PD control adds a zero to the negative real axis. In the root-location domain, the closed-loop pole locations move in the direction of system zero locations as the controller gain, in this case K_d , is increased. For spacecraft attitude, the PD open-loop zero moves the system poles into the negative domain. The end-result is a stable response. First, the closed-loop transfer function becomes:

$$CL = \frac{K_d s + K_p}{I s^2 + K_d s + K_p} \quad (3.13)$$

For $K_p = 1$ and $K_d = 10$, the following root location is produced:

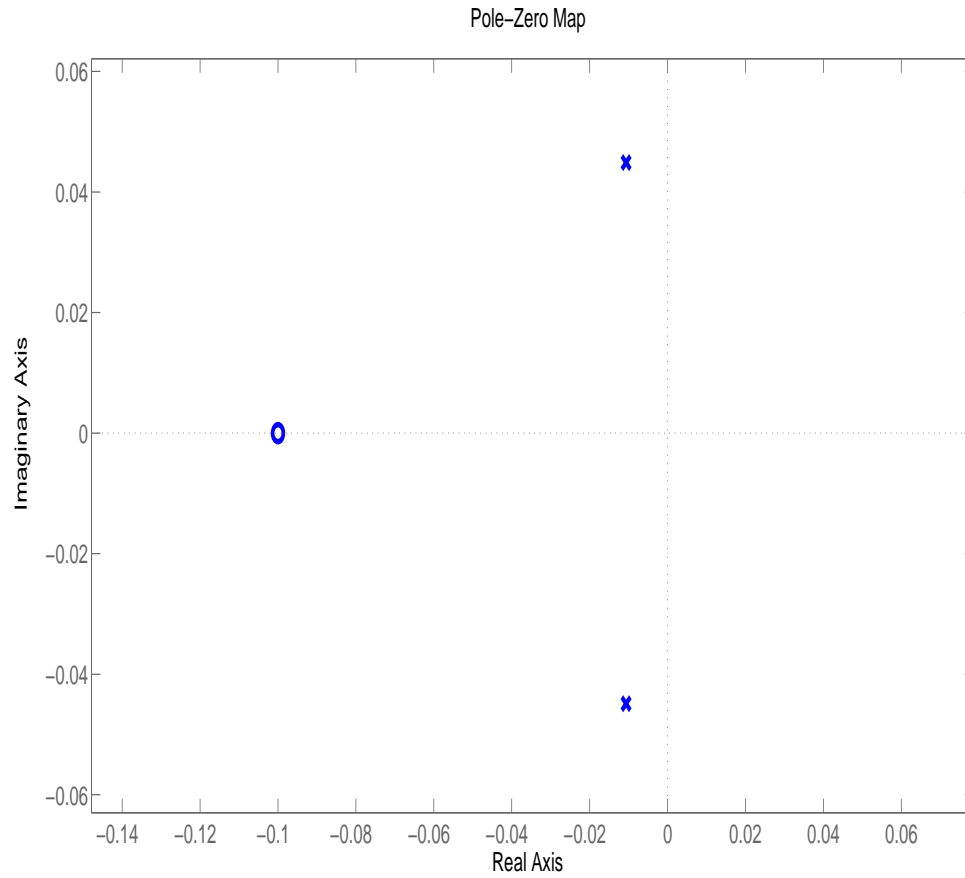


Figure 3.8: PD Control Root Location

From Figure 3.8 and Equation 3.13, the closed-loop response contains one zero and two poles. The closed-loop zero draws the the oscillatory poles into the negative real domain. The system now converges to the commanded response. This is seen from the unit-step response, given in Figure 3.9:

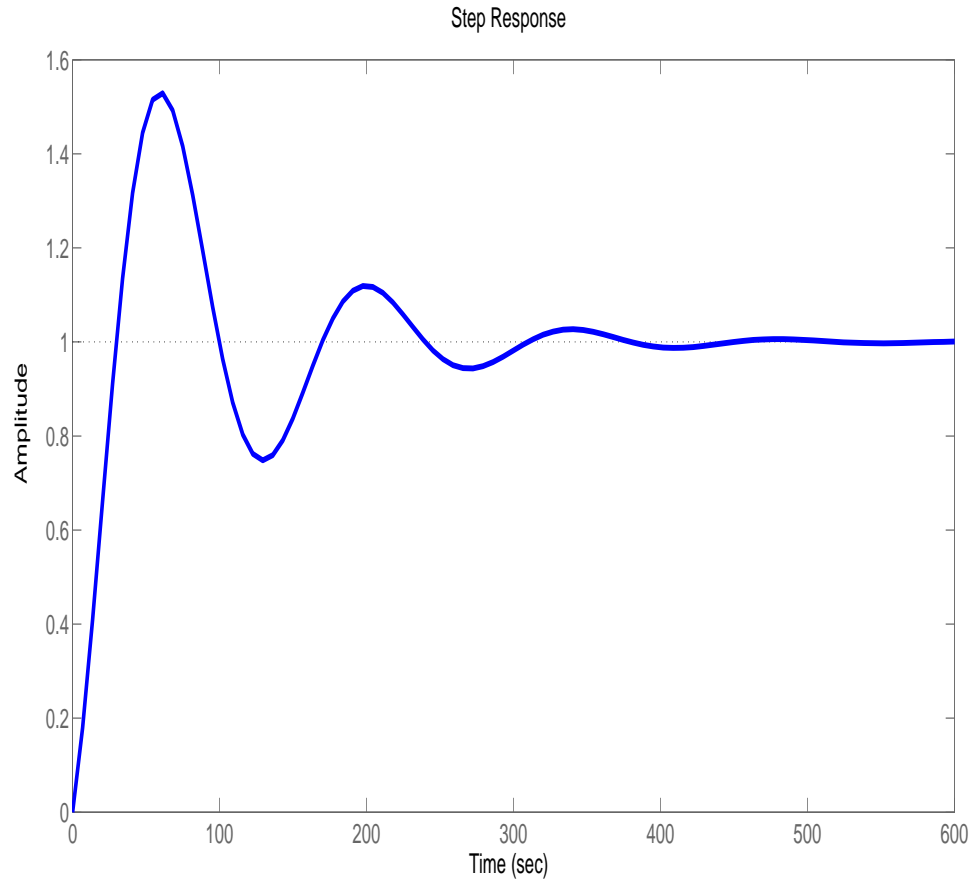


Figure 3.9: PD Control Step Response

PD controllers are effective at managing attitude transient response. Through an iterative design process, called *tuning*, gains are selected for proportional and derivative weighting that cause the commanded signal to converge within a specified time, called *settling time*, and handle desired levels of signal overshoot, or *percent overshoot*.

3.7 Proportional Integral Derivative (PID) Control

For spacecraft behavior, a PD controller is effective at controlling attitude, and the error converges to zero. However, certain systems contain substantial steady-state error when using purely PD control laws. Weighting the integral, or cumulative sum, of the total error can significantly improve the steady-state performance. A control law for PID would resemble:

$$U(t) = K_p \Delta\theta(t) + K_d \Delta\dot{\theta}(t) + K_i \int_0^t \Delta\theta(t) dt \quad (3.14)$$

The integral gain K_i weights the integrated error. The transfer function for this control law is:

$$G_c = \frac{U(s)}{\Delta\theta(s)} = K_p + K_d s + \frac{K_i}{s} \quad (3.15)$$

The PID control law adds one integrator and two zeros to the open-loop response. For spacecraft dynamics, the closed-loop transfer function becomes:

$$CL = \frac{K_d s^2 + K_p s + K_i}{I s^3 + K_d s^2 + K_p s + K_i} \quad (3.16)$$

Using $K_p = 1$, $K_d = 10$, and $K_i = 0.1$ generates the following root-location:

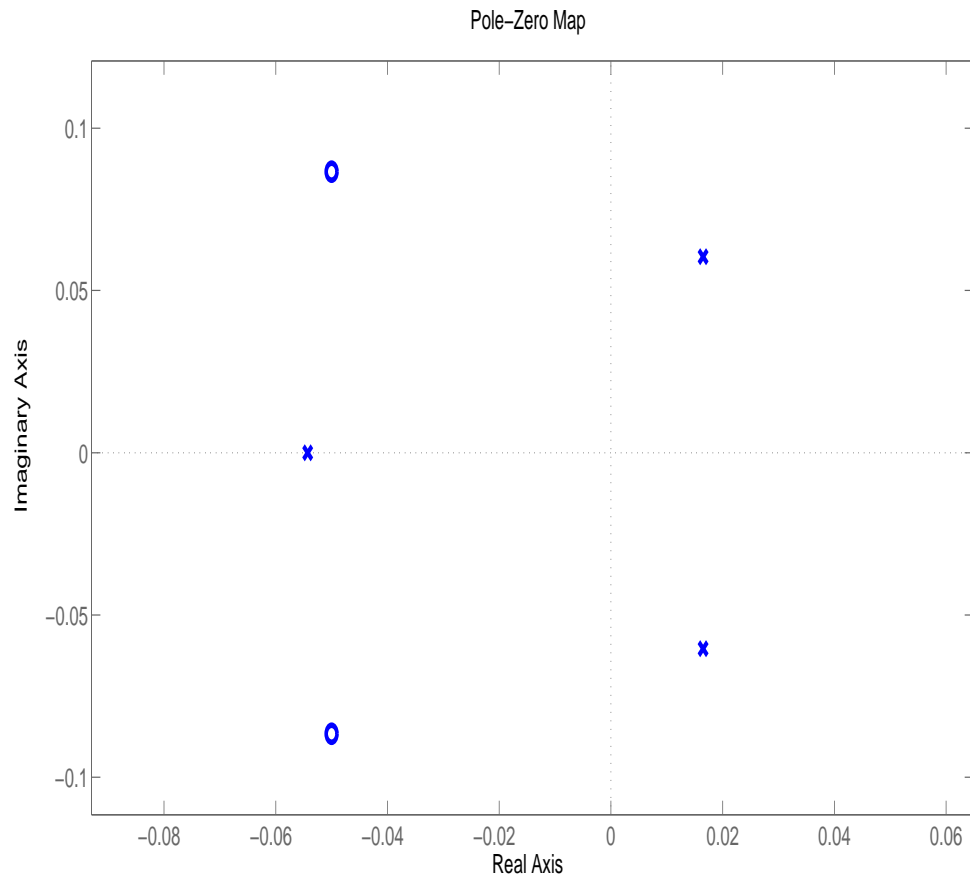


Figure 3.10: PID Control Root Location Configuration 1

For spacecraft dynamics, the integral gain causes closed loop-poles to actually exist in the positive plane. This drives the system unstable, as seen from Figure 3.11:

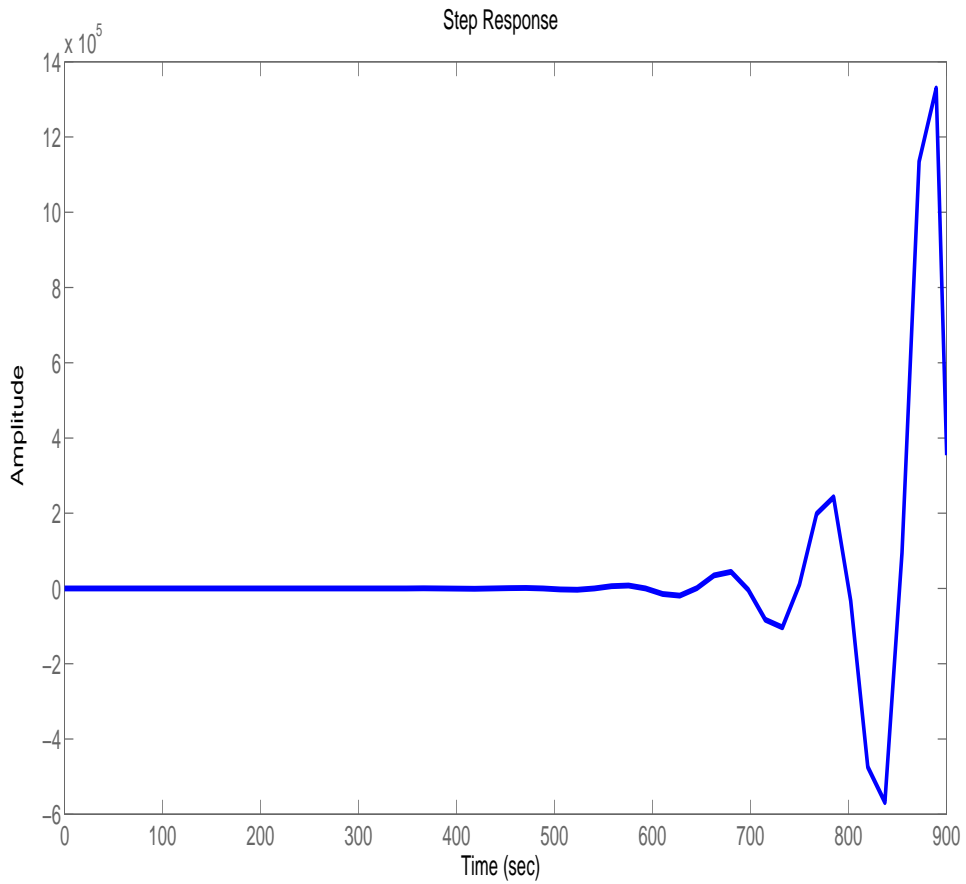


Figure 3.11: PID Control Step Response Configuration 1

Careful selection of the integral gain is necessary to ensure closed-loop stability. Reducing the integral gain by two orders of magnitude to $K_i = .001$ produces the following root-location:

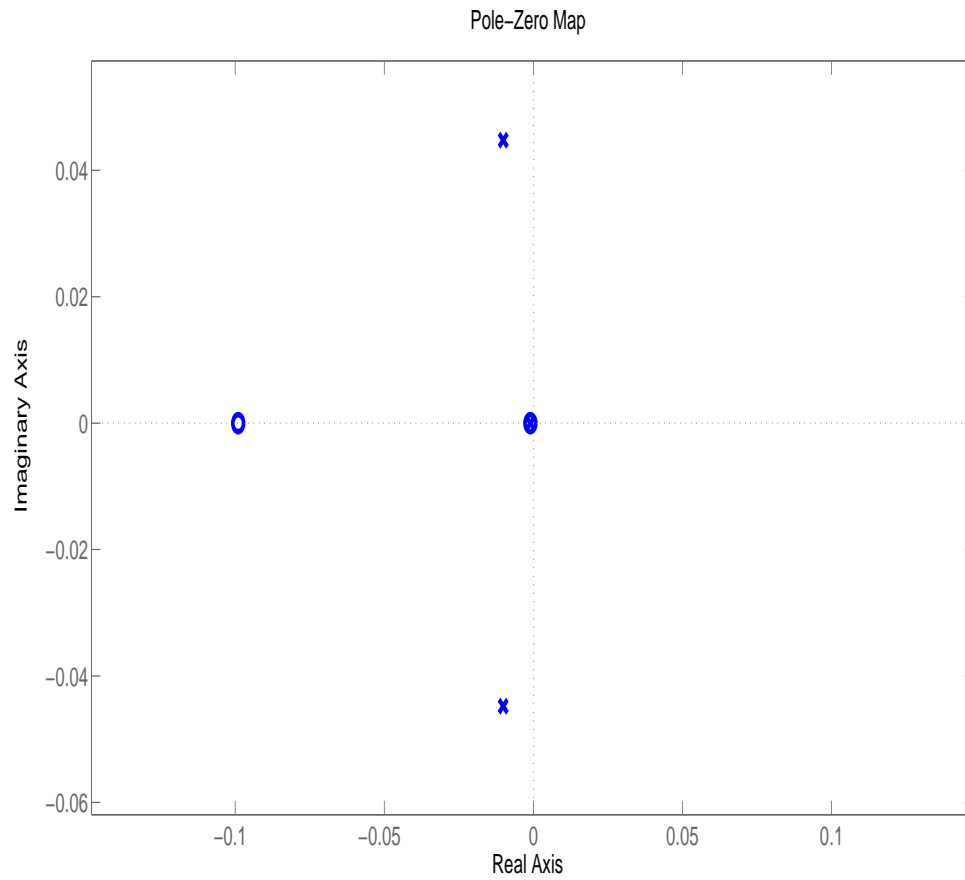


Figure 3.12: PID Control Root Location Configuration 2

Decreasing the integral gain causes the closed-loop poles to move back into the negative-half plane. The unit-step response is now stable:

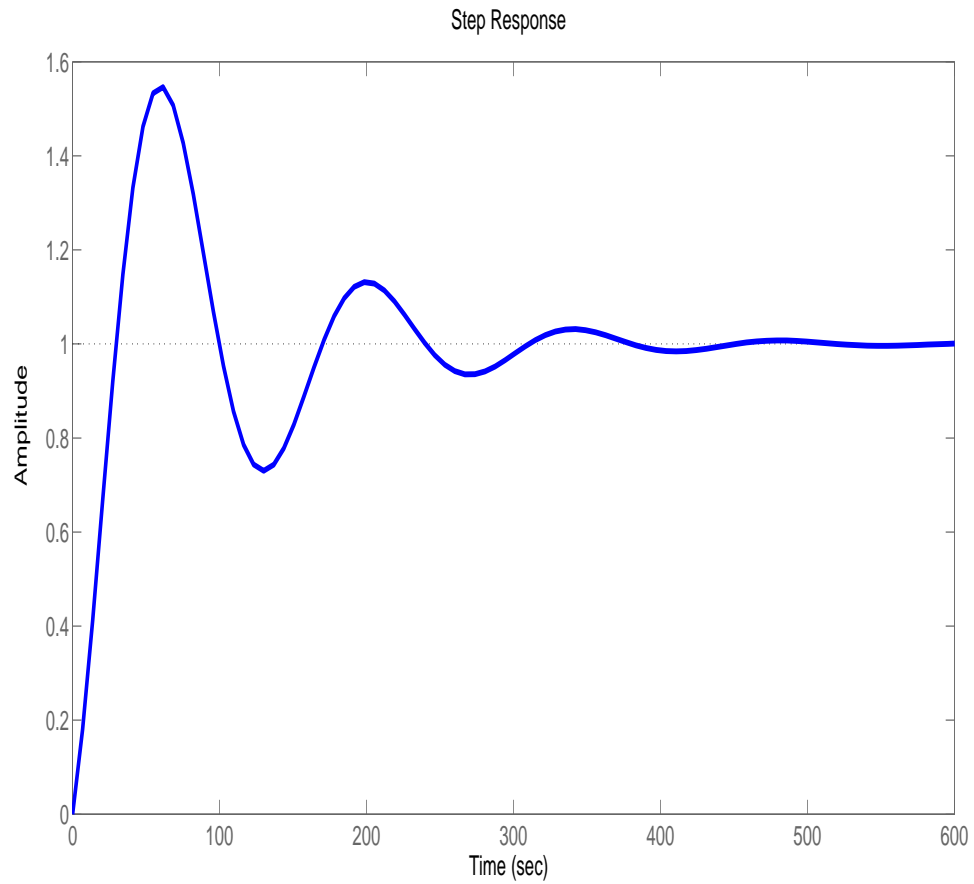


Figure 3.13: PID Control Step Response Configuration 2

While integral control tends to reduce the steady-state error, integral gain contains within it additional effects that must be carefully considered prior to implementation. The integrated error is generally larger in the first stages of the control time history. Therefore, the size of the integral gain must be orders of magnitude smaller than the other gains. Integral control has

the additional effect of inducing additional oscillations in the system transient response, causing the percent overshoot and settling time to increase.

For the idealized linearized model considered without disturbances, integral control does not significantly affect steady-state error in response to unit-step inputs, so it need not be included in the final design. In actuality, some integral control may be necessary for disturbance rejection. The PID gain selection is directly related to the plant transfer function, and control mode priorities. A summary of PID dependencies are given in Table 3.1 [14]:

Table 3.1: Effect of **Increasing** PID Gain

Gain	Settling Time	Percent Overshoot	Steady-State Error	Stability
K_p	None	Increase	Decrease Slightly	Decrease
K_d	Decrease	Decrease	None	Increase
K_i	Increase	Increase	Decrease	Decrease

3.8 Stability Analysis through Frequency Response

One major advantage of linear control is the relative ease through which stability performance can be assessed. Thus far, the various control laws have been designed assuming ideal conditions: i.e. perfect knowledge and availability of states, continuous time systems, unlimited control effort, etc. In reality, systems are limited by physical constraints and imperfections. If the control law implemented is not sufficiently robust, the transient response can be driven unstable.

Some metric must be utilized to determine stability robustness. For lin-

ear control, this is conducted using frequency-response techniques. Frequency techniques follow from the concept of the sinusoidal input-output response. For a linear system, a sinusoidal input will produce a sinusoidal output, each with a different magnitude and phase. A schematic of this process is given in Figure 3.14 [14]:

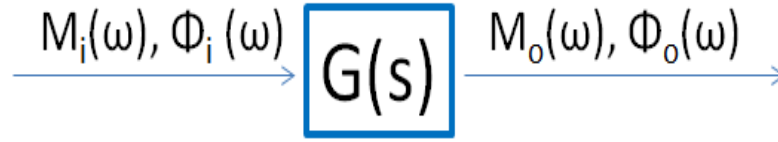


Figure 3.14: Frequency Response Schematic

The magnitude frequency response is the output/input sinusoidal magnitude ratio:

$$M(\omega) = \frac{M_o(\omega)}{M_i(\omega)} \quad (3.17)$$

The phase frequency response is the output/input phase difference:

$$\Phi(\omega) = \Phi_o(\omega) - \Phi_i(\omega) \quad (3.18)$$

Taken together, the magnitude and phase frequency responses is called the frequency response of the system. There are numerous techniques used to visualize frequency responses. For this paper, the Bode diagram will be examined, which graphs the magnitude and phase responses into separate plots. First, the substitution $s = j\omega$ is made for the Laplace variable s .

$$G(j\omega) = G(s), s \rightarrow j\omega \quad (3.19)$$

This transforms the transfer function to a complex variable. If the function is written as:

$$G(j\omega) = X(\omega) + jY(\omega) \quad (3.20)$$

Then the magnitude and phase expressions are equal to [14]:

$$\begin{aligned} M(\omega) &= \sqrt{X^2 + Y^2} \\ \Phi(\omega) &= \text{atan2}(Y, X) \end{aligned} \quad (3.21)$$

The Bode visualization plots the magnitude and phase separately on log-log and linear-log scales respectively. The abscissa is the $\log(\omega)$ in rad/s. For the magnitude graph, the ordinate is decibel magnitude, or $M(db) = 20\log M(\omega)$. For the phase graph, the ordinate is the phase angle in degrees. The standard presentation is to place the magnitude graph above the phase graph. Stability robustness is inferred from gain and phase margins.

Gain margin is defined as the magnitude value when the phase crosses -180 degrees, and phase margin is defined by the phase offset from -180 degrees when the magnitude crosses 0 dB. The gain margin quantifies how much additional gain is required to make the linear system unstable. The additional gain can occur due to imperfections and mismodelings in the linear system behavior. The phase margin quantifies the system's ability to handle additional delays, such as latency or time-offset. An example open-loop Bode diagram for a spacecraft using PID control, using $K_p = 1$, $K_d = 10$, and $K_i = 0.001$, is shown in Figure 3.15:

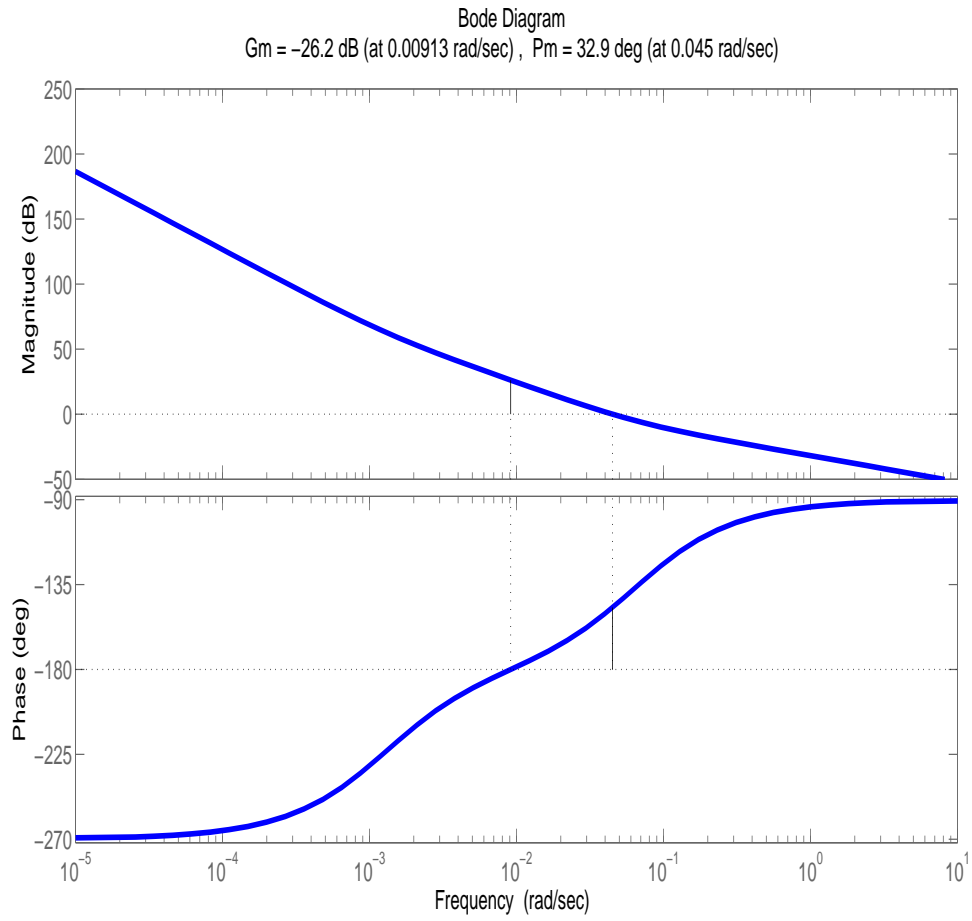


Figure 3.15: Bode Plot Example

For the example response, the controller generates a system with approximately 26 dB gain margin and 33 degree phase margin. For spacecraft attitude systems, standard margins are typically designed around 6 dB gain margin and 30 degree phase margin. Both of these guidelines are met for the example case.

3.9 GRACE PD Control

The control algorithms for the GRACE ACS system were selected by Space Systems Loral, and may be ITAR restricted [17]. In a general sense, the PD controller designed produces a damped step response with a “rise time” of less than 200 seconds. An example step response function with these qualities is given in Figure 3.16:

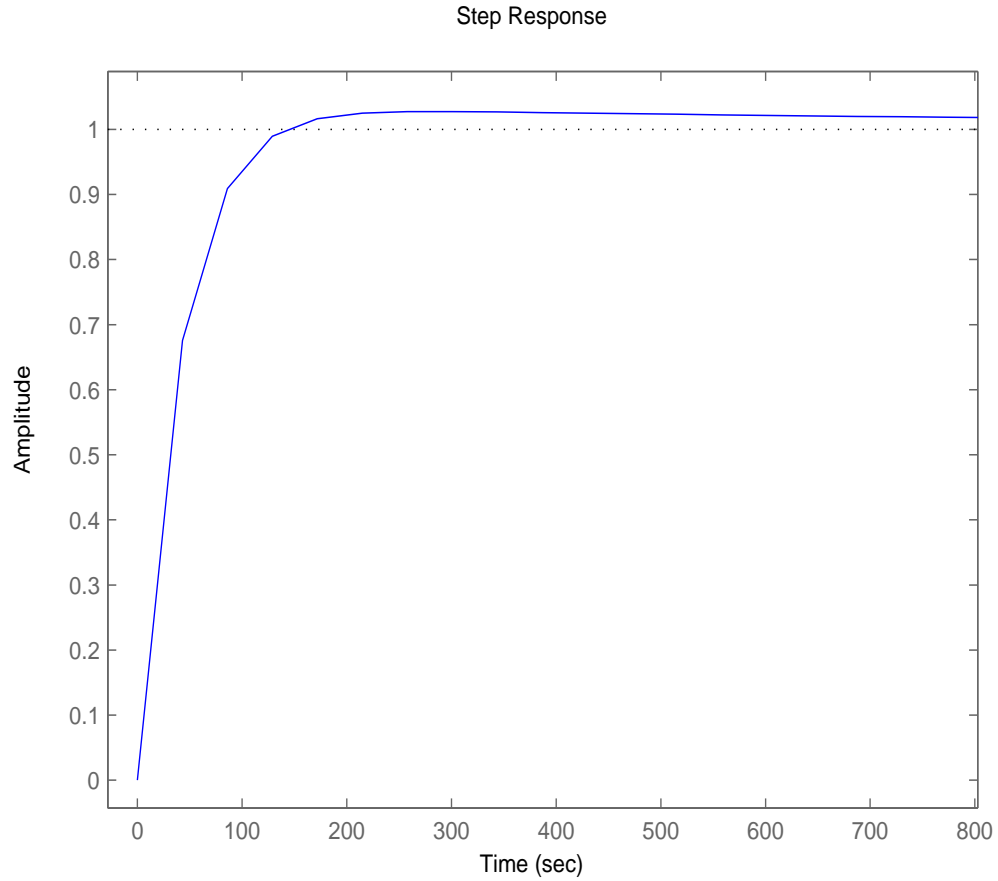


Figure 3.16: Step Resonse of PD Configuration used in GRACE Science Mode

In the ideal feedback diagram, shown in Figure 3.4, the control response is delivered in a constant, continuous fashion to the spacecraft dynamics. In reality, physical constraints limit the amount of effective control that can be delivered. For the GRACE science mode requirements, the way that control is managed is through a deadband-limited construct, introduced in Figure 1.7.

When the attitude error e exceeds a predefined threshold, only then is control activated. As thrusters are used as the primary actuator, this construct acts to conserve fuel over the length of the mission. This type of implementation, referred to as “limiting” control, is in contrast to so-called “maneuver” based control, in which the attitude is commanded to desired value.

For “limiting” control, a small amount of steady state error is acceptable. In this implementation, the higher priority is to reduce the amount of time the error lies outside the deadband, to optimize the overall control effort, and to limit the magnitude of oscillations induced by the control algorithms. Unwanted oscillations can have detrimental effects on the attitude acceleration behavior, which in turn affects the scientific solution. For all of these reasons, the choice of a quick rise-time, PD controller is selected. The benefits of reduced steady state error are not worth the oscillatory characteristics that PID brings. Now that the foundation of the GRACE dynamics and control have been established, a simulation can be discussed that represents the ACS process.

Chapter 4

Simulation Construction and Validation

4.1 Introduction

Simulation environments are the primary tools through which ACS system performance and behaviors are assessed. Before the sensitivity experiments comprising this case study can be conducted, a simulation model mimicking satellite attitude behavior must be constructed. This study examines the control example utilizing a PD control law, with magnetic torquers and deadband-limited thrusters as actuators, and with star cameras as knowledge sensors. The GRACE ACS system for science mode is used as the exemplar from which sensitivity experiments are performed. All simulations are constructed in a MATLAB/SIMULINK environment.

4.2 Satellite Attitude Block Diagrams

A block-diagram representation of the GRACE ACS science mode is given in Figure 4.1.

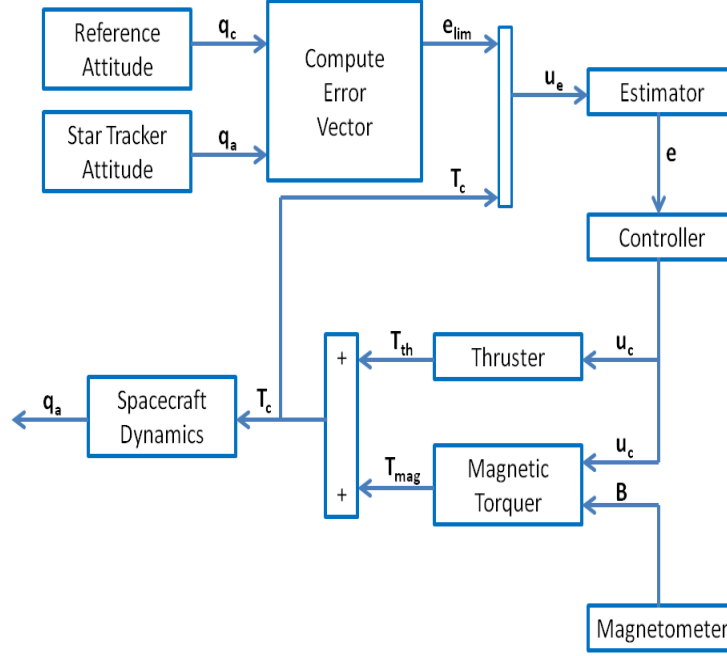


Figure 4.1: GRACE ACS Science Mode Block Diagram

This identical attitude control configuration is implemented aboard each GRACE satellite. The processes use a 1 Hz sampling frequency [9]. A reference quaternion q_c representing the line-of-sight connecting the CM of each satellite is uploaded to the spacecraft. It is then compared with the actual orientation of the spacecraft using quaternion data from a star camera q_a . A limited attitude error signal e_{lim} is computed representing the deviation between the reference attitude frame and the star camera attitude frame. A linear quadratic estimator (LQE) is used to re-construct the rate signal, and

improves the angle estimate using the limited signal and the applied torques. This estimated signal e , composed of angles and rates for each axis, is then sent to a PD control law. The control signal formed u_c is then routed to the actuator dynamics. The complete control signal is sent to the thruster logic. The thrusters use pulse-width modulation in a deadband-limited capacity, which produce a torque T_{th} . In addition, the control signal is de-weighted and sent to the magnetic control logic, producing magnetic torque T_{mag} . Finally, the combined control torque is delivered to the spacecraft, and the loop is closed in a negative feedback sense [17].

The ultimate goal of simulation is to reproduce satellite ACS behavior for the science configuration (i.e. PD control law, thruster and magnetic actuation, star camera sensing, fine-pointing requirements) analyzed in this case study. To achieve this, the GRACE science mode ACS is used as the example. Two simulation models are considered as the focus of this chapter. First, a simulation containing the actual GRACE science mode ACS configuration is validated against flight data. The purpose of this simulation is to ensure that all components in the ACS logic are working properly when compared to actual telemetry. This validation simulation is “open-loop”, in the sense that spacecraft dynamics are not modeled. Rather, this model verifies that the computed control actuation delivered to the spacecraft matches the actual results.

After it has been demonstrated that the ACS components are all working as expected, the spacecraft dynamics are modeled to form a “closed-loop”

simulation. This “closed-loop” simulation is not intended to replicate the GRACE attitude, but rather models a representative spacecraft using the ACS logic of the GRACE science mode. This model is used as a starting point from which the sensitivity analysis can be performed. Each model is now discussed in detail.

4.3 GRACE ACS Validation Model

The Simulink implementation of Figure 4.1 is given in Figure 4.2. In contrast to Figure 4.1, Figure 4.2 does not model the spacecraft dynamics. As mentioned earlier, the purpose of the model in Figure 4.2 is to recreate an attitude control implementation for the ACS configuration under examination (PD control, deadband-limited thrusters, etc.). The blocks in this Simulink diagram are validated using GRACE specific algorithms and telemetry [17].

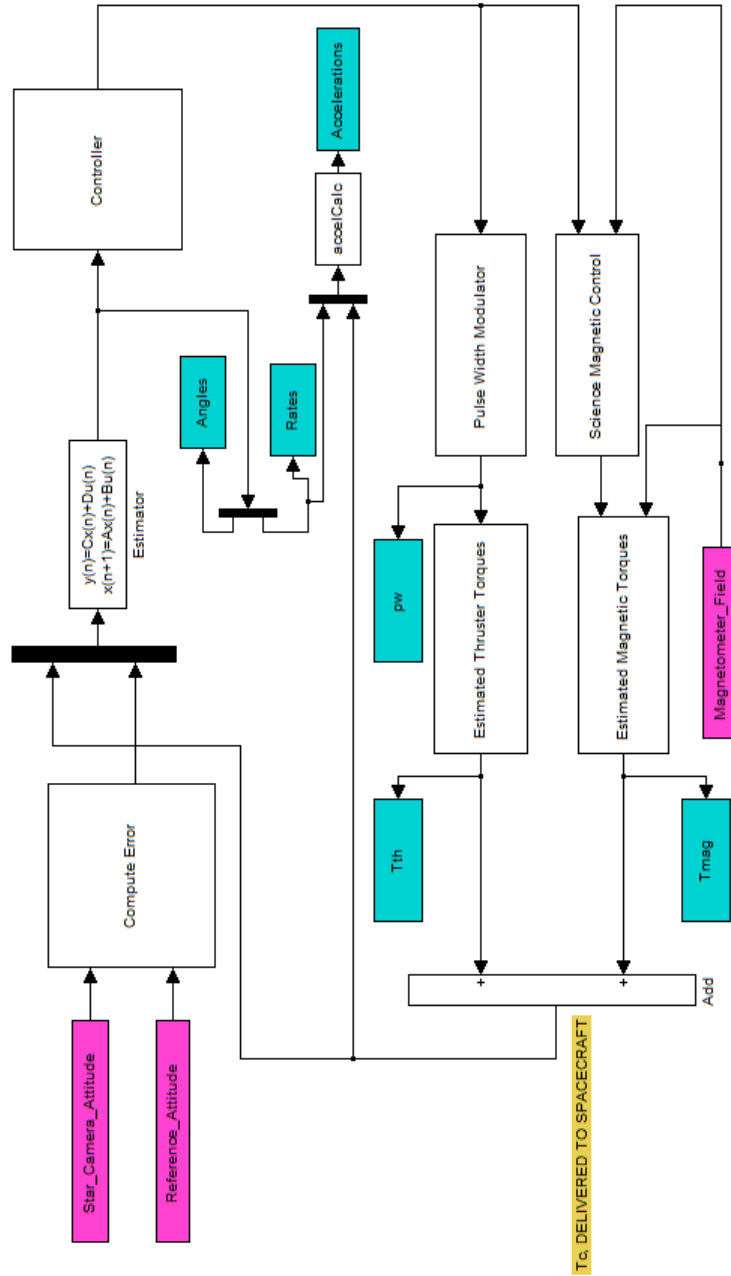


Figure 4.2: Validation Simulation Model

Inputs to the simulation are labeled in magenta. These are sampled at 1 Hz, and are extracted from telemetry data for the GRACE satellite on a selected day. This telemetry is extracted using the telemetry database at the University of Texas Center for Space Research (CSR), called the OFFRED database. The inputs required to run the GRACE ACS science mode simulation are summarized in Table 4.1.

Table 4.1: GRACE Validation Model Required Inputs

Star Camera Attitude (q_a)
Reference Attitude (q_c)
Magnetometer Magnetic Field (B)

A date is selected where the satellite is primarily in science mode. One such day is April 2, 2011. To validate this model, selected outputs available for comparison, labeled in teal, are compared between simulation and flight data. The data available for comparison is given in Table 4.2:

Table 4.2: GRACE Validation Model Available Outputs

Angles (ϕ, θ, ψ)
Rates ($\dot{\phi}, \dot{\theta}, \dot{\psi}$)
Accelerations ($\ddot{\phi}, \ddot{\theta}, \ddot{\psi}$)
Thruster Pulse-Width (pw)
Magnetic Torque (T_{mag})

An LQE is used to estimate the Angles and Rates, a pulse-width modulation scheme calculates the required thruster on-time, and a magnetic control algorithm is used in combination with the magnetic field data to produce the

magnetic torques. In addition, angular acceleration is calculated from the Euler equations [10]. The validation model is run for a half-day time arc at a 1 Hz sample, and the outputs from simulation are compared with the telemetry outputs.

4.3.1 Angle Validation

A time-history comparison of the simulation and telemetry attitude angles is given in Figure 4.3:

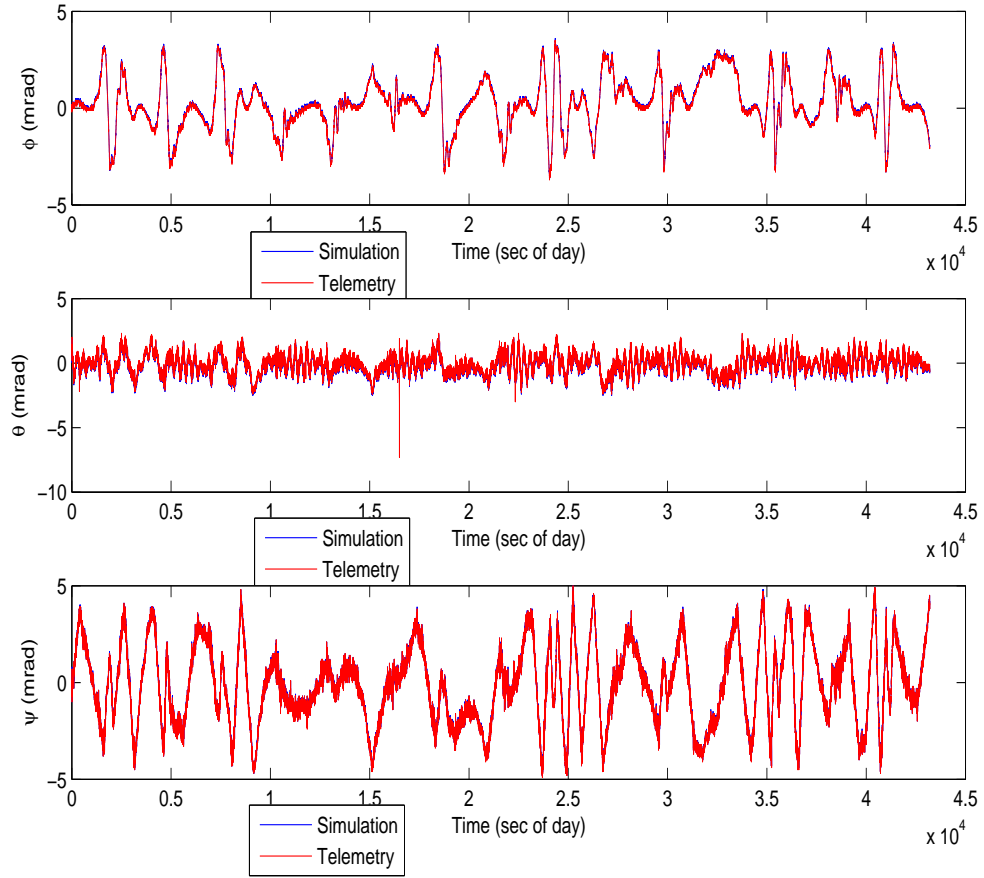


Figure 4.3: Validation/Telemetry Comparison: Attitude Angle Time-Domain

The attitude is deadband-limited between 3-5 mrad amongst the three axes [18]. When the attitude exceeds the deadband threshold, attitude thrusting is initiated. The simulated and telemetry time-history results are very similar. The frequency response is compared using the PSD of the angle time-history, given in Figure 4.4:

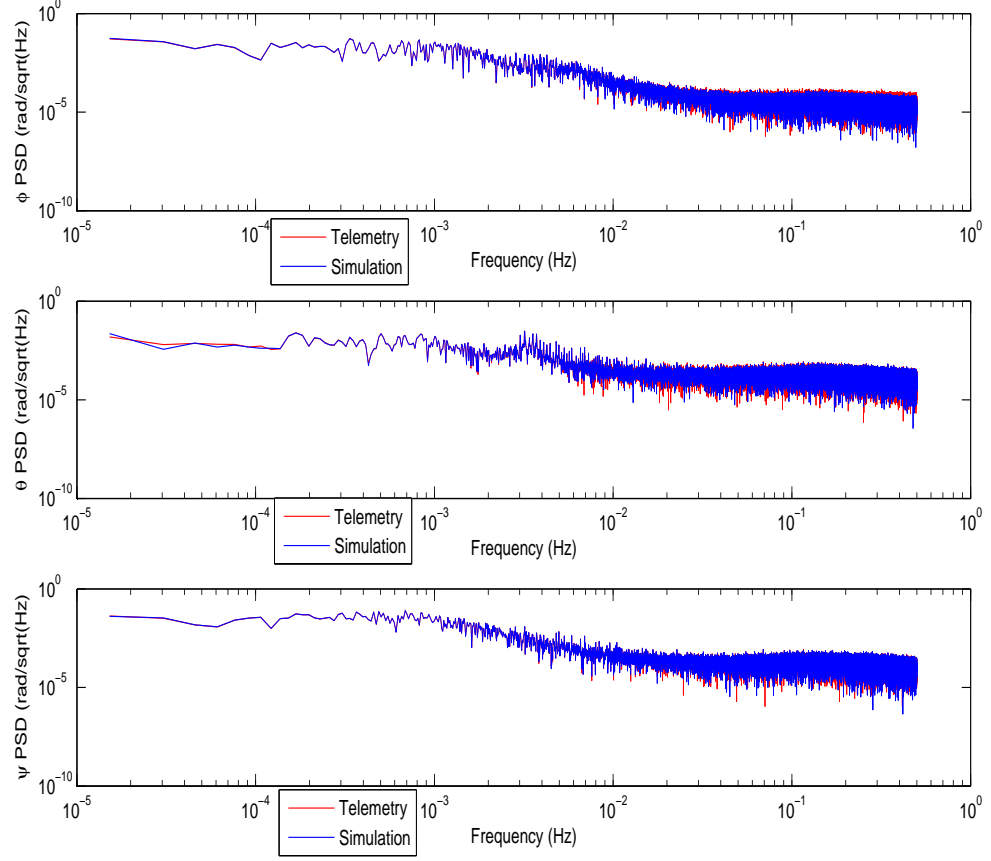


Figure 4.4: Validation/Telemetry Comparison: Attitude Angle Frequency-Domain

The frequency behavior of the two signals is also very similar across the spectrum. The RMS of the residuals are summarized in Table 4.3:

Table 4.3: Attitude Angle Simulation/Telemetry Residual Mean and RMS

Metric	Residual Mean (mrad)	Residual RMS (mrad)
ϕ	0.06	0.08
θ	0.08	0.3
ψ	0.02	0.3

4.3.2 Rate Validation

The rate time histories are given in Figure 4.5. As with the angles, the simulation and telemetry histories match a general trend.

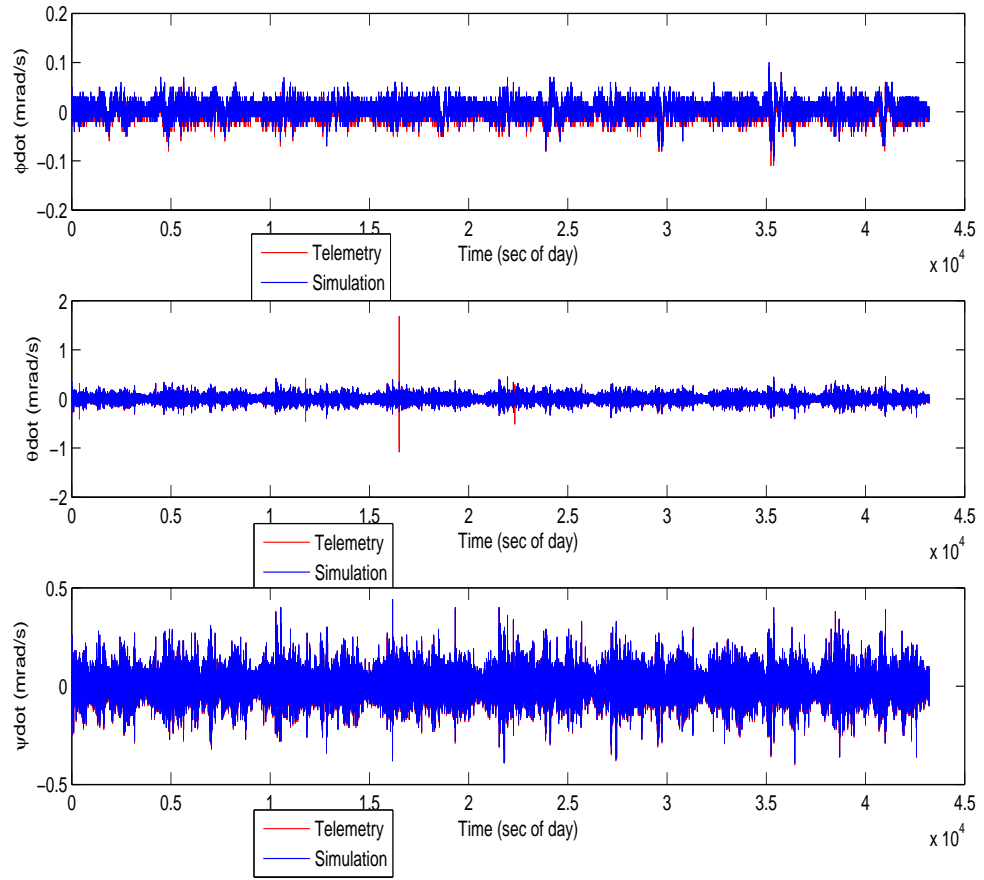


Figure 4.5: Validation/Telemetry Comparison: Attitude Rate Time-Domain

The rate signal PSD is also comparable between simulation and telemetry, as seen in Figure 4.6:

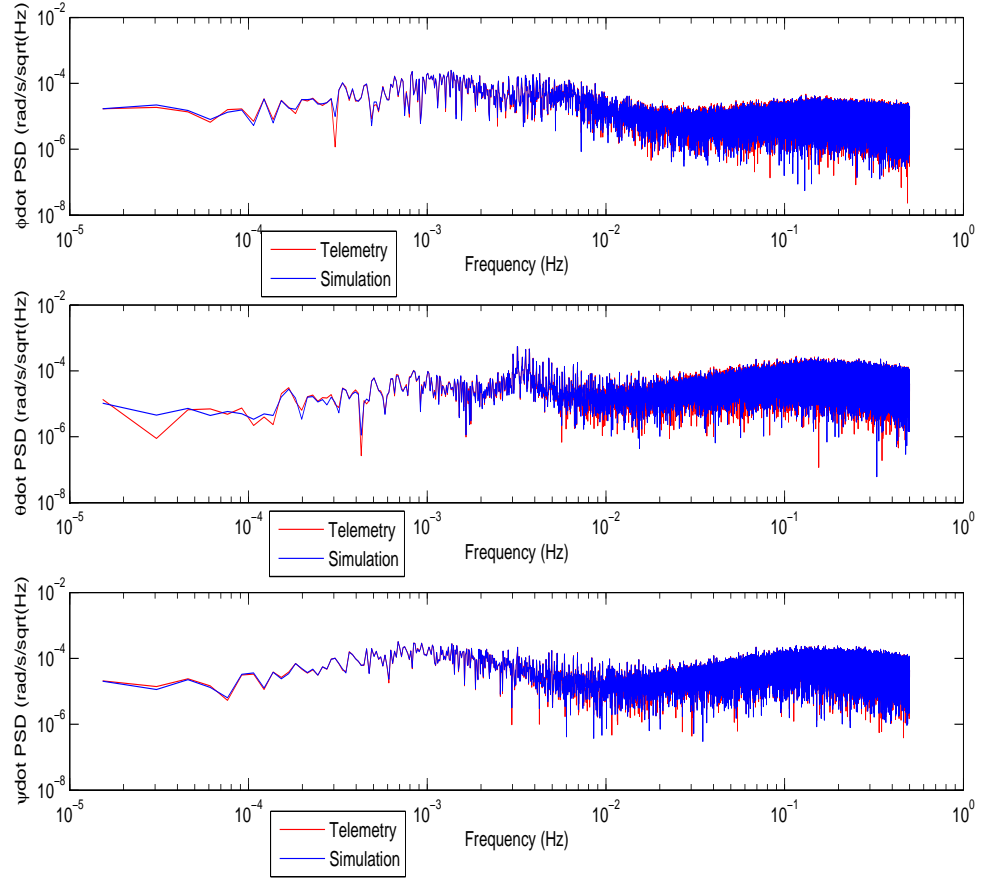


Figure 4.6: Validation/Telemetry Comparison: Attitude Rate Frequency-Domain

The RMS residuals are given in Figure 4.4:

Table 4.4: Attitude Rate Simulation/Telemetry Residual Mean and RMS

Metric	Residual Mean (mrad/s)	Residual RMS (mrad/s)
$\dot{\phi}$	0.005	0.02
$\dot{\theta}$	0.005	0.1
$\dot{\psi}$	0.005	0.1

The time and frequency responses of the angles and rates match very closely to the telemetry outputs. Therefore, the attitude error construction and estimation processes are properly realized in their representative blocks within the simulation environment.

4.3.3 Magnetic Torque Validation

After the estimated angles and rates are sent to the PD controller, the control signal formed is sent to the actuator dynamics. The magnetic torquers operate by generating an electrical moment that, combined with the ambient magnetic field, produces a control torque [11]. For GRACE, the torquers are capable of generating a maximum 30 A m^2 of magnetic moment M_c . The magnitude of the moment generated is proportional to the size of the control signal utilized by the “Science Magnetic Control” scheme. In order to minimize magnetically induced angular accelerations, the full control signal is multiplied by a de-weighting scale factor prior to use in the “Science Magnetic Control” process. The magnetic moment signal generated is smaller than if the full control signal is used. This limits the amount of magnetic torque delivered to the spacecraft, which minimizes the angular accelerations. The comparison

between simulation and telemetry for the magnetic torques is given in Figure 4.7:

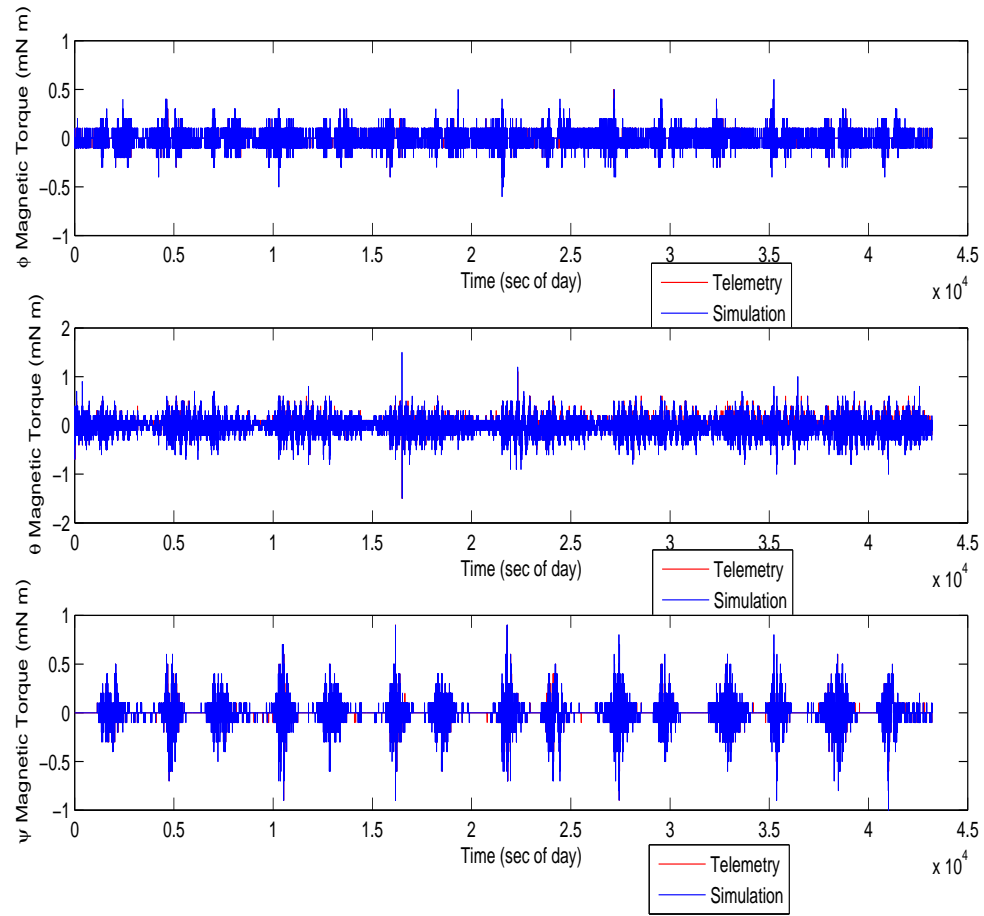


Figure 4.7: Validation/Telemetry Comparison: Magnetic Torque Time-Domain

The orientation of the magnetic field is such that the pitch axis becomes the prime candidate for magnetic actuation; this is reflected in the overall

magnitude of the pitch magnetic control effort [19]. Additionally, the data from telemetry is limited to four significant figures. Hence, there are periods when the telemetry reports no magnetic actuation due to truncation. For the purposes of validation, the magnetic torque produced in the Validation Simulation is also limited to four significant figures. The general trends are very similar, as seen in Figure 4.7. The RMS of the magnetic residuals are seen in Table 4.5:

Table 4.5: Magnetic Torque Simulation/Telemetry Residual Mean and RMS

Metric	Residual Mean (mN m)	Residual RMS (mN m)
T_ϕ	0.0002	0.09
T_θ	0.030	0.2
T_ψ	0.0003	0.1

4.3.4 Thruster Pulse Width Validation

As thrusters are the primary actuator, the full control signal is sent to this logic. A pulse-width modulation scheme calculates the on-time required for all attitude thrusters. This pulse-width is the best available telemetry output for thruster validation, and the time-history comparison is given in Figure 4.8:

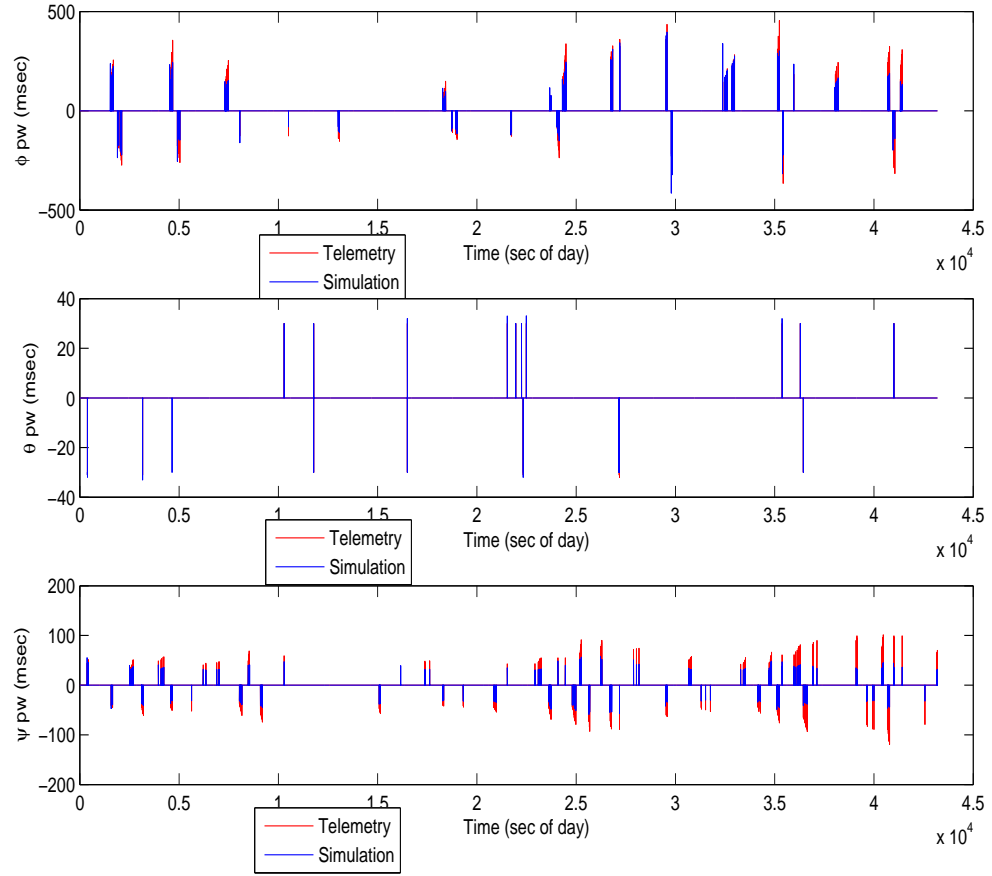


Figure 4.8: Validation/Telemetry Comparison: Pulse Width Time-Domain

As seen from this graph, the pulse-widths match well for the roll and pitch axis, but are slightly off in yaw. The residuals are summarized in Table 4.6:

Table 4.6: Pulse Width Simulation/Telemetry Residual Mean and RMS

Metric	Residual Mean (sec)	Residual RMS (sec)
pw_ϕ	0.07	0.002
pw_θ	0.0004	0.0002
pw_ψ	0.01	2

The discrepancy in yaw-axis pulse width is approximately of order two. However, the general trend is very similar. Specifically, the pulse-width modulation scheme activates whenever the attitude behavior breaks the deadband-limits. From Figure 4.8, the time at which pulse-widths are commanded matches closely between telemetry and simulation. Therefore, the simulation correctly identifies when the attitude behavior breaks the deadbands. The discrepancy lies in the magnitude of the commanded on-time. Therefore, the fundamental logic works as expected, it is simply the magnitude of the pulse width that is different. To account this discrepancy, the magnitude of the pulse-width is empirically corrected by a scale factor of 2.

4.3.5 Attitude Acceleration Validation

The time-history comparison of the attitude accelerations is given in Figure 4.9:

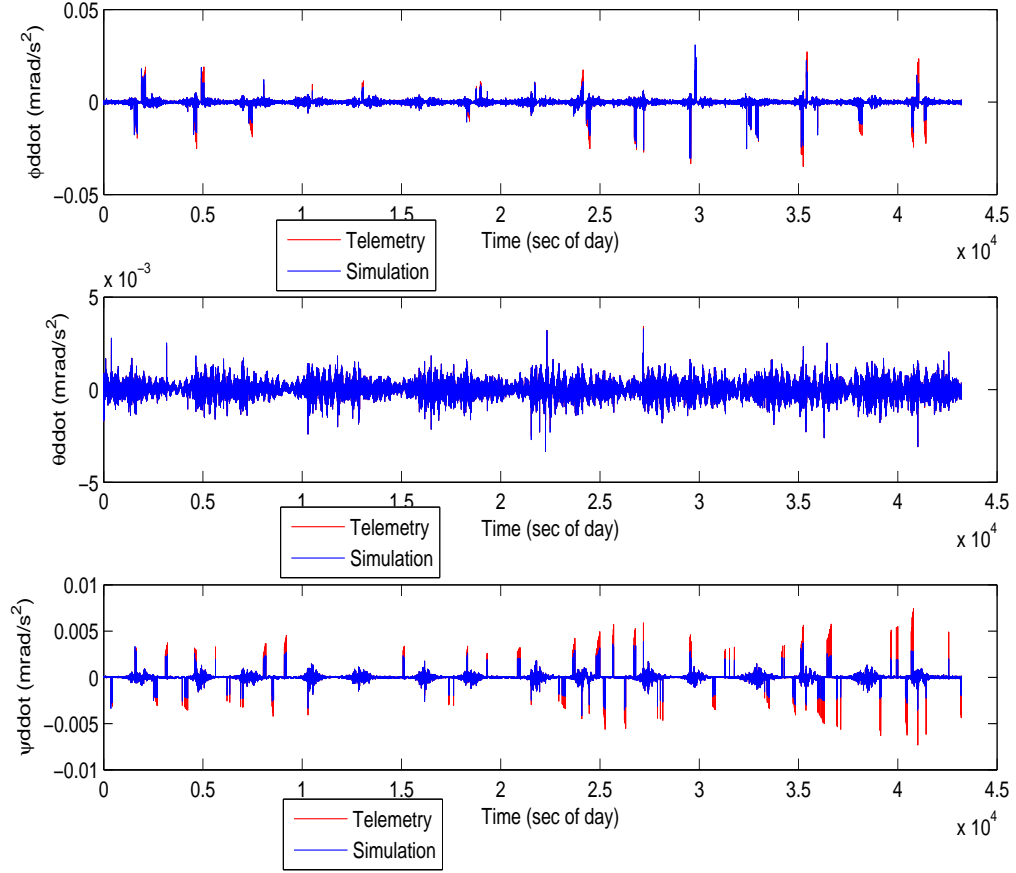


Figure 4.9: Validation/Telemetry Comparison: Attitude Acceleration Time-Domain

The accelerations are highly dependent on torques and angular rates. The thruster firing impulses are clearly reflected in the acceleration time history. The yaw axis shows the discrepancy in the thruster on-time discussed in the previous section. However, as recalled from Chapter 1, the attitude accel-

ations performance requirements are specified in the frequency domain. The PSD of the attitude accelerations is given in Figure 4.10:

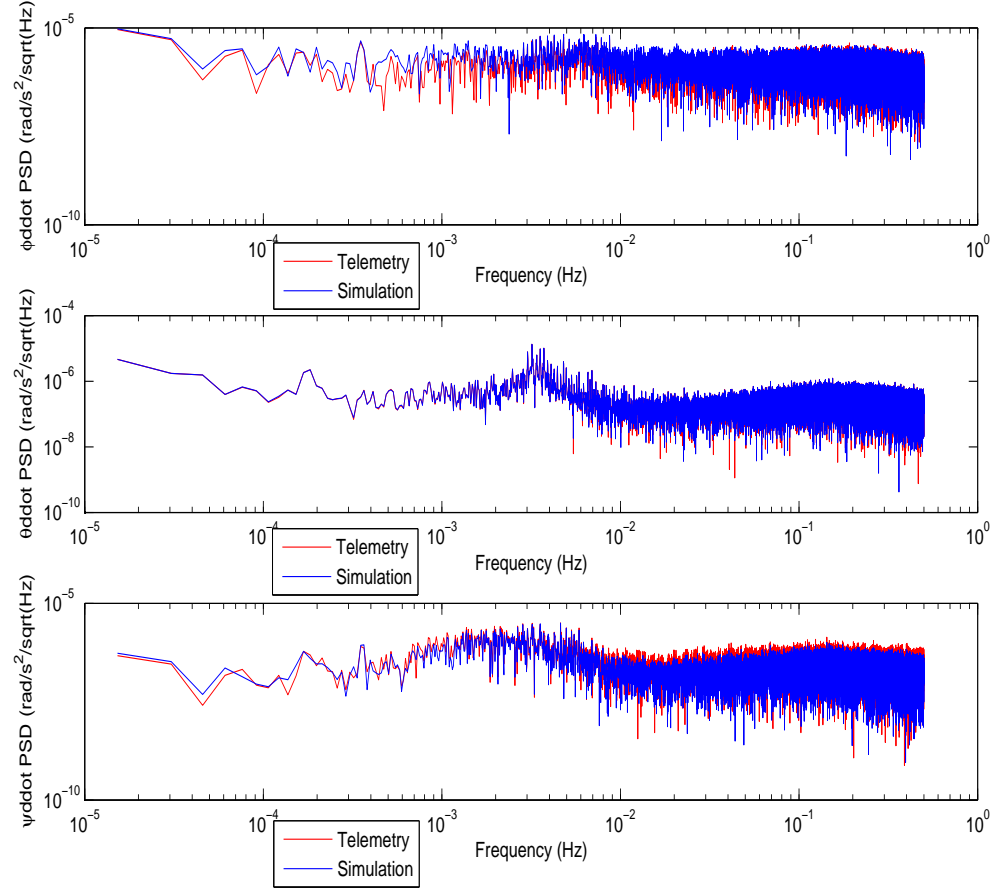


Figure 4.10: Validation/Telemetry Comparison: Attitude Acceleration Frequency-Domain

As seen from Figure 4.10, the existing thrust discrepancy does not have a sizable effect on the angular acceleration PSD. This result does not mean

that angular acceleration PSD is independent of thruster firing magnitude. It only means that the current discrepancy in pulse-width is not significant enough to affect the PSD behavior. Sensitivity of the angular acceleration PSD to thruster firing is further explored in the sensitivity study results. The residuals of the angular acceleration are given in Table 4.7. The mean value of the roll attitude acceleration is higher than the other two axes by at least two orders of magnitude. The environmental disturbance is greatest in the roll axis [17], requiring larger commanded thruster on-times. The on-time discrepancy previously mentioned is magnified, causing the subsequent thruster torque and attitude acceleration to experience larger residual mean and rms values.

Table 4.7: Attitude Acceleration Simulation/Telemetry Residual Mean and RMS

Metric	Residual Mean (nrad/s ²)	Residual RMS (nrad/s ²)
$\ddot{\phi}$	5	70
$\ddot{\theta}$	0.008	1
$\ddot{\psi}$	0.07	15

4.4 GRACE ACS Experimental Model

The blocks that make up the ACS logic for GRACE science mode have now been sufficiently tested and validated with respect to GRACE telemetry. This configuration is now used to create a simulation model that will be used in the sensitivity experiments. The purpose of this simulation is not to exactly recreate the attitude history of the GRACE satellite. Rather, it is meant to be a representative ACS system for a satellite in the same ACS class as GRACE.

The GRACE implementation is used as the example implementation from which this experimental model is built. From this model, sensitivity tests can be performed to test which components comprising the system have the greatest impact on attitude responses for the class of PD control. In order to create this model, the simulation in Figure 4.2 is altered to include spacecraft dynamics, and is given in Figure 4.11:

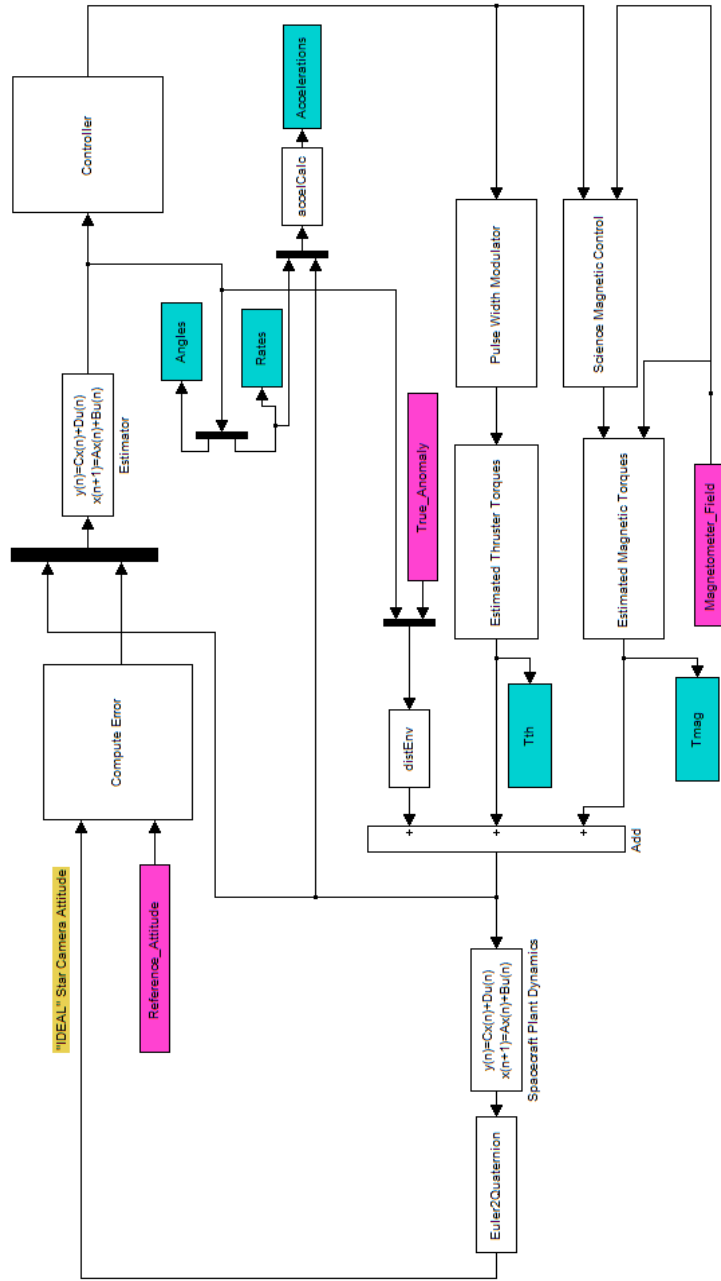


Figure 4.11: Experimental Simulation Model

In Figure 4.11, the computed control torque at a given time step is sent to the spacecraft dynamic plant model. The ideal version of the model given in Figure 4.11 does not include any instrument noise, misalignments, or other imperfections. These are treated in greater detail during the sensitivity study. The telemetry inputs required for this model are given in Table 4.8.

Table 4.8: GRACE Experimental Model Required Inputs

Reference Attitude (q_c)
Magnetometer Magnetic Field (B)

The outputs of this simulation are the actual Euler angles ϕ , θ , and ψ representing the deviation between the target frame TF and the K frame KF. Since the processes in this model are considered “ideal”, the deviation of these two reference frames are exactly reflective in the star camera quaternion. Therefore, the star camera attitude is modeled using a calculation that converts the angle deviations to an “ideal” star camera quaternion. This is then compared with an uploaded reference attitude. In addition, a disturbance environment is simulated accommodating for atmospheric and gravity gradient disturbances [18]. One reason it is difficult to exactly re-create the GRACE behavior in simulation is a lack of knowledge of the exact disturbance environment for GRACE. For the purposes of this case study, a model incorporating gravity gradient and atmospheric torques is used. The simulation then proceeds in a feedback control loop for a user-specified amount of time. A summary of the spacecraft plant implementation and the modeled

disturbance environment is given in Appendix B. A noise-free, ideal version of this experimental simulation is run for a half-day time arc and the results are presented.

4.4.1 Ideal Angle Results

The attitude angle response for the experimental simulation is given in Figure 4.12.

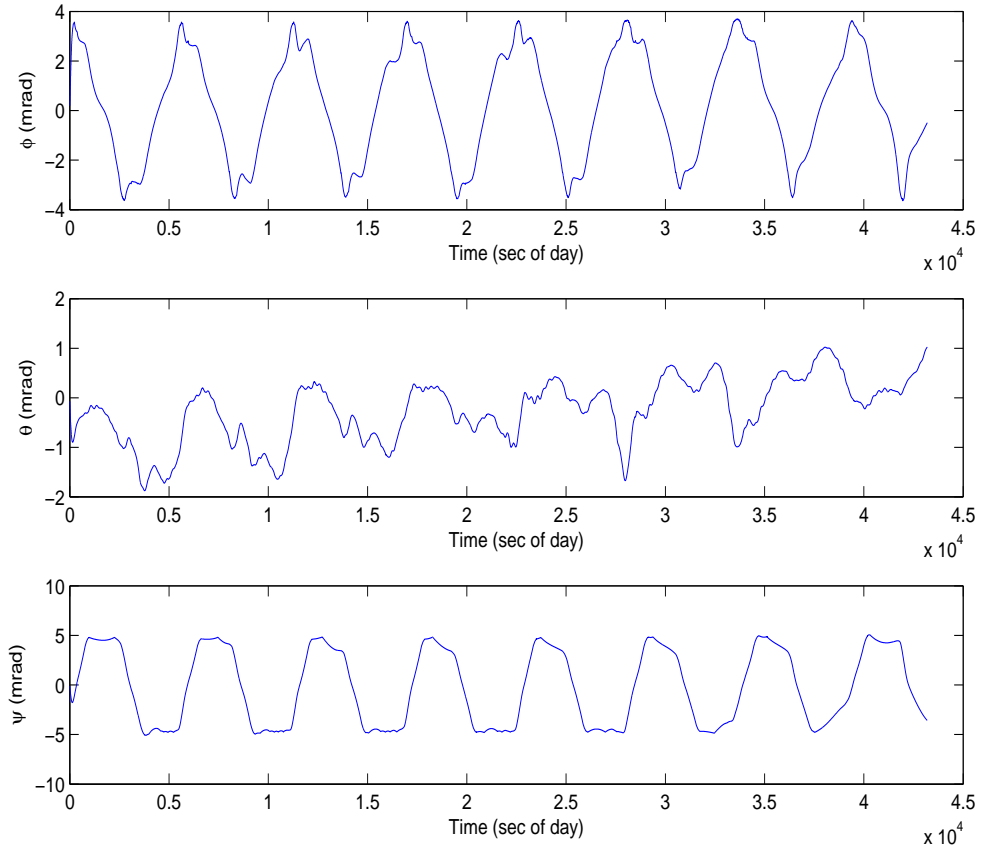


Figure 4.12: Experimental Simulation - Ideal Attitude Angle Response

Similar to the actual GRACE response, roll and yaw angles obey semi-periodic behavior owing to deadband-excursion and subsequent thruster actuation. The pitch axis breaks deadbands at a lower rate due to the higher magnetic control authority in this axis. A few remarks are made in comparison to actual GRACE response, whose behavior is overlaid in Figure 4.13

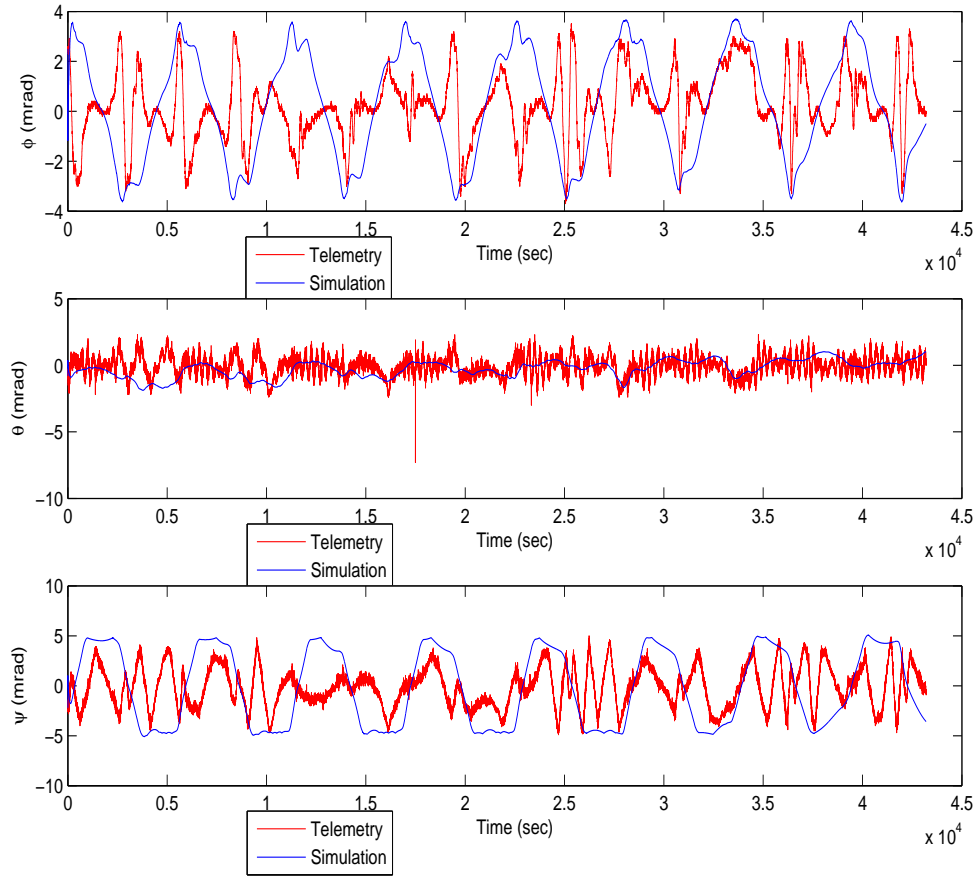


Figure 4.13: Experimental/Telemetry Comparison - Attitude Angle Time-Domain

The actual GRACE response contains greater numbers of high frequency deviations, and non-uniformity in the semi-periodic behavior. This can be the result of a number of factors including inertia uncertainty, uncertainty in the disturbance environment, actuator misalignments, and star

camera noise. Star camera noise and actuator misalignments are considered as sensitivity experiments, and are treated in greater detail in future chapters. The high frequency discrepancies are reflective in the PSD, but the general character of the responses are similar, as seen in Figure 4.14:

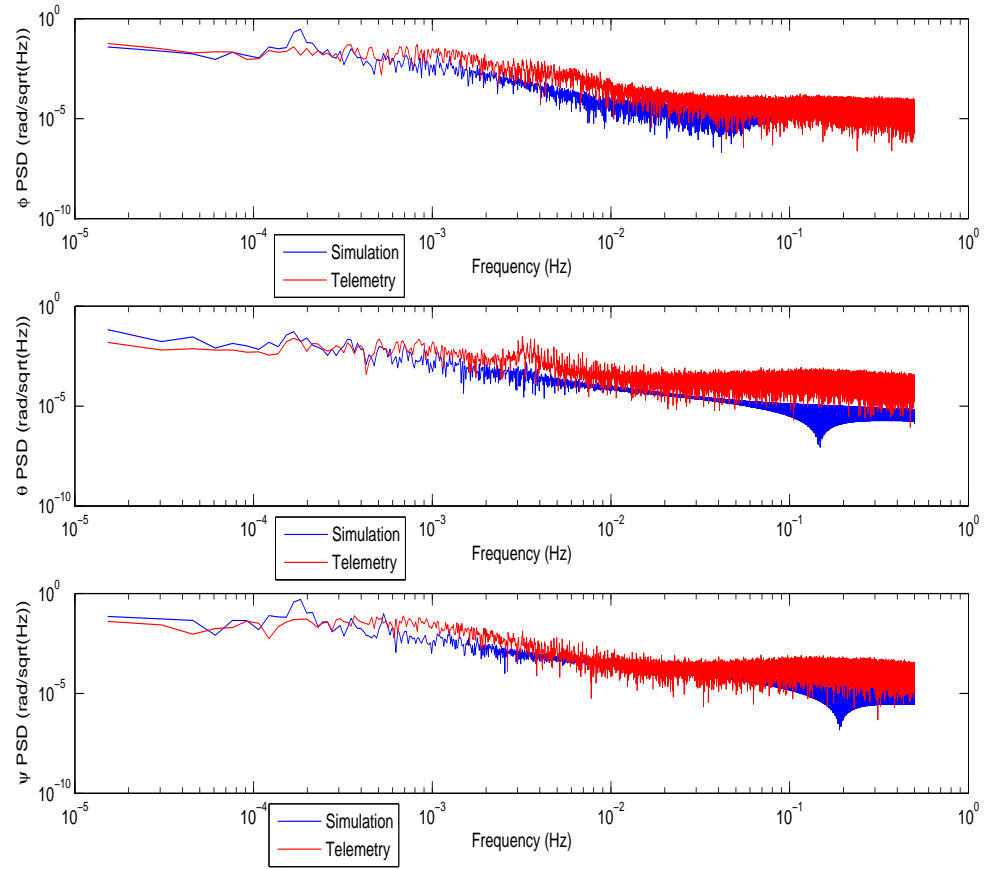


Figure 4.14: Experimental/Telemetry Comparison - Attitude Angle Frequency-Domain

As seen from Figure 4.14, the simulation and telemetry angular PSD both decrease as the frequency increases. However, the overall PSD is higher in telemetry, especially at higher frequencies, owing to instrument noise. One such difference is a spike at 3.3 mHz of the θ telemetry PSD. Since the magnetic torquers have greatest authority in the pitch axis, the cause of this frequency excitation is likely due to electrical imperfections in the magnetic torque rods [19].

An additional test is performed on this experimental simulation to see the effect of pulse-width discrepancy. The twice pulse-width scale factor is used as a comparison to the ideal pulse-width modulation logic, and the effect on angular behavior is given in Figure 4.15:

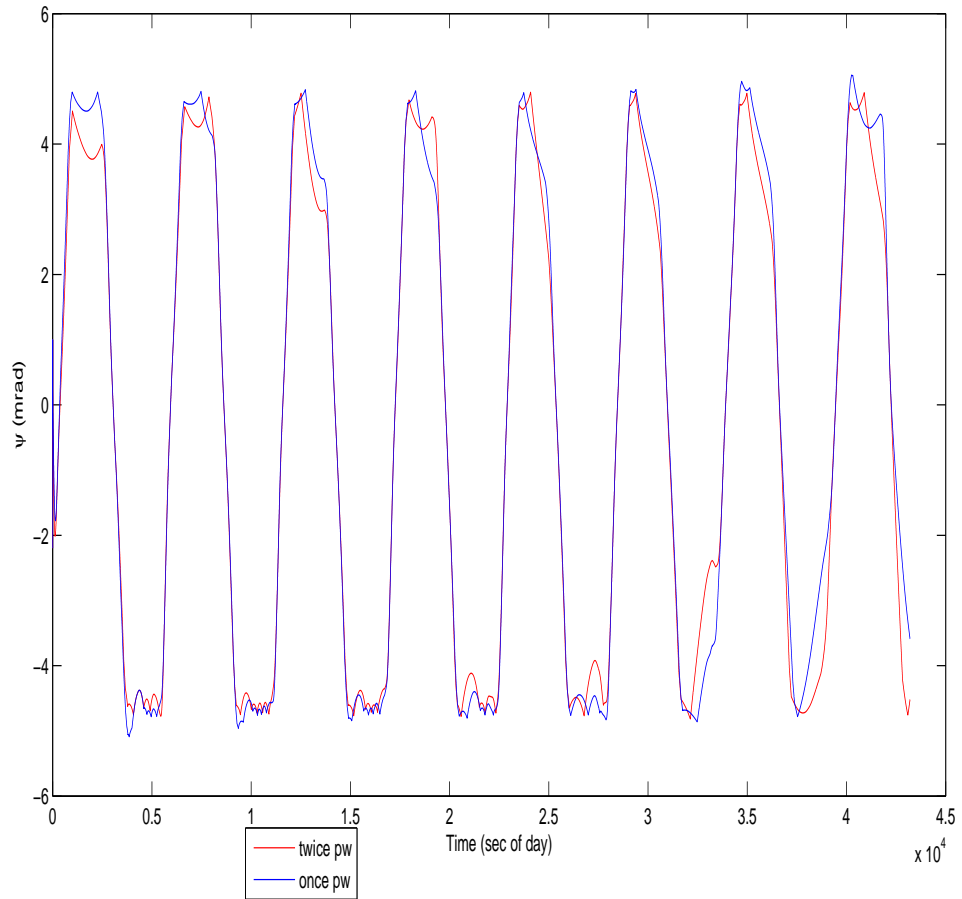


Figure 4.15: Pulse Width Comparison - Attitude Angle Time-Domain

The general trend of the attitude response is not greatly affected, only the initial pulse required to return within the deadband limits. This is reflected in the PSD, given in Figure 4.16, which shows a slightly higher PSD but similar overall behaviors.

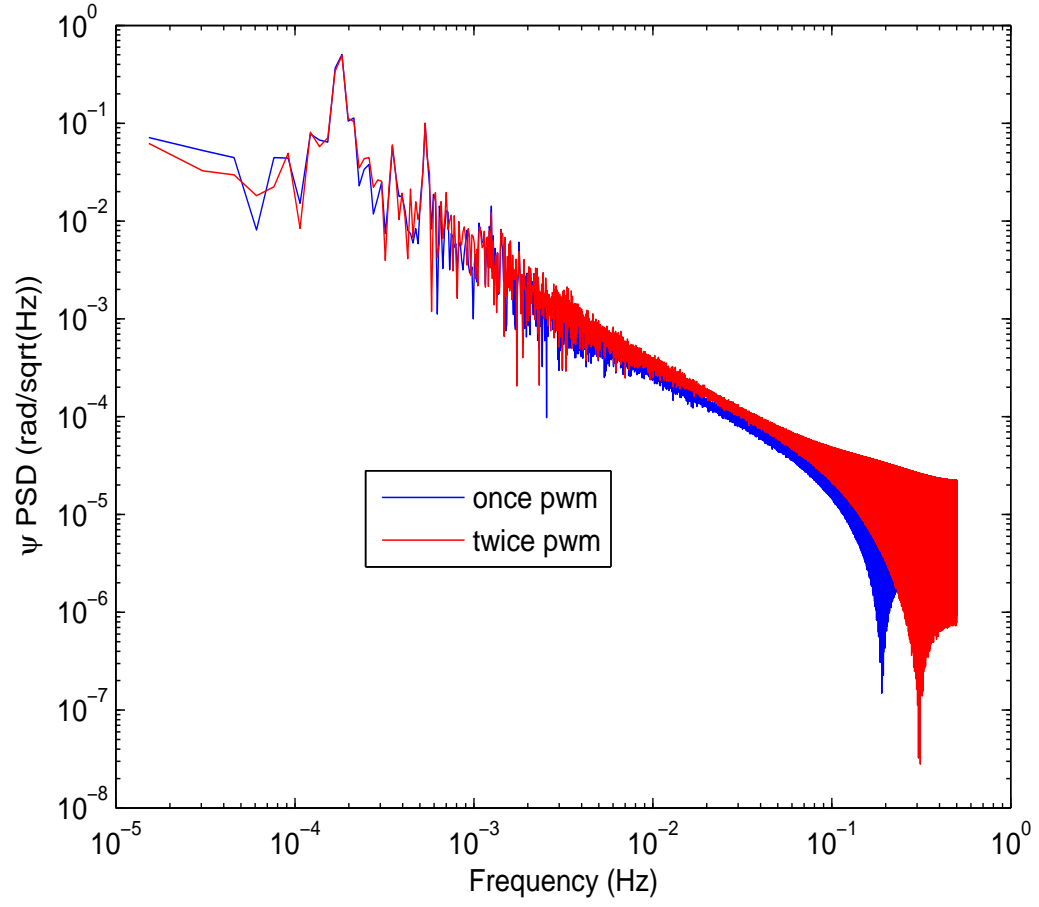


Figure 4.16: Pulse Width Comparison - Attitude Angle Frequency-Domain

4.4.2 Ideal Rate Results

The rate histories for the experimental model are given in Figure 4.17:

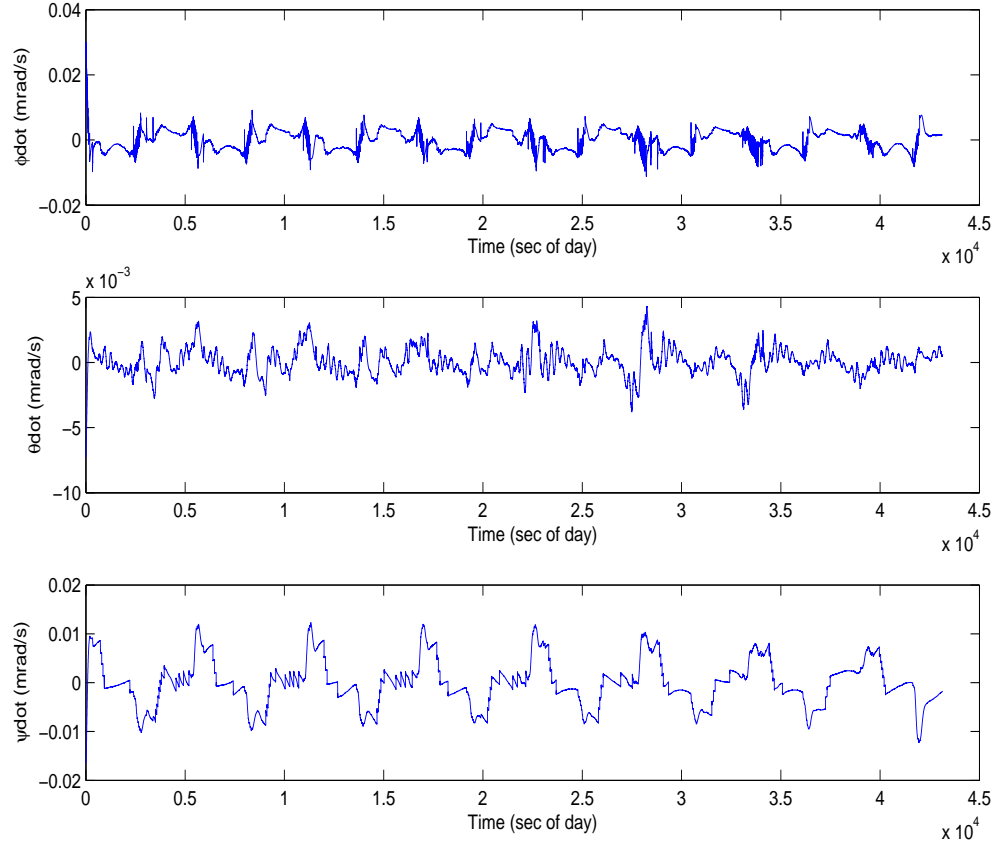


Figure 4.17: Experimental Simulation - Ideal Attitude Rate Response

For an ideal process, the rate estimation obeys a fairly periodic behavior reflective of angular velocity. However, in reality, the rate is estimated based on imperfect attitude knowledge due to star camera noise processes. The comparison with respect to telemetry is given in the following Figure 4.18:

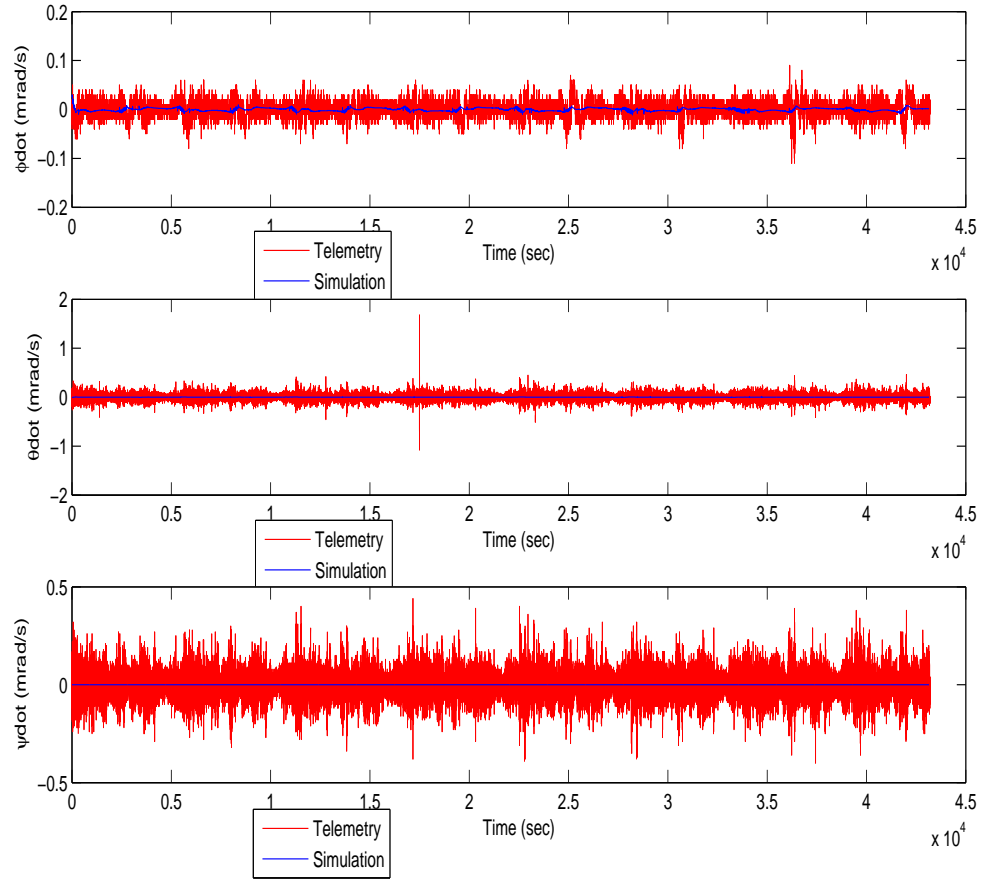


Figure 4.18: Experimental/Telemetry Comparison - Attitude Rate Time-Domain

Since attitude rate is not directly measured, it is much more susceptible to measurement noise. This is also reflected in the PSD, shown in Figure 4.19.

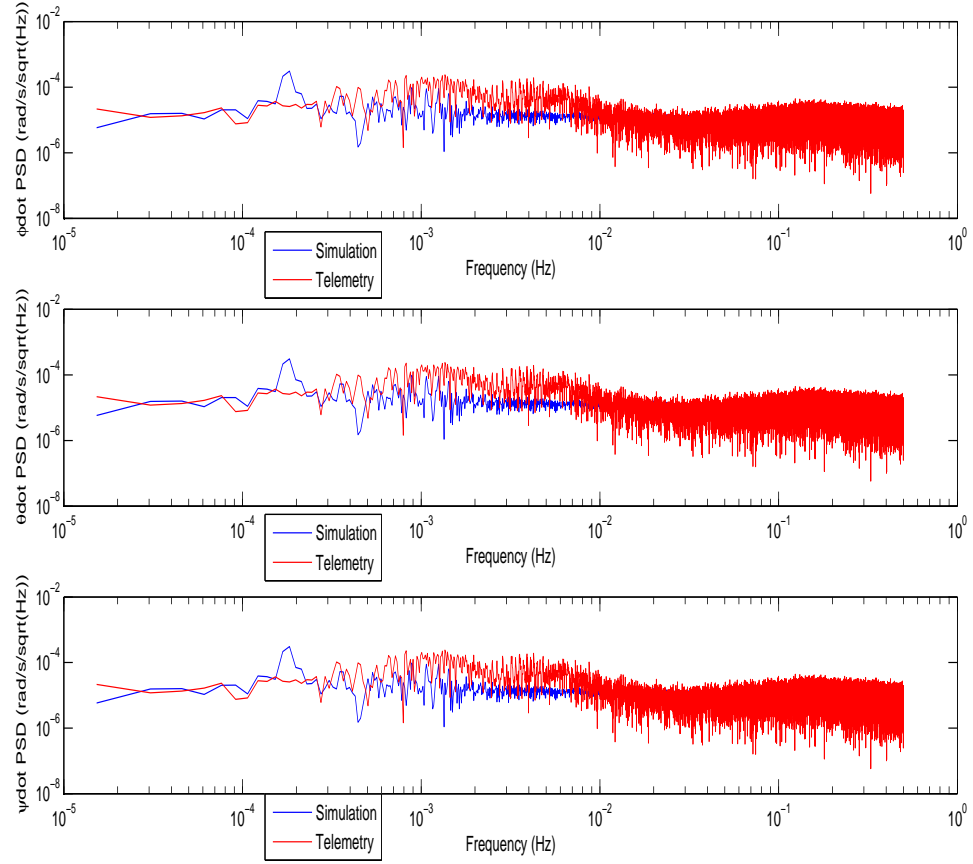


Figure 4.19: Experimental/Telemetry Comparison - Attitude Rate Frequency-Domain

4.4.3 Ideal Control Responses

The thruster and magnetic torquer responses are given in Figure 4.20 and 4.21:

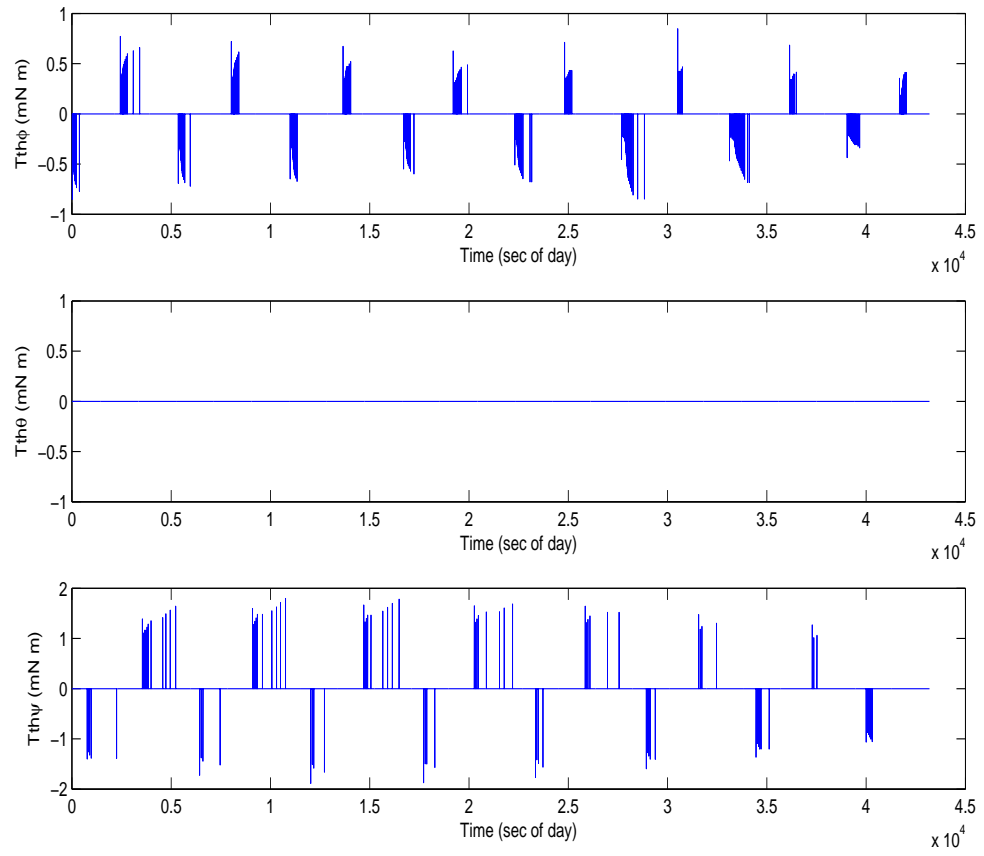


Figure 4.20: Experimental Simulation - Ideal Thruster Torque Response

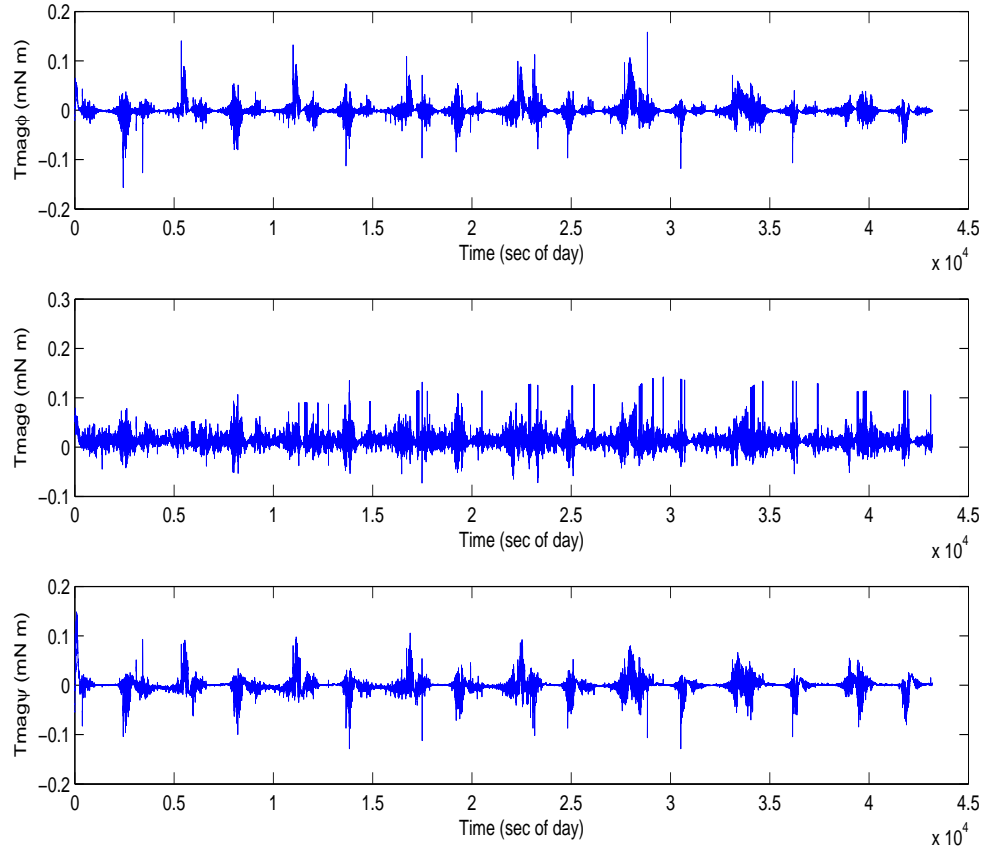


Figure 4.21: Experimental Simulation - Ideal Magnetic Torque Response

The thruster and magnetic torque time histories are not compared to telemetry. The effect of noise and non-idealities reflects in the telemetry attitude angle as a change in the periodicity of the deadband excursions. This, in turn, affects the time at which thruster firings occur, which in turn affects the total overall magnitude of the magnetic actuations. Therefore, the time at

which control actuations occur is quite different between this ideal simulation and actual telemetry. The aim of these graphs is to demonstrate the control actuation occurs when expected, i.e. when the attitude deadband limits are exceeded, for the given ideal response. As seen from Figures 4.12 and 4.20, the time of the thruster actuations corresponds to the points when attitude behavior breaks deadband limits. As expected, thruster actuation magnitudes are highest in roll and yaw. For the defined deadbands, no actuation is necessary in pitch due to minimal disturbance and higher magnetic compensation. Thruster actuation has a significantly larger overall magnitude than the torquer actuation, reflecting its higher overall control authority.

4.4.4 Acceleration Response

Finally, the attitude acceleration time-history summarizes control, disturbance, and rate effects, as seen in Figure 4.22:

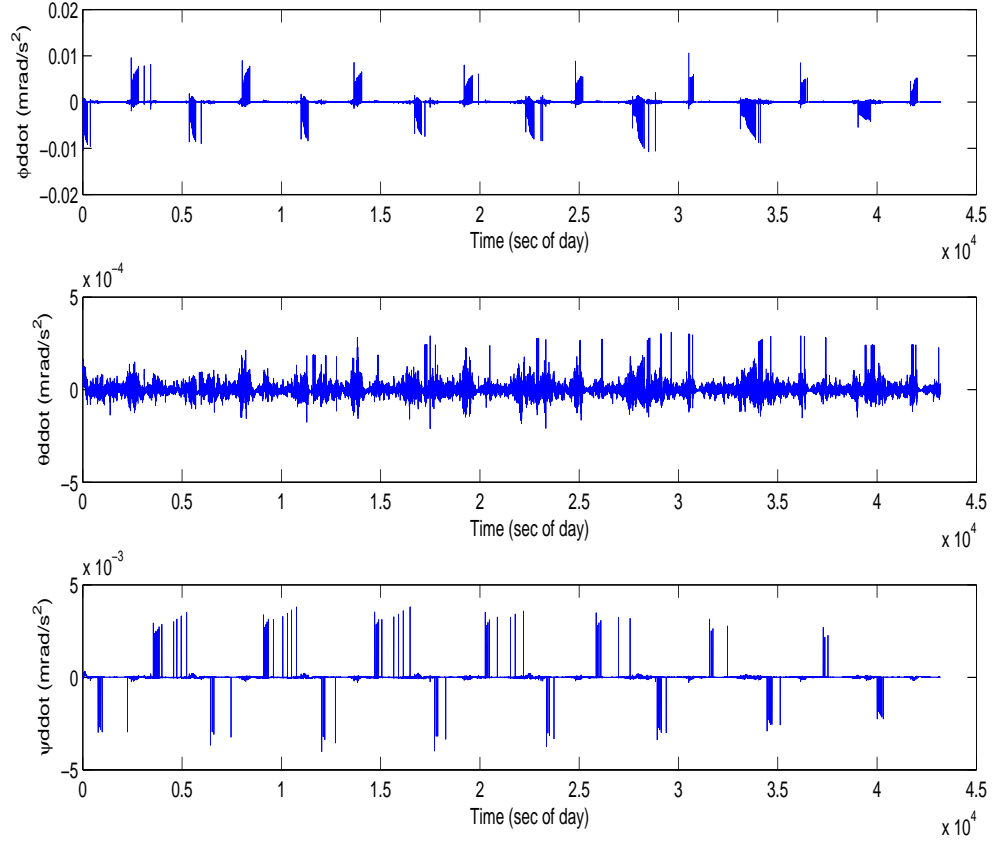


Figure 4.22: Experimental Simulation - Ideal Attitude Acceleration Response

As with the control torques, the attitude acceleration is not compared to telemetry because of the deadband excursion discrepancies. The thruster and magnetic firings, along with the attitude rate, is reflected in the angular acceleration results. Angular acceleration, therefore, becomes a key component from which the behaviors of multiple attitude parameters can be assessed.

4.5 Summary

The ACS algorithms and implementations of the GRACE science mode have been validated against telemetry data. Using these algorithms, an exemplar ACS simulation is constructed that is useful for analyzing generic spacecraft attitude responses in the presence of a predefined disturbance environment. This experimental simulation has been constructed with instrument noise-free assumptions, and the results have shown that measurement noise generally affects the periodicity of the deadband-limited excursion response. This, in turn, affects the thruster and magnetic torquer activation frequency and magnitude. In addition, the presence of these noise terms significantly affects the attitude rate quality. However, the ideal response is a useful starting point from which sensitivity experiments can be performed. The ideal response is perturbed using known imperfections in the ACS suite as guidelines, and their effect on attitude angle and acceleration performance can be assessed. These sensitivity experiments are now discussed in further detail.

Chapter 5

Experimental Setup

5.1 Introduction

The “ideal” simulation set up in Chapter 4 is meant to represent spacecraft attitude behavior for an exemplar spacecraft that uses PD control, deadband-limited thrusters, magnetic torquers, and attitude knowledge sensing. Experiments performed on this model provide insight into the dependencies encompassed in this type of ACS configuration. This study is an analysis procedure, not a design iteration. In ACS design, a rigorous tuning process is performed where attitude metrics are observed in response to Monte-Carlo level disturbances. Monte-Carlo experiments are not performed for this study; rather, ACS components are perturbed independently in the presence of individual non-idealities. Their effects on attitude responses are then analyzed. The sensitivity experiments are selected for broadest possible relevance. As discussed in Chapter 4, all simulations encompassed in this analysis are conducted in a MATLAB/Simulink environment.

5.2 Experimental Selection and Procedure

The objective of this study is an assessment of how attitude behaviors, particularly angles and accelerations, respond in the presence of non-idealities for the given ACS configuration. The end goal is to identify the factors that are most sensitive to attitude performance and data quality. The types of tests performed in this framework can be explored in many possible directions. For this study, the experiments are limited to those that examine the physical components comprised in the ACS sensor and actuator suite: i.e. the star camera, magnetometer, thruster, and magnetic torquer. These four sensors and actuators form the extrinsic basis of the ACS configuration under examination. Since hardware selection is a common procedure in systems-level ACS design, these tests have a high degree of relevance for future study.

The choice of component-level experiments is determined based on the expected imperfections existent in the hardware and integration of the sensors and actuators. Examples of these types of non-idealities are measurement noise and biases in the hardware processes, and misalignments caused by imperfect integration with the spacecraft bus. A summary of the sensitivity experiments performed for this case study are presented in Table 5.1.

Table 5.1: Sensitivity Experiments Summary for ACS Science Mode

Label	Component	Type of Test
SC1	Star Camera	White Noise
SC2	Star Camera	Colored Noise
SC3	Star Camera	Misalignment
Mag1	Magnetometer	White Noise
Mag2	Magnetometer	Bias
Mag3	Magnetometer	Misalignment
Th1	Thruster	Misalignment
Th2	Thruster	Misfire
Tor1	Magnetic Torquer	Residual Dipole
Tor2	Magnetic Torquer	Misalignment

During each sensitivity experiment, the “ideal” simulation model shown in Figure 4.11 is modified to incorporate the given non-ideality. Each non-idealities is assigned a nominal, numerical value based on a manufacturing documented tolerance. This tolerance represents the maximum level of imperfection expected. For each experiment in Table 5.1, the simulation is run twice. First, the simulation is run using the nominal tolerances assigned for each non-ideality, taken from hardware documentation. Then, the simulation is run again using a three-fold increase of these nominal tolerances. Results from the two runs are then compared to see how the magnifications affects the attitude angle and acceleration data quality and performance. In the following sections, the basic definitions of each sensitivity experiment in Table 5.1 is described in detail. In addition, the expected tolerances for each experiment are also specified.

5.3 Star Camera Experiments

Star cameras are used to determine the spacecraft orientation. This orientation is then compared with the reference attitude, and the difference between the two is used to form the error vector. Three star camera experiments are performed; two related to measurement noise, and one dealing with misalignment.

5.3.1 SC1 - Star Camera White Noise

In an ideal scenario, the star camera contains perfect knowledge of satellite attitude at all time intervals. In reality, physical imperfections induce some level of measurement noise in the star camera readings. Measurement noise arises due to non-idealities existent in the electrical processes, and these can be exacerbated by the complex thermal interaction between the spacecraft hardware and the orbit environment. For modeling purposes, the cumulative effect of all measurement noise effects can be synthesized as either an additive or multiplicative random effect applied to the measurement signal. Specifically for star cameras, the noise is modeled as two separate processes: white noise and colored noise. First, the white noise process obeys a Gaussian, normal distribution with specified mean and 1σ standard deviation. For the purposes of this study, the time series of the white noise is defined by zero mean, and non-zero standard deviation. The nominal value for the standard deviation is taken from the expected 1σ tolerances for the star camera noise levels, specified in the hardware documentation [16]. Examples of a white noise process in time

and frequency domains are given in Figure 5.1 and 5.2.

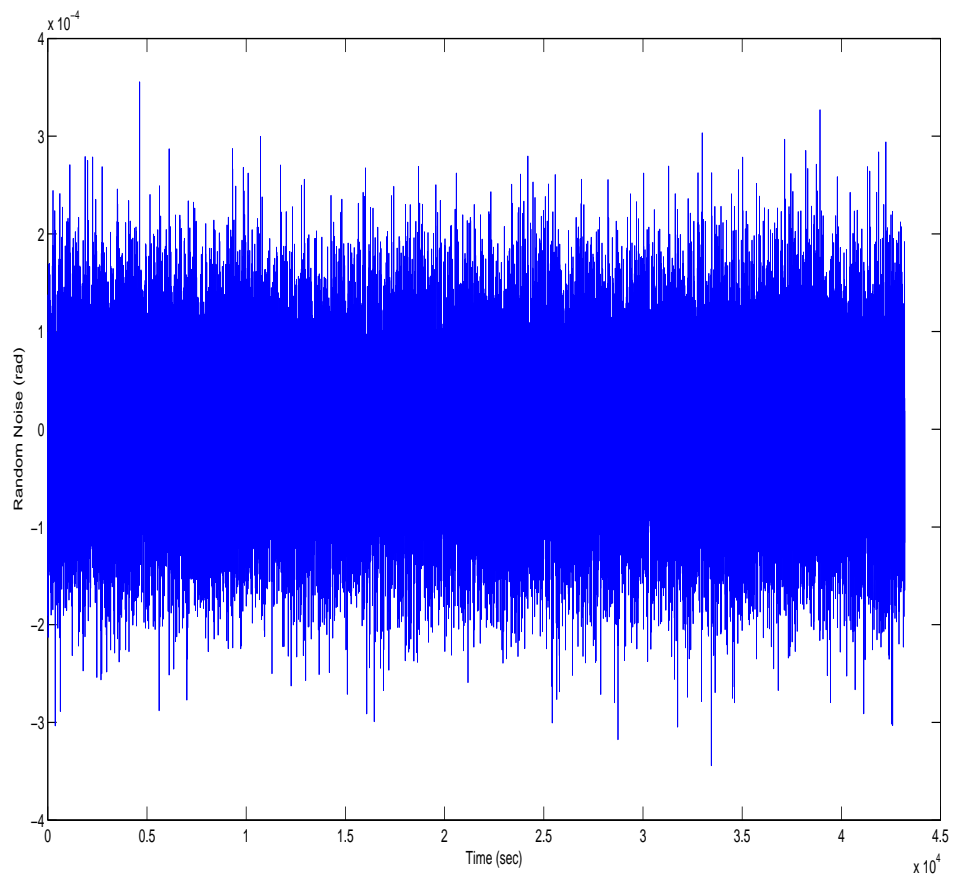


Figure 5.1: Random Noise Process - Time Domain

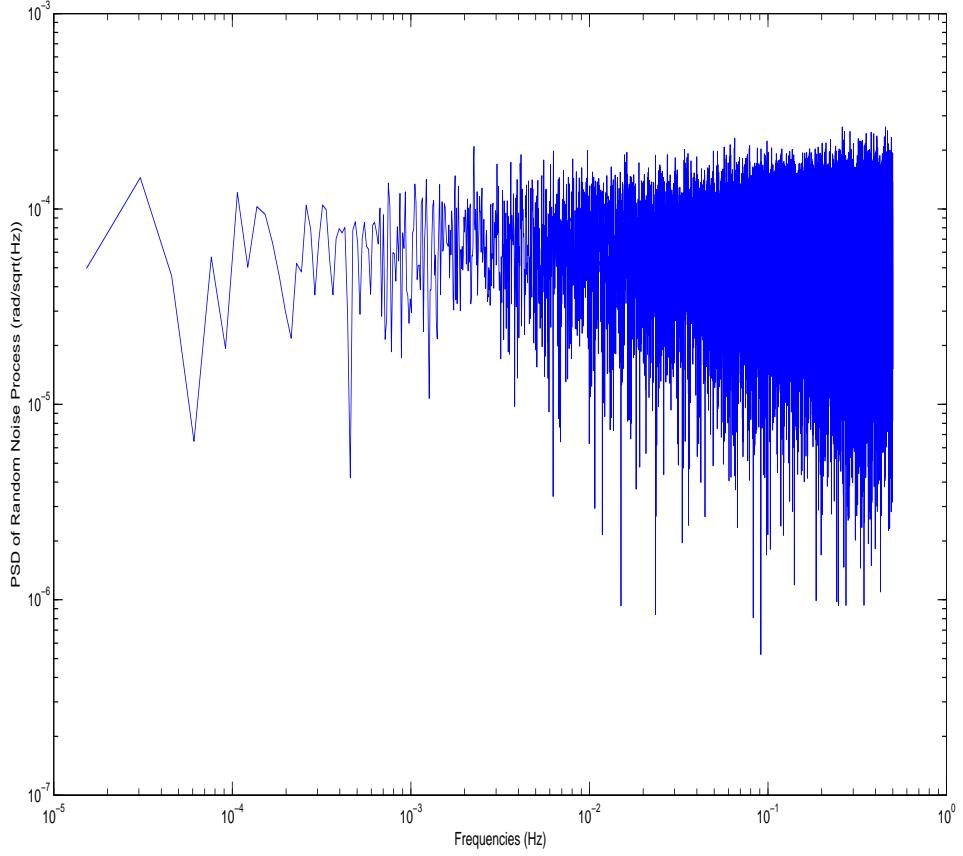


Figure 5.2: Random Noise Process - Frequency Domain

The white noise process has a relatively flat slope in the frequency spectrum; this denotes a randomly weighted noise across all frequencies. In simulation, the white noise time series is generated in MATLAB using a pseudorandom generator:

$$w(t) = N[0, \sigma_{wN}] \quad (5.1)$$

For GRACE, the 1σ of the expected star camera Gaussian noise, with respect to line-of-sight, is given in Table 5.2 [20]:

Table 5.2: Star Camera White Noise

Axis	σ_{WN}
Roll(ϕ)	80 μrad
Pitch(θ)	10 μrad
Yaw(ψ)	10 μrad

5.3.2 SC2 - Star Camera Colored Noise

In addition to the white noise effect, it was discovered from post-processing of science data that the effective attitude knowledge error was also affected by a frequency-dependent noise, generally referred to as colored noise [20] [11]. For the GRACE star cameras, the colored noise is represented by a red-noise process with a floor. In contrast to white noise, which has a flat slope across the frequency band, the PSD slope of a red noise process is $1/f^2$. Examples of this type of noise spectra in time and frequency domain are given in Figures 5.3 and 5.4:

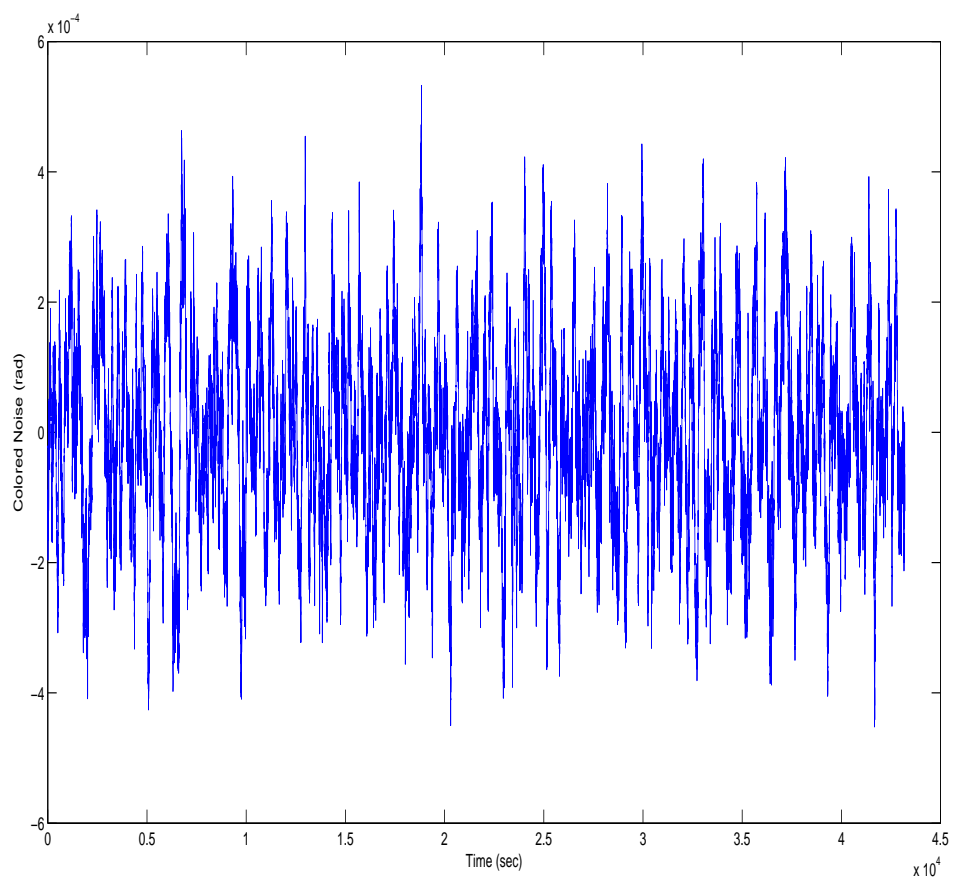


Figure 5.3: Colored Noise Process - Time Domain

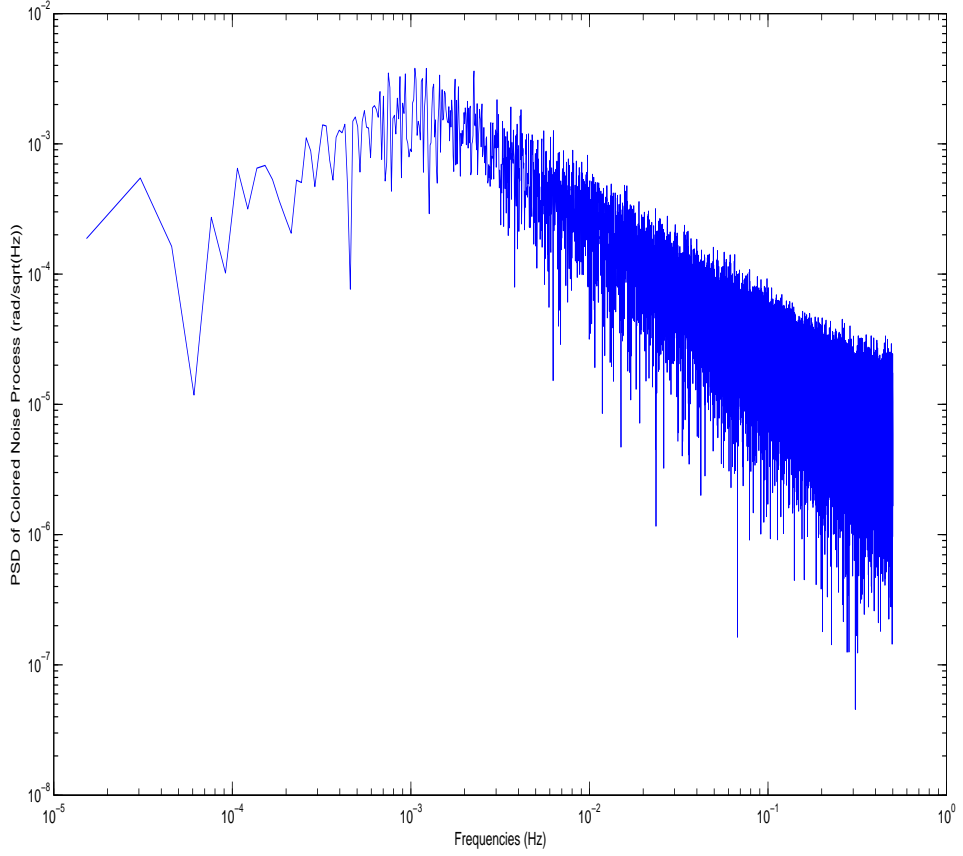


Figure 5.4: Colored Noise Process - Frequency Domain

The colored noise for the GRACE star cameras is manifested as a red noise component, with negative slope of $1/f^2$ at frequencies above 1 mHz, and a flat slope floor at frequencies below 1 mHz. For modeling purposes, this colored noise behavior is realized as the sum of two parts: a white noise series and a red noise series, synthesized using a shaping filter. First, the white noise series

is generated:

$$w_c(t) = N[0, \sigma_{CNw}] \quad (5.2)$$

The 1σ value for the white noise floor is calculated by:

$$\sigma_{CNw} = \sqrt{P_{CNw}/\Delta T} \quad (5.3)$$

Where P_{CNw} is the expected power spectral density of the attitude behavior. Table 5.3 summarizes the worst-case low-frequency parameters, taken from post-processing of star camera results [20]:

Table 5.3: Star Camera Colored Noise: White Noise Component

Axis	P_{CNw} (rad ² /Hz)	ΔT (sec)	σ_{CNw} (μ rad)
Roll(ϕ)	6e-6	5	1100
Pitch(θ)	6e-6	5	1100
Yaw(ψ)	4e-7	5	283

Next, the red noise series is generated. To compute the red noise component, first a Gaussian time series characteristic of the red noise is produced:

$$\sigma_{CNr} = \sqrt{P_{CNr}/\Delta T} \quad (5.4)$$

The red noise σ_{CNr} is different from σ_{CNw} and σ_{WN} . From star camera models, this value is summarized in Table 5.4 [20]:

Table 5.4: Star Camera Colored Noise: Red Noise Component

Axis	P_{CNr} (rad ² /Hz)	ΔT (sec)	σ_{CNr} (μ rad)
Roll(ϕ)	2e-9	5	20
Pitch(θ)	2e-9	5	20
Yaw(ψ)	2e-9	5	20

The red noise series is produced by integrating the characteristic white noise in Equation 5.4:

$$r_c(t) = \sum_{i=0}^t w_{RN}(t_i)T_s \quad (5.5)$$

Where w_{RN} is Gaussian white noise with standard deviation given in Table 5.4:

$$w_{RN}(t) = N[0, \sigma_{CNr}] \quad (5.6)$$

The modeled colored noise process is formed by adding the terms $w(t)_c$ and $r(t)_c$ through the use of a shaping filter. The white noise $w(t)_c$ is sent through a low-pass filter, and the red noise $r(t)_c$ is sent through a high pass filter. For GRACE, the cutoff frequency for low and high frequencies is 0.001 Hz. A second order Butterworth format $H(z)$ is used with gains **Bf** and **Af**. The discrete transfer function of this filter is given by the second order polynomial:

$$H(z) = \frac{B_{f2}z^2 + B_{f1}z + B_{f0}}{A_{f2}z^2 + A_{f1}z + A_{f0}} \quad (5.7)$$

Equation 5.7 is constructed using a z-transform and a sampling time of 1 Hz. The gains are determined using the “butter” command in MATLAB, and are given in Table 5.5.

Table 5.5: Butterworth Filter Gains

Gain	Low-Pass	High-Pass
B_{f2}	0.09826e-4	0.9956
B_{f1}	0.19652e-4	-1.9911
B_{f0}	0.09826e-4	0.9956
A_{f2}	1.0000	1.0000
A_{f1}	-1.9911	-1.9911
A_{f0}	0.9912	0.9912

5.3.3 SC3 - Star Camera Misalignment

In addition to noise, misalignment effects are also included as a test. The star camera misalignment occurs due to imperfections in the spacecraft integration process. In other words, the star camera reference frame (SCF) shown in Figure 1.1 is offset from its expected orientation. The end result is that the quaternion produced by the star camera, q_a is off by an expected tolerance. The worst-case misalignment tolerances for the GRACE star cameras are given in Table 5.6 [15]:

Table 5.6: Star Camera Misalignment Specifications

Axis	Misalignment (mrad)
Roll(ϕ)	10
Pitch(θ)	0.8
Yaw(ψ)	0.8

5.3.4 Star Camera Experiments Simulation Implementation

All three of the star camera non-idealities explained in the previous section manifest themselves as a multiplicative perturbation on the quaternion generated by the star camera. Each non-ideality can be realized as an attitude angle perturbation:

$$\delta ST = \begin{bmatrix} \delta\phi \\ \delta\theta \\ \delta\psi \end{bmatrix} \quad (5.8)$$

This can be converted to a quaternion [10]:

$$\delta ST \rightarrow \mathbf{q}_{pert} \quad (5.9)$$

The disturbance quaternion is then multiplied by the “ideal” star camera attitude [10]:

$$\mathbf{q}_{SCpert} = \mathbf{q}_{pert} * \mathbf{q}_{ideal} \quad (5.10)$$

These experiments are implemented in simulation as shown in Figure 5.5:

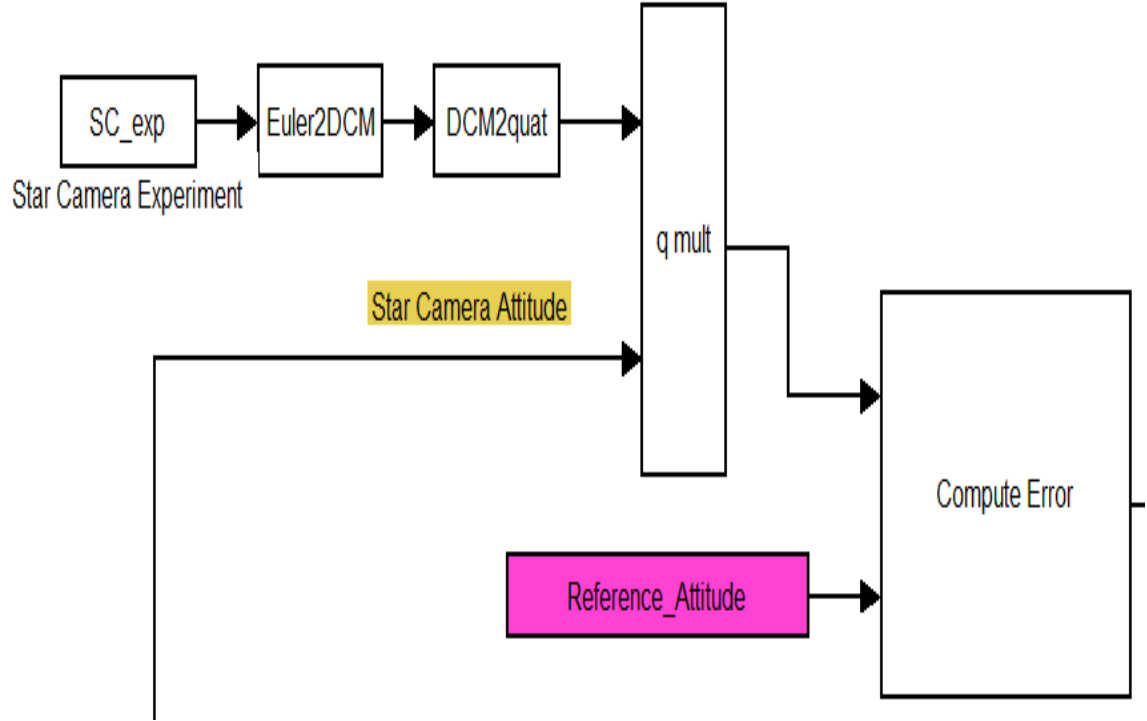


Figure 5.5: Star Camera Experiments - Simulation Modification

Each experiment perturbs the “ideal” star camera quaternion computed from the plant dynamics. The offset is converted to a quaternion according to Equation 5.9, which then perturbs the “ideal” attitude according to 5.10.

5.4 Magnetometer Experiments

A magnetometer is mounted on an extendable boom beneath the spacecraft. It reads the ambient magnetic field \mathbf{B} throughout the spacecraft orbit. Three magnetometer experiments are performed; two related to hardware effects, and

one dealing with misalignment.

5.4.1 Mag1 - Magnetometer White Noise

Magnetometer measurement noise is modeled as a white noise Gaussian process with zero mean and expected 1σ :

$$w(t) = N[0, \sigma_{Mag}] \quad (5.11)$$

The tolerances for GRACE are given in Table 5.7 [16]:

Table 5.7: Magnetometer Noise Magnitudes

Axis	σ_{Mag} (nT)
Roll(ϕ)	3
Pitch(θ)	3
Yaw(ψ)	3

The measurement noise of the GRACE magnetometers does not experience significant frequency-based effects, and so colored noise is not considered [16].

5.4.2 Mag2 - Magnetometer Bias

In addition to measurement noise, biases are induced in the magnetometer behavior. Due to complex interactions between the magnetometer hardware, electromagnetic torquing coils, and residual magnetic fields, a magnetic induction \mathbf{B}_c is caused by all localized current distribution contained within the spacecraft [11]. This induction is modeled as a constant additive

bias term to the sensed magnetic field measurement. The expected bias tolerances for GRACE are summarized in Table 5.8 [16]:

Table 5.8: Magnetometer Biases

Axis	Bias (nT)
Roll(ϕ)	100
Pitch(θ)	100
Yaw(ψ)	100

5.4.3 Magnetometer Noise and Bias Simulation Implementation

For magnetometers, the measurement noise and bias effects are included as additive terms. A simulation schematic is given in Figure 5.6:

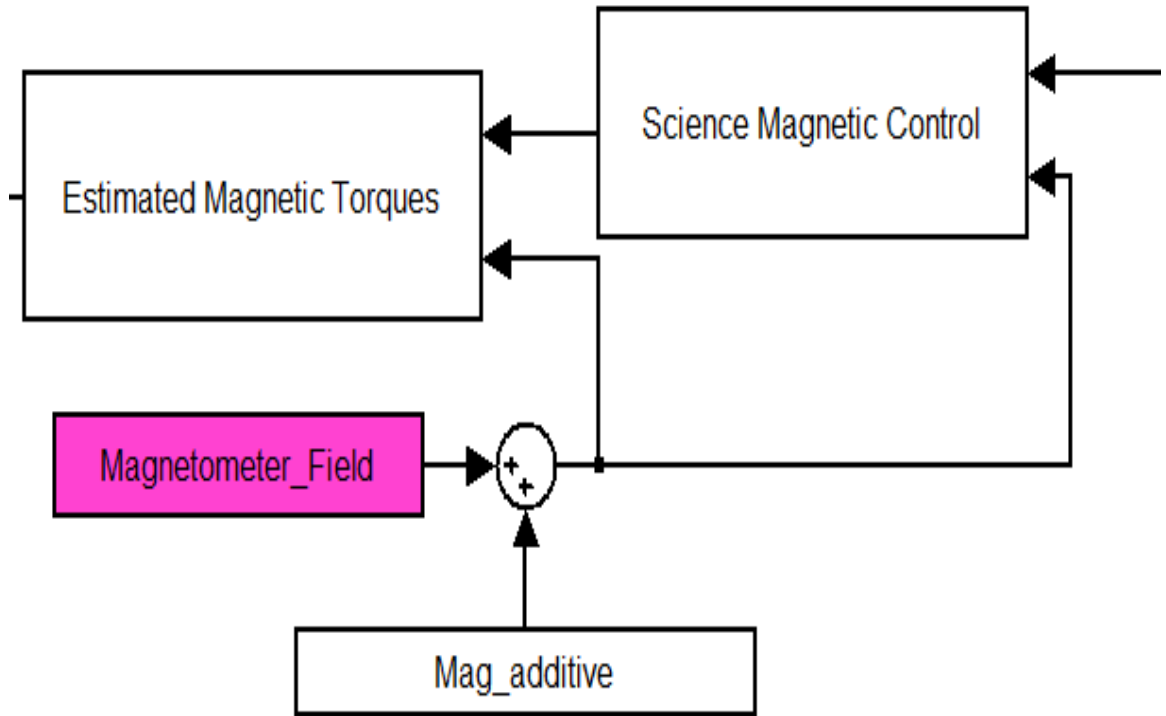


Figure 5.6: Magnetometer Hardware Experiments - Simulation Modification

5.4.4 Mag3 - Misalignment

As with the star camera, the magnetometer experiences characteristic misalignments due to integration with the spacecraft bus. This causes an offset in the sensed magnetic field measurement. For GRACE, the expected magnetometer misalignment tolerances are given in Table 5.9 [16]:

Table 5.9: Magnetometer Misalignment Specifications

Axis	Misalignment (deg)
Roll(ϕ)	1.5
Pitch(θ)	1.5
Yaw(ψ)	1.5

5.4.5 Magnetometer Misalignment Simulation Implementation

Since magnetometer data is a three parameter vector, and not a four parameter quaternion, it is convenient to represent the misalignment using a 3-2-1 direction cosine matrix:

$$\delta Mag = \begin{bmatrix} \delta\phi \\ \delta\theta \\ \delta\psi \end{bmatrix} \rightarrow \mathbf{M}_{Bmisal}(\delta\phi, \delta\theta, \delta\psi) \quad (5.12)$$

The misalignment matrix is a multiplicative relationship:

$$\begin{bmatrix} B_x \\ B_y \\ B_z \end{bmatrix}_{pert} = \mathbf{M}_{Bmisal}^{321}(\delta\phi, \delta\theta, \delta\psi) * \begin{bmatrix} B_x \\ B_y \\ B_z \end{bmatrix} \quad (5.13)$$

The schematic of the magnetometer misalignment test is shown 5.7:

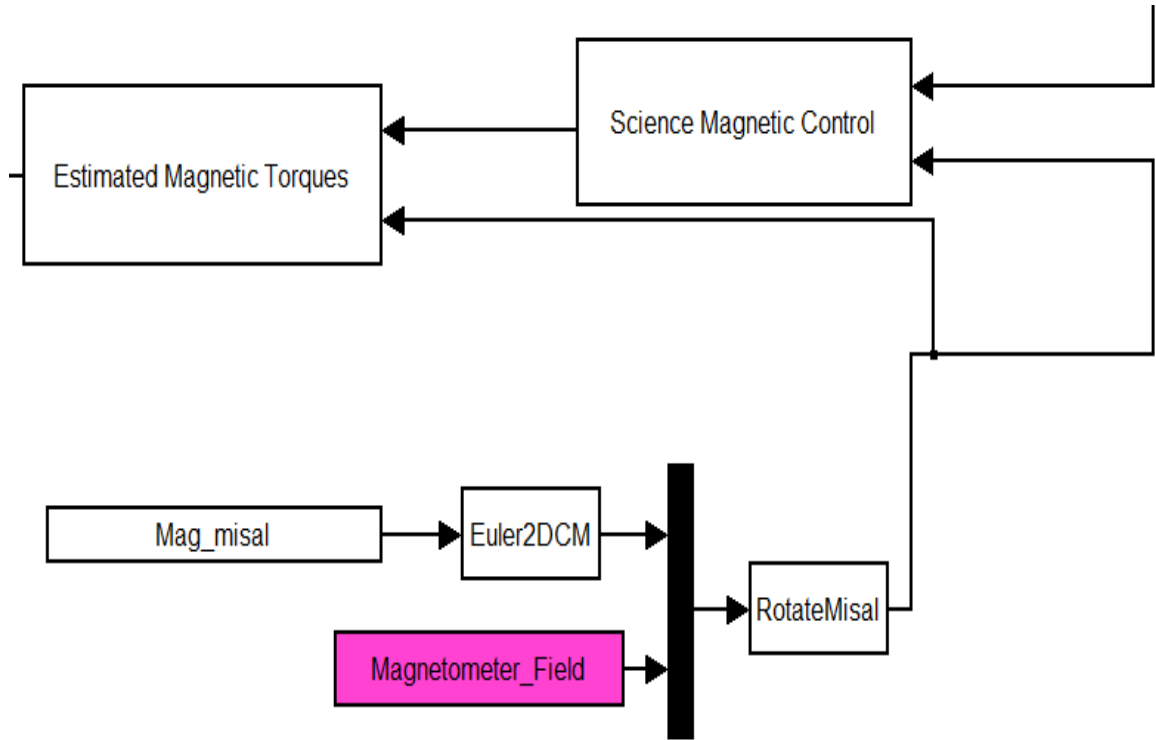


Figure 5.7: Magnetometer Misalignment Experiments - Simulation Modification

The “Rotate Misal” function computes the rotation sequence in 5.13 for a specified DCM.

5.5 Thruster Experiments

The thruster locations, design forces, and design torques are given in Tables 5.10, 5.11, and 5.12 respectively [18].

Table 5.10: Attitude Thruster Locations

Thruster	R_x (mm)	R_y (mm)	R_z (mm)
A1-1	-1450	-719	0
A1-2	-1450	0	-444
A1-3	-1450	719	0
A1-4	-1450	0	275
A1-5	0	-970	300
A1-6	0	-467	-300
A2-1	1450	719	0
A2-2	1450	0	275
A2-3	1450	-719	0
A2-4	1450	0	-444
A2-5	0	467	-300
A2-6	0	970	300

Table 5.11: Thruster Forces

Thruster	F_x (N)	F_y (N)	F_z (N)
A1-1	0	0.01	0
A1-2	0	0	0.01
A1-3	0	-0.01	0
A1-4	0	0	-0.01
A1-5	0	0.01	0
A1-6	0	0.01	0
A2-1	0	-0.01	0
A2-2	0	0	-0.01
A2-3	0	0.01	0
A2-4	0	0	0.01
A2-5	0	-0.01	0
A2-6	0	-0.01	0

Table 5.12: Thruster Torques

Thruster	T_x (N m)	T_y (N m)	T_z (N m)
A1-1	0	0	-0.0145
A1-2	0	0.0145	0
A1-3	0	0	0.0145
A1-4	0	-0.0145	0
A1-5	-0.003	0	0
A1-6	0.003	0	0
A2-1	0	0	-0.0145
A2-2	0	0.0145	0
A2-3	0	0	0.0145
A2-4	0	-0.0145	0
A2-5	-0.003	0	0
A2-6	-0.003	0	0

Thruster torques are generated via the following relationship:

$$\mathbf{T} = \mathbf{R} \times \mathbf{F} \quad (5.14)$$

Two thruster experiments are performed; one for misfire and one for misalignment.

5.5.1 Th1 - Misalignment

As for the star camera and magnetometer, the thrusters are also expected to contain some misalignment due to integration with the spacecraft. When this misalignment occurs, the force produced by the attitude thrusters is not exclusively generated in the thruster firing direction. In other words, the off-axis terms of the forces specified in Table 5.11 will become non-zero. The end-result is that off-axis disturbance torques are induced. The thruster

misalignments are characterized by a cone-angle offset tolerance, and this offset is applied to the thruster force terms in Table 5.11. The attitude thrusters are designed to only generate force in the y- and z- body direction. This is performed to reduce probability of K-band science quality degradation. For simulation purposes, the cone-angle offset is applied to the thruster forces in Table 5.11 in such a way to produce the greatest amount of cross-axis disturbance. After trial and error, the misalignment effects selected for this case study are defined in the following manner:

$$\begin{aligned}
\begin{bmatrix} F_x \\ F_y \\ F_z \end{bmatrix}_{roll}^{misaligned} &= \mathbf{M}_{misal}^3(\delta cone) * \begin{bmatrix} F_x \\ F_y \\ F_z \end{bmatrix}_{roll}^{ideal} \\
\begin{bmatrix} F_x \\ F_y \\ F_z \end{bmatrix}_{pitch}^{misaligned} &= \mathbf{M}_{misal}^1(\delta cone) * \begin{bmatrix} F_x \\ F_y \\ F_z \end{bmatrix}_{pitch}^{ideal} \\
\begin{bmatrix} F_x \\ F_y \\ F_z \end{bmatrix}_{yaw}^{misaligned} &= \mathbf{M}_{misal}^1(\delta cone) * \begin{bmatrix} F_x \\ F_y \\ F_z \end{bmatrix}_{yaw}^{ideal}
\end{aligned} \tag{5.15}$$

A “3” rotation is applied to the thruster forces that generate roll (ϕ) torque, and a “1” rotation is applied to the thruster forces that generate pitch(θ) and yaw(ψ) torque. This rotation sequence is treated as a non-stochastic constant offset applied to every attitude thruster.

5.5.2 Th2 - Misfire

For attitude thrusters, hardware non-idealities also manifest themselves as a force misfire. The misfire is caused by imperfections in the interaction between

the pressure vessels, valve dynamics, and ambient environment of the thruster actuation system. The misfire is modeled in simulation as:

$$F^{misfired} = F^{ideal} * \left(1 + \frac{misfire}{100}\right) \quad (5.16)$$

As with the misalignment test, the misfire experiment is applied to the forces generated by all the attitude thrusters in Table 5.11.

For GRACE, a summary of expected thruster misfire and misalignment terms is given Table 5.13 [16]:

Table 5.13: Thruster Misfire and Misalignment

Misfire(%)	5
Misalignment Cone Angle (deg)	5

5.5.3 Thruster Experiments Simulation Implementation

The thruster experiment implementation schematic is given in Figure 5.8:

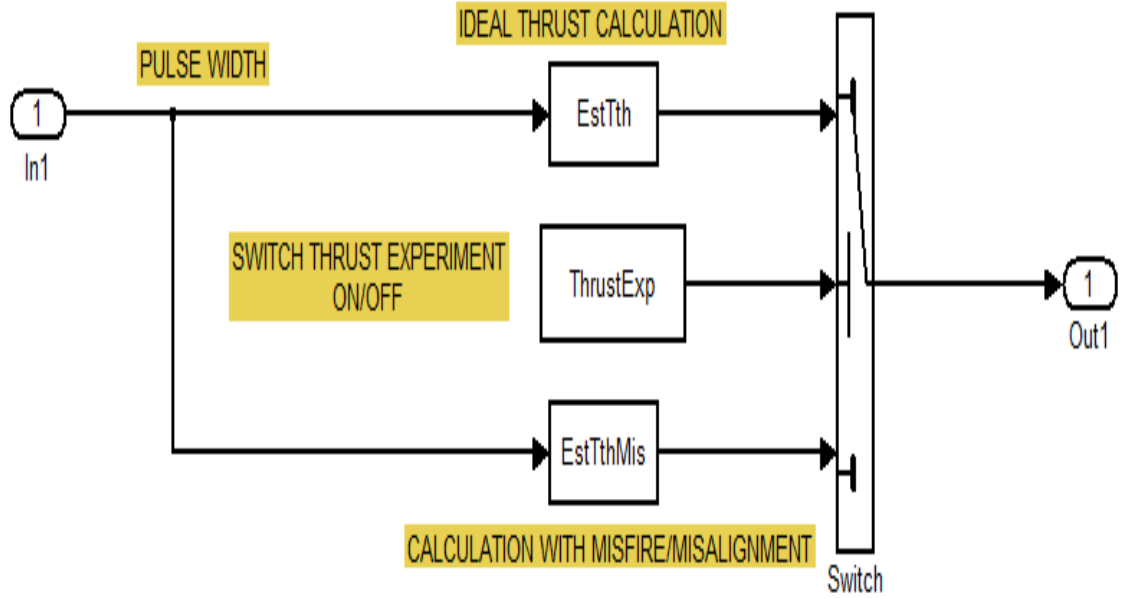


Figure 5.8: Thruster Experiments - Simulation Modification

From Equation 5.14, the thruster torque is dependent on the force allowable and the thruster location. In simulation, the “ideal” case is considered using the “EstTh” block, as shown in Figure 5.8. When the thruster experiments Th1 and Th2 are examined, the “EstThMis” block is used instead.

5.6 Torquer Experiments

The three magnetic torque rods are aligned with the spacecraft body axes. Torque rods exert control torques by generating an electrical dipole moment.

The GRACE magnetic torquers produce electrical moments that saturate at 30 Amp-m². Two torquer experiments are performed; one for hardware imperfection and one for misalignment.

5.6.1 Tor1 - Residual Dipole

Previously, the concept of the induced magnetic field \mathbf{B}_c was introduced. For the magnetometer experiments, this effect causes an additive bias to manifest in the magnetic field readings. In addition to the magnetometer, the induced magnetic field also affects the magnetic torque rods. It produces a residual dipole that affects the torque rod actuation, and is modeled as an additive bias to the magnetic moment generated. The magnitude of this bias is dependent on the torque rod saturation limits [11]:

$$m_{bias} = ResidDipole * m_{saturation} \quad (5.17)$$

5.6.2 Magnetic Torquer Residual Dipole Simulation Implementation

As mentioned, the residual dipole effect is implemented as an additive bias to the magnetic moment, as shown in Figure 5.9:

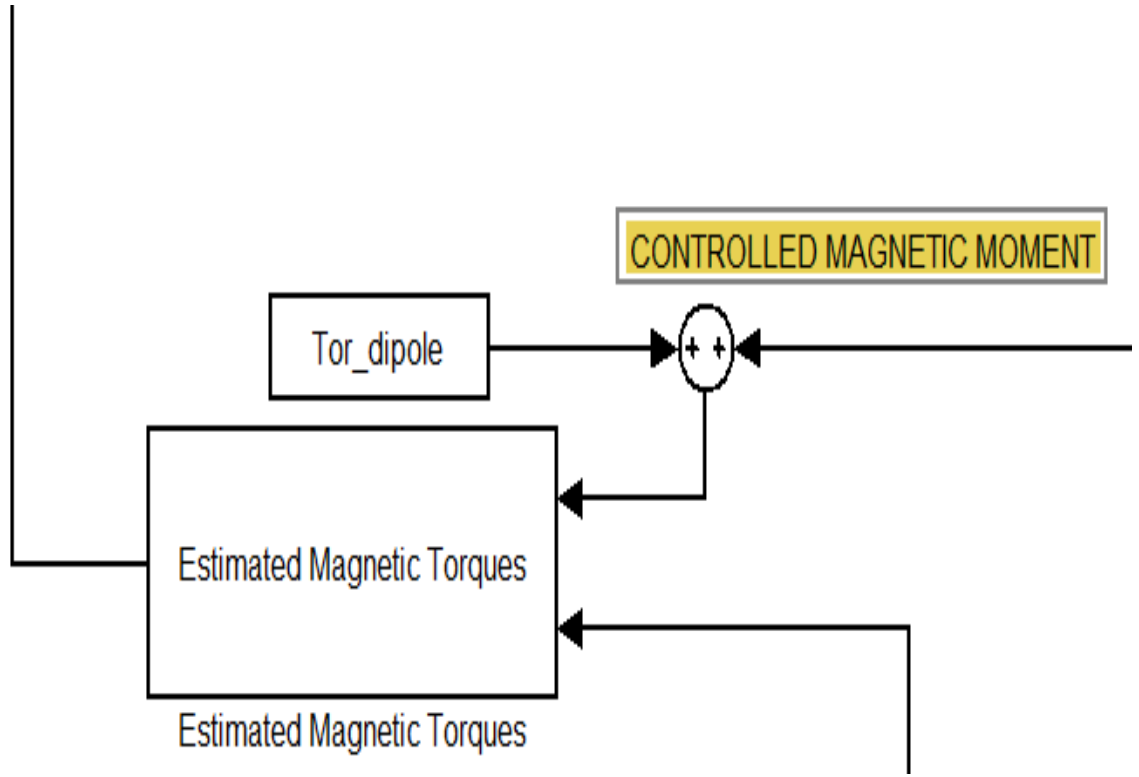


Figure 5.9: Torquer Residual Dipole Experiment - Simulation Modification

5.6.3 Tor2 - Misalignment

Similar to previous sensors, the torque rods experience misalignment during spacecraft integration. The misalignment affects the value of the magnetic moment that is applied to the torquer actuation scheme [11]. The expected misalignment tolerances are applied using a 3-2-1 DCM rotation:

$$\begin{bmatrix} m_x \\ m_y \\ m_z \end{bmatrix}_{misaligned} = \mathbf{M}_{Tormisal}^{321}(\delta\phi, \delta\theta, \delta\psi) * \begin{bmatrix} m_x \\ m_y \\ m_z \end{bmatrix}_{ideal} \quad (5.18)$$

This multiplicative relationship is included in the simulation as shown in Figure 5.10:

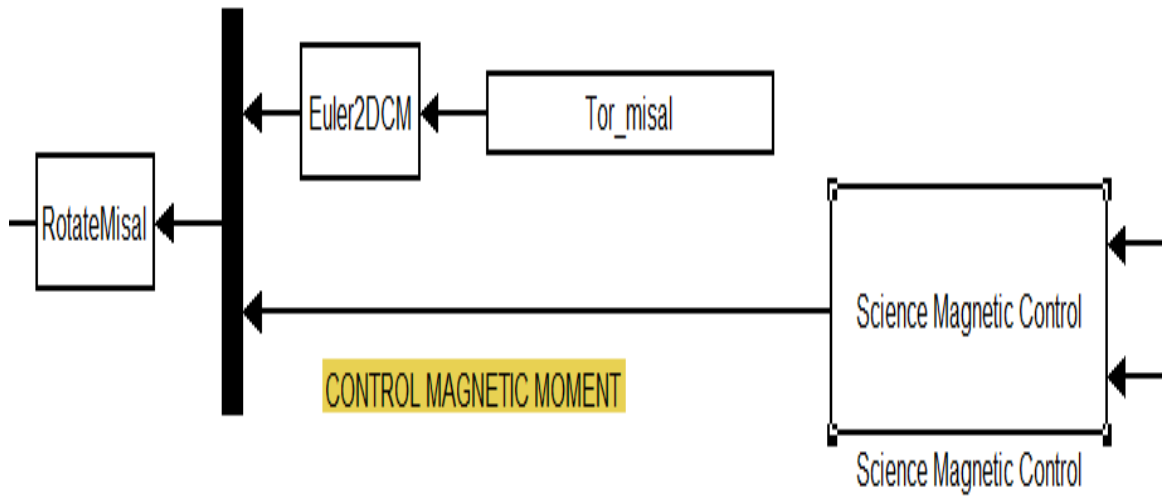


Figure 5.10: Torquer Misalignment Experiment - Simulation Modification

5.6.4 Magnetic Torquer Misalignment Simulation Implementation

For GRACE, the expected residual dipole and misalignments for the magnetic torquers are given in Table 5.14 [16]:

Table 5.14: Magnetic Torquer Residual Dipole and Misalignment

Residual Dipole (% of sat)	0.3
Misalignment (deg, all axes)	5

5.7 Analysis Procedure

For each experiment, the simulation is run independently using the nominal and threefold increase scenarios. As discussed in Chapter 1, the primary items of interest are the attitude angles and accelerations. Both of these terms play a significant role in the quality of the geodetic science data. The time responses of both these behaviors are cataloged during each sensitivity simulation.

Due to the deadband-limited nature of the control system implementation, time-response changes occur over longer time-scales. In addition to the time response, a frequency-based analysis is useful in determining the overall change in the attitude response character. This is done using the PSD of the attitude angle and acceleration response. Up to this point, all PSD plots have been given in periodogram representation. The periodogram function displays the greatest level of detail among the representative frequencies. However, when comparing frequency contents of two separate test cases, it is more worthwhile to use a smoothed PSD content. For this study, a Thomson-multitaper version of the PSD is used during the comparative analysis. A comparison of these techniques is given in the Appendix. The sensitivity of the attitude angles and accelerations, due to the given sensitivity tests, are as-

sessed through examination of the change in time-response data quality, and the change in the PSD. From these results, conclusions can be made in a broad sense of the driving factors that determine attitude performance.

5.8 General Guidelines

Some general guidelines are made with respect to how the simulations of this case study are run and analyzed. When performing analysis of the attitude behavior, a proper runtime must be selected to sufficiently capture all relevant ACS processes. Deadband-limited implementation is characterized by relative infrequency in control actuations; for GRACE, these activations occur on an hourly time scale. For simulation purposes, a half-day time arc was selected to capture significant attitude control characteristics independent of long-term orbital trends. Additionally, the ACS hardware suite and control algorithms are identical for both GRACE satellites, and the line-of-sight vector is uploaded as a telemetry input. Therefore, performing experiments for one GRACE satellite provides equivalent information regarding both spacecraft. For this case study, experiments are performed on GRACE A.

An additional remark is made regarding the simulation results themselves. In reality, ACS systems are composed of multiple levels of hardware and software interactions. Each of the blocks in the experimental simulation, shown in Figure 4.11, actually contain mechanical and electrical components that exhibit a complex interaction with the ambient environment. It is very difficult to model all of these processes in their entirety; as such, the results

from the simulation model will not predict the exact response that an actual ACS system will demonstrate. Rather, the results produced will give high-level understandings of the systems-level interactions that form the basis of the ACS behavior. Although this simulation model ignores some of the intricate details, and simplifies many of the complex interactions, this study is still very useful because it produces a high-level understanding of the overarching dependencies inherent in this type of system.

Chapter 6

Results

6.1 Introduction

The experiments performed in this case study are conducted by modifying the noise-free, “ideal” experimental simulation model, shown in Figure 4.11. This model is meant to represent the attitude behaviors of a spacecraft ACS system using a PD control law, deadband-limited thruster activation, supplementary magnetic control, and star camera sensing. The results of the study are now presented. The magnitude of each non-ideality experiment is characterized by certain nominal statistics. For each of the experiments detailed in Table 5.1, the model is run twice: first using the nominal statistics, and then using three times the nominal statistics. The noise free ideal has been presented in Chapter 4, but will not be considered for the sensitivity analysis. The attitude angles and accelerations are cataloged for analysis. The time-history and PSD is produced for both the nominal and three times the nominal scenarios. The PSD is produced using a Thomson-multitaper method in a MATLAB environment. The Thomson-multitaper method is selected because it demonstrates the greatest level of detail across the representative frequency band, and is smoother than the classical periodogram technique. The time-histories are produced in order to assess the impact of non-idealities on

attitude quality. The PSD responses are generated to identify which frequency ranges are most affected by experimental non-idealities. Taken together, these results show the various levels of sensitivity inherent in the modeled attitude angles and accelerations for this ACS system.

In each sensitivity experiment, the results are analyzed for all axes. For presentation purposes, plots are presented in detail for the yaw(ψ) axis, and condensed results are given for the pitch(θ) and roll(ϕ) axes. In the frequency analysis, particular attention is given to the spectrum of the GRACE scientific processes. This frequency band ranges from 100 μ Hz (10^{-4} Hz) to 30 mHz ($\approx 10^{-1.523}$ Hz). The tests examine the effects of non-idealities present in the star camera, magnetometer, thrusters, and magnetic torquers. The attitude angle and acceleration plots are given for each of the ten component tests. At the end of each section, the results of the sensitivity experiments are presented. When applicable, refined experiments are conducted to see if the component-level non-idealities can be compensated through adjustment of intrinsic control parameters. The implications of these results are discussed, and future experiments are proposed examining possible improvements to the present ACS structure.

6.2 Star Camera Tests

Three star camera tests are performed for this case study. All three of these are multiplicative perturbations to the “ideal” star camera quaternion, and they encompass white noise, colored noise, and misalignment components.

6.2.1 SC1

The attitude angle time response for the white noise star camera test is given in Figure 6.1.

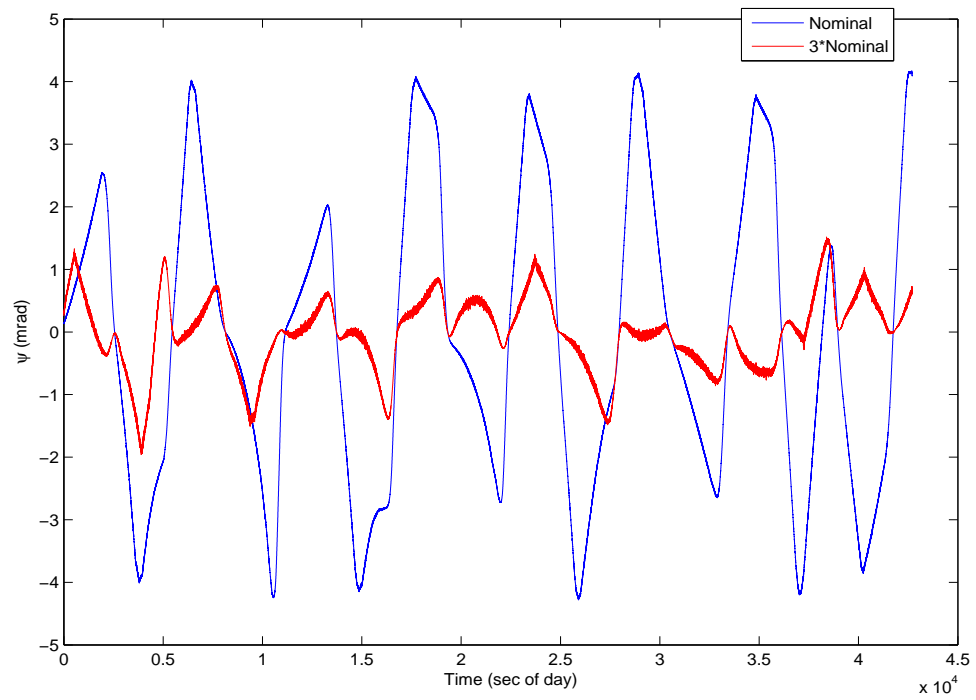


Figure 6.1: SC1 - Yaw Attitude Angle Time Response

The attitude angle PSD for the white noise star camera test is given in Figure 6.2.

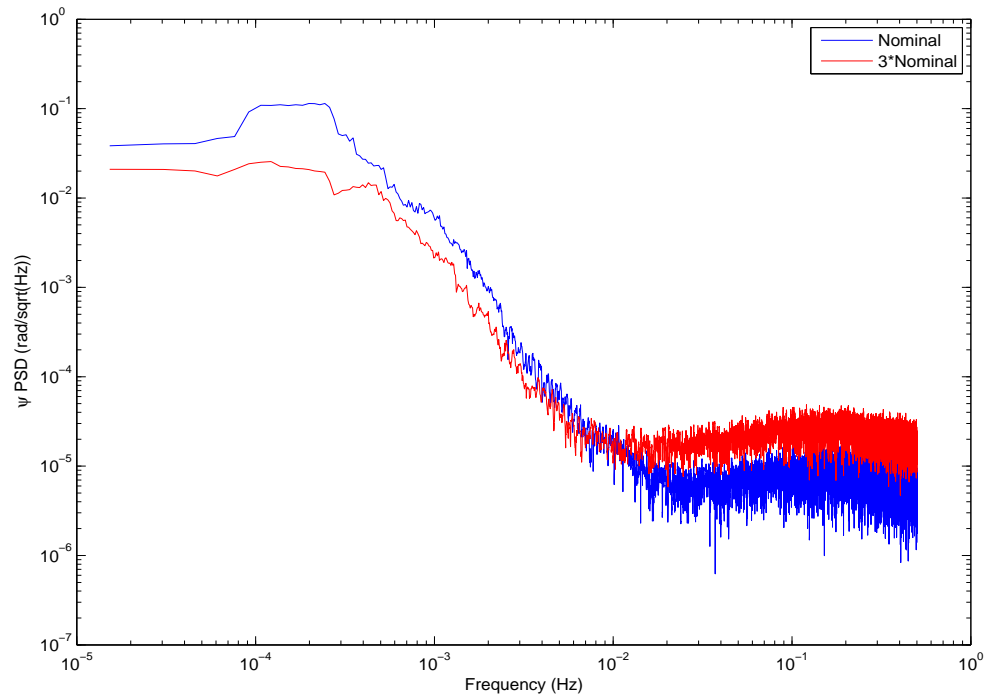


Figure 6.2: SC1 - Yaw Attitude Angle PSD

The attitude acceleration time response for the white noise star camera test is given in Figure 6.3.

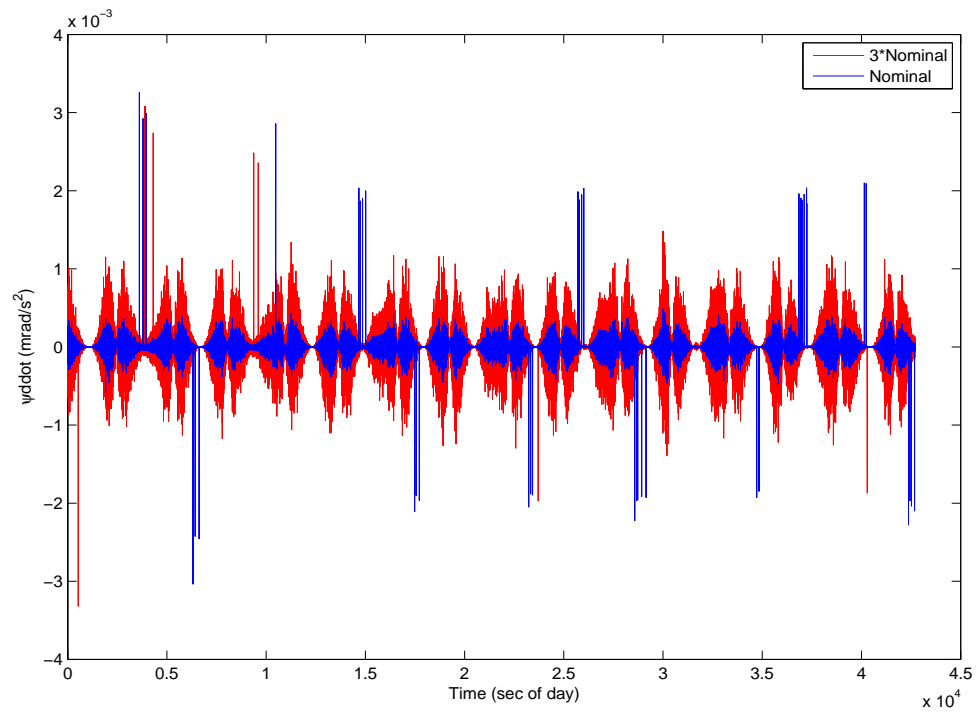


Figure 6.3: SC1 - Yaw Attitude Acceleration Time Response

The attitude acceleration PSD for the white noise star camera test is given in Figure 6.4.

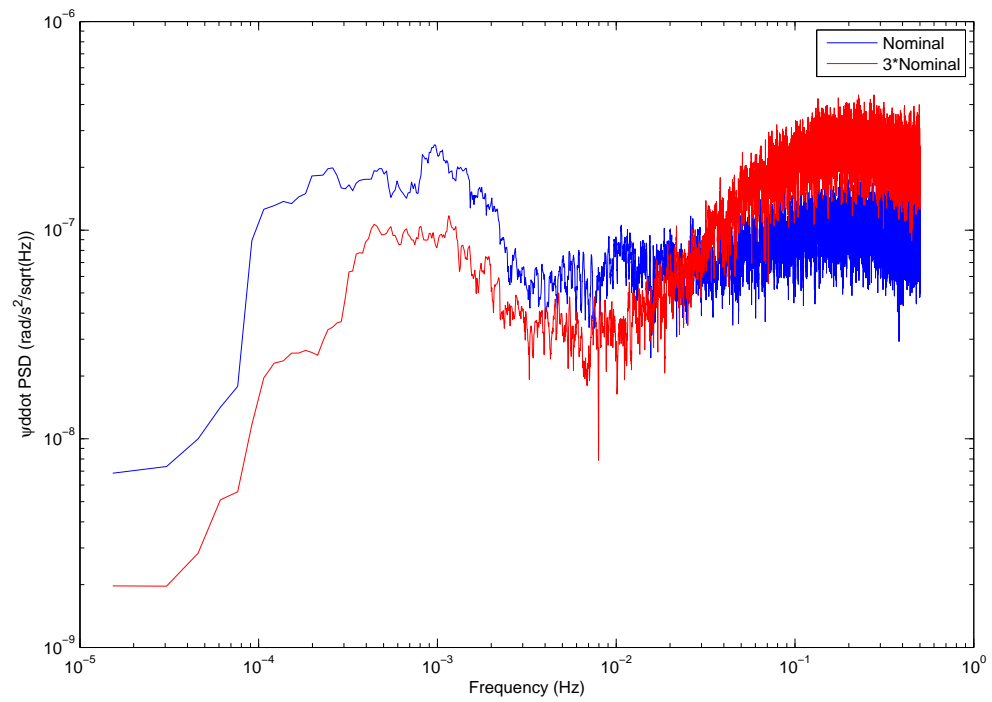


Figure 6.4: SC1 - Yaw Attitude Acceleration PSD

The attitude angular and acceleration results for roll(ϕ) and pitch(θ) are given in Figures 6.5 and 6.6.

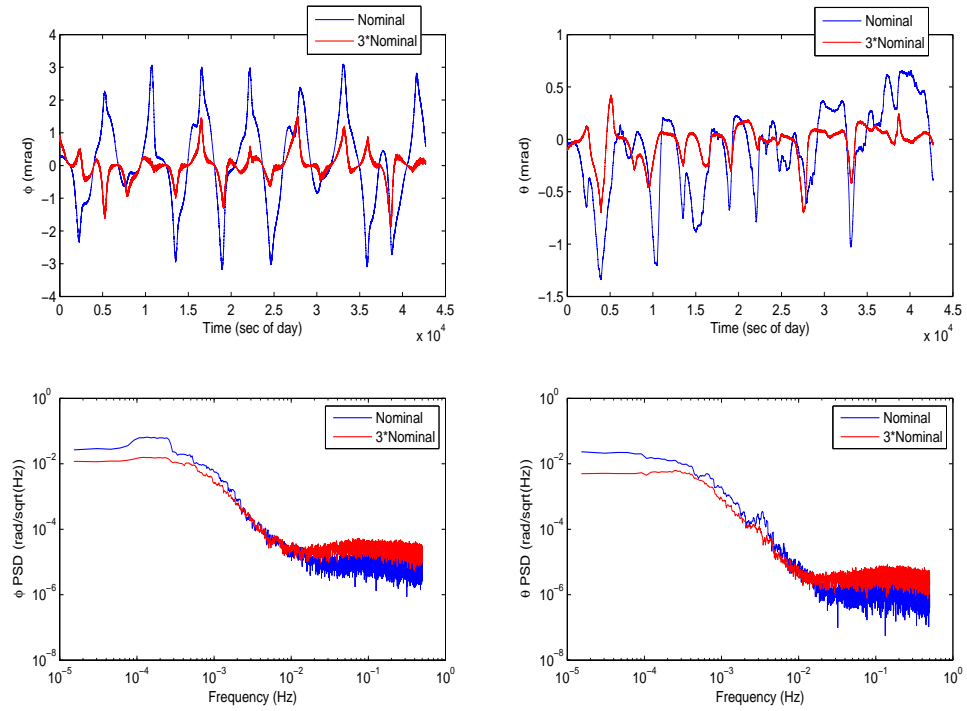


Figure 6.5: SC1 - Roll and Pitch Attitude Angle Behavior

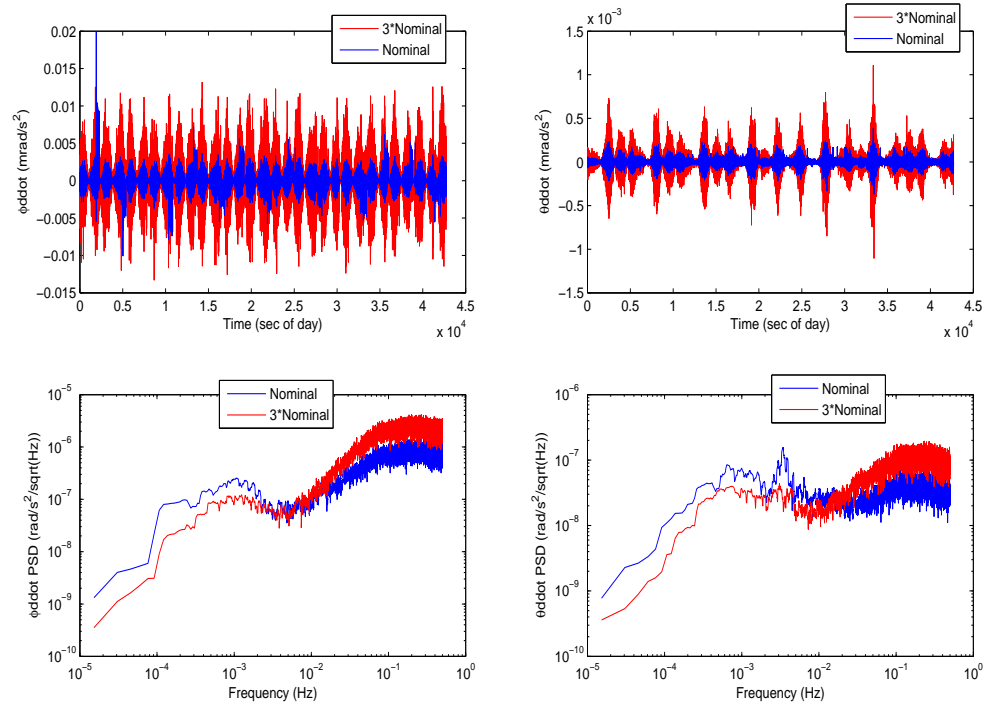


Figure 6.6: SC1 - Roll and Pitch Attitude Acceleration Behavior

6.2.2 SC2

The attitude angle time response for the colored noise star camera test is given in Figure 6.7.

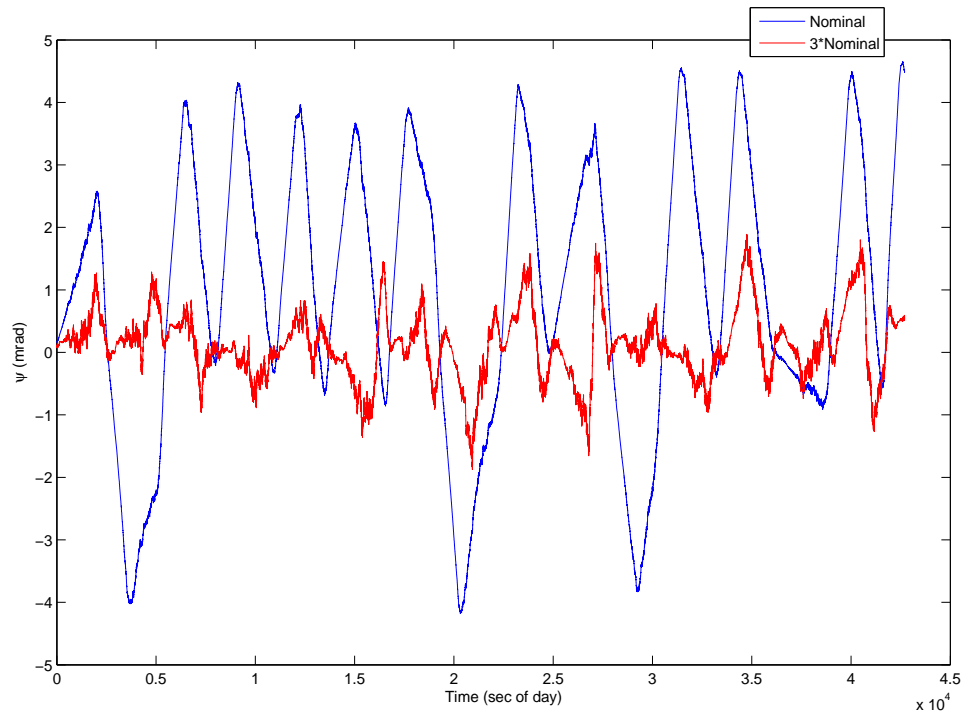


Figure 6.7: SC2 - Yaw Attitude Angle Time Response

The attitude angle PSD for the colored noise star camera test is given in Figure 6.8.

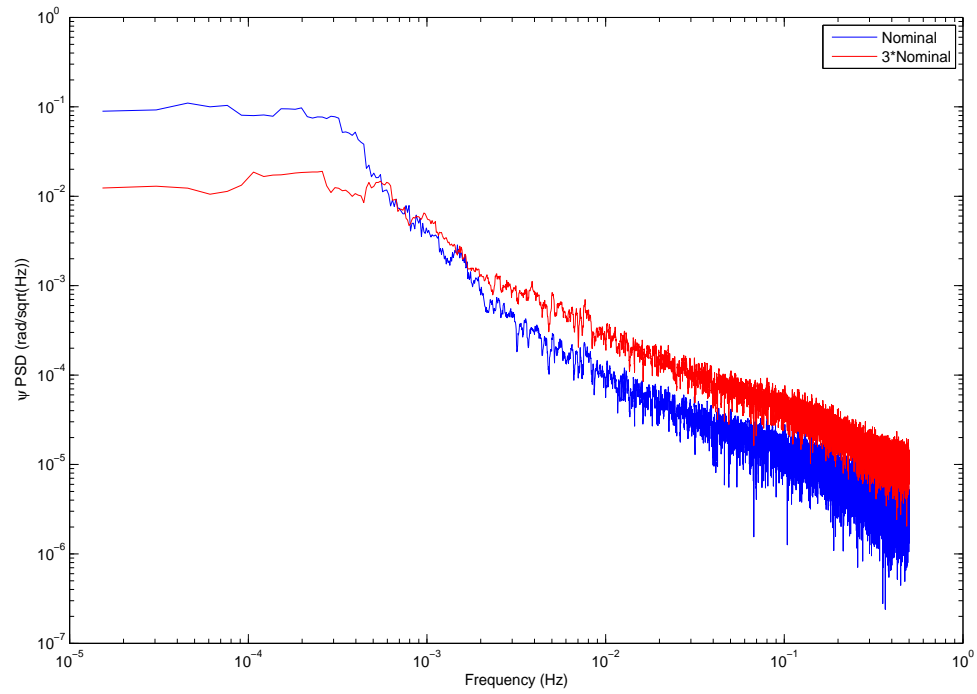


Figure 6.8: SC2 - Yaw Attitude Angle PSD

The attitude acceleration time response for the colored noise star camera test is given in Figure 6.9.

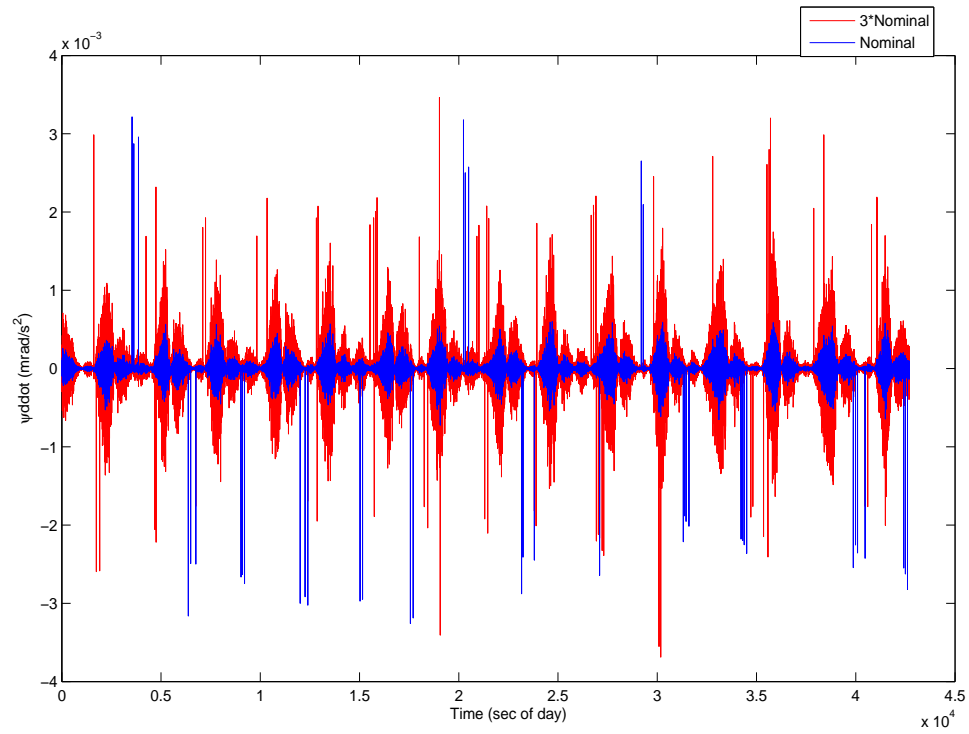


Figure 6.9: SC2 - Yaw Attitude Acceleration Time Response

The attitude acceleration PSD for the colored noise star camera test is given in Figure 6.10.

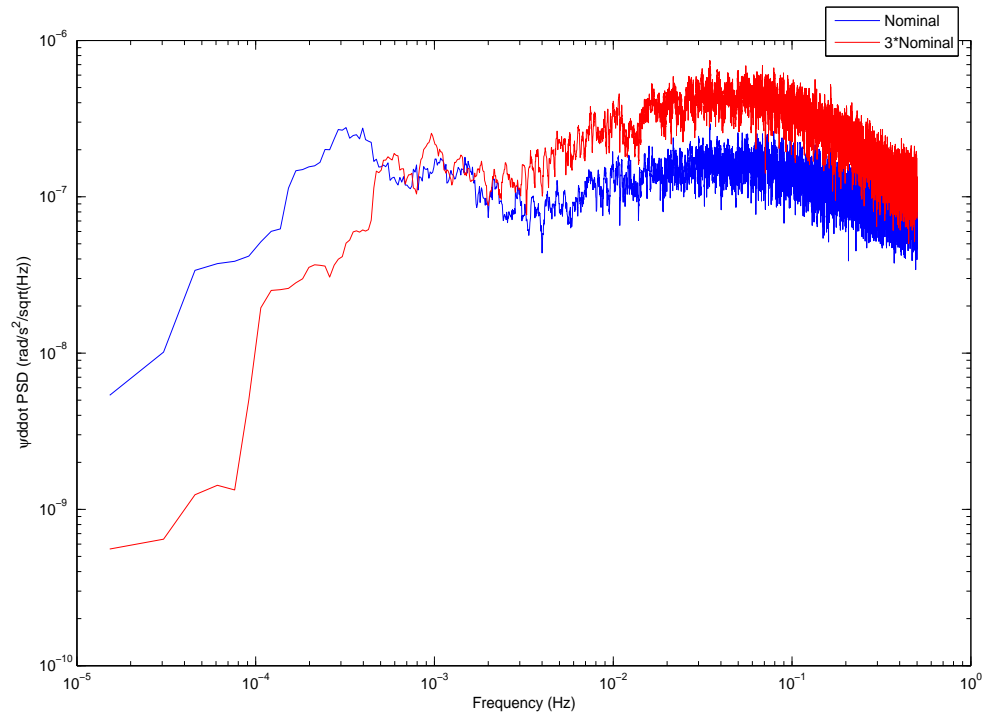


Figure 6.10: SC2 - Yaw Attitude Acceleration PSD

The attitude angular and acceleration results for roll(ϕ) and pitch(θ) are given in Figures 6.11 and 6.12.

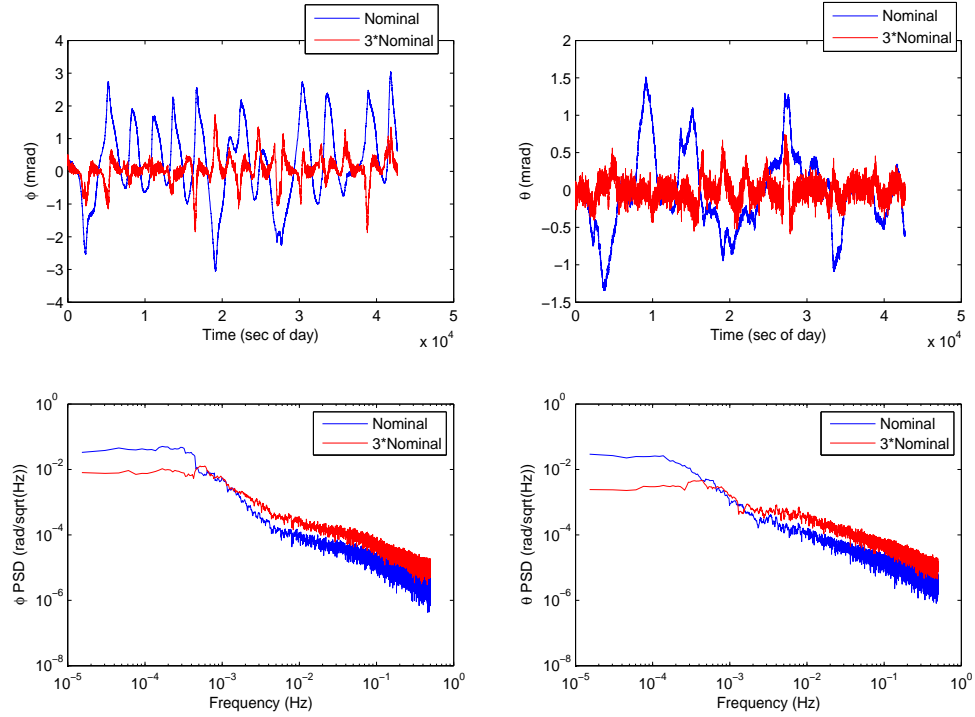


Figure 6.11: SC2 - Roll and Pitch Attitude Angle Behavior

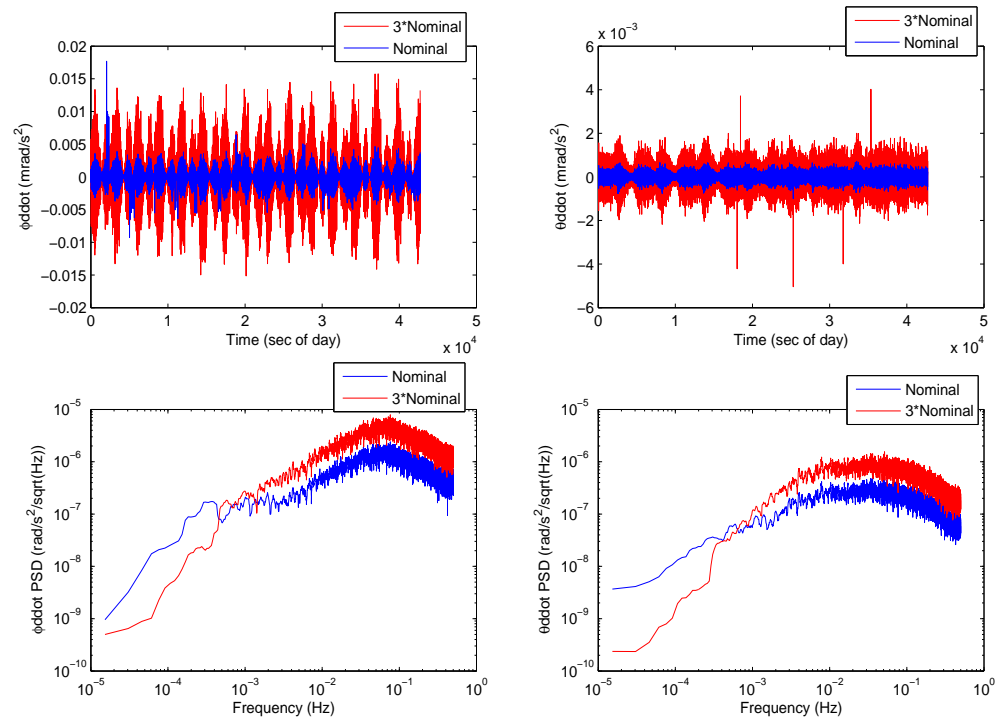


Figure 6.12: SC2 - Roll and Pitch Attitude Acceleration Behavior

6.2.3 SC3

The attitude angle time response for the star camera misalignment test is given in Figure 6.13.

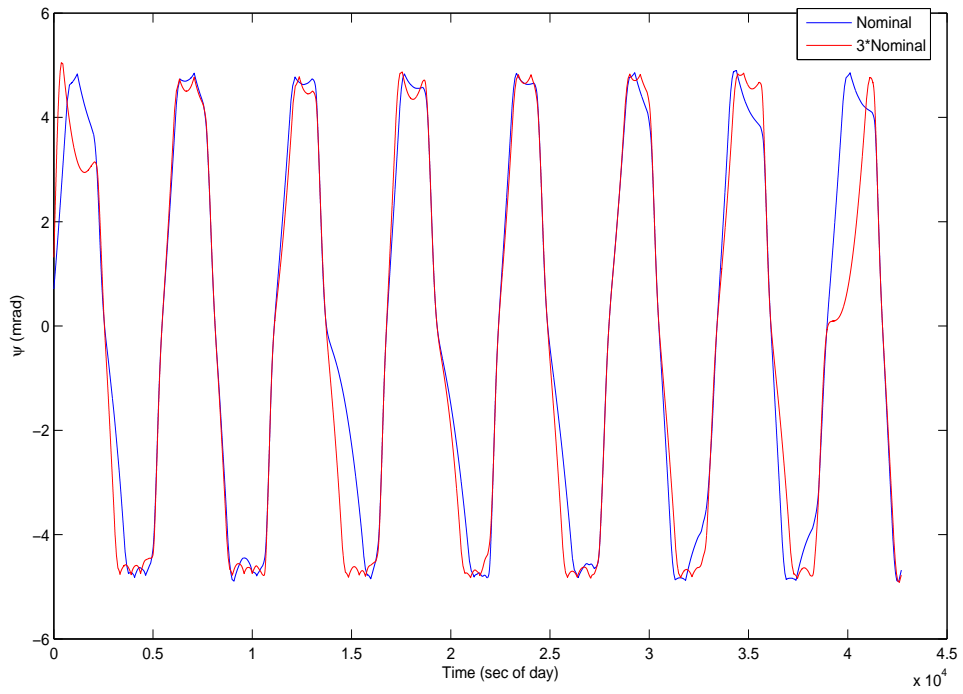


Figure 6.13: SC3 - Yaw Attitude Angle Time Response

The attitude angle PSD for the star camera misalignment test is given in Figure 6.14.

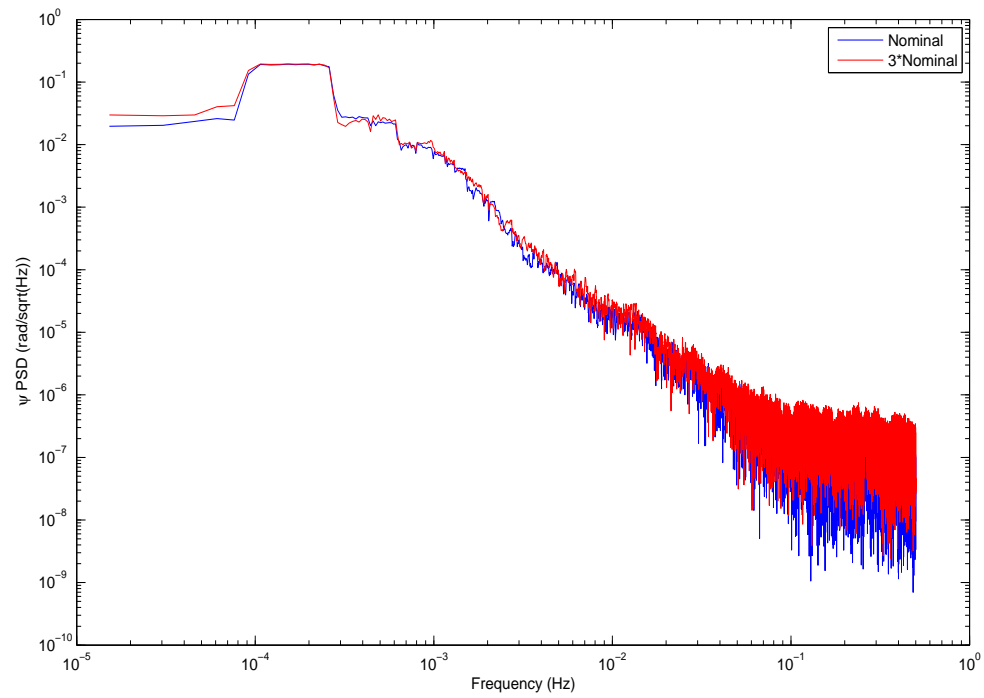


Figure 6.14: SC3 - Yaw Attitude Angle PSD

The attitude acceleration time response for the star camera misalignment test is given in Figure 6.15.

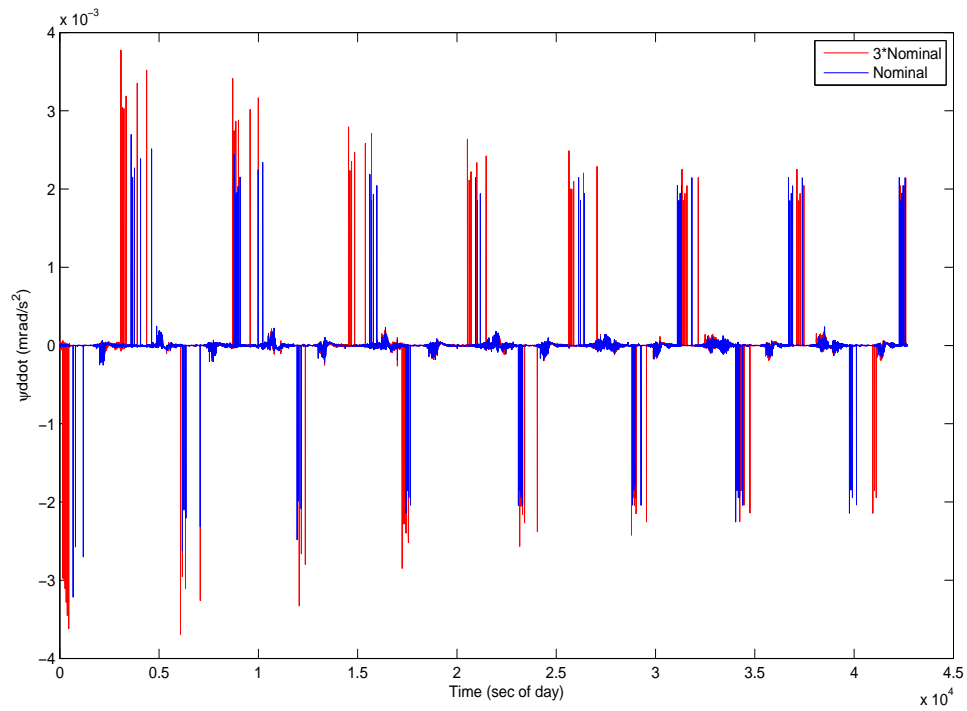


Figure 6.15: SC3 - Yaw Attitude Acceleration Time Response

The attitude acceleration PSD for the star camera misalignment test is given in Figure 6.16.

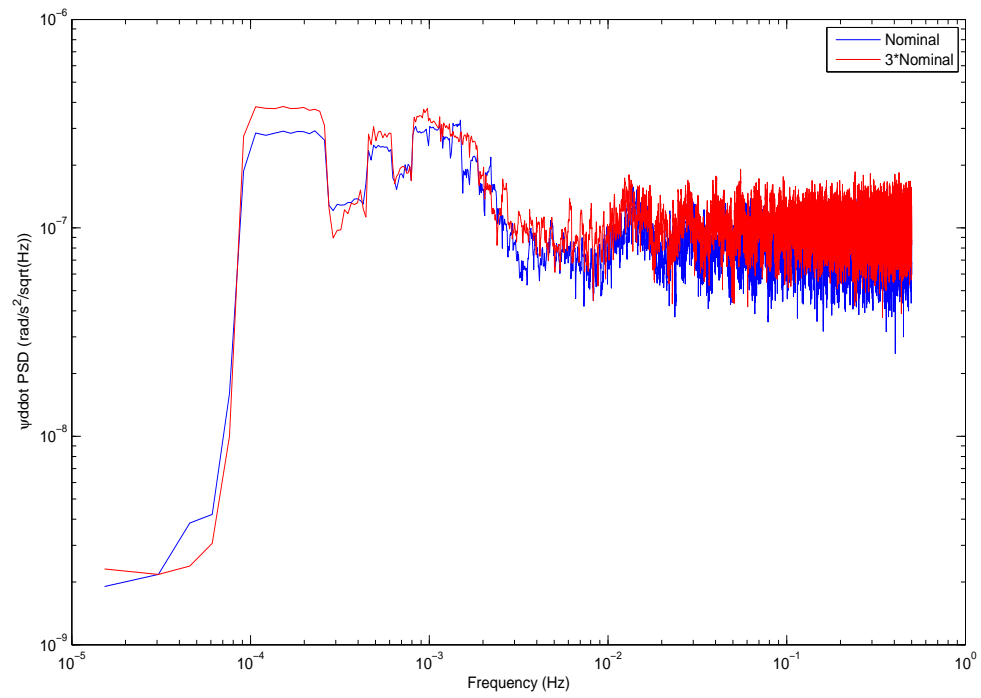


Figure 6.16: SC3 - Yaw Attitude Acceleration PSD

The attitude angular and acceleration results for roll(ϕ) and pitch(θ) are given in Figures 6.17 and 6.18.

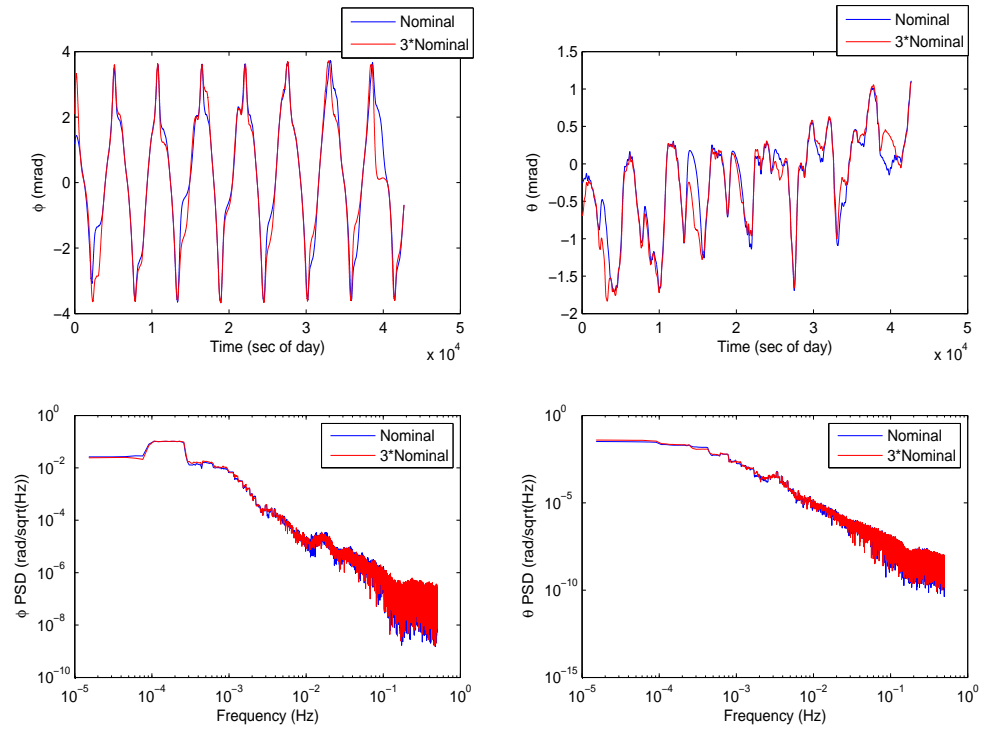


Figure 6.17: SC3 - Roll and Pitch Attitude Angle Behavior

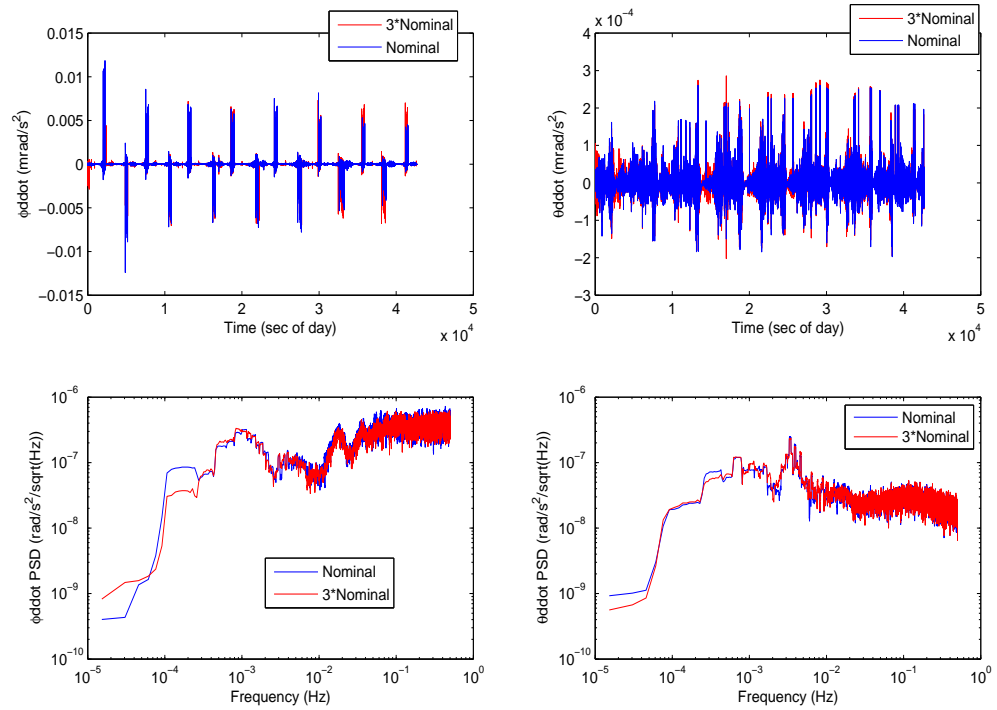


Figure 6.18: SC3 - Roll and Pitch Attitude Acceleration Behavior

6.2.4 Star Camera Implications

The star camera sensitivity results demonstrate some very noticeable effects. First, the time-series angular behavior for the measurement noise experiments, SC1 and SC2, show significant changes in the overall signal character. If the star camera measurement noise is sufficiently magnified, the limits of the angular response decrease significantly. As an example, consider the yaw angle result for the SC2 test, given in Figure 6.7. For a nominal colored noise perturbation, the signal quality behaves as expected, i.e. angles are constrained within a predefined deadband value of approximately 4 mrad. The control response is captured in the acceleration plot, shown in Figure 6.9. Whenever the angular behavior exceeds the deadband, impulsive thruster maneuvers are activated. This is the expected deadband-limited response.

When the measurement noise is magnified, the limits decrease. The behavior no longer breaks the deadband limits. From Figure 6.9, the high frequency magnetic actuation increases by a large percentage. The control system in this scenario is responding to the noise in the input, and less to the actual angular deviations from the target attitude. The attitude signal, in other words, is plagued by a high degree of uncertainty, causing unnecessary high frequency actuations. A useful term that depicts the control effort character is the integrated attitude acceleration. A comparison of the integrated attitude acceleration for SC2 and Mag1 is shown in Figures 6.19 and 6.20. The cumulative control signal response is contained within this integrated term.

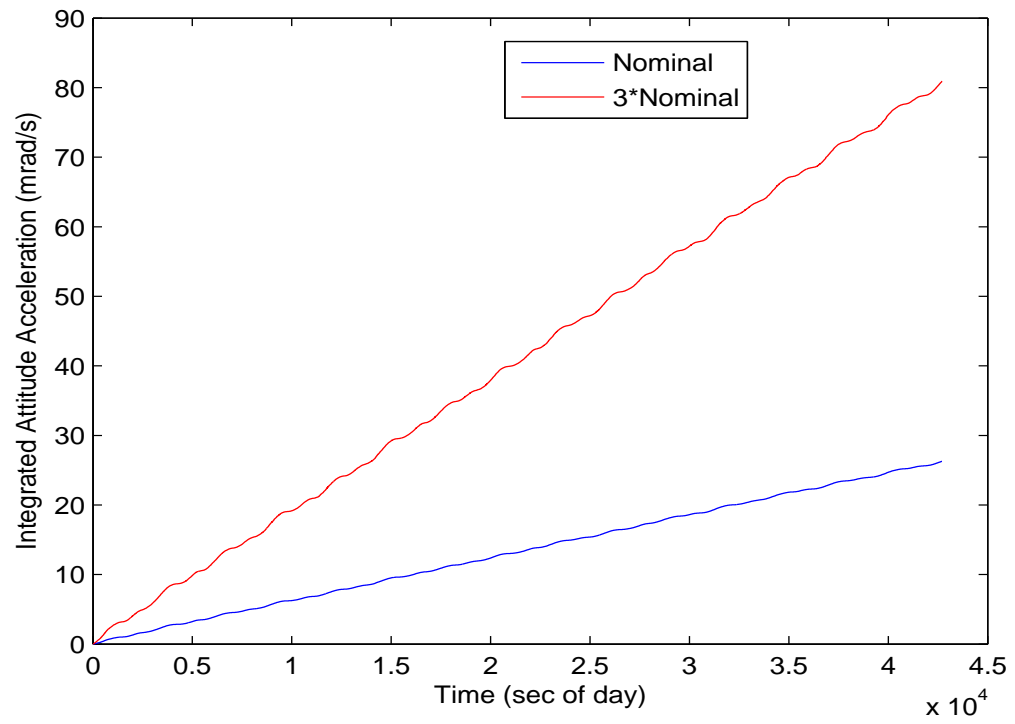


Figure 6.19: SC2 - Integrated Attitude Acceleration

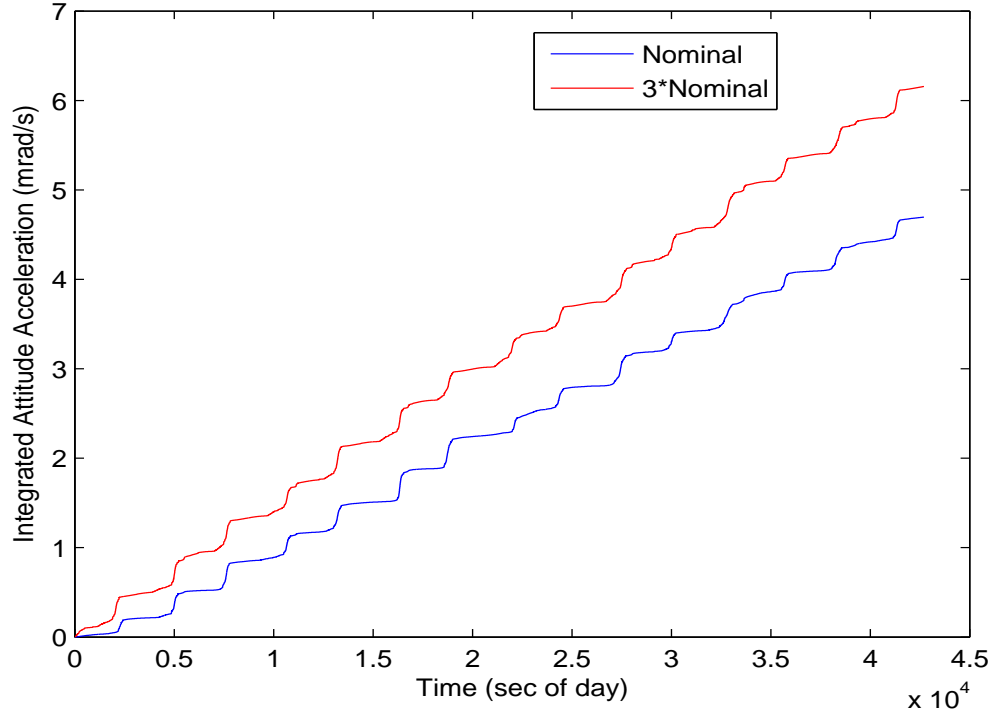


Figure 6.20: Mag1 - Integrated Attitude Acceleration

For the Mag1 test, which contains no star camera noise, the slope of the integrated attitude acceleration experiences an approximately 20% increase. However, the general character of the control response is not significantly affected. The frequency of thruster activity and magnetic activity effort is similar between the Nominal and 3*Nominal test cases. This is not so for the SC2 test. As seen from Figure 6.19, as the amount of measurement noise is amplified, the integrated attitude acceleration slope experiences a sharp increase of almost 300%. The control effort, particularly the magnetic actuation, is now

responding to system noise instead of deadband excursion. The larger control effort has ramifications with respect to power and propellant usage, and the attitude signal uncertainty also rises.

Deleterious effects are also seen in the angular and acceleration PSD responses. For the white noise test, the angular and acceleration PSD histories are given in Figures 6.2 and 6.4. The reduction in the angular limits cause the low frequency content to decrease, particularly in the frequency regime of 100 μHz to 300 μHz . On the other hand, high frequency content above 10 mHz is amplified, reflective of the increased magnetic strength. An even more pronounced trend is observed in the colored noise results, particularly in Figure 6.8. As discussed in Chapter 5, the colored noise series examined for this study is a red noise effect with a low frequency floor. As the input colored noise is amplified, the high frequency red noise increases, and the low frequency floor extends from 300 μHz to 600 μHz . This indicates that the input angular signal is approaching the colored noise disturbance. From the acceleration response, given in Figure 6.10, the frequency content above 3 mHz is amplified, also reflective of the increased magnetic power.

In contrast to measurement noise, star camera misalignment does not significantly affect the attitude signal quality. The uncertainty introduced by magnification of misalignment causes thruster impulses to slightly increase in magnitude, as seen in Figure 6.15. This in turn affects propellant expenditure, and causes a small increase in the attitude acceleration PSD, seen in Figure 6.16. One noteworthy trend identified in the acceleration PSD is an

amplification in frequency ranges of 100-300 μHz , and 500-700 μHz . These bands are characteristic of the thruster activation period. This result is significant because these amplifications lie in an important bandwidth of the gravity estimation process.

In total, these modeled results have demonstrated that amplification of measurement noise in star camera readings can cause highly detrimental effects on the attitude signal quality. This has multiple impacts on the scientific process. In an SST framework, attitude reliability is crucial to the correction of K-band ranging data signal. The attitude knowledge is used to correct for instrument CM offset, and acceleration information is used to account for non-gravitational forces. Deleterious impacts on these processes can significantly degrade the quality of the scientific solution.

The reason that star camera measurement noise plays such a significant role is seen in the ACS structure, given in Figure 4.1. The only source of attitude knowledge for the science mode algorithms is from the star camera quaternion. Data from this sensor is used as the primary input to form the error signal, the rate signal estimate, and the control response. Hence, errors in this sole source of information are compounded as they pass through subsequent blocks of ACS code.

From these modeled results, it is clear that the effects of star camera measurement noise must be limited in order to preserve the quality of the attitude signal, and ensure high performance of the ACS response. One potential way to achieve this is through adjustment of intrinsic parameters comprised

in the control algorithm scheme. Some of these tests are now considered.

6.2.5 Star Camera Measurement Noise - Refinement Tests

The first preference when attempting to compensate for existing star camera measurement noise is adjustment of intrinsic control parameters. If unforeseen levels of noise are present when the spacecraft is in orbit, it is desirable to reduce the noise effect by simply adjusting these parameters through ground upload. Refined experiments are conducted in which the “ideal” simulation is modified to include both white noise and colored noise, using the 3*Nominal statistics. Intrinsic gains associated with different control processes are adjusted to see if significant improvement in the signal quality is achieved.

For the first of these refined experiments, the deadband-limits constraints are modified. The nominal limits are based on the expected attitude angle performance needed to achieve a certain level of accuracy in the scientific solution. By increasing these deadbands, the frequency of thruster actuations decreases, but the magnitude of control effort increases. The goal is to identify whether these reduced frequency actuations improve the attitude signal quality response in the presence of star camera noise. The time history of the angle response is given in Figure 6.21.

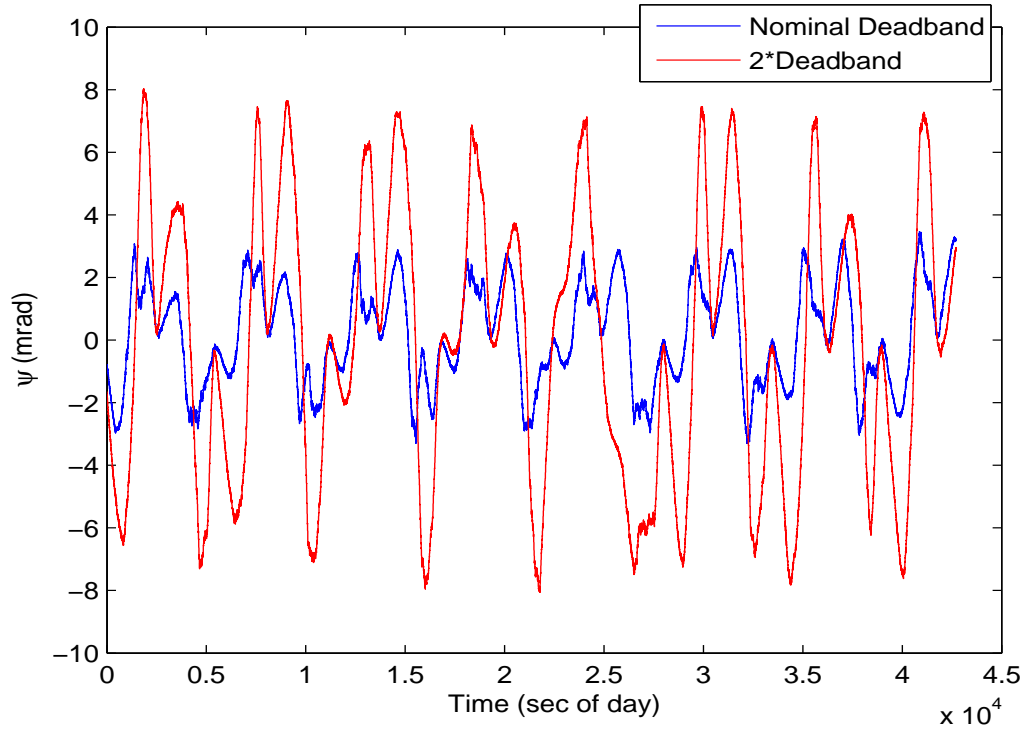


Figure 6.21: Deadband Experiment - Attitude Angle Time Response

As expected, opening up the deadband decreases the frequency of thruster actuations. The attitude error limits are now at higher values. The angular PSD response is given in Figure 6.22.

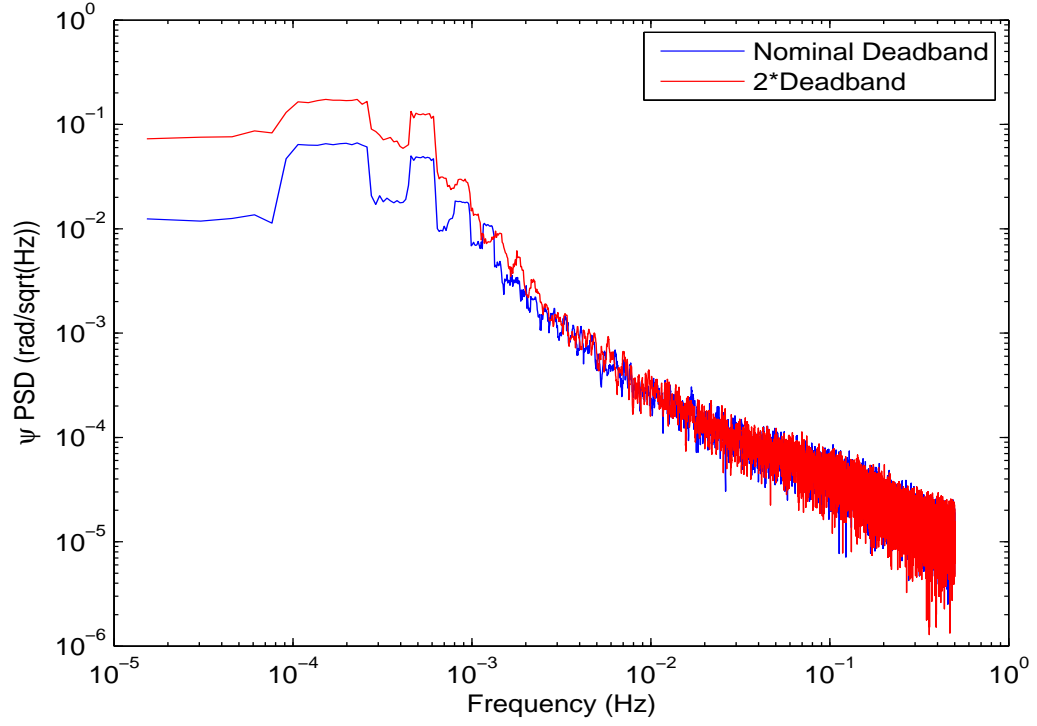


Figure 6.22: Deadband Experiment - Attitude Angle PSD

Increasing the deadband limits comes with a cost, as the modeled control effort increases. This is seen in the attitude acceleration time response, given in Figure 6.23.

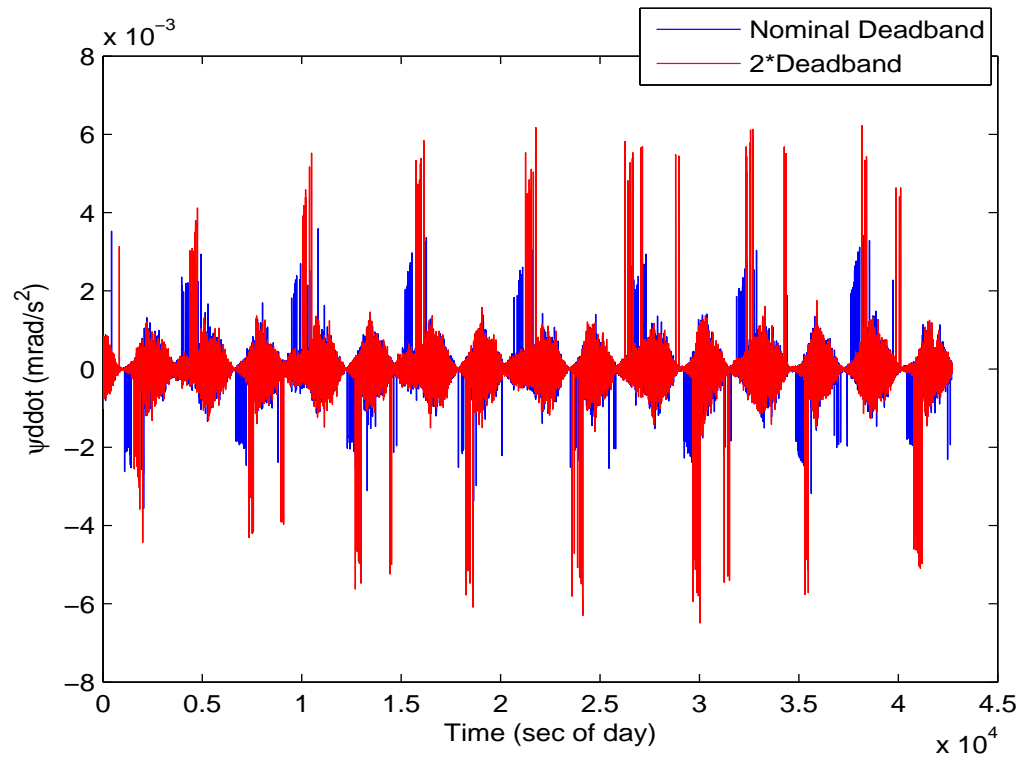


Figure 6.23: Deadband Experiment - Attitude Acceleration Time Response

Although magnetic control does not significantly rise, the thruster firings do increase, reflecting the attitude deadband excursion. The attitude acceleration PSD is seen in 6.24.

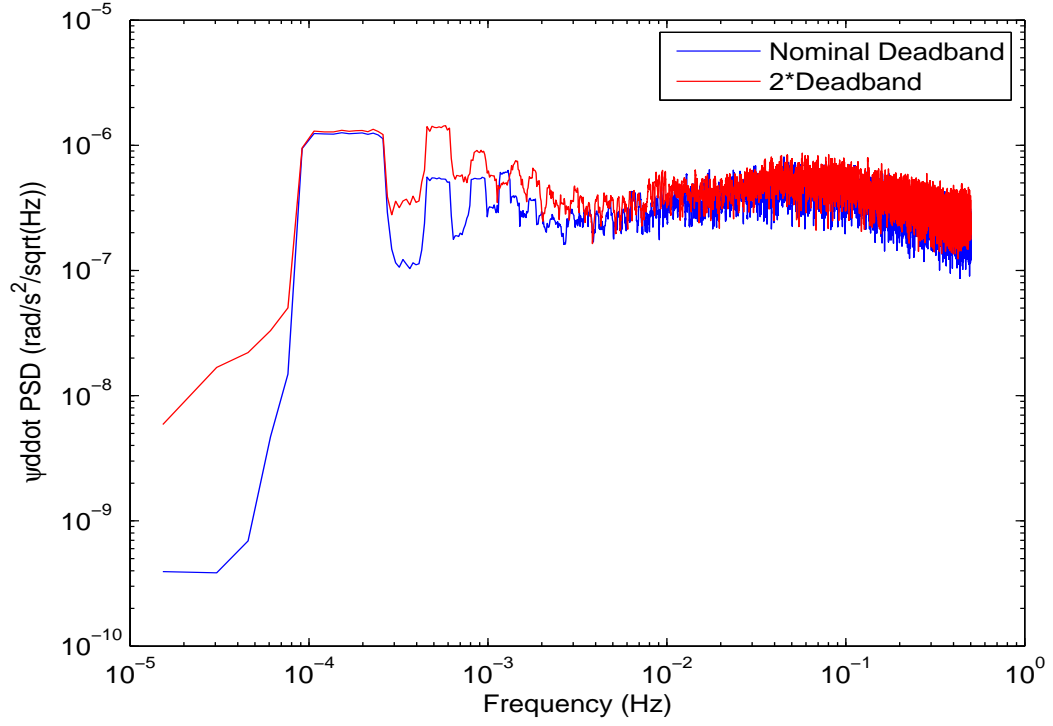


Figure 6.24: Deadband Experiment - Attitude Acceleration PSD

The rise in acceleration PSD is less than a factor of two, so opening up the deadband limits does not significantly affect the attitude acceleration PSD. However, from examination of the integrated acceleration, no significant change is seen in the quality of the control response. This is shown in Figure 6.25.

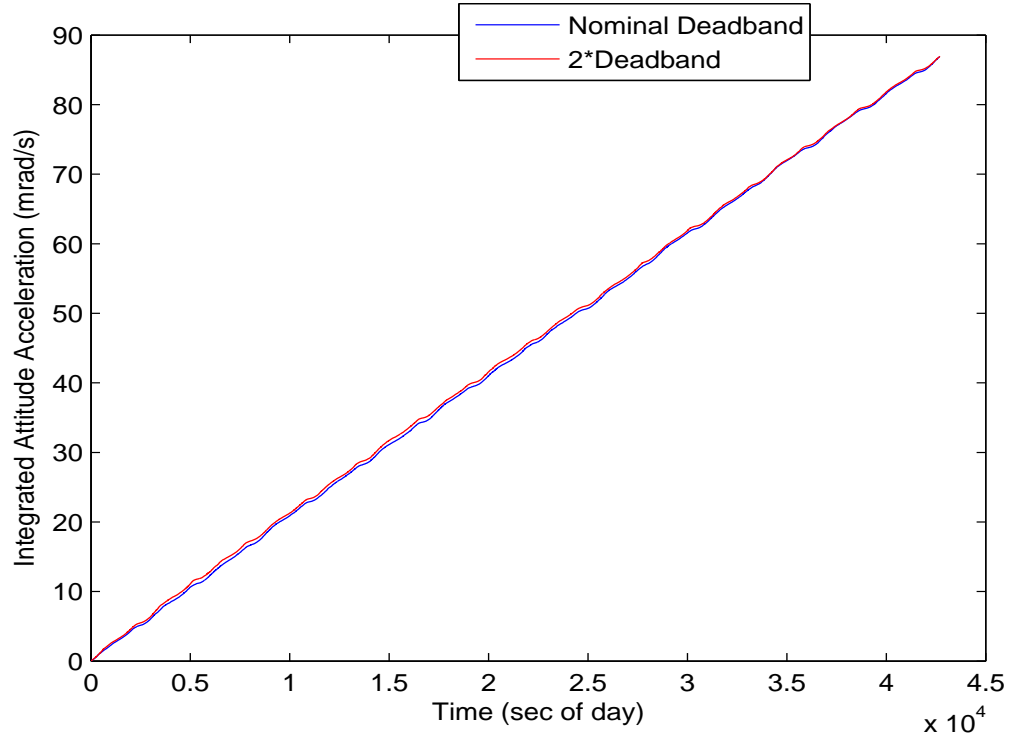


Figure 6.25: Deadband Experiment - Integrated Attitude Acceleration

The slope of the integrated acceleration does not markedly change as the deadband limits are raised. A high percentage of the control system effort is in response to noise levels present in the attitude signal. Therefore, no significant improvement is made in terms of attitude data quality as the deadband limits are increased.

Among the various components comprising the ACS logic, the PD control law is perhaps the most critical to attitude performance and stability. The PD controller gains are selected to minimize attitude angular deviations

in the line-of-sight frame, enhancing the quality of the K-band data. High oscillatory behavior and frequent effort of the control actuators can affect both attitude angle and acceleration signals. In addition, high control effort can quickly reduce the fuel levels, which is a major constraint when dealing with thrusters as primary actuators. The PD configuration thus selected contains a fairly slow settling time, with a small overshoot, but fast rise time. This is designed to optimize control actuation while limiting the time the error signal remains outside the deadband. For this refined PD experiment, the “ideal” simulation model is again modified to include white and colored noise, with 3*Nominal statistics. PD gain configurations with slower and faster responses are tested to see if improvements in the attitude data quality are achieved. This is employed by magnifying the derivative and proportional gains respectively. Example step responses of these PD configurations are shown in Figure 6.26.

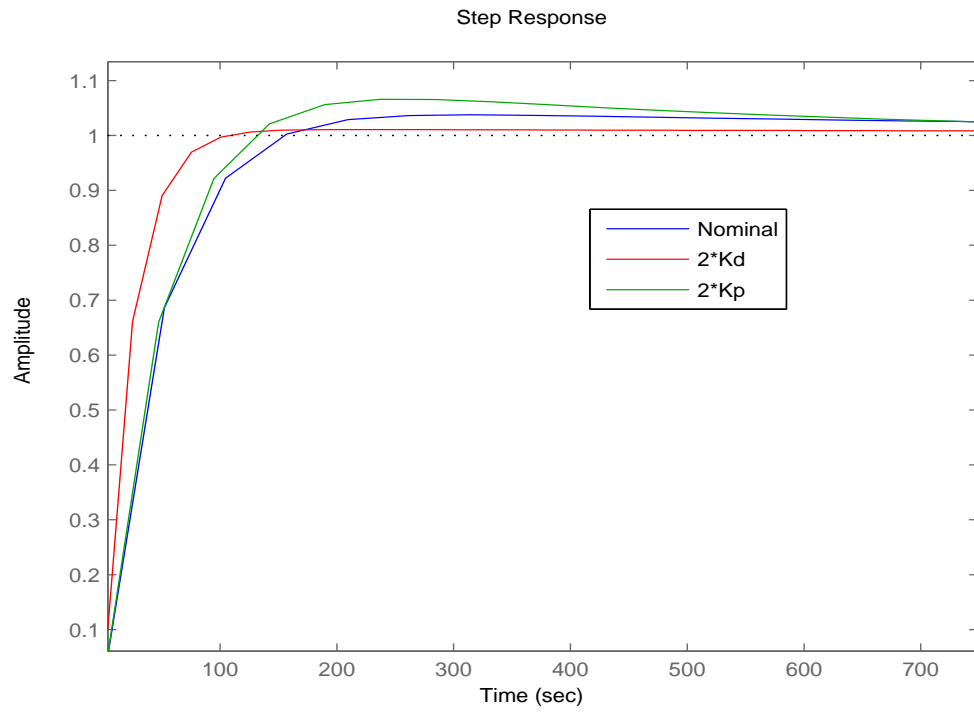


Figure 6.26: PD Configuration Comparisons

The attitude angle time response for the PD refined experiment is given in Figure 6.27.

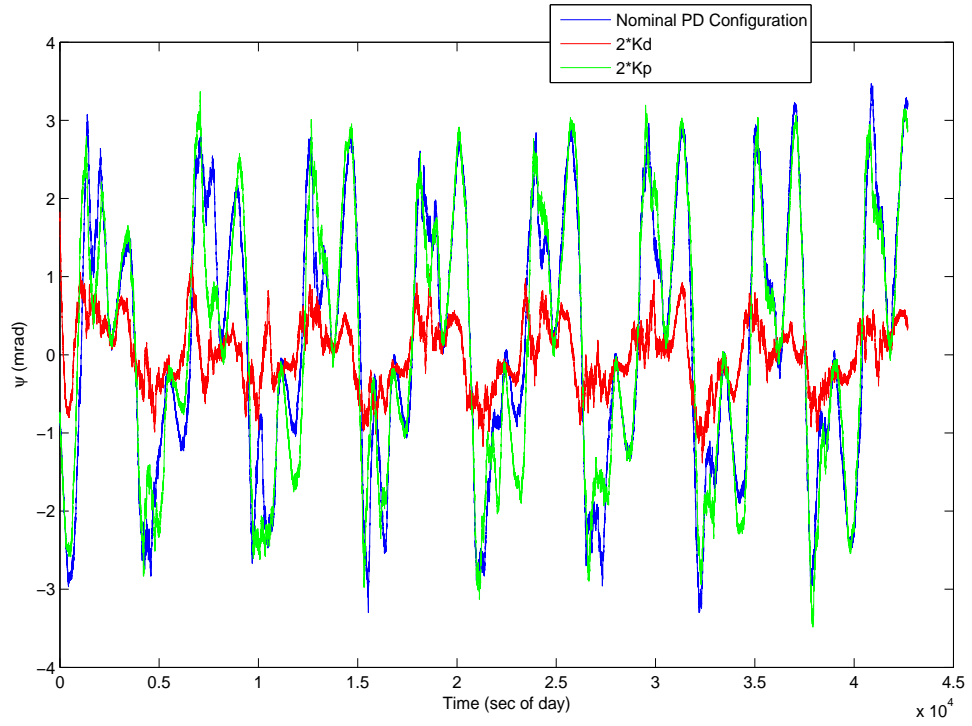


Figure 6.27: PD Controller Experiment - Attitude Angle Time Response

A noticeable result is that the higher proportional gain experiment has a minimal effect on the angular response. However, the derivative gain does affect the performance quality. Increasing the derivative gain further decreases the signal quality of the attitude angle excursions. The PSD of the angular behavior is given in Figure 6.28.

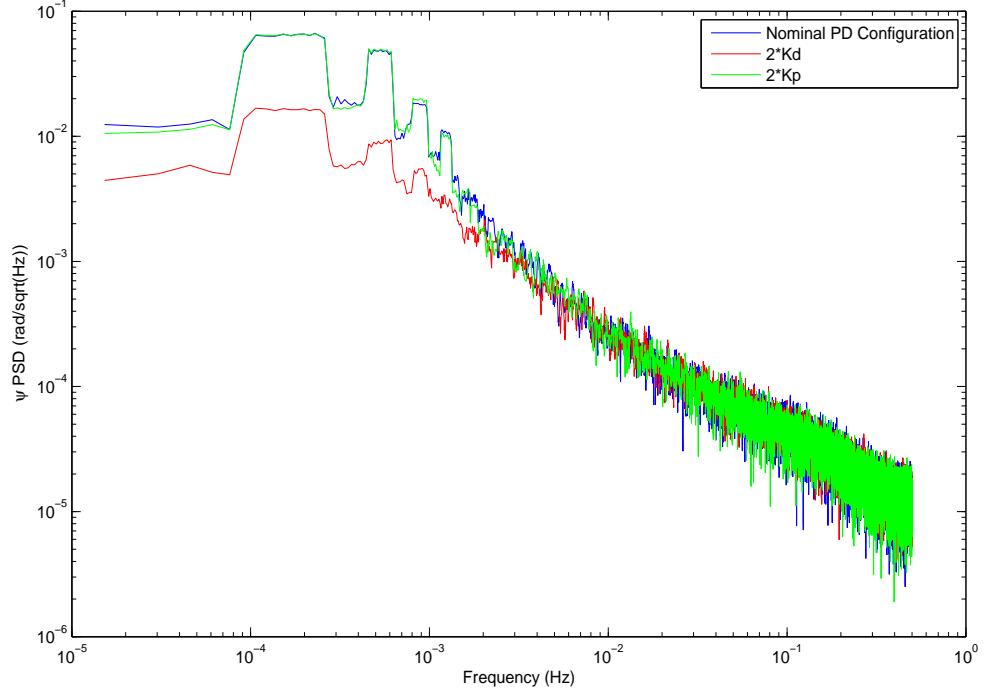


Figure 6.28: PD Controller Experiment - Attitude Angle PSD

The low frequency content reduces significantly when K_d is magnified. The purpose of K_d is to improve the transient response through a weight of the attitude error slope. The slope, in this case, corresponds to the attitude rate. As mentioned previously, attitude rate is not directly sensed in this control architecture. Therefore, magnifications of this signal must be performed judiciously; otherwise, noise terms can also be magnified. This behavior is demonstrated in the modeled results of the magnified K_d test. The acceleration behavior shows similar magnifications, as seen in Figure 6.29.

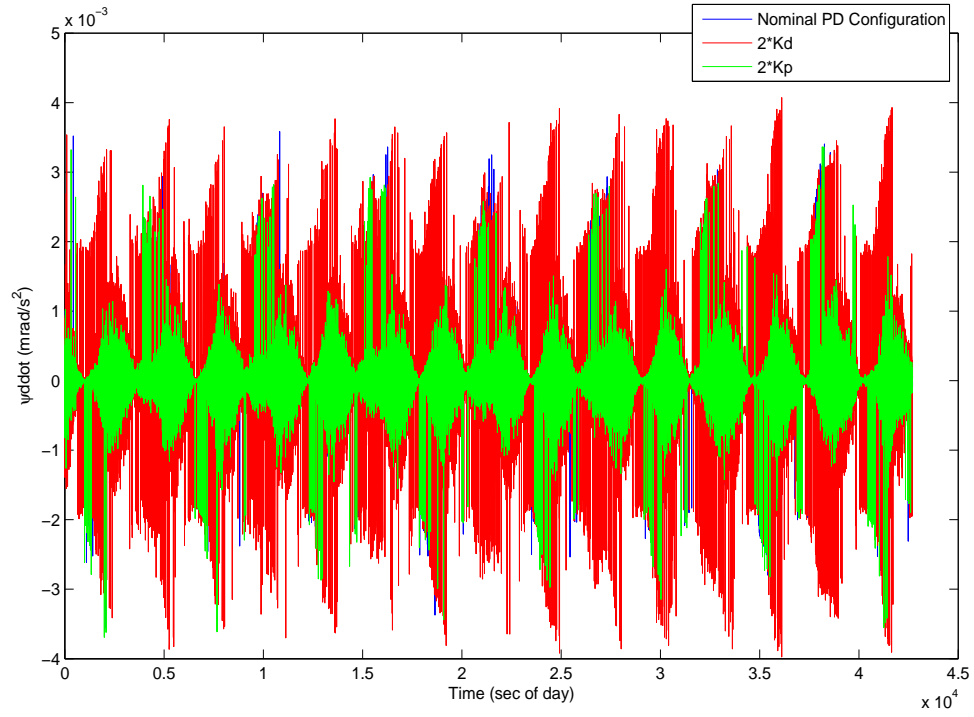


Figure 6.29: PD Controller Experiment - Attitude Acceleration Time Response

The overall control effort, particularly the magnetic response, grows by a large percentage when an increased K_d gain is used. Therefore, the benefits of a fast response controller are accompanied by detrimental effects on both the attitude quality and the acceleration magnitude. This is seen in both the attitude acceleration PSD and integrated attitude acceleration, shown in Figures 6.30 and 6.31.

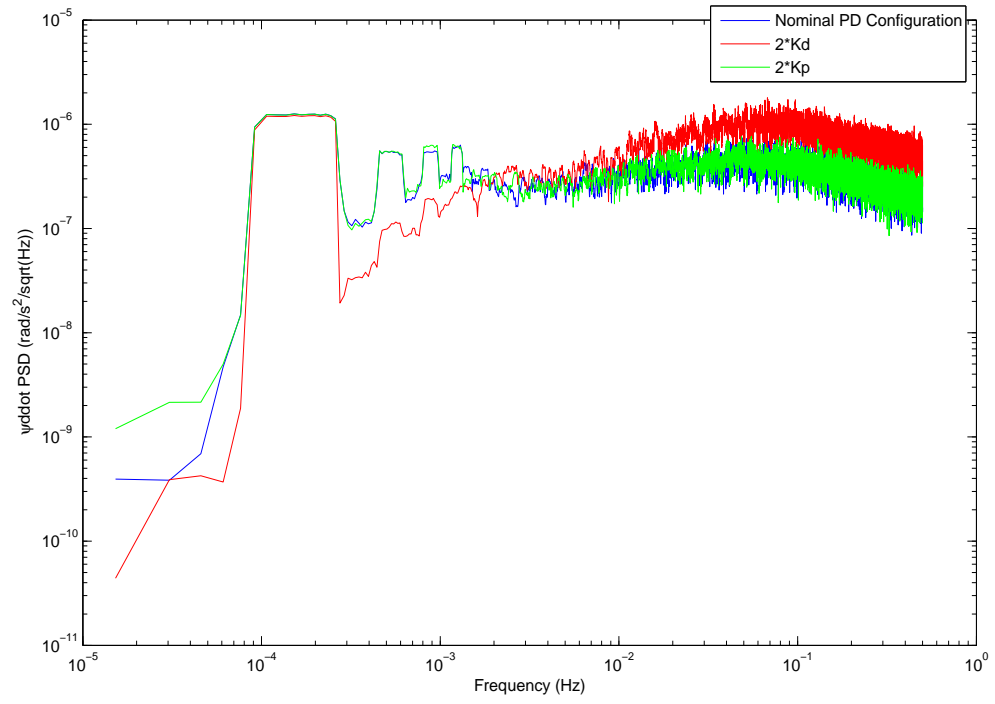


Figure 6.30: PD Controller Experiment - Attitude Acceleration PSD

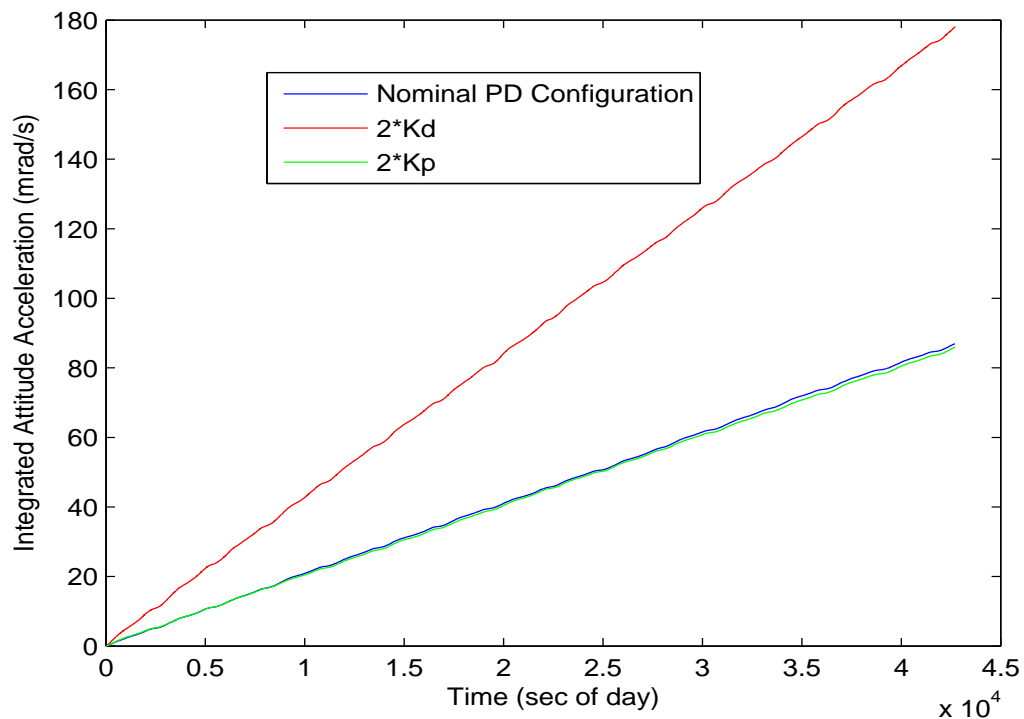


Figure 6.31: PD Controller Experiment - Integrated Attitude Acceleration

As mentioned at the start of Chapter 5, control design involves a rigorous tuning process, in which modeled attitude is perturbed using Monte-Carlo level disturbances. In this test, various configurations of PD gains are selected to optimize the attitude behavior. This is beyond the scope of this case study. However, the PD refinement results demonstrate the necessity in selecting the proper gain configuration.

A final refined experiment is performed by adjusting parameters related to the estimation process used to construct the improved attitude error

signal. Estimation is performed using an LQE technique. Parameters related to the expected process and measurement noise inherent to the system are used to weight which parameters (i.e. angles, rates, and control torques) are emphasized in improving the error estimate. The nominal parameters used in the GRACE algorithms weight all three terms equally [17]. The goal of this experiment is to examine whether selective weighting improves the attitude quality in the presence of noise. As with the previous refined experiment, this is performed using 3*Nominal statistics of both the white and colored noise. Selective weighting is then utilized on the angle, rate, and control torque information. Previous weights are increased by two orders of magnitude for each term. The angular time-history of this refined experiment is given in Figure 6.32.

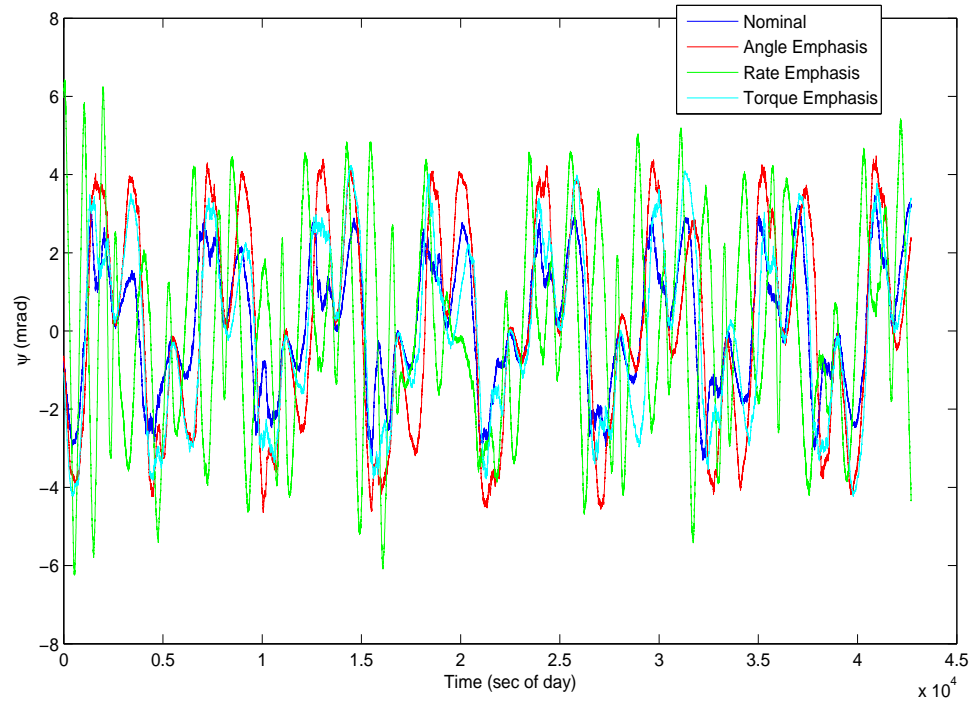


Figure 6.32: LQE Estimation Experiment - Attitude Angle Time Response

Among the different emphases, angular emphasis restores the deadband excursion characteristic to its expected value, torque emphasis has minimal effect, and rate emphasis induces oscillatory behavior in the angular response. Of these tests, the angular emphasis has shown the most beneficial results. The angular PSD is shown in Figure 6.33.

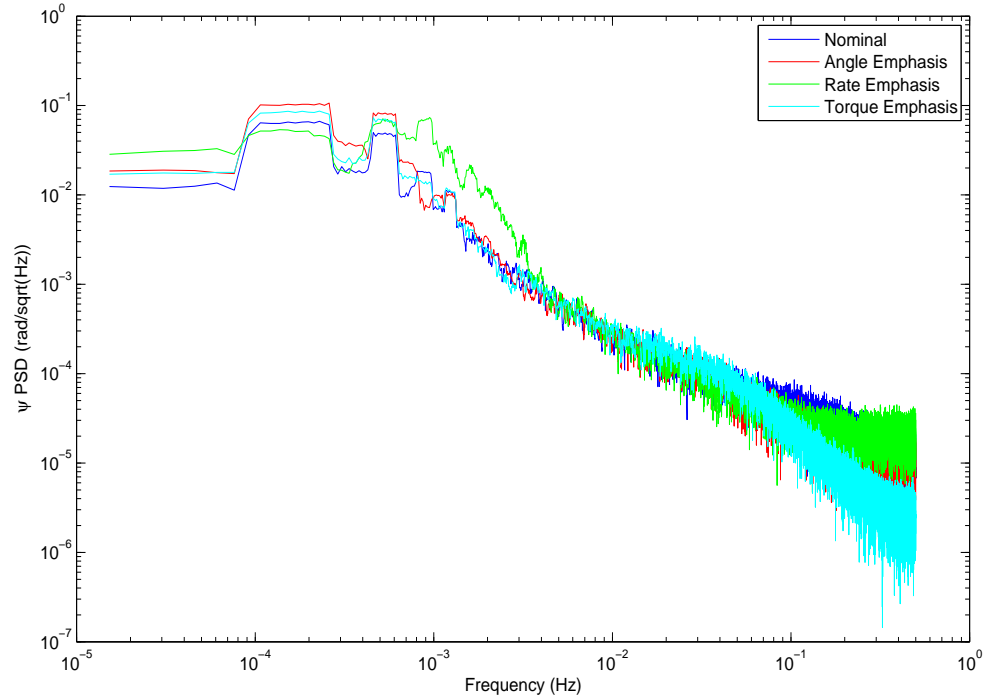


Figure 6.33: LQE Estimation Experiment - Attitude Angle PSD

The angular emphasis test shows an increase in low frequency angular content, particularly in the ranges of 100-300 μHz and 400-600 μHz . The acceleration response is shown in Figure 6.34.

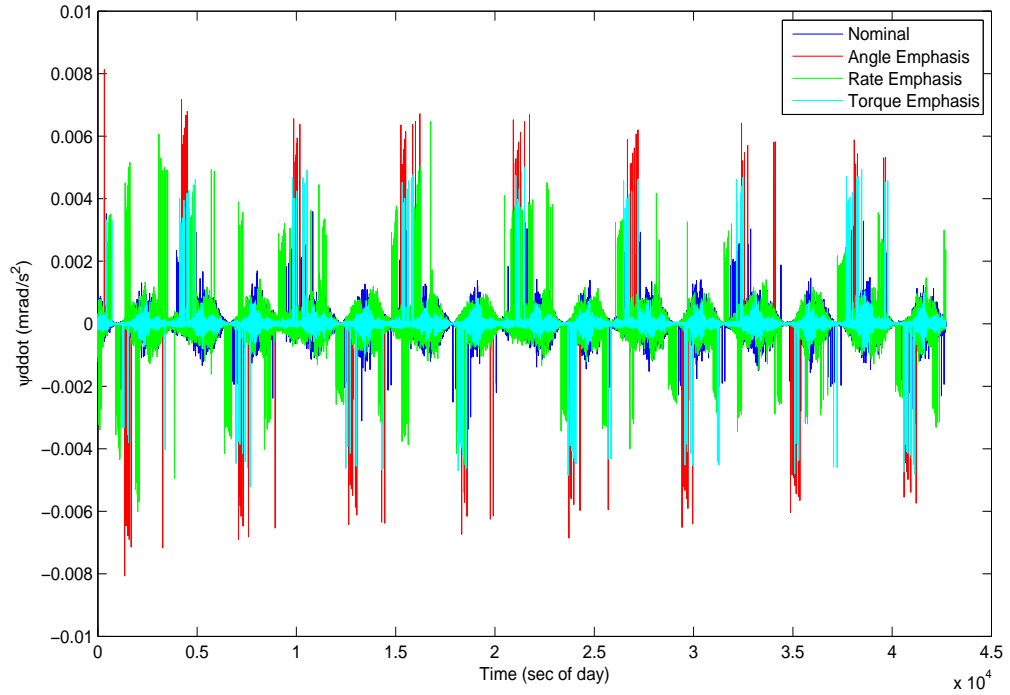


Figure 6.34: LQE Estimation Experiment - Attitude Acceleration Time Response

Emphasis of angular data causes the overall thruster activity to slightly increase. The attitude acceleration PSD is given in Figure 6.35.

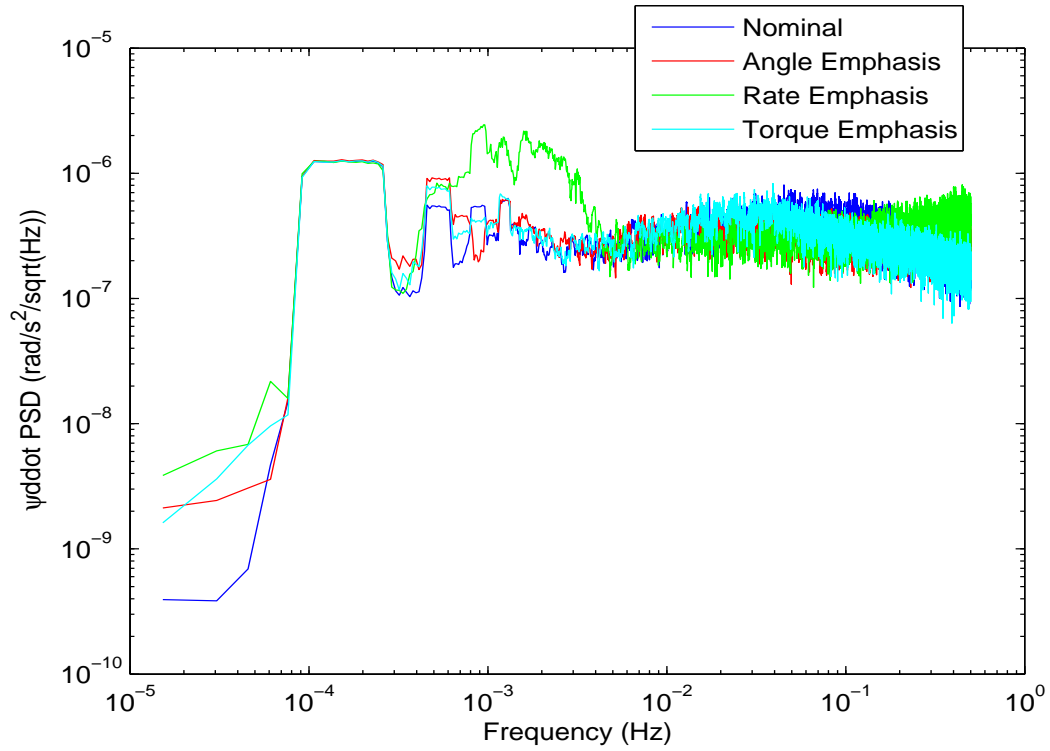


Figure 6.35: LQE Estimation Experiment - Attitude Acceleration PSD

What is noticeable from this graph is that low frequency PSD from 100-200 μHz is not affected at all by the adjustment in estimation parameters. Slight changes are seen from 300-500 μHz . However, significant changes are noticed in the integrated attitude acceleration, shown in Figure 6.36.

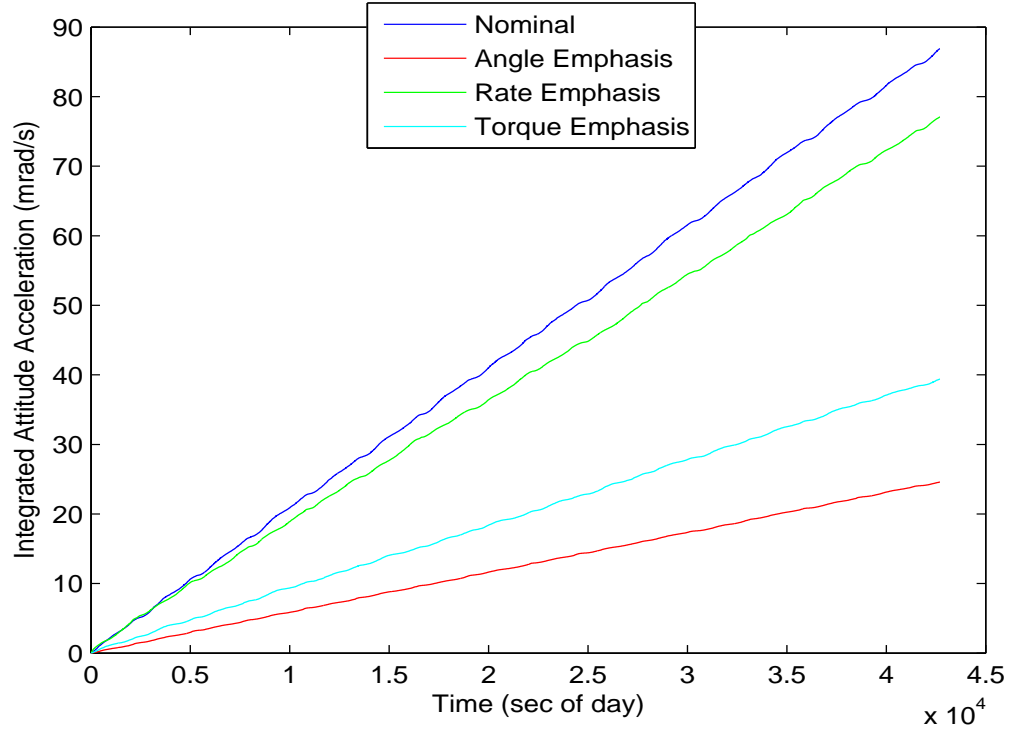


Figure 6.36: LQE Estimation Experiment - Integrated Attitude Acceleration

Selective estimator weighting improves the attitude signal quality, allowing the control system to respond to deadband excursion as opposed to noise levels. The emphasis term that produces the best results is the angular emphasis test. Emphasizing the angular input does not induce additional oscillations in the angular signal, like the rate emphasis test. In addition, increasing the measurement noise weights in the angular response dramatically reduces the integrated attitude acceleration, which is reflective of the overall control effort. In particular, the high frequency magnetic activity is reduced.

One tradeoff of using a greater angular emphasis is significant increase in the thruster activity, which causes larger propellant expenditure. However, the attitude angle deadband excursion now remains within expected limits, 4 mrad for this particular case.

6.2.6 Potential Future Experiments

From the intrinsic tests, possible improvements on attitude quality can be achieved in the presence of star camera noise by adjusting the estimator gains. However, the intrinsic tests are limited in their scope; they do not consider other non-idealities present in the system. Therefore, definitive conclusions cannot be reached until further experimentation is performed. However, these results are useful because the modeled ACS structure comprised in this study has clearly shown high levels of sensitivity to star camera measurement noise. The major source of this dependency is the fact that star camera measurements are the sole attitude knowledge source in the control process.

One option of future study is a trade study analysis when other sources of knowledge are included. If data from rate gyro and accelerometer sensing is combined with existing star camera information, it is possible that a filtered result will produce an error signal that is robust in the presence of sensor measurement noise. One major advantage of using a direct rate signal is improved results in the estimation process, producing a rate signal that is much more reliable than in the star camera only construct. Additionally, since PD control relies upon rate information in the algorithmic development,

an improved rate signal will produce a more reliable control response.

However, inclusion of additional sensors contains ramifications related to system-level considerations. Rate and accelerometer information used in ACS processes can significantly increase power used by the electrical systems. This, in turn, can reduce the spacecraft battery life, which can reduce the mission life. Also, additional sensors contain their own inherent noise statistics. It is possible that noise from multiple sources may be more detrimental than noise from a single source. However, a robust trade study must be performed to identify the relative benefits and costs related to additional sensor inclusion, with particular emphasis on the degree of improvement, if any, achieved in the attitude response in the presence of sensor measurement noise.

As this case study is an analysis procedure and not a design iteration, a Monte-Carlo study has not been considered. Since the ten component experiments have been considered independently, non-idealities related to magnetometer, thruster, and magnetic torque rods are performed in a star camera noise-free environment. Since the modeled attitude results have been demonstrated to display a high degree of sensitivity to star camera measurement noise, future analysis can be placed on studying the effects of star camera measurement noise on the effect of other non-idealities. In these experiments, the “ideal” simulation given in Figure 4.11 can be modified to include measurement noise as a baseline state. The non-idealities related to the actuation processes (magnetometer, thrusters, torque rods) can be included and analyzed for their effect in the presence of noise. It is expected that noise existence will

exacerbate the other non-idealities, and this can be quantified through future study.

6.3 Magnetometer Tests

Three magnetometer tests are performed for this case study. Two are additive perturbations accounting for white noise and biases in the magnetic field measurement, and one is multiplicative due to instrument misalignment.

6.3.1 Mag1

The attitude angle time response for the white noise magnetometer test is given in Figure 6.37.

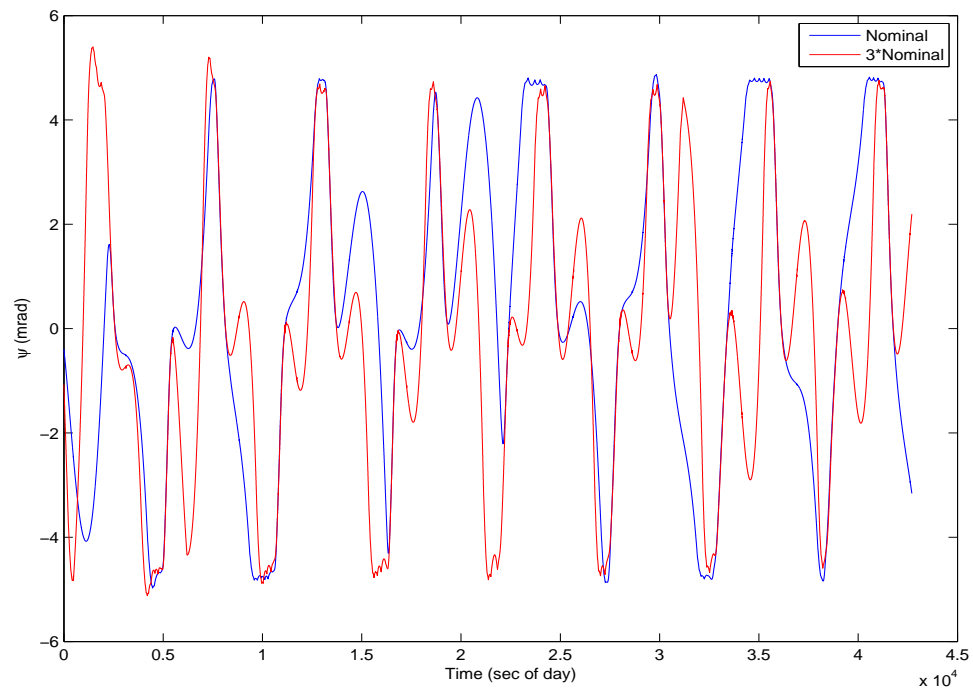


Figure 6.37: Mag1 - Yaw Attitude Angle Time Response

The attitude angle PSD for the white noise magnetometer test is given in Figure 6.38.

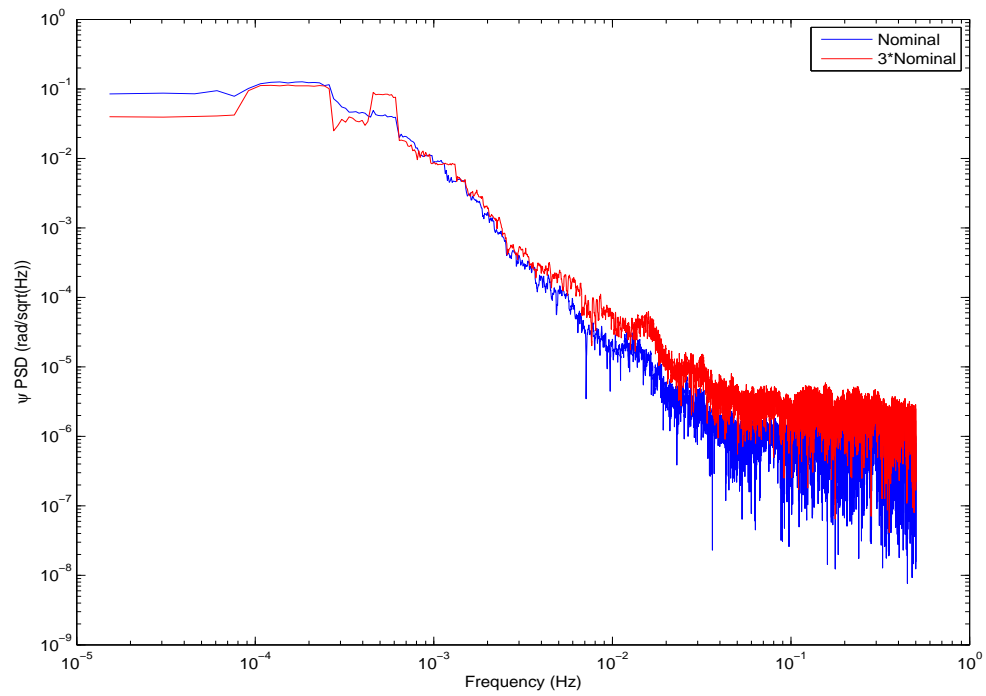


Figure 6.38: Mag1 - Yaw Attitude Angle PSD

The attitude acceleration time response for the white noise magnetometer test is given in Figure 6.39.

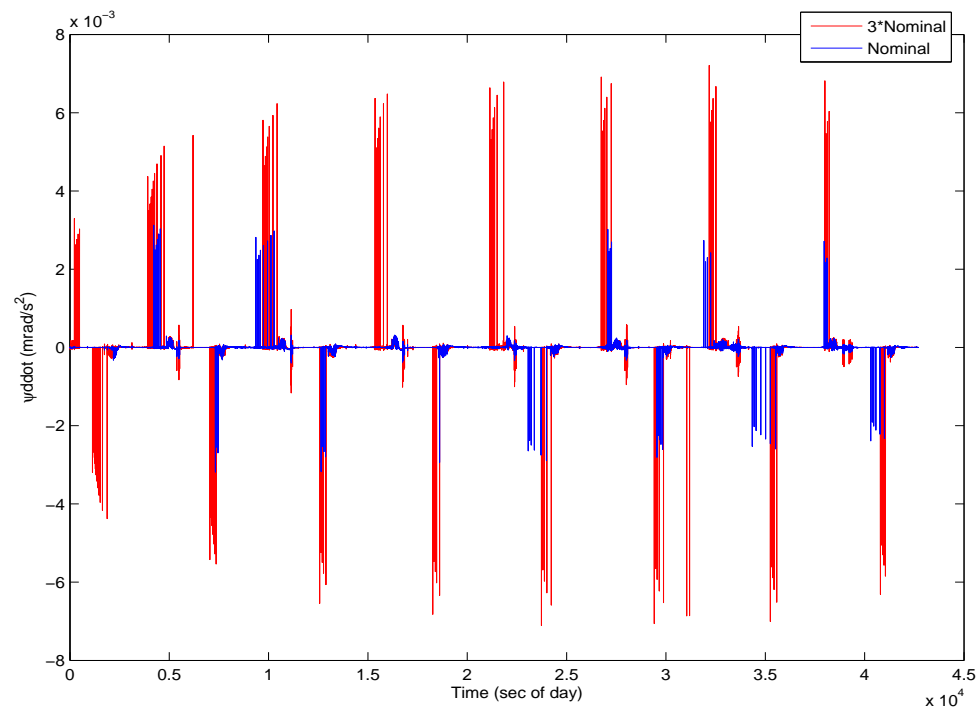


Figure 6.39: Mag1 - Yaw Attitude Acceleration Time Response

The attitude acceleration PSD for the white noise magnetometer test is given in Figure 6.40.

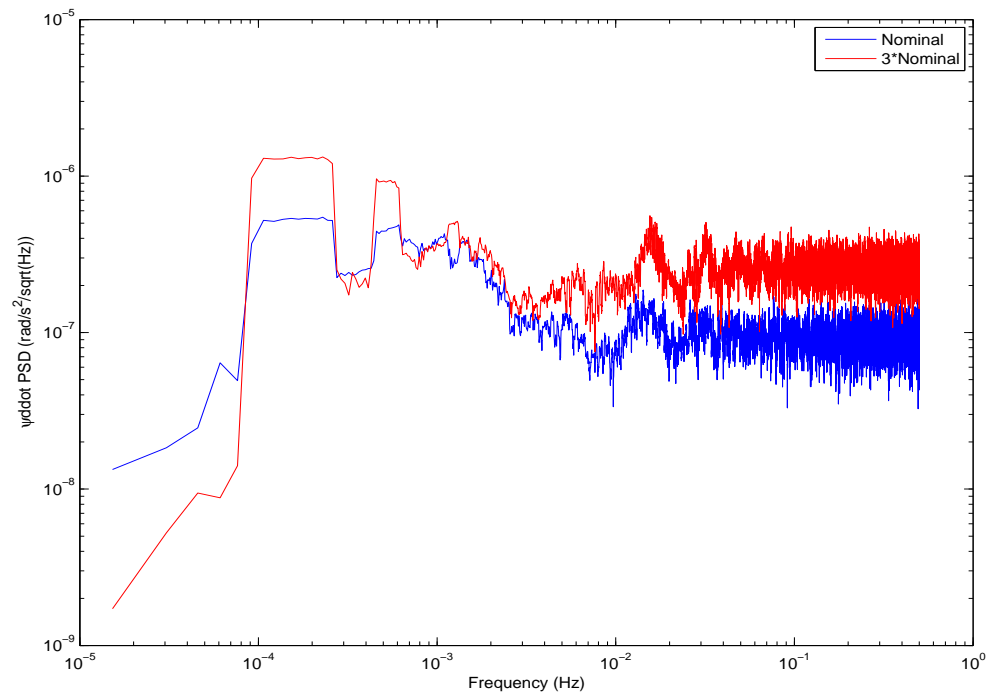


Figure 6.40: Mag1 - Yaw Attitude Acceleration PSD

The attitude angular and acceleration results for roll(ϕ) and pitch(θ) are given in Figures 6.41 and 6.42.

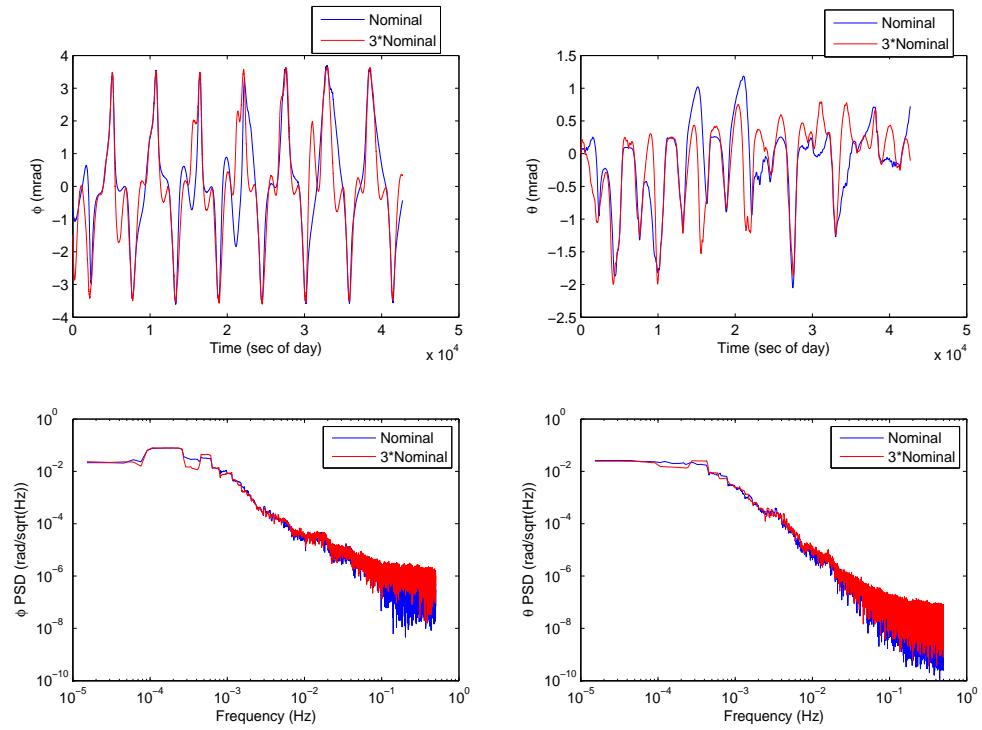


Figure 6.41: Mag1 - Roll and Pitch Attitude Angle Time Response

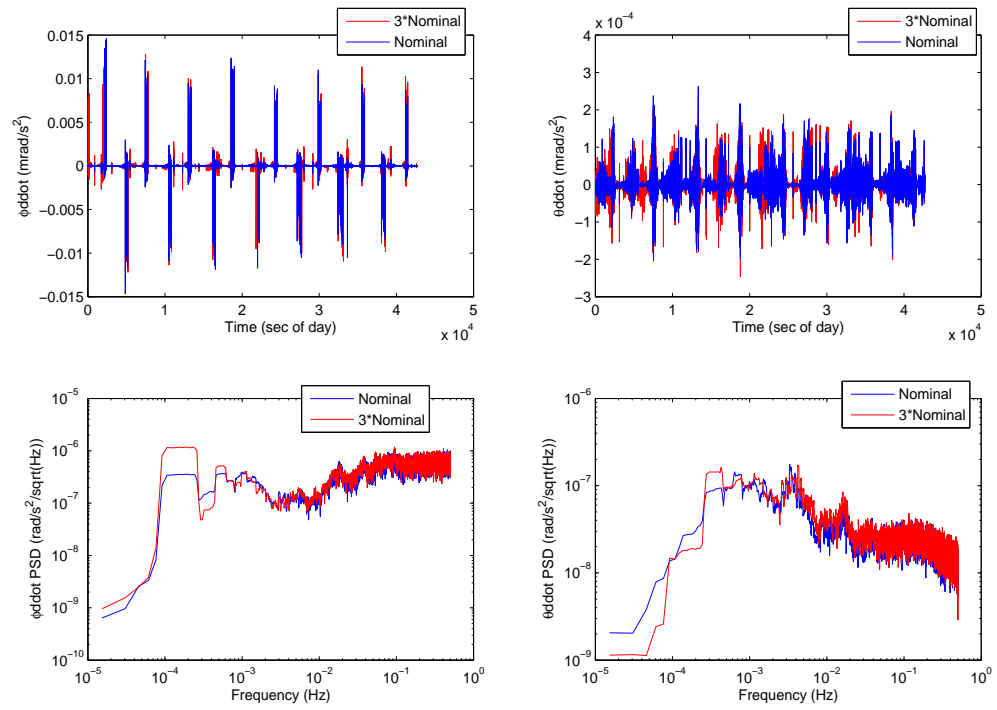


Figure 6.42: Mag1 - Roll and Pitch Attitude Angle Time Response

6.3.2 Mag2

The attitude angle time response for the magnetometer bias test is given in Figure 6.43.

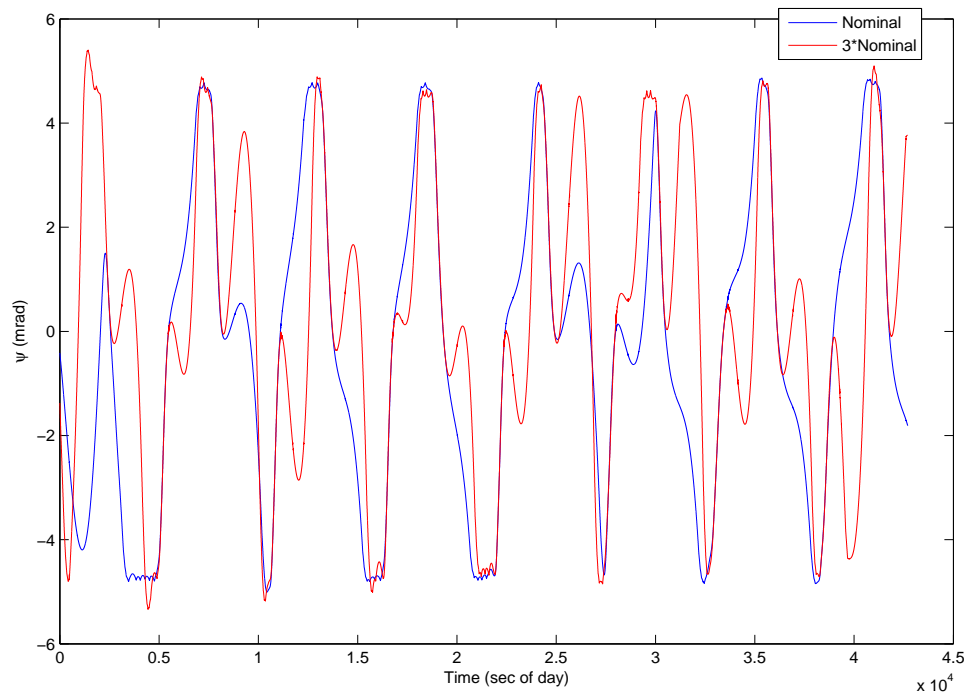


Figure 6.43: Mag2 - Yaw Attitude Angle Time Response

The attitude angle PSD for the magnetometer bias test is given in Figure 6.44.

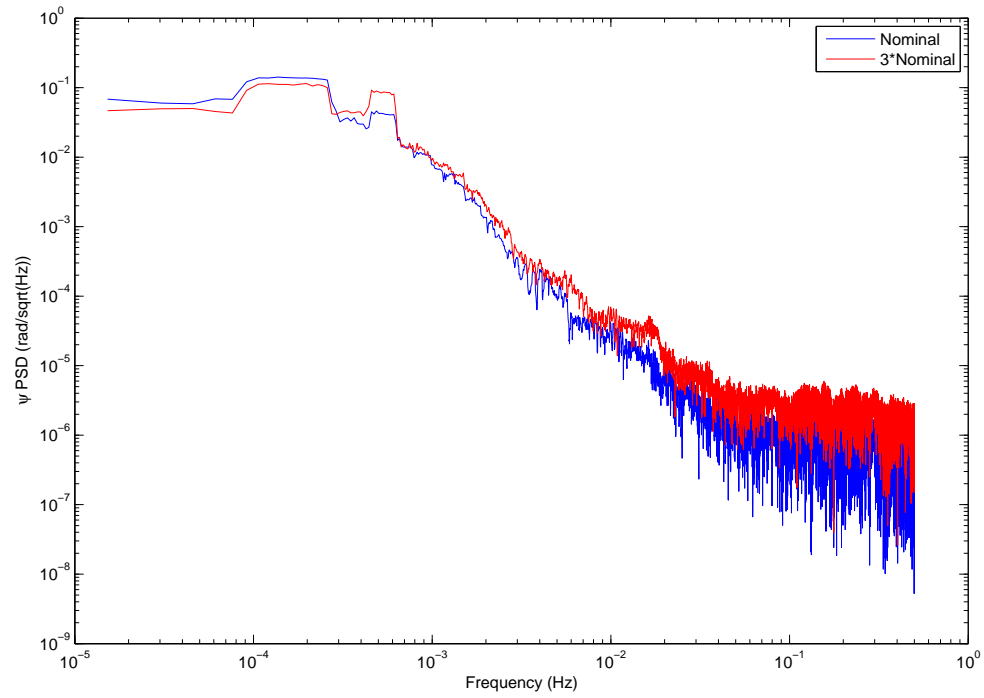


Figure 6.44: Mag2 - Yaw Attitude Angle PSD

The attitude acceleration time response for the magnetometer bias test is given in Figure 6.45.

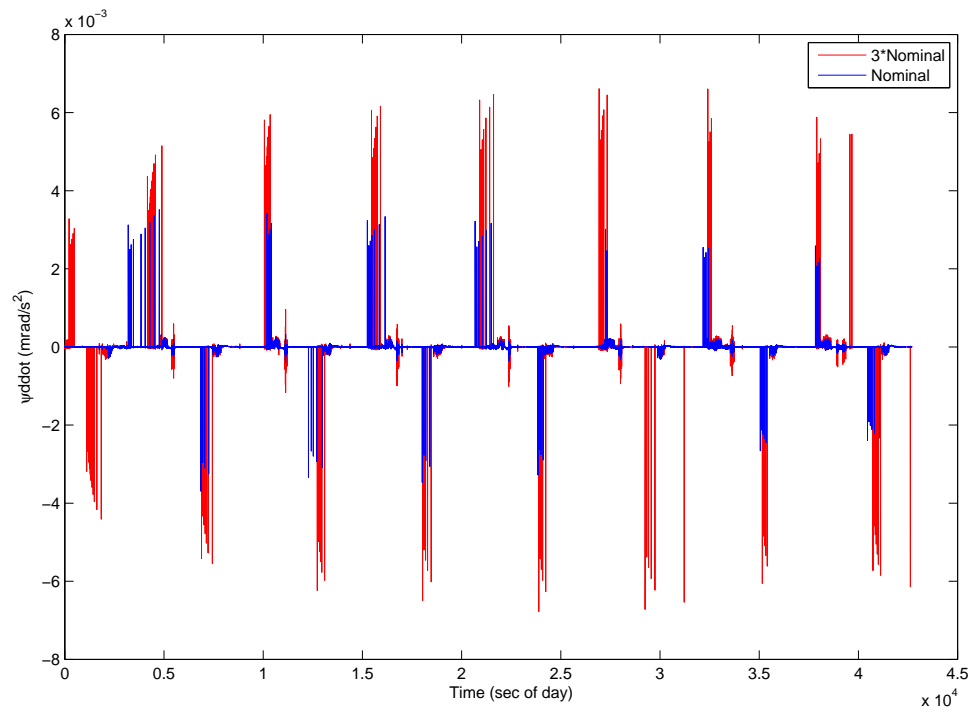


Figure 6.45: Mag2 - Yaw Attitude Acceleration Time Response

The attitude acceleration PSD for the magnetometer bias test is given in Figure 6.46.

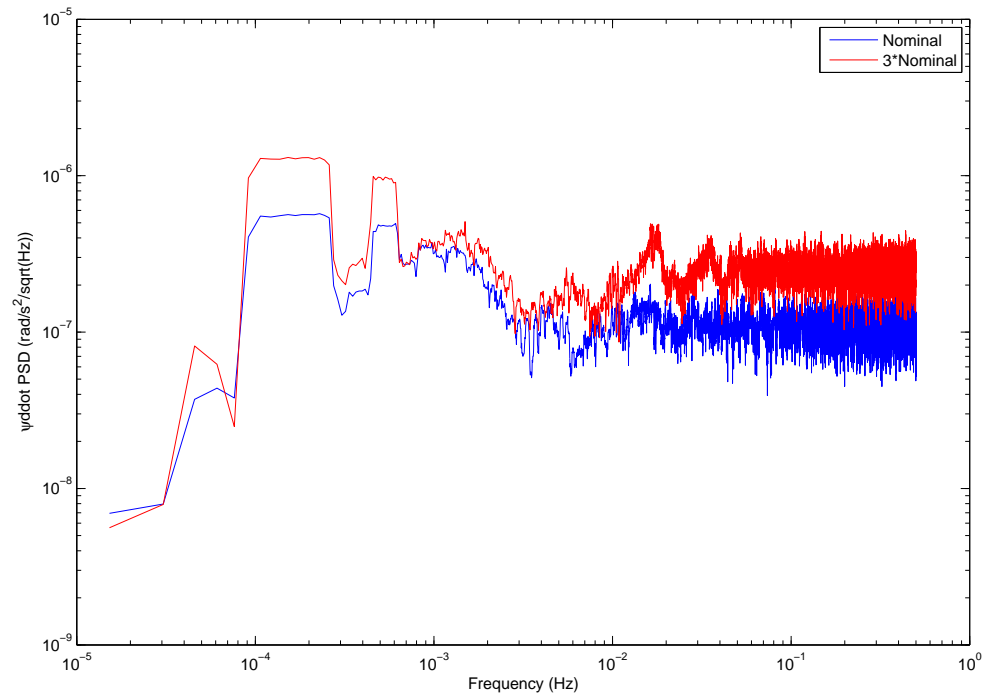


Figure 6.46: Mag2 - Yaw Attitude Acceleration PSD

The attitude angular and acceleration results for roll(ϕ) and pitch(θ) are given in Figures 6.47 and 6.48.

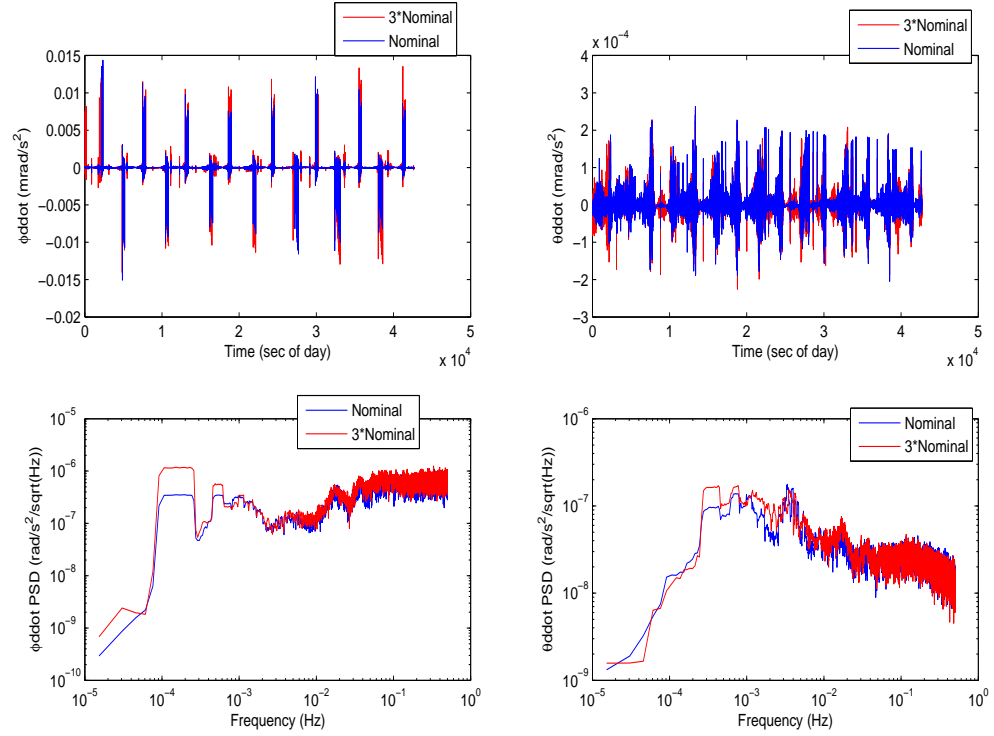


Figure 6.47: Mag2 - Roll and Pitch Attitude Angle Behavior

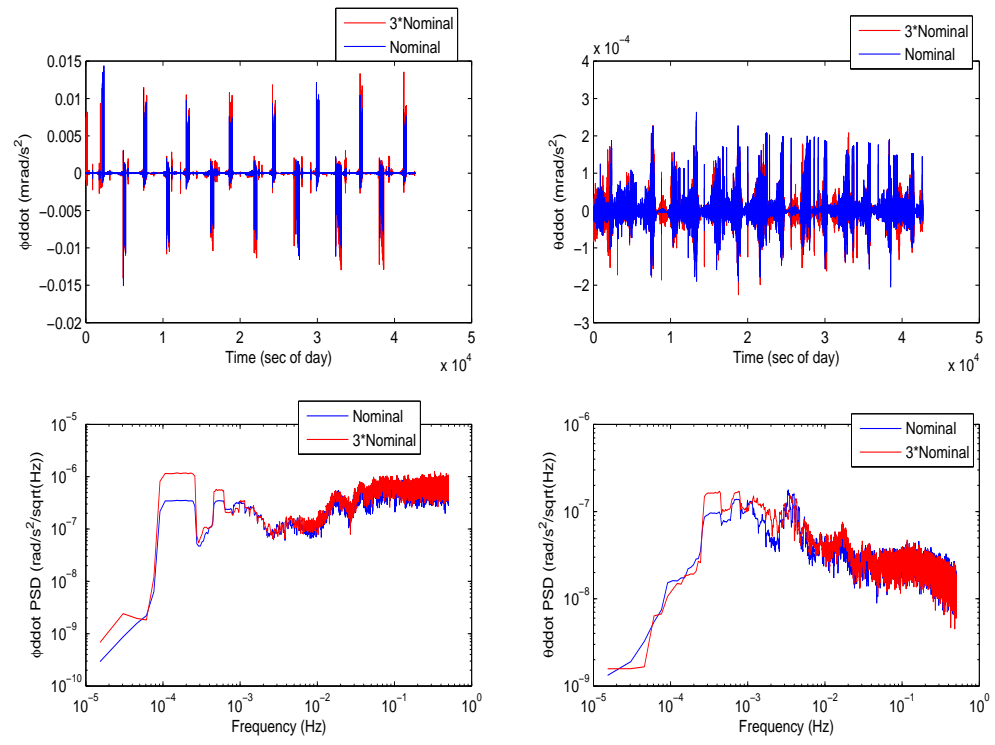


Figure 6.48: Mag2 - Roll and Pitch Attitude Acceleration Behavior

6.3.3 Mag3

The attitude angle time response for the magnetometer misalignment test is given in Figure 6.49.

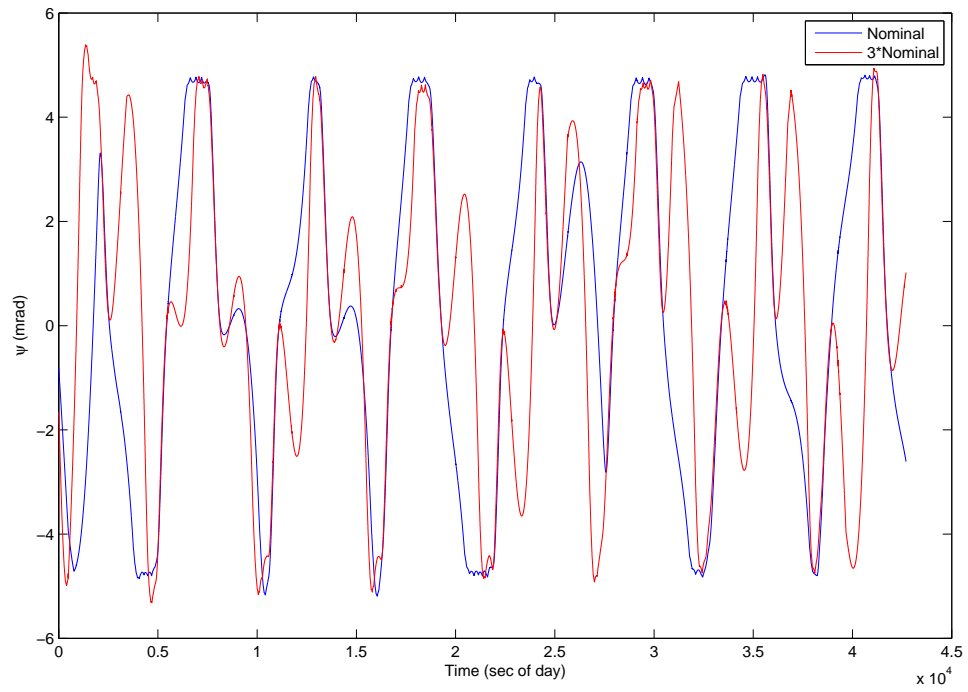


Figure 6.49: Mag3 - Yaw Attitude Angle Time Response

The attitude angle PSD for the magnetometer misalignment test is given in Figure 6.50.

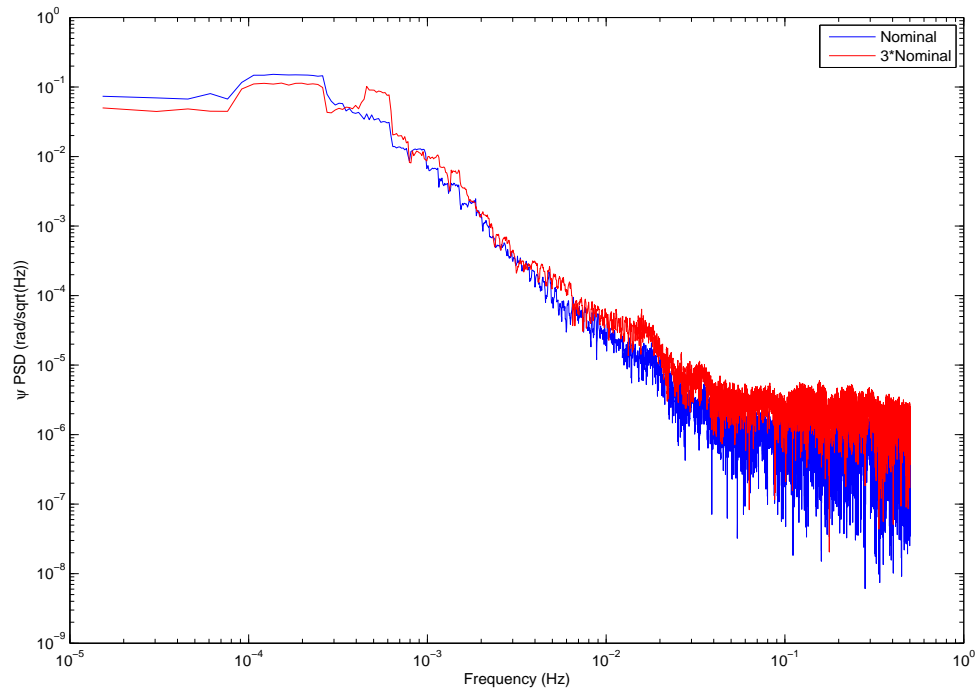


Figure 6.50: Mag3 - Yaw Attitude Angle PSD

The attitude acceleration time response for the magnetometer misalignment test is given in Figure 6.51.

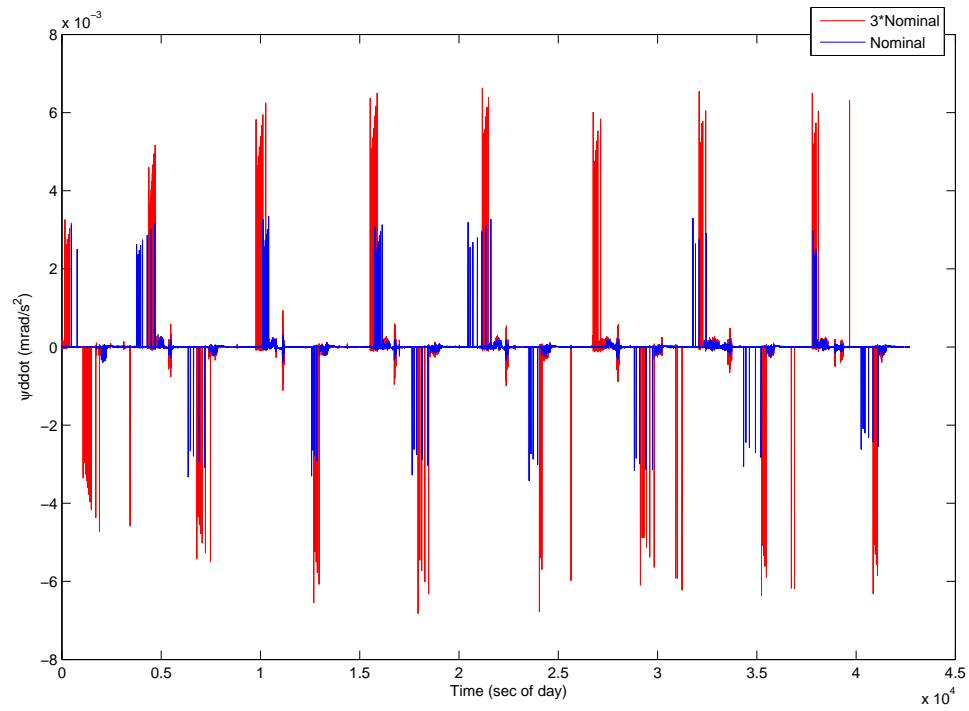


Figure 6.51: Mag3 - Yaw Attitude Acceleration Time Response

The attitude acceleration PSD for the magnetometer misalignment test is given in Figure 6.52.

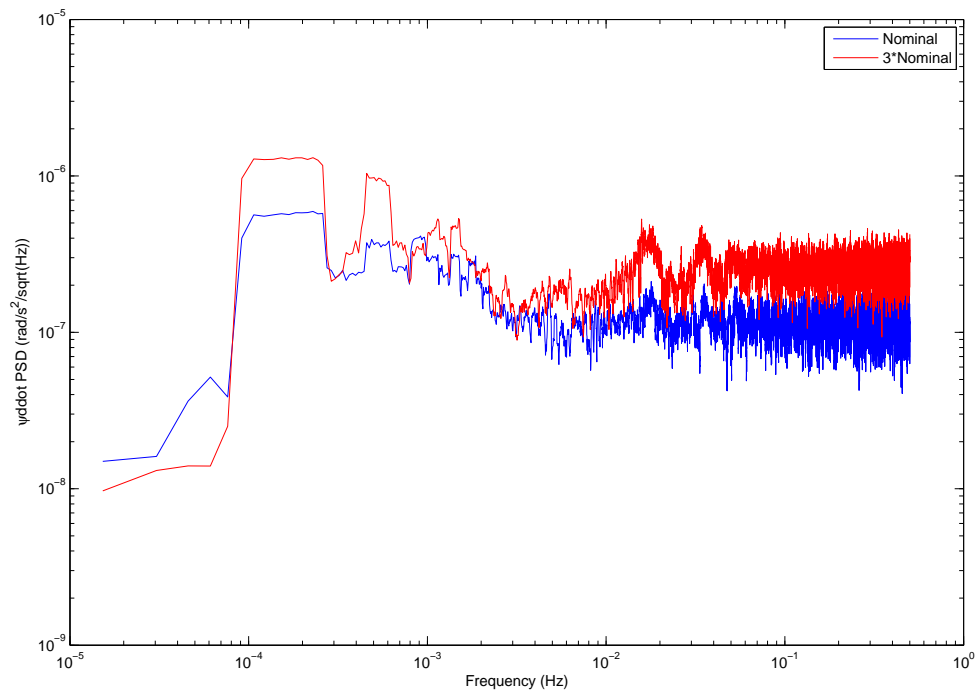


Figure 6.52: Mag3 - Yaw Attitude Acceleration PSD

The attitude angular and acceleration results for roll(ϕ) and pitch(θ) are given in Figures 6.53 and 6.54.

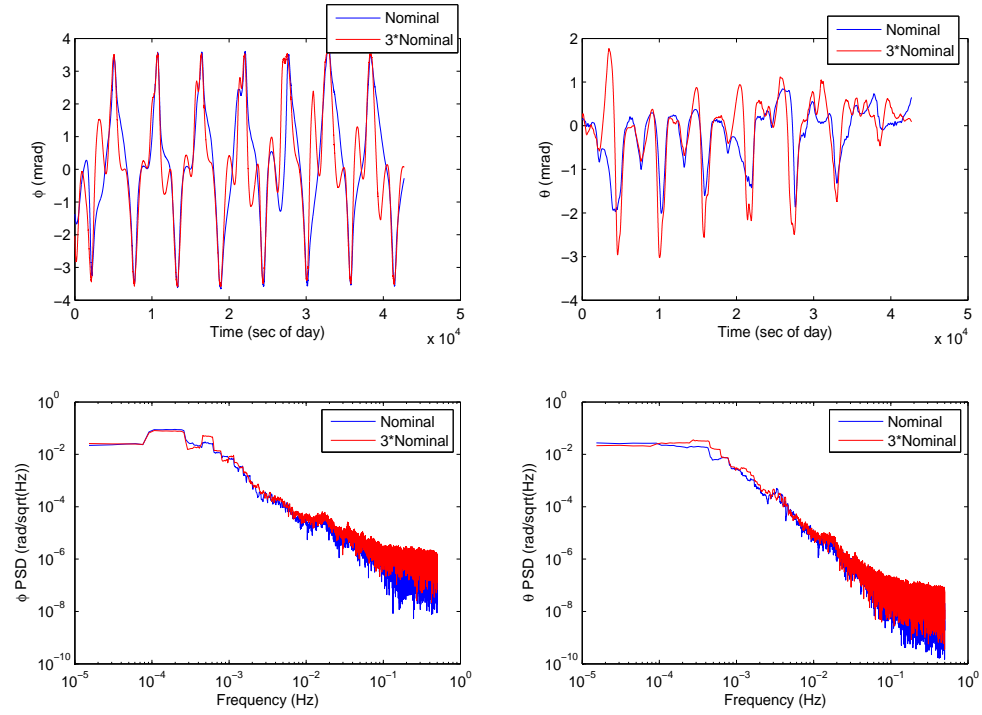


Figure 6.53: Mag3 - Roll and Pitch Attitude Angle Behavior

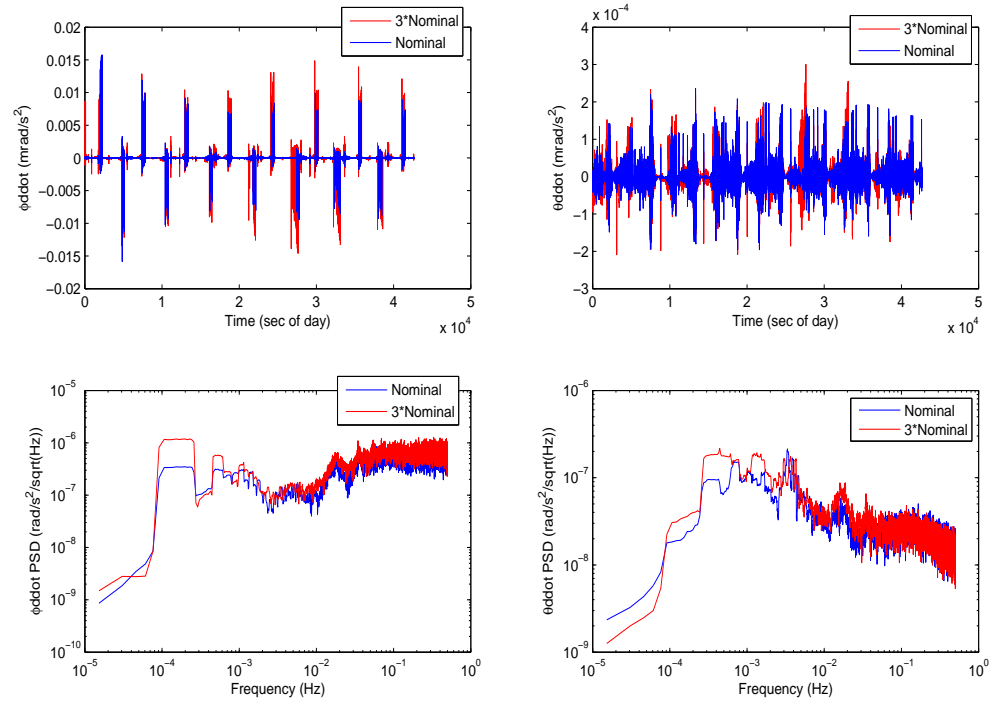


Figure 6.54: Mag3 - Roll and Pitch Attitude Acceleration Behavior

6.3.4 Magnetometer Implications

The three magnetometer experiments, measurement noise, bias, and misalignment, all produce similar effects on the attitude angular and acceleration behavior. In these experiments, the value of the magnetic field measurement used in the science magnetic control process is perturbed from its actual state. The magnetic field data is used both in construction of the electrical moment control, generated by the torque rods, and the generation of control actuation delivered to the spacecraft dynamics [11].

Consistent trends are seen with regards to the acceleration response. As an example, consider Mag2, in Figure 6.45. Imperfections in the magnetic field measurement perturb the magnetic control exerted on the spacecraft from the torque rods. However, the resulting effect on deadband excursions causes the thruster firing magnitudes to increase. This is reflected in the acceleration PSD, given in Figure 6.46. Low frequency amplifications are observed as a result of magnetic imperfection magnification. The range of these increases is 100-200 μHz and 400-500 μHz ranges. These are characteristic frequencies from which the thruster pulses operate. This behavior was also observed in the star camera misalignment experiment. Changes are also seen in higher frequency PSD, reflective of the magnetic torquer behavior. These occur in the 10-20 mHz range.

The resulting effect on angular behavior is a change in the periodicity of the deadband excursion. This is seen in Figure 6.43. This causes the angular PSD to increase at a frequency band between 400-600 μHz . These results are

similar for roll(ϕ) and yaw(ψ). For pitch(ϕ), the magnetic control authority is high due to the alignment of the Earth magnetic field. This allows the amount of thruster firings to be least in this axis. As seen from Figures 6.47 and 6.48, there is no significant detrimental effect on the pitch attitude, but pitch acceleration does increase in the 300-500 μHz range, slightly different than the other axes. In addition, it is important to note that the trend of the magnetic actuation is dictated according to the deadband excursion period and the magnetic field variation. This results in excitations of pitch acceleration around 3-5 mHz and 20 mHz. The former of these has been observed in telemetry [19].

The major finding of these results is that magnetic perturbations cannot be de-coupled from thruster effects. Not only do imperfections in the magnetic field measurement affect the torque rod actuation, the resulting uncertainty on the angular response causes the thruster behavior to increase its magnitude as a form of compensation. This has ramifications with regards to thruster propellant use. However, another notable result is that magnetometer imperfections do not have sizable effect on the modeled attitude angle data quality. In other words, the attitude angle plots in Figures 6.37, 6.43, and 6.49 show the angular deviations remaining within previously set deadbands.

The only parameter affected is the periodicity with which these excursions occur. The quality of the angular data is still high, as seen in the minimal effects on the angular PSD results, shown in Figures 6.38, 6.44, and 6.50. The overall sensitivity of the magnetometer tests, therefore, is less when

compared with star camera experiments. As mentioned in the star camera results, potential future experiments can examine if magnetic non-idealities are exacerbated in the presence of star camera measurement noise.

6.4 Thruster Tests

Two experiments are conducted for the thrusters, one for instrument misalignment and one for actuator misfire.

6.4.1 Th1

The attitude angle time response for the thruster misalignment test is given in Figure 6.55.

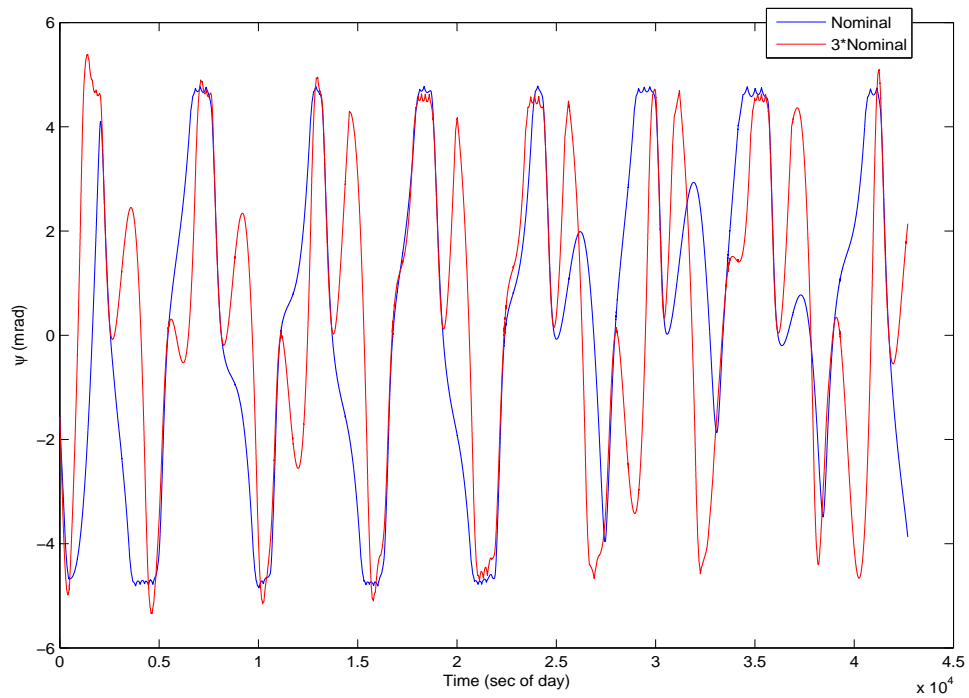


Figure 6.55: Th1 - Yaw Attitude Angle Time Response

The attitude angle PSD for the thruster misalignment test is given in Figure 6.56.

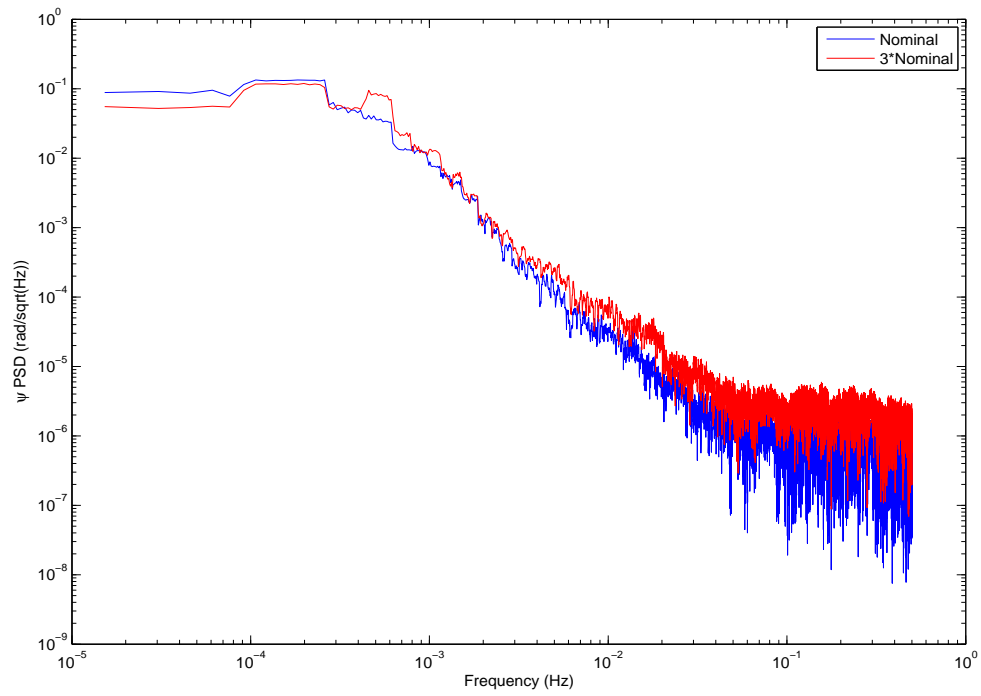


Figure 6.56: Th1 - Yaw Attitude Angle PSD

The attitude acceleration time response for the thruster misalignment test is given in Figure 6.57.

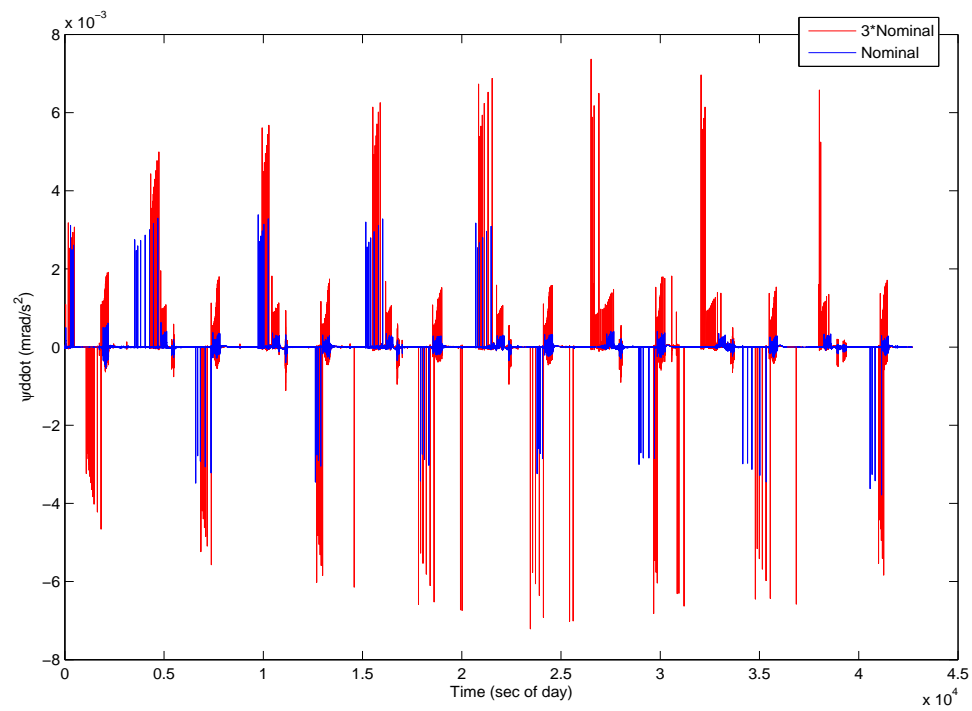


Figure 6.57: Th1 - Yaw Attitude Acceleration Time Response

The attitude acceleration PSD for the thruster misalignment test is given in Figure 6.58.

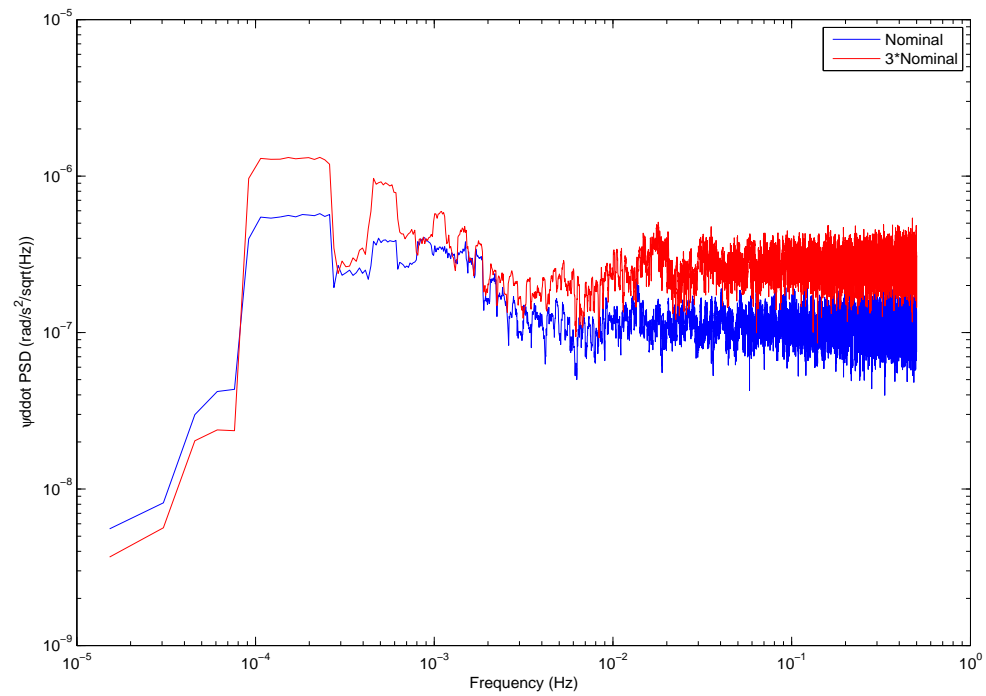


Figure 6.58: Th1 - Yaw Attitude Acceleration PSD

The attitude angular and acceleration results for roll(ϕ) and pitch(θ) are given in Figures 6.59 and 6.60.

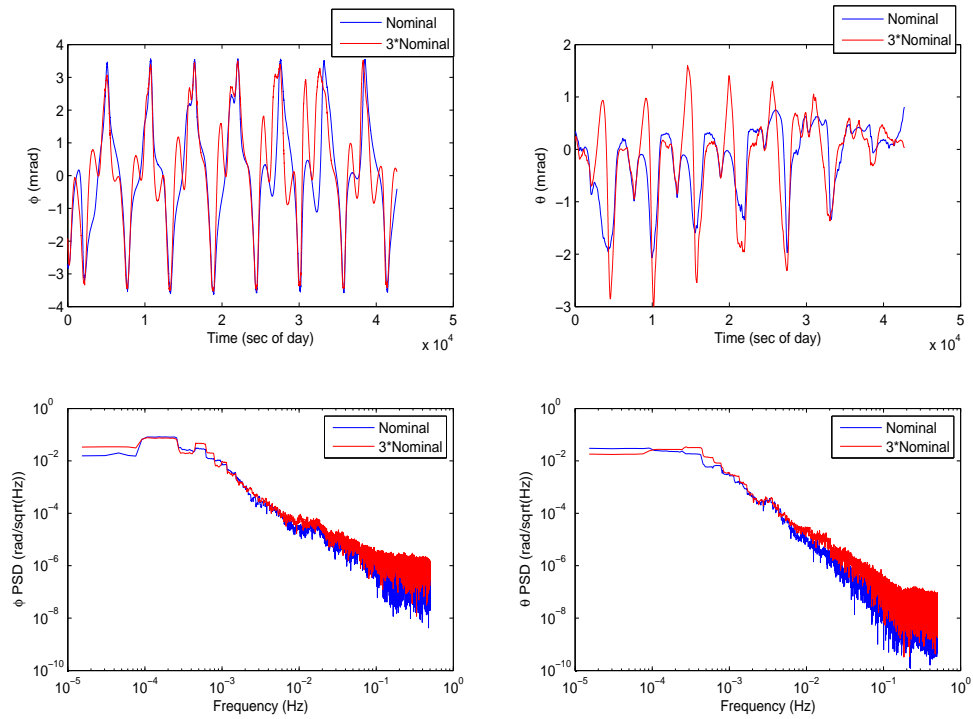


Figure 6.59: Th1 - Roll and Pitch Attitude Angle Behavior

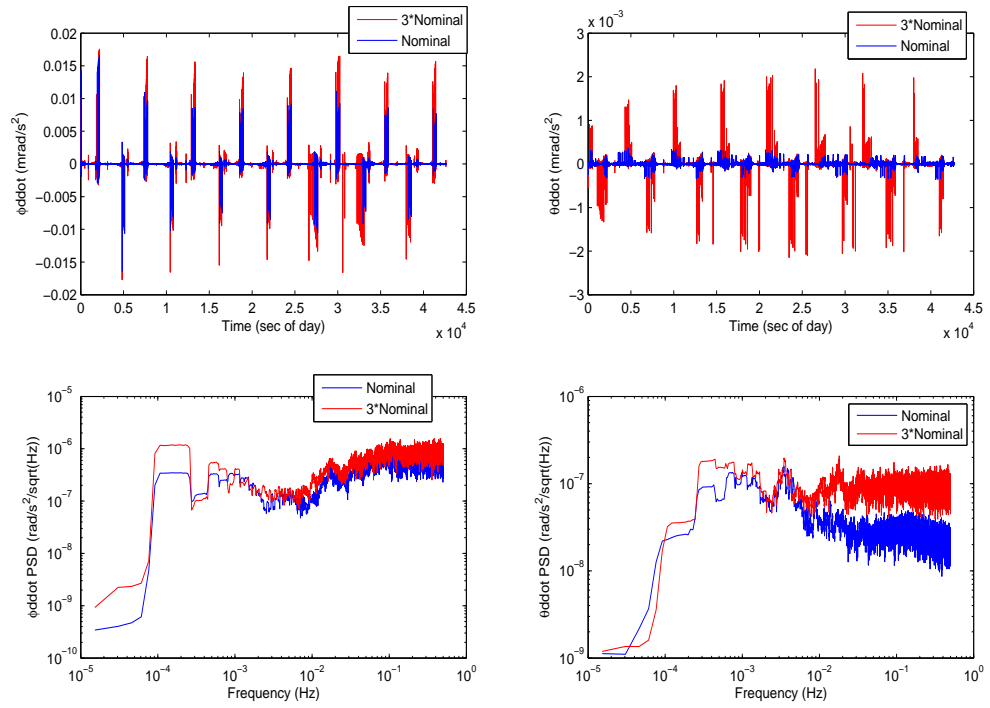


Figure 6.60: Th1 - Roll and Pitch Attitude Acceleration Behavior

6.4.2 Th2

The attitude angle time response for the thruster misfire test is given in Figure 6.61.

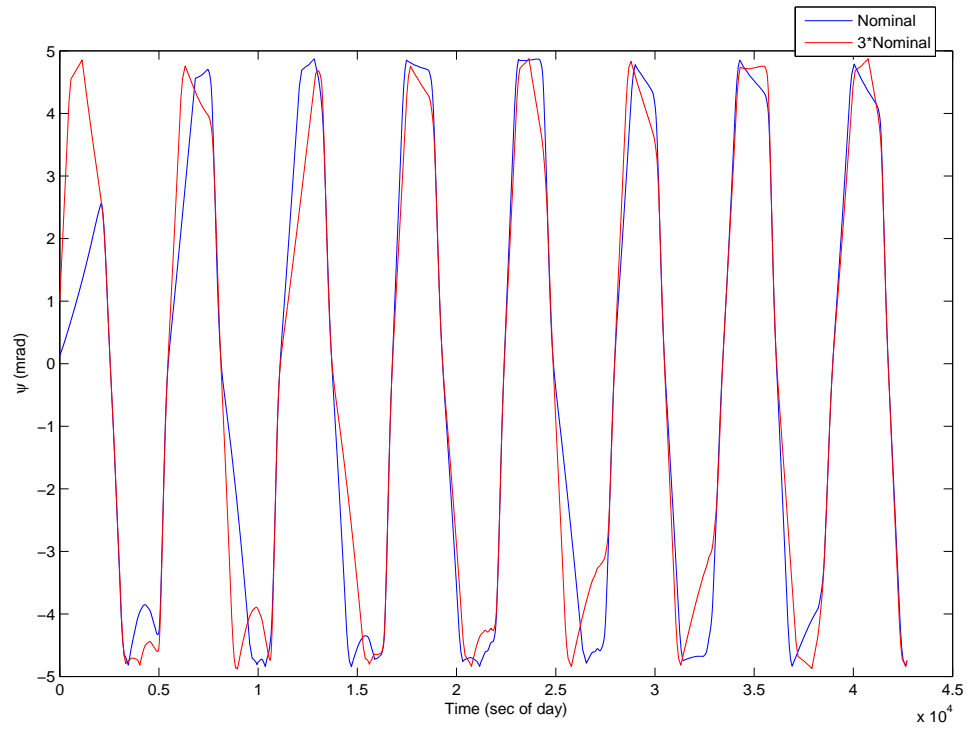


Figure 6.61: Th2 - Yaw Attitude Angle Time Response

The attitude angle PSD for the thruster misfire test is given in Figure 6.62.

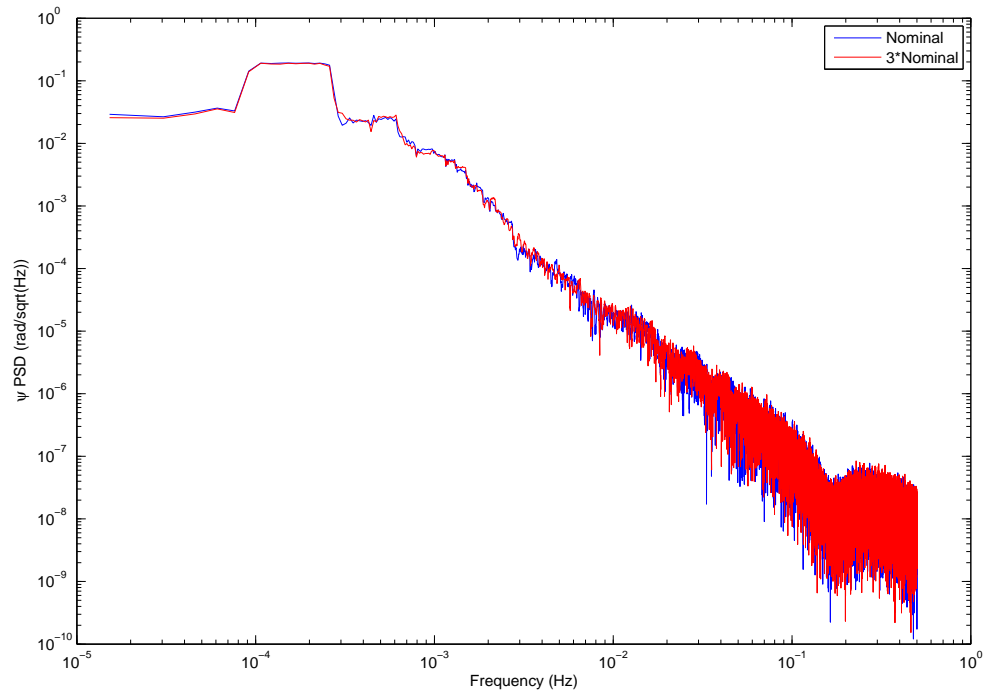


Figure 6.62: Th2 - Yaw Attitude Angle PSD

The attitude acceleration time response for the thruster misfire test is given in Figure 6.63.

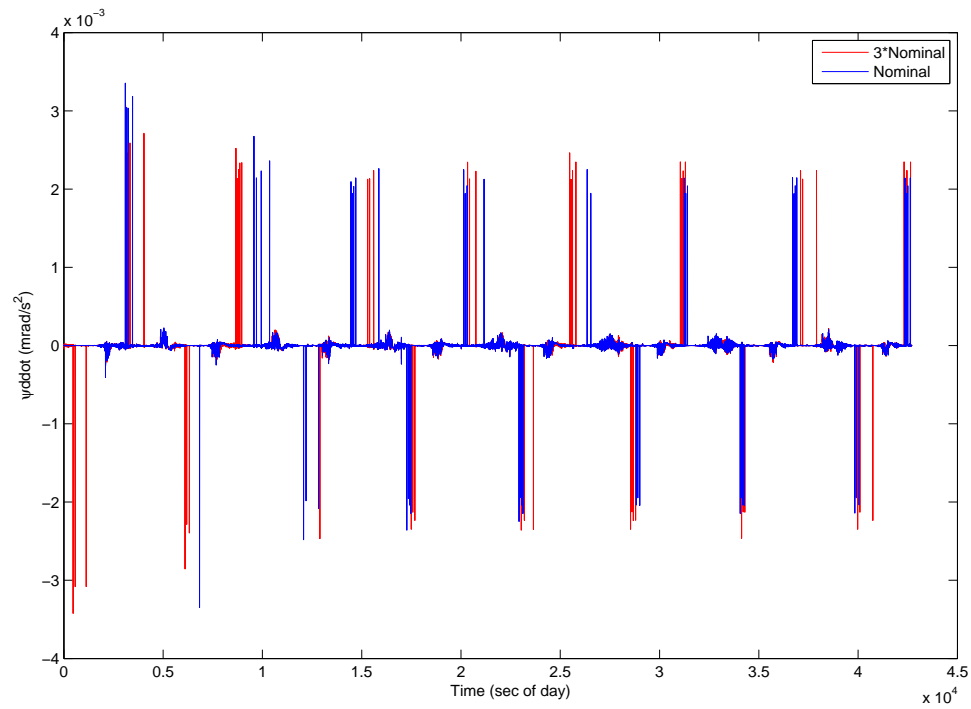


Figure 6.63: Th2 - Yaw Attitude Acceleration Time Response

The attitude acceleration PSD for the thruster misfire test is given in Figure 6.64.

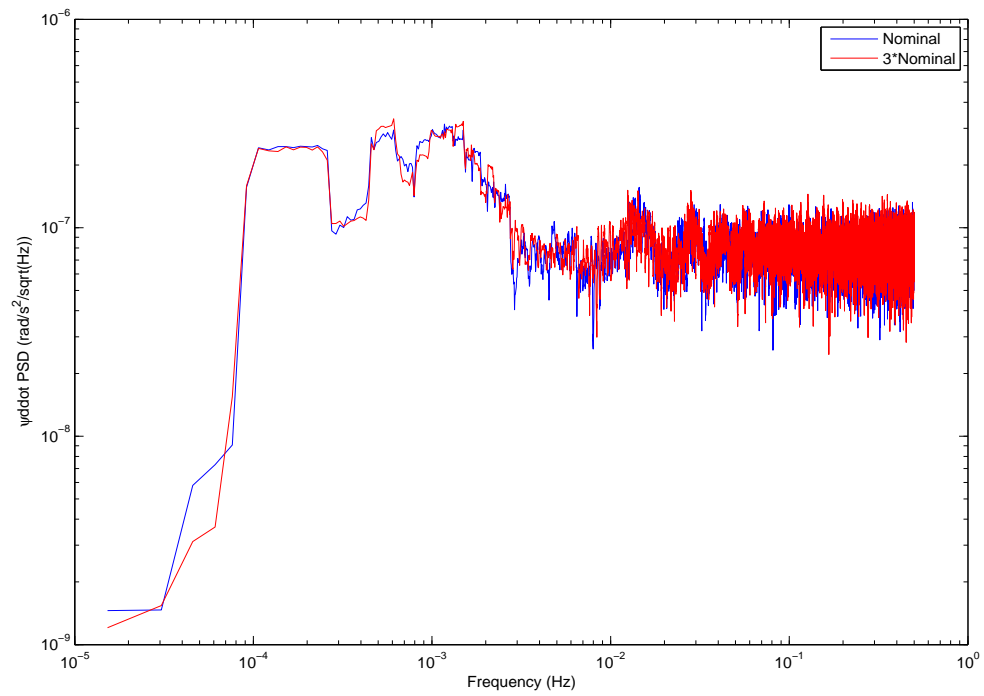


Figure 6.64: Th2 - Yaw Attitude Acceleration PSD

The attitude angular and acceleration results for roll(ϕ) and pitch(θ) are given in Figures 6.65 and 6.66.

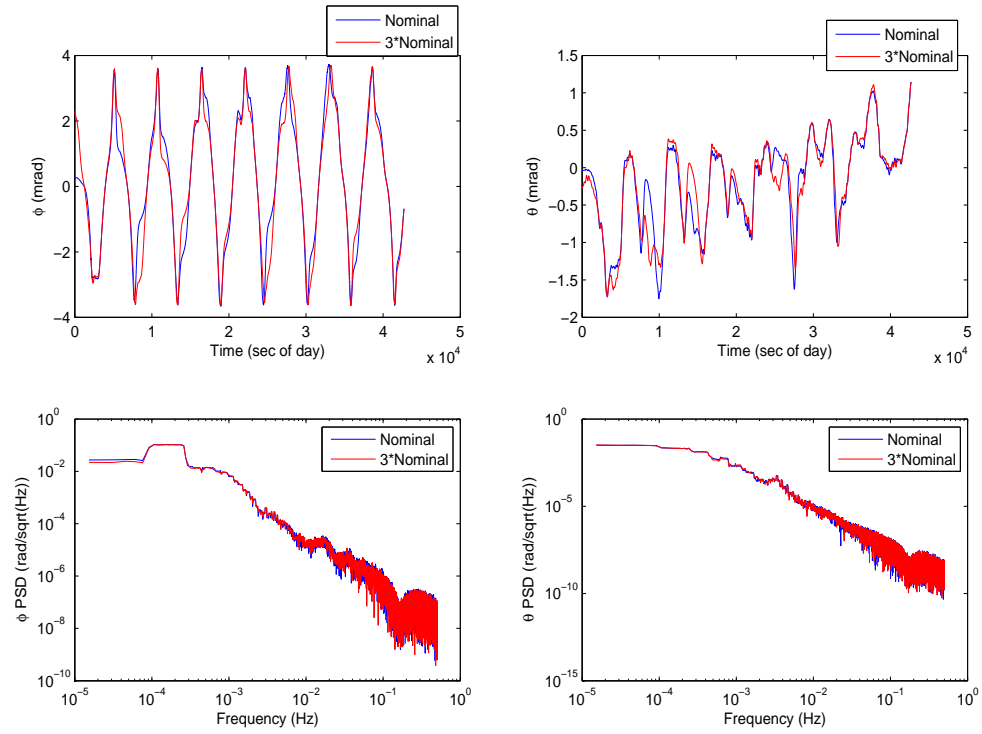


Figure 6.65: Th2 - Roll and Pitch Attitude Angle Behavior

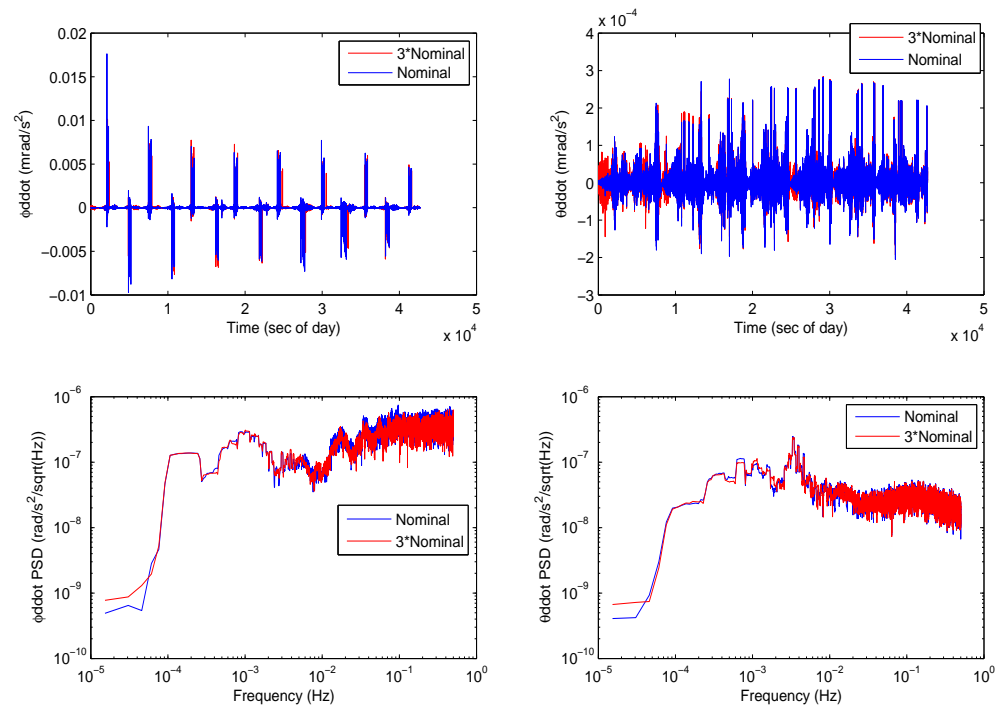


Figure 6.66: Th2 - Roll and Pitch Attitude Acceleration Response

6.4.3 Thruster Implications

The thrusters are the primary actuators for the GRACE control architecture. They contain high control authority in all axes, allowing for fine-pointing control. Since thrusters are used as the primary actuators, they analyze the full control signal output from the PD control law. Whenever the control deadbands are exceeded, the thrusters pulses activate. Since these experiments directly affect the modeled thruster forces, the misalignment and misfire imperfections have causal effects on the control torque history, both delivered to the spacecraft and used in the error estimation scheme.

Despite this configuration, the attitude effects caused by the thruster experiments are very similar to those caused by the magnetometer experiments. First, the modeled attitude is much more significantly affected by thruster misalignment than by thruster misfire by itself. When the thrusters are misaligned, the resulting force delivered to the spacecraft is not solely in one axis, as described in Table 5.11. Instead, forces are delivered in all three axis, causing the cross-axis disturbance torque to increase. The misalignment can be manifested as a rotation of the nominal force configuration in Table 5.11. The experimental configuration selected for the thruster misalignment experiment is given in Equation 5.15. This orientation was chosen after trial and error. This result to produced the greatest cross-axis disturbance for a given rotation cone angle.

From the attitude acceleration plot in yaw(ψ), given in Figure 6.57, the thruster firings magnitudes increase as a result of the misalignment effect.

The acceleration PSD, seen in Figure 6.58, shows that the low frequencies excited during magnetometer tests are magnified by comparable degrees. In addition, the range of high frequencies reflective of magnetic actuations are also amplified by similar degrees. The end result is a periodicity discrepancy in the attitude angle behavior, shown in Figure 6.55. As with the magnetometer tests, the quality of the angular signal is not degraded, and the angular PSD is only slightly increased, as seen in Figure 6.56. In addition, the same range of frequencies is excited, around 400-600 μHz , in the angular PSD. A final remark is made with regards to the pitch(θ) results, shown in Figures 6.59 and 6.60. The misalignment configuration chosen for this experiment causes pitch axis firing to increase more significantly than the other two axes. This is a function of the rotation applied to the thruster firing direction in Table 5.11. In a noise-free environment, it is inferred that cross-axes disturbances caused by thruster misalignments can be predictable if the star camera misalignment direction is known. This is a function of the spacecraft integration process, and will vary for each mission.

The major finding in these results is that thruster non-idealities have very similar effects on attitude performance in comparison to magnetic field perturbations. This is despite the fact that the thruster imperfections are more directly applied to the thruster torque signal. As with the magnetometer experiments, the perturbation to the torque delivered to the spacecraft does not affect the attitude error estimation signal as significantly as the star camera knowledge error. As with the other experiments, it is useful to perform future

tests where the thruster misalignment experiment is analyzed in the presence of star camera noise. Although in a noise free environment, the effect of magnetometer and thruster effects are similar, their behaviors might be different in the presence of star camera measurement noise.

As mentioned in Chapter 1, many standard three-axis stabilized control configurations use reaction wheels as primary actuators, and thrusters are employed as supplementary momentum compensation devices. The constraints related to accelerometer vibration requirements suggest the exclusion of reaction wheels in the GRACE system. However, it was demonstrated that thruster misalignments can excite frequency bands contained in the GRACE scientific process. Disturbances related to other non-idealities can affect thruster firing magnitude, which causes higher propellant use and can reduce the mission lifetime. An important future trade study can examine the relative benefit of using reaction wheels instead of thrusters as primary actuators. Particular attention must be paid to the relative vibration magnitudes induced by the wheels, and whether these actuators more severely amplify angular and acceleration PSD in the GRACE science frequency range. A corollary experiment can examine the relative benefits of thrusters versus magnetic torque rods as supplementary actuators, used for wheel momentum dumping.

6.5 Magnetic Torquer Tests

Two magnetic torquer experiments are conducted, one related to an additive effect caused by residual dipole, and one multiplicative effect caused by instrument misalignment.

6.5.1 Tor1

The attitude angle time response for the residual dipole test is given in Figure 6.67.

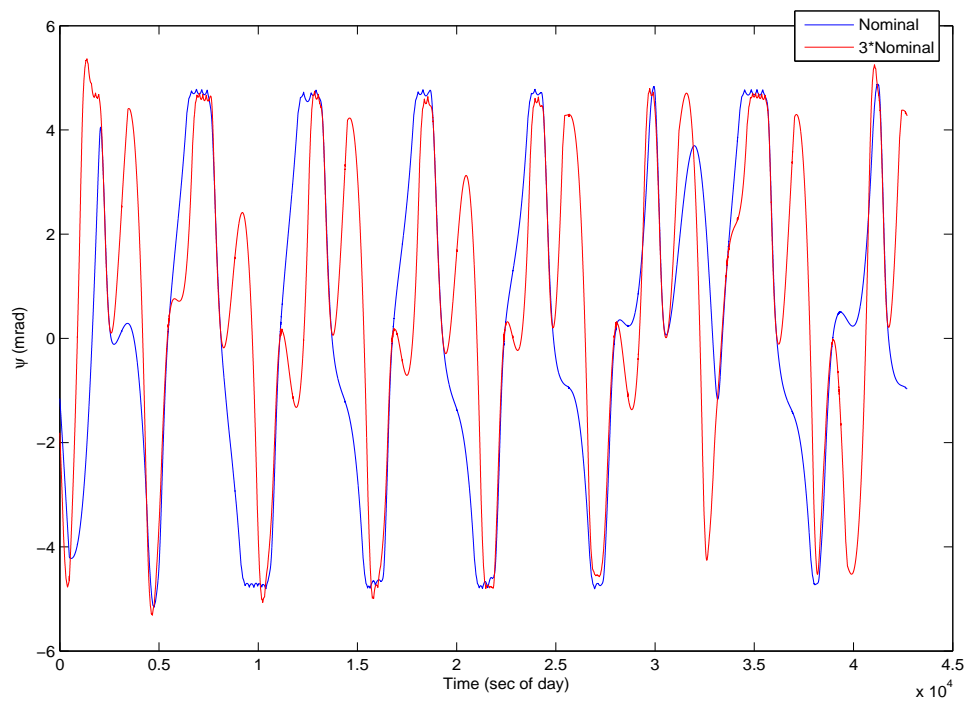


Figure 6.67: Tor1 - Yaw Attitude Angle Time Response

The attitude angle PSD for the residual dipole test is given in Figure 6.68.

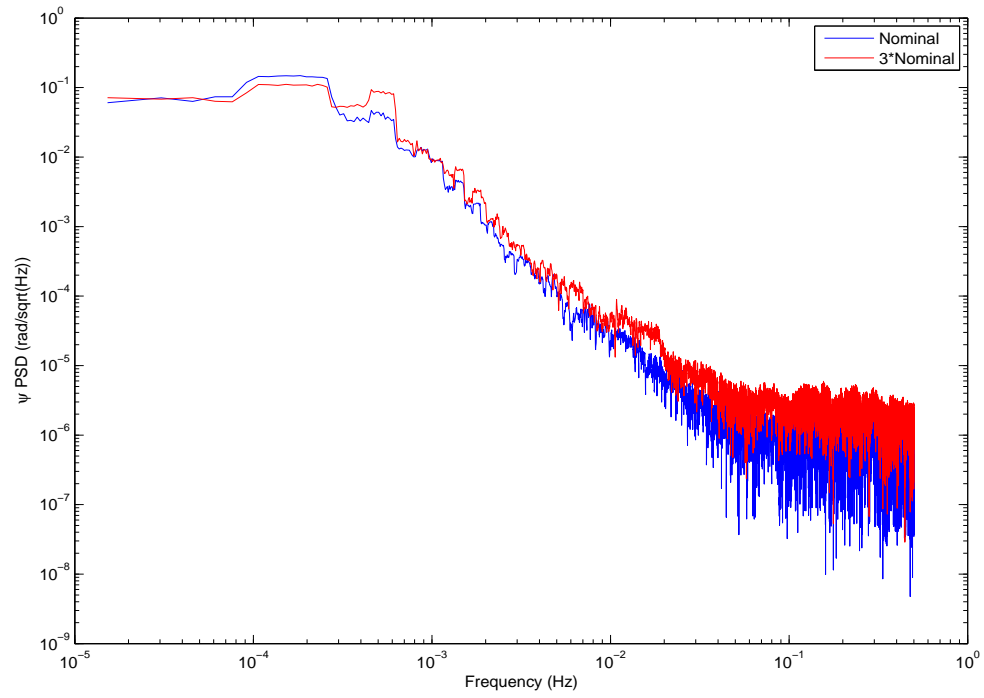


Figure 6.68: Tor1 - Yaw Attitude Angle PSD

The attitude acceleration time response for the residual dipole test is given in Figure 6.69.

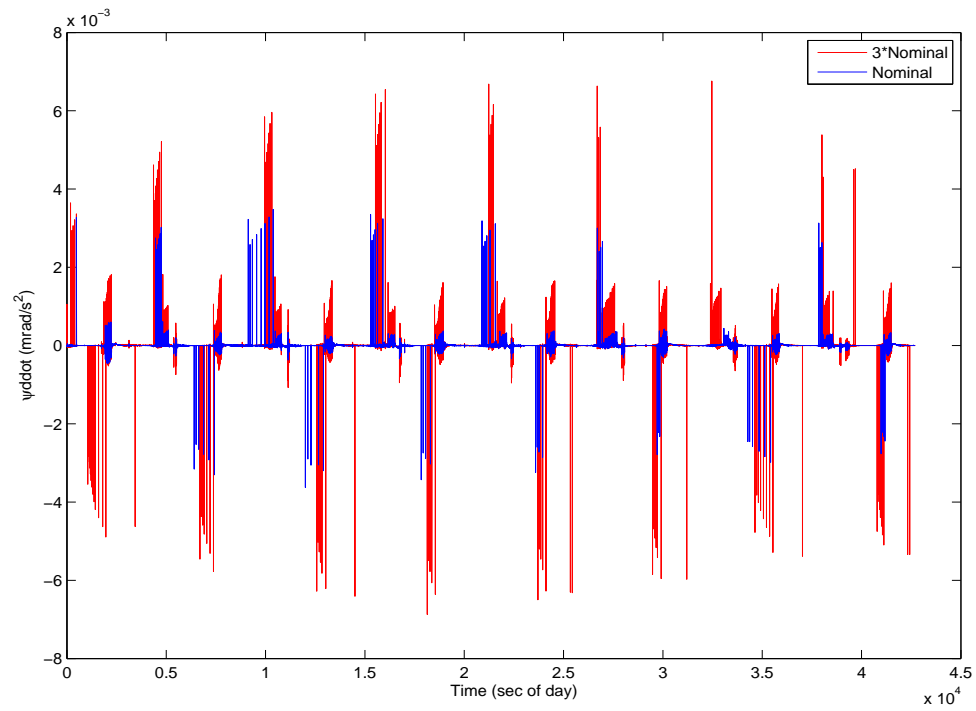


Figure 6.69: Tor1 - Yaw Attitude Acceleration Time Response

The attitude acceleration PSD for the residual dipole test is given in Figure 6.70.

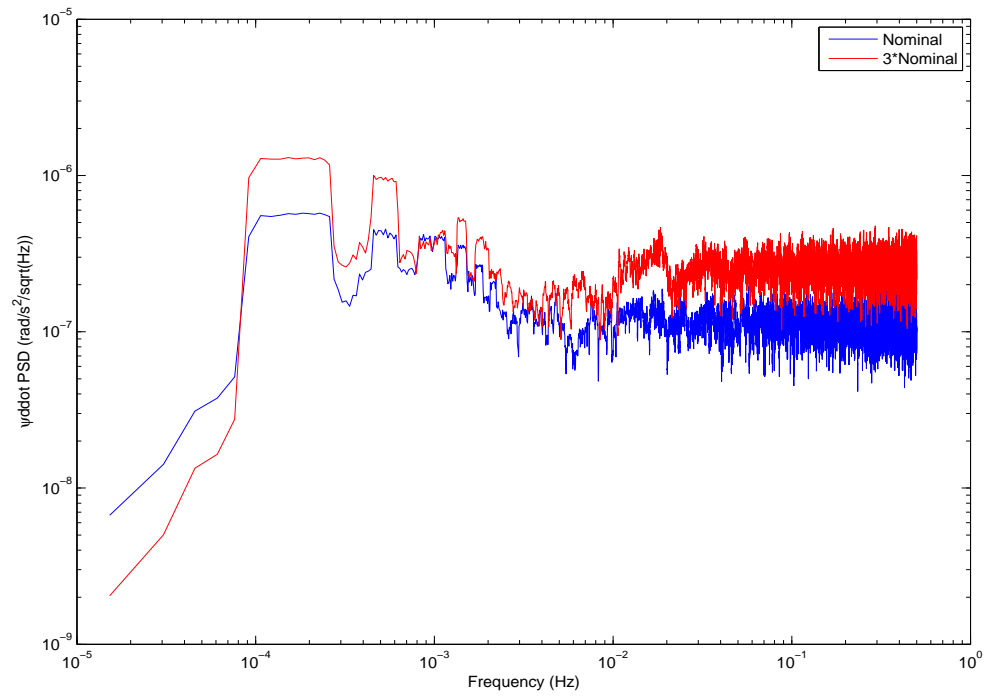


Figure 6.70: Tor1 - Yaw Attitude Acceleration PSD

The attitude angular and acceleration results for roll(ϕ) and pitch(θ) are given in Figures 6.71 and 6.72.

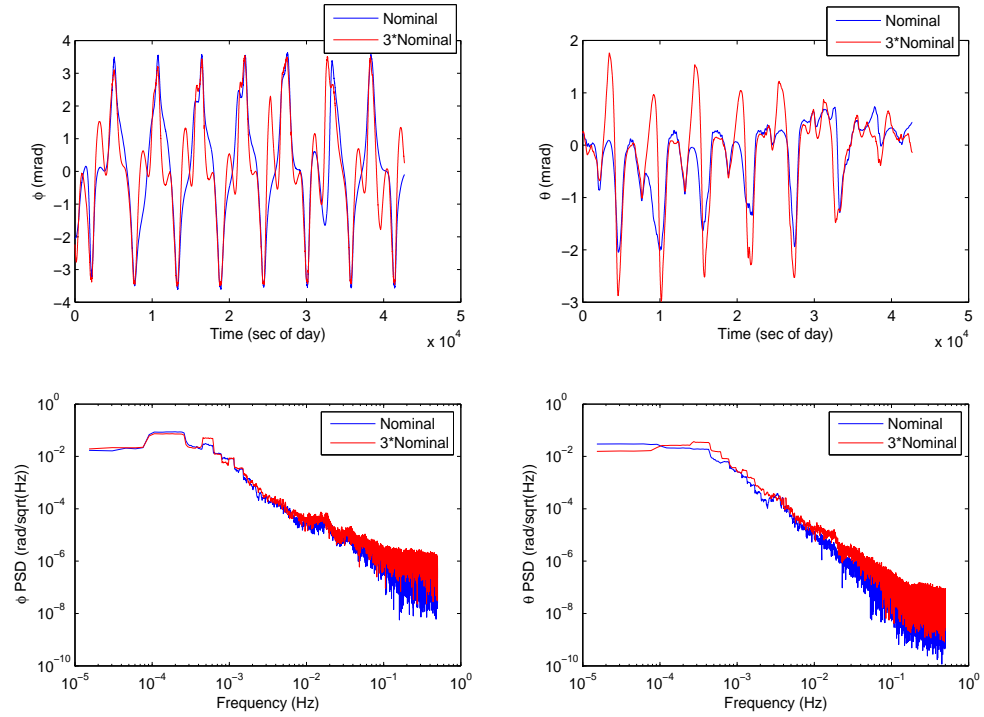


Figure 6.71: Tor1 - Roll and Pitch Attitude Angle Behavior

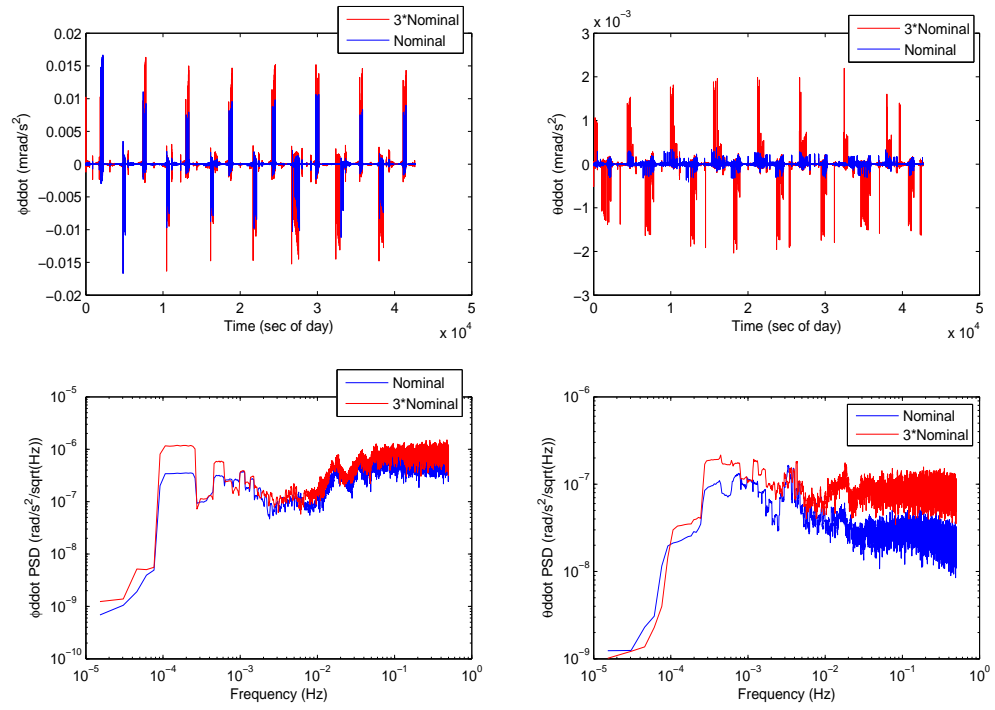


Figure 6.72: Tor1 - Roll and Pitch Attitude Acceleration Behavior

6.5.2 Tor2

The attitude angle time response for the magnetic torquer misalignment test is given in Figure 6.73.

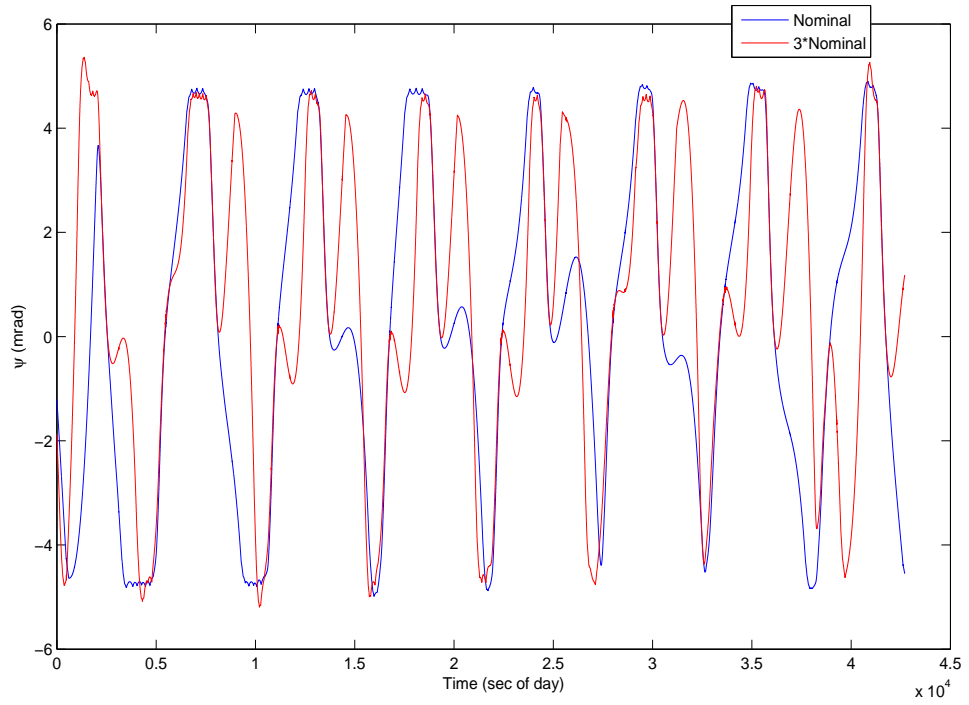


Figure 6.73: Tor2 - Yaw Attitude Angle Time Response

The attitude angle PSD for the magnetic torquer misalignment test is given in Figure 6.74.

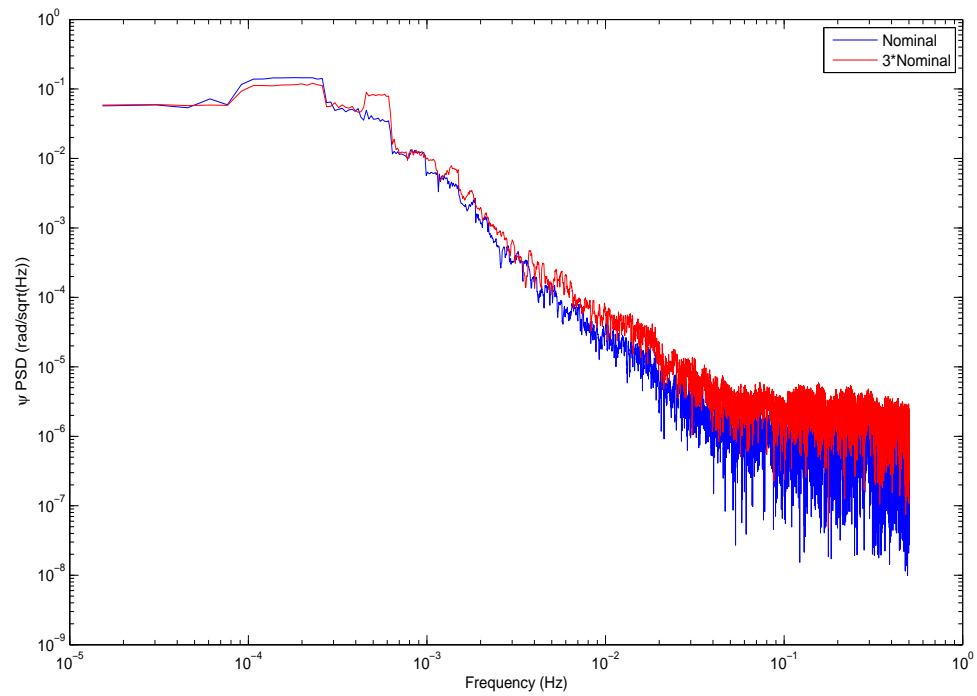


Figure 6.74: Tor2 - Yaw Attitude Angle PSD

The attitude acceleration time response for the magnetic torquer misalignment test is given in Figure 6.75.

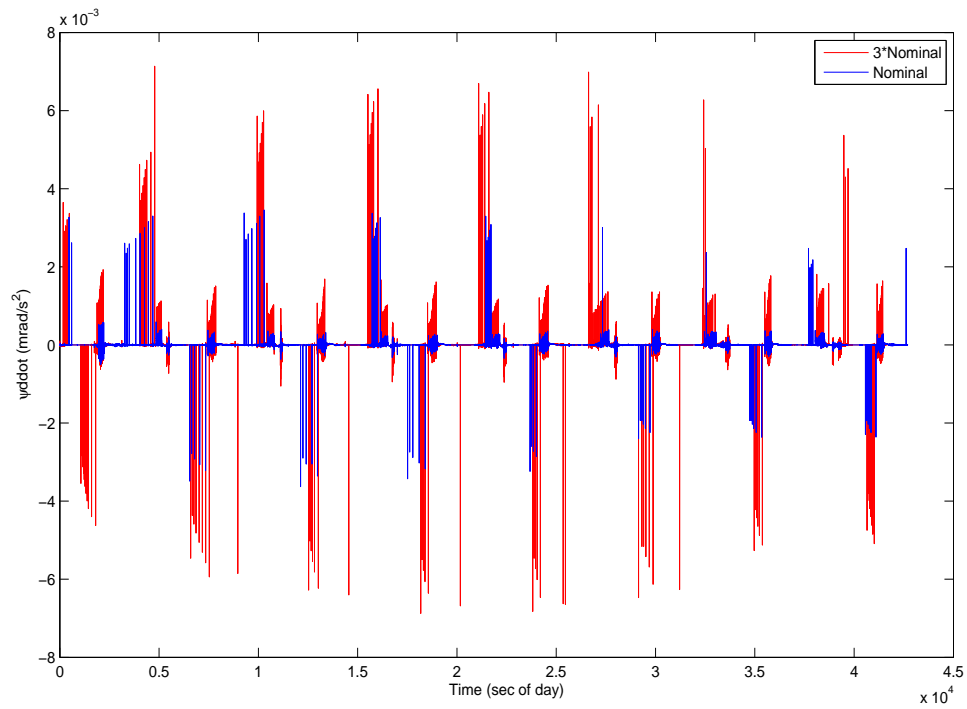


Figure 6.75: Tor2 - Yaw Attitude Acceleration Time Response

The attitude acceleration PSD for the magnetic torquer misalignment test is given in Figure 6.76.

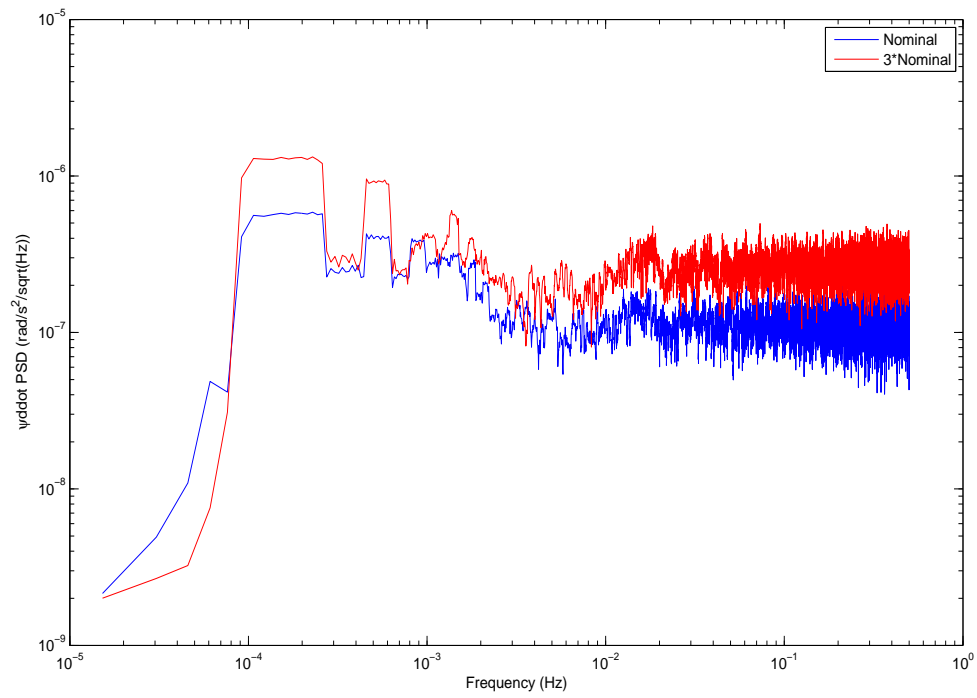


Figure 6.76: Tor2 - Yaw Attitude Acceleration PSD

The attitude angular and acceleration results for roll(ϕ) and pitch(θ) are given in Figures 6.77 and 6.78.

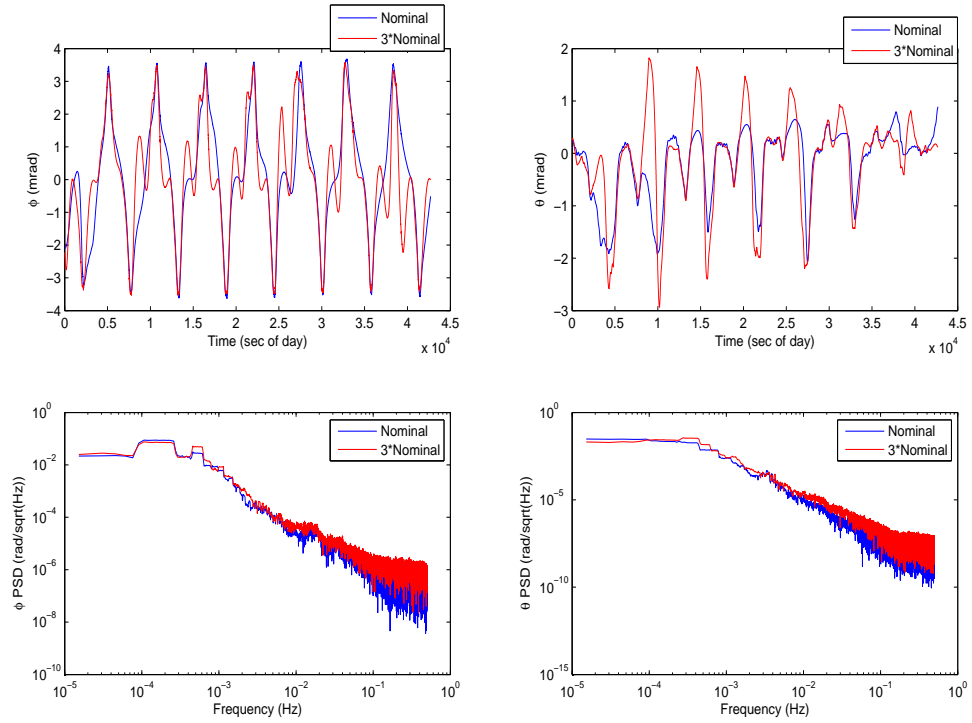


Figure 6.77: Tor2 - Roll and Pitch Attitude Angle Behavior

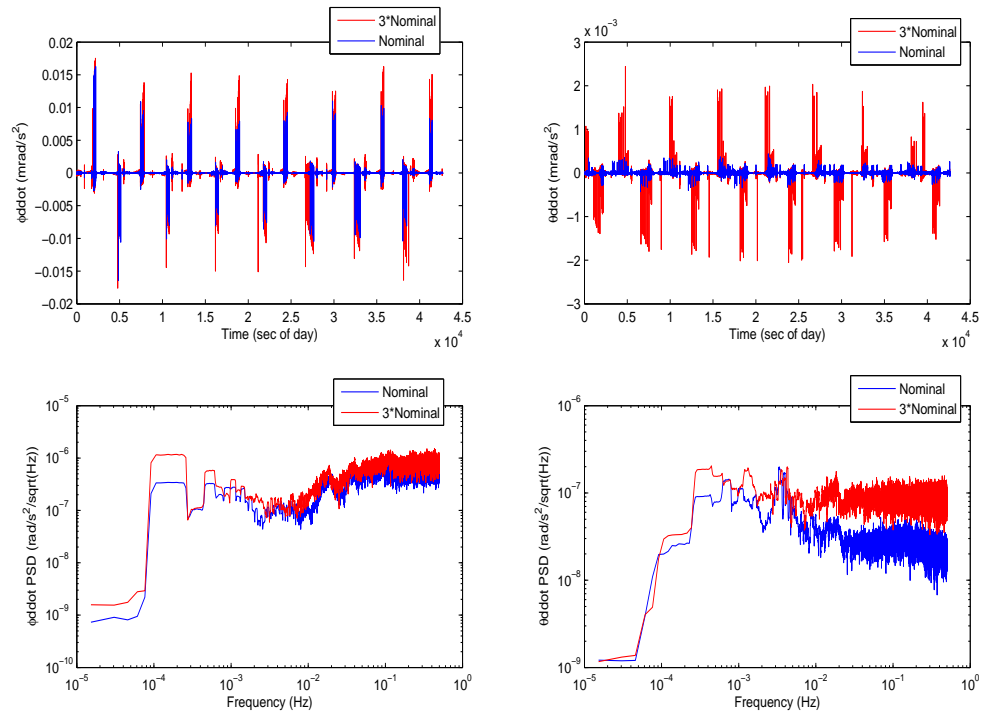


Figure 6.78: Tor2 - Roll and Pitch Attitude Acceleration Behavior

6.5.3 Magnetic Torquer Implications

As discussed in previous sections, magnetic torque rods are supplementary actuators in the GRACE ACS process. They have reduced control authority, especially in roll(ϕ) and yaw(ψ) due to the alignment of the Earth magnetic field. As a supplement, they reduce the overall effort exerted by the thrusters, and this acts to preserve propellant over the length of the mission. As such, the science magnetic control process makes use of a de-weighted amount of the control signal u_c [17]. The magnetic torque rod experiments only perturb the generated magnetic moment [11]. As such, the effects of the torque rod experiments are less extensive than the magnetometer imperfections [11], but they do directly affect the control torque delivered to the spacecraft. The results of these experiments show strong similarities with the magnetometer perturbations and the thruster misalignment perturbations.

Perturbations in the magnetic moment cause an increase in the high frequency content, resulting from the perturbed magnetic effort. This is seen in the attitude acceleration PSD, shown in Figure 6.76. The results from residual dipole and misalignment experiments are very similar. As with previous actuator tests, the same range of low frequencies is magnified in the attitude acceleration PSD. From observing the time history of the attitude acceleration, given in Figure 6.75, the magnetic moment perturbation causes the thruster firing magnitudes to also increase. This is not surprising, since magnetic field non-idealities were demonstrated to produce a similar result. In the angular PSD, the same small band of low frequencies is magnified, as given in Figure

6.74. The same change in deadband excursion periodicity is displayed in Figure 6.73. The attitude angle signal quality is also not significantly affected for this noise-free simulation.

The simulated results have shown that even though the magnetic torque rods use a de-weighted portion of the control signal, and are used as supplementary actuators, the perturbed responses are similar to those demonstrated in the thruster misalignment test. Namely, thruster effort magnitude increases, affecting the systems-level propellant usage. In addition, the quality of the attitude angle signal is not significantly degraded. As previously mentioned, a major trade study that can be examined studies the relative benefits of using torque rods versus thrusters as supplementary actuators in a reaction wheel control system. Since a coupling effect has already been demonstrated between the magnetic actuators and the thrusters, it is possible that imperfections in the presence of reaction wheels will not excite frequencies in the GRACE science band. In addition to the reaction wheel trade study, a more thorough examination of torque rod non-idealities in the presence of star camera measurement noise can also be conducted. It is possible that the de-weighting effect will cause these non-idealities to have less of an impact than thruster misalignment in the presence of measurement noise.

Chapter 7

Conclusions

7.1 Scientific Implications

The sensitivity experiments performed on the GRACE exemplar ACS model have depicted the dependency between component-level non-idealities and attitude performance characteristics. The frequency content of these results is important in classifying the effect of ACS system processes on the scientific results. For the purposes of gravity modeling, two frequency bands are of particular interest. The first of these is a low frequency spectrum ranging from approximately $100\ \mu\text{Hz}$ to $3\ \text{mHz}$, corresponding with an orbit cycle per revolution (cpr) of approximately 1 to 18. The second band ranges from approximately $3\ \text{mHz}$ to $10\ \text{mHz}$, corresponding to an orbit cpr of approximately 18 to 60. For the GRACE mission, time-variable gravity field terms are captured in the low frequency band. These terms are classified on a month to month basis, and form a major component of the scientific results. Time-variable components are not captured as accurately in the higher frequency band. However, the error terms become important in this regime as it applies to the static gravity field model. A major outcome of the sensitivity experiments is identification of ACS related effects that can influence the behavior in the frequency range of the GRACE scientific processes.

The simulated attitude is highly sensitive to star camera measurement noise. Magnification of these noise terms can cause significant degradation of the attitude signal, causing the ACS system to respond mostly to noise instead of actual deadband excursion. Although the other component-level experiments do not degrade attitude quality, they do produce results that contain implications in the GRACE science regime. It has been demonstrated that the imperfections related to magnetometer data, thruster activity, and magnetic torquer logic all affect the ACS behavior in similar ways. Perturbations in these components affect the periodicity of the angular excursions. This causes the magnetic actuation to increase slightly, and the thruster effort to magnify significantly. This causes propellant expenditure and power usage to rise.

In addition to these systems-related effects, the frequency content of the modeled attitude angles and accelerations are perturbed in regions of importance associated with GRACE science. In particular, the amplified thruster activity produces higher attitude acceleration PSD at frequencies of 100 to 200 μHz and 400 to 700 μHz for roll(ϕ) and yaw(ψ), and 300 to 500 μHz for pitch(θ). This demonstrates that sufficient magnification of component-level non-idealities can cause undesired acceleration amplifications in the GRACE science regime. Since acceleration information is used to correct the K-band ranging signal for non-gravitational effects, these amplifications can directly affect the gravity estimation signal quality. In addition, the attitude angle signal is also amplified in a regime from 400 to 600 μHz . Attitude data is used

to estimate instrument offsets, such as the accelerometer offset from the spacecraft CM. As with the acceleration data, this directly affects the time-variable gravity field capture.

In the second regime of interest, from 3 to 10 mHz, the acceleration PSD is dominated by magnetic activity. Although there is still an increase, the degree of the PSD magnification is less than for the low frequency behavior. This is not surprising since magnetic actuation is a supplementary component of the attitude control scheme. As such, it uses a de-weighted portion of the full control signal. Since the fine-pointing control is dominated by thruster activity, this actuator utilizes the full control signal. Therefore, for this configuration of control, using a PD control law class, with deadband-limited thrusters, supplementary magnetic torque rods, and star camera sensing, non-idealities in the component-level processes can cause undesired effects in the scientific regime related to time-variable gravity modeling.

7.2 Summary of Results

The major finding of the sensitivity results performed on the GRACE exemplar ACS system is high dependency of the attitude on star camera knowledge accuracy, specifically due to measurement noise. In the GRACE system, star camera attitude is the sole knowledge source. As such, any measurement noise existent cannot be compensated by accurate sensing from other sources. Any imperfections in the star camera attitude become magnified in the error estimation and control process. Of all the experiments performed through

modification of the noise-free “ideal” simulation, star camera measurement noise was the only one that significantly altered the attitude data quality. In an SST framework, attitude data quality is especially important due to its direct incorporation in the scientific estimation process. High uncertainties in the attitude signal quality can detrimentally affect the corrections to the K-band ranging data. Subsequently, this causes the gravity solution quality to decrease.

The results from this study have opened avenues for multiple future experiments. A major priority for examination is star camera noise compensation. One intrinsic test found to improve signal quality was adjustment of estimator gains. It is possible that other intrinsic adjustments can also be identified. However, more robust studies must be conducted to account for non-idealities related to other processes. In addition to intrinsic gain adjustment, an important trade study can be performed that studies the relative cost-benefit of additional sensor information inclusion. Examples of such sensors include rate gyros and accelerometers. It is possible that filtering these supplementary sources will cause measurement noise effects to minimize. The study must account for the inherent noise of these sensors, along with analyses that examine potential improvements in the attitude signal quality. In addition, a more thorough Monte-Carlo simulation that examines the effect of the star camera measurement noise on other non-idealities can be conducted. These results can possibly identify more complex dependencies that may cause ramifications on the attitude performance.

A closer inspection of the frequency content has demonstrated that component-level perturbations related to magnetometers, thrusters, and magnetic torquers cause increases in attitude acceleration PSD in the region related to time-variable component of the gravity field. These amplifications are found to be the result of increased thruster activity. The thruster effort rises to compensate for uncertainties in the attitude angle periodicity. A major trade study that can be performed is one that weights the relative costs and benefits of utilizing reaction wheels, instead of thrusters, as a primary actuator. It is possible that the frequencies of scientific interest will not be significantly affected by the characteristic frequencies of the reaction wheel mechanics. Reaction wheels were not included in the GRACE system due to their vibrational effects on the accelerometer measurement. Therefore, a major component of the trade study would examine the degradation in accelerometer performance relative to benefit gained by minimal thruster disturbance in the time-variable frequency regime. An additional study can focus on choice of supplementary actuator. Namely, this study would involve comparison of using thrusters or magnetic torquers as dedicated supplementary actuators.

Throughout this case study, the effect of attitude behavior has been analyzed independent of its influence on the scientific solution. Since the overarching necessity of improved attitude behavior is to produce more accurate scientific results, another study can be performed that focuses specifically on the attitude effect on the gravity solution. In this study, varying levels of attitude quality can be examined for their effects on the gravity estimation

process. Through this approach, a tolerance can be benchmarked for minimal attitude quality. From this, the sensor trade studies can be analyzed with this benchmark in mind as the attitude quality goal. It is possible that a modified sensor suite can be found which optimizes the attitude data quality, resulting in improved scientific results.

Appendix

Power Spectral Density (PSD) Background

The psd of a signal is defined as:

$$S(f) = \int_{-\infty}^{\infty} R(\tau) e^{-2\pi i f \tau} d\tau \quad (1)$$

Where $R(\tau)$ is the autocorrelation function of a given time-series:

$$R(\tau) = \frac{E[(X_t - \mu)(X_{t+\tau} - \mu)]}{\sigma^2} \quad (2)$$

The psd reflects the relative power distribution for a time signal over representative frequencies captured in said signal. It is visualized using a log-log scale, with frequencies ranging from lowest represented value to the Nyquist frequency, which is half the sampling rate:

$$f_{Nyq} = f_s/2 \quad (3)$$

The psd is visualized in a number of formats. A standard method for representing raw psd is through a periodogram. An example periodogram of an angular signal is given in Figure 1.

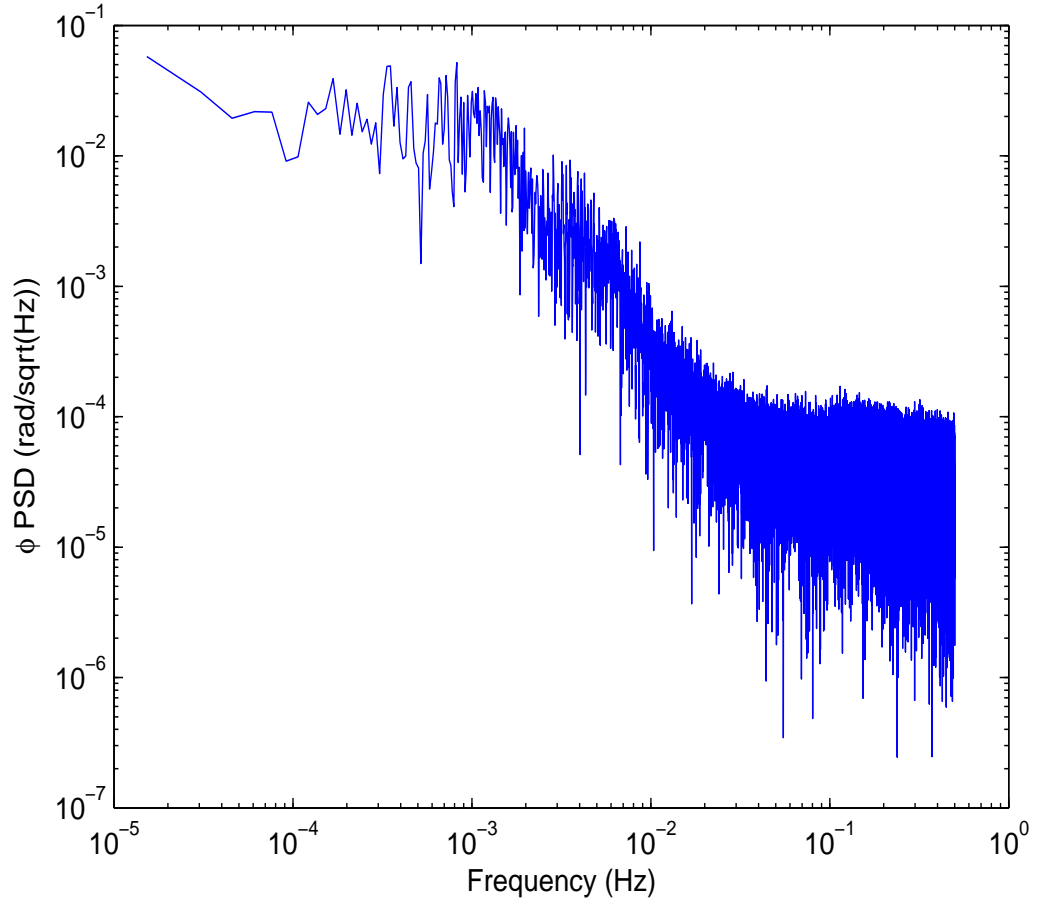


Figure 1: Periodogram of an attitude signal

The periodogram provides the greatest level of frequency content detail. However, when performing comparative analyses, it is more useful to use a smoothed version of the PSD data. For this case study, a Thomson-multitaper technique was used during comparative analysis. A Thomson-multitaper plot of the signal in Figure 1 is given in Figure 2.

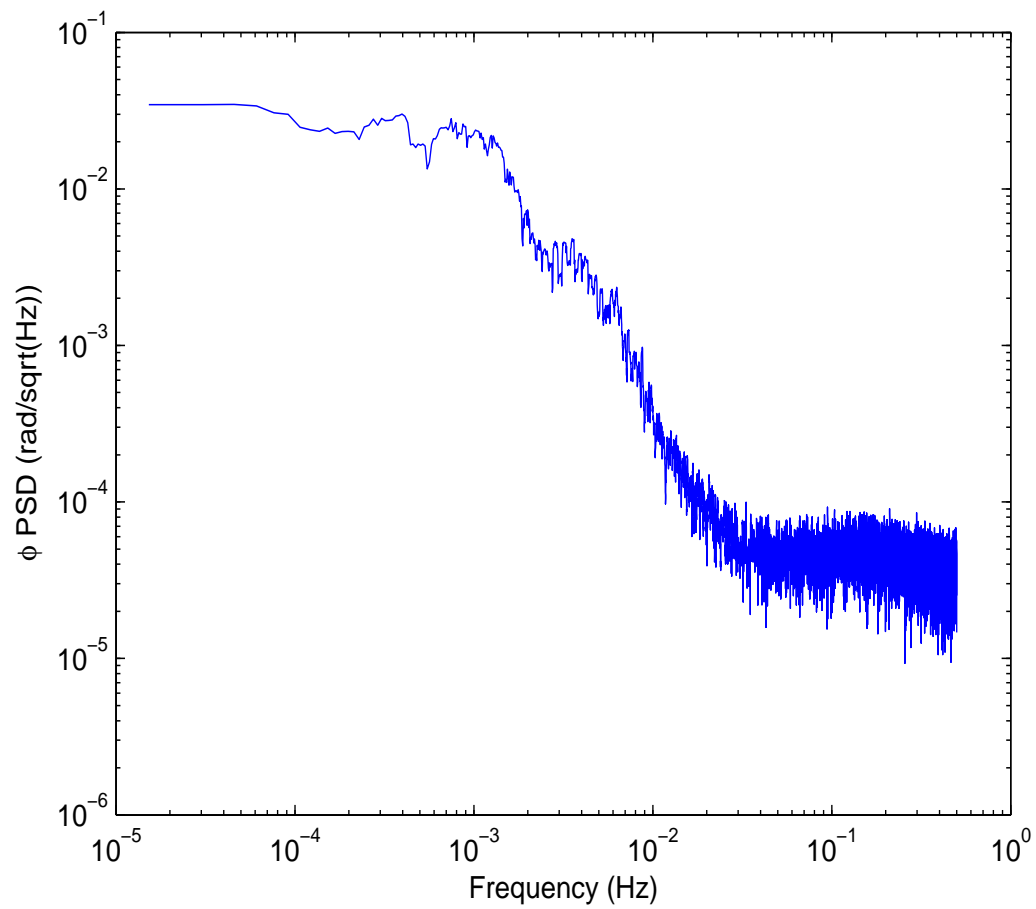


Figure 2: Thomson multitaper PSD of an attitude signal

Figure 2 depicts a smooth version of the frequency content, especially at higher frequencies. Changes in the psd are much easier to visualize than for the periodogram.

Bibliography

- [1] Tapley, B. D., Schutz, B. E., and Born, G. H., *Statistical Orbit Determination*, Elsevier Academic Press, Burlington, MA, 2004.
- [2] “Western Hemisphere Geoid,” GRACE Science Data System at the Center for Space Research, University of Texas at Austin.
- [3] Gutro, R., “CALIPSO, Cloudsat, GRACE, Science Writer’s Guide,” *National Aeronautics and Space Administration (NASA) Science Mission Directorate*, Vol. NP-2005-8-709-GSFC, August 2005, pp. 29–39.
- [4] “GRACE Mission Synopsis,” <http://www.csr.utexas.edu/grace/mission/>, [accessed 22 July 2012].
- [5] NASA, “Key GRACE Facts,” *Earth Science Reference Handbook*, December 2004, pp. 157–161.
- [6] Dunn, C., “Application Challenge: Instrument of GRACE, GPS Augments Gravity Measurements,” *GPS World*, February 2003.
- [7] Touboul, P., Foulon, B., Rodrigues, M., and Marque, J. P., “In orbit nanog measurements, lessons for future space missions,” *Aerospace Science and Technology*, Vol. 8.5, July 2004, pp. 431–441.

- [8] Bettadpur, S., “Gravity Recovery and Climate Experiment: Product Specification Document Version 4.6,” <http://podaac.jpl.nasa.gov/GRACE>, May 2012, [accessed 07 August 2012].
- [9] Herman, J., Presti, D., Codazzi, A., and Belle, C., “Attitude Control for GRACE, The First Low-Flying Satellite Formation,” *Proceedings of the 18th International Symposium on Space Flight Dynamics*, October 2004, pp. 27–32.
- [10] Wie, B., *Space Vehicle Dynamics and Control*, American Institute of Aeronautics and Astronautics, Inc., Reston, VA, 2nd ed., 2008.
- [11] Wertz, J. R., *Spacecraft Attitude Determination and Control*, D. Reidel Publishing Company, Dordrecht, Holland, 1978.
- [12] Wertz, J. R. and Larson, W. J., *Space Mission Analysis and Design*, Microcosm Press, Hawthorne, CA, 3rd ed., 1999.
- [13] “GRACE Spacecraft Configuration,” <http://www.csr.utexas.edu/grace/spacecraft/config.html>, [accessed 22 July 2012].
- [14] Nise, N., *Control Systems Engineering*, John Wiley and Sons, Danvers, MA, 4th ed., 2004.
- [15] Wang, F., *Study on Center of Mass Calibration and K-band Ranging System Calibration of the GRACE Mission*, Ph.D. thesis, University of Texas at Austin, Austin, TX, 2003.

- [16] Stanton, R., “Gravity Recovery and Climate Experiment Science and Mission Requirements Document Version 7.5,” *GRACE Project Internal Document*, Vol. 327-200, August 2000.
- [17] Stevens, H. D., “Topology for GRACE Science Mode,” *GRACE Project Internal Document*, Vol. 3UU610-99-073 Revision J, April 2001.
- [18] Stevens, H. D., “GRACE Attitude and Orbit Control System (AOCS) Specification and Description,” *GRACE Project Internal Document*, Vol. 327-440, June 2001.
- [19] Bandikova, T., Flurry, J., and Ko, U.-D., “Characteristics and accuracies of the GRACE inter-satellite pointing,” *Advances in Space Research*, Vol. 50.1, July 2012, pp. 123–135.
- [20] Wang, F., *GRACE Simulation Noise Models*, University of Texas: Center for Space Research Internal Document, June 2011.

Vita

Suyog Benegalrao was born on March 14, 1986 in Bangalore India, and moved to the United States of America with his family in 1988. After graduating from Martinsburg High School in Martinsburg, WV, he attended Georgia Institute of Technology (Georgia Tech) in Atlanta, GA. He graduated *summa cum laude* with a Bachelor of Science in Aerospace Engineering from Georgia Tech. After receiving a graduate co-op offer from NASA Goddard Space Flight Center (GSFC), he completed a Master of Science in Aerospace Engineering from the University of Texas at Austin, working on the Gravity Climate and Recovery Experiment (GRACE) mission at the Center for Space Research (CSR). He is currently employed in the Attitude Control Systems Branch, Code 591, at NASA GSFC in Greenbelt, MD.

Permanent address: 50 Babbling Brook Lane
Martinsburg, West Virginia 25403

This Thesis was typeset with L^AT_EX[†] by the author.

[†]L^AT_EX is a document preparation system developed by Leslie Lamport as a special version of Donald Knuth's T_EX Program.